



**HAL**  
open science

# Scalability and improvement of exchange bias properties for Thermally Assisted MRAM

Giovanni Maria Vinai

► **To cite this version:**

Giovanni Maria Vinai. Scalability and improvement of exchange bias properties for Thermally Assisted MRAM. Materials Science [cond-mat.mtrl-sci]. Université de Grenoble, 2013. English. NNT : 2013GRENY035 . tel-01558898

**HAL Id: tel-01558898**

**<https://theses.hal.science/tel-01558898>**

Submitted on 10 Jul 2017

**HAL** is a multi-disciplinary open access archive for the deposit and dissemination of scientific research documents, whether they are published or not. The documents may come from teaching and research institutions in France or abroad, or from public or private research centers.

L'archive ouverte pluridisciplinaire **HAL**, est destinée au dépôt et à la diffusion de documents scientifiques de niveau recherche, publiés ou non, émanant des établissements d'enseignement et de recherche français ou étrangers, des laboratoires publics ou privés.

## THÈSE

Pour obtenir le grade de

## DOCTEUR DE L'UNIVERSITÉ DE GRENOBLE

Spécialité : **Physique des Matériaux**

Arrêté ministériel : 7 août 2006

Présentée par

**Giovanni Maria VINAI**

Thèse dirigée par **Jean-Pierre NOZIERES**

et codirigée par **Bernard DIENY** et **Ioan-Lucian PREJBEANU**

préparée au sein du **Laboratoire SPINTEC, UMR8191**  
**CEA/CNRS/UJF** et de la société **CROCUS Technology**  
dans l'**École Doctorale de Physique de Grenoble**

# Scalability and improvement of exchange bias properties for Thermally Assisted MRAM

Thèse soutenue publiquement le **16 Décembre 2013**,  
devant le jury composé de :

**M. Olivier FRUCHART**

D.R. CNRS, Institut Néel, Grenoble (Président)

**M. Michel HEHN**

Prof., Institut Jean Lamour, Nancy (Rapporteur)

**M. Ricardo FERREIRA**

D.R., International Iberian Nanotechnology Laboratory INL (Rapporteur)

**M. Michel VIRET**

D.R., CEA Saclay (Examinateur)

**M. Jean-Pierre NOZIERES**

D.R., CNRS, SPINTEC, Grenoble (Directeur de Thèse)

**M. Ioan-Lucian PREJBEANU**

Ingenieur chercheur, CEA, SPINTEC, Grenoble (Encadrant CIFRE)





# Summary

<b>Introduction</b>	<b>1</b>
<b>1 Exchange bias: physical principles and state of the art</b>	<b>5</b>
1.1 Magnetism in a ferromagnetic layer	7
1.1.1 Magnetic energies	7
1.1.2 The hysteresis loop: Stoner-Wohlfarth model	8
1.2 Exchange bias phenomenon	10
1.2.1 First model: order of magnitude issue	12
1.2.2 Domain wall model	13
1.2.3 Random field theory	16
1.2.4 Polycrystalline structures: structural model	17
1.2.5 Polycrystalline structures: behaviour in temperature	18
1.2.6 Granular model of exchange biased polycrystalline systems	21
1.3 Exchange bias in patterned nanodots	22
Bibliography	25
<b>2 Exchange bias: technological applications</b>	<b>29</b>
2.1 Spin valve	31
2.1.1 From Anisotropic Magnetoresistance to Giant Magnetoresistance	31
2.1.2 The role of exchange bias coupling in spin valve structure	33
2.1.3 Technological application: hard disk read head	35
2.2 Magnetic Random Access Memory (MRAM)	36
2.2.1 Tunnel Magnetoresistance	36
2.2.2 First generation MRAM	38
2.2.3 Thermally Assisted MRAM (TA-MRAM)	41
2.2.4 Spin Transfer Torque MRAM (STT-MRAM)	43
Bibliography	46
<b>3 Sample preparation, experimental analysis and atomistic simulation</b>	<b>49</b>
3.1 Sample preparation	49
3.1.1 Sputtering deposition and annealing process	49
3.1.2 Patterning samples: from spin coating to SEM imaging	51
3.2 Sample characterization	53
3.2.1 Atomic Force Microscopy and Magnetic Force Microscopy	53
3.2.2 Focalized Magneto-optic Kerr effect	56
3.2.3 X-ray diffraction (XRD)	58
3.3 Atomistic simulation	59
3.3.1 Heisenberg model and physical parameters	59
Bibliography	65

---

---

<b>4</b>	<b>Exchange bias variability on patterned arrays of IrMn/Co square dots</b>	<b>67</b>
4.1	Aim of the study	68
4.1.1	Finite size effects on exchange patterned dots	68
4.1.2	Variability of magnetic properties on patterned systems	69
4.2	Micromagnetic effects of Co thickness on IrMn/Co square dots	69
4.2.1	Full sheet samples	69
4.2.2	Patterned samples – MFM imaging	71
4.2.3	Patterned samples – Focalized Kerr measurements	73
4.2.4	Patterned samples – Atomistic simulations	78
4.2.5	Micromagnetic effects: conclusions	84
4.3	IrMn grain size effects on exchange bias variability on IrMn/Co square dots	85
4.3.1	How to tailor IrMn grain size?	85
4.3.2	Full sheet samples – Structural and magnetic analysis	88
4.3.3	Patterned samples – MFM and Focalized Kerr measurements	93
4.3.4	IrMn microstructural effects: conclusions	97
4.4	Atomistic simulations – Influence of IrMn anisotropy axis	98
4.5	Conclusions of the chapter	101
	Bibliography	103
<b>5</b>	<b>Exchange bias enhancement: (Pt(Pd)/Co)<sub>3</sub>/IrMn/Co trilayer structure</b>	<b>107</b>
5.1	Out-of-plane anisotropy: (Pt/Co), (Pd/Co) multilayers	108
5.1.1	(Pt(Pd)/Co)/IrMn systems	109
5.2	Effects of trilayer structures on IrMn critical thickness	110
5.2.1	Hysteresis loops at room temperature	110
5.3	Effects of trilayer structures on IrMn/Co blocking temperature	113
5.3.1	Measurements in temperature	114
5.3.2	Blocking temperature distribution	118
5.4	Discussion	120
5.4.1	Structural analysis	121
5.4.2	Granular model: effects of the out-of-plane layer on IrMn/Co coupling	123
5.5	Interest of trilayer structures for technological applications	127
5.5.1	Annealing effects on bilayer and trilayer thermal properties	127
5.6	Conclusions of the chapter	129
	Bibliography	131
<b>6</b>	<b>Cu dusting at IrMn/Co interface in bilayer and trilayer structures</b>	<b>133</b>
6.1	Long range exchange bias: an open question	133
6.2	Cu interlayer in IrMn/Co bilayers	134
6.2.1	Effects on exchange bias	135
6.2.2	Microstructural analysis	137
6.2.3	Effects on blocking temperature	137
6.3	Cu interlayer in (Pt(Pd)/Co) <sub>3</sub> /IrMn/Co trilayers	140
6.3.1	Effects on exchange bias	140
6.3.2	Effects on blocking temperature	142
6.4	Discussion	143
6.5	Conclusions of the chapter	145
	Bibliography	147
	<b>Conclusions and perspectives</b>	<b>149</b>

---

## Appendix

<b>I</b>	<b>Macrospin model in Mi_Magnet simulations</b>	<b>155</b>
AI.1	Coupling between macrospins of the same material	156
AI.2	Coupling at the F/AF interface	157
<b>II</b>	<b>Scalabilité et amélioration des propriétés d'échange pour TA-MRAM</b>	<b>159</b>
AII.1	Introduction	159
AII.2	Couplage d'échange: principes physiques et état de l'art	162
AII.3	Couplage d'échange: applications technologiques	163
AII.4	Préparation des échantillons, analyse expérimentale et simulations atomistiques	164
AII.5	Variabilité de couplage d'échange dans des réseaux de plots carrés d'IrMn/Co	165
AII.6	Amélioration du couplage d'échange: la structure en tricouche (Pt(Pd)/Co)/IrMn/Co	167
AII.7	Insertion d'une "poudre" de Cu à l'interface IrMn/Co dans des structures bicouche et tricouche	168
AII.8	Conclusions et perspectives	170
	Bibliographie	174

---



*A nonno Pierino e nonna Caterina*

*“Magnetes Geheimnis, erkläre mir das!  
Kein größer Geheimnis als Liebe und Haß”  
Johann Wolfgang von Goethe*



# Remerciements

Ce n'est pas simple remercier en quelque ligne toutes les personnes qui ont été partie de ces quatre ans de vie grenobloise (je considère le stage M2 et la thèse comme une seule expérience), très enrichissants du point de vue humaine et professionnel. Je vais donc faire de mon mieux pour exprimer ma gratitude, même si je sais bien de n'être pas très fort avec les mots.

En première lieu, je voudrais remercier les personnes qui ont suivi mon travail de thèse, dans les différentes phases qu'elle a vécu. Pour commencer, Jérôme Moritz, qui m'a introduit au monde du magnétisme à partir de mon stage M1, pour m'avoir transmis sa passion pour la recherche. Je lui souhaite plain de satisfactions dans sa nouvelle aventure professionnelle. Ensuite, je remercie Lucian Prejbeanu pour avoir suivi mon travail, avant à Crocus et après à Spintec, pour sa grande disponibilité et son soutien continu, pour les corrections de ce manuscrit et les nombreux conseils professionnels. Merci également à Bernard Dieny, cœur de Spintec, pour sa culture scientifique impressionnante, sa grande humanité et pour tous les conseils qu'il ma donné pendant la thèse. Merci aussi à Sébastien Bandiera pour avoir continué le rôle de encadrant CIFRE, et pour les discussions quotidiens sur la route vers Crocus avec son première jeune Padawan (moi). Enfin, merci à Jean-Pierre Nozières pour avoir accepté d'être mon directeur de thèse. Le travaille présenté dans cette thèse n'aurait pas pu être là sans l'aide de tous ces personnes, grâce à leurs conseils scientifiques et leur soutien.

Je voudrais aussi remercier les membres du jury de thèse: tous d'abord Michel Hehn et Ricardo Ferreira pour leur rôle de rapporteurs, le président de jury Olivier Fruchart et Michel Viret qui a assisté à la soutenance. Merci pour l'intérêt montré vers mon travaille et pour les stimulants questions.

Pour bien travailler, c'est très important de pouvoir le faire dans une ambiance amicale et compétente. Pour cette raison je remercie tout le personnel Spintec pour les bons moments partagé tous les jours au boulot. Merci donc à tous ces qui m'ont aidé dans les différents étapes de la thèse, à mes co-bureau pour avoir supporté mes "discussions" en italien avec l'ordinateur, aux amis de la pause thé, aux compagnons d'aventure dans les différentes

conférences, à Vancouver pour les batailles de Jenga, à Rhodes (“Трубы горят!”) et à Denver pour les **bold** experiences. Merci aussi à l’équipe de Crocus pour leur amitié et pour les discussions philosophiques pendant les repas, à l’équipe de L\_Sim pour m’avoir amicalement accueilli dans leur labo de simulation et à l’Institut Néel, en particulier Jan Vogel, Stefania Pizzini et Manlio Bonfim, pour l’aide avec les mesures au Kerr focalisé.

Cette expérience n’été pas seulement quatre ans de dur travaille, mais aussi quatre ans de vie dans un pays étranger, où j’ai eu la chance de rencontrer plain de personnes intéressantes et de me faire des vrais, grands amis. Merci donc à La Coloc pour le soutien quotidien, les rituels après boulot (“Je pense que j’ai bien mérité une bière”) et tous les bons moments partagés ensable. Merci à la grande famille italienne – oui, il y a du vrai dans les stéréotypes – maintenant distribué entre Grenoble, Marseille, Hambourg et Jérusalem. Merci aux métalleux pour les excellentes concerts (les inoubliables Hellfest, DTP à Montpellier, les soirée à l’AmpéRage), aux amis Nanotech en Europe et aux US, aux amis du CNRS, aux “pots d’Eric” (“C’est la limite!”), aux Erasmus, aux amis du Quazar, aux nouveaux colocs “russes”, aux rencontres trop brefs et à tous ce qui ne rentrent dans aucune de ces groups mais ont été quand même importants pour moi. Merci enfin à Grenoble, ville Quechua, à ses montagnes l’hiver et ses lacs l’été, qui est devenue ma deuxième maison.

Je voudrais aussi remercier, en ordre casuel, la tartiflette, le pelle-pomme, Devin Townsend, Atom Mothers Temple, Om’s “Advaitic songs”, Electric Wizard, Frank Zappa, le Bar Bayard, la Bobine, le barman du D’Enfer, le Tårnværelse, le feuerzangenbowle, Metrovélo, le Petit Journal, le drapeau polonais, le Zombie walk, la pizza du Paparazzi, Walter White, Dr.Sheldon Cooper, Kaleesi, Dovahkiin et Charlie the Unicorn.

Un très grand merci à ma famille. Merci à mes parents, ma sœur et mon frère pour leur soutien et leur support.

Et maintenant, bonne lecture !

# Introduction

Magnetism is a fascinating physical phenomenon, first reported by Wang Xu in the fourth century B.C. in the Chinese culture and Plinius the Old in 77 A.D. in the occidental culture. They both describe the ability of lodestone to attract iron. Its first “technological” application dates of around 3000 years ago in China, where a geomagnetic lodestone was used for divination. The use for navigation purposes of a magnetite needle floating in a bowl of water as a compass, pointing to the magnetic earth poles, dates between the IX and XI century, always in China, and it is first reported in Europe in 1187 by Alexander Neckam.

First descriptions of magnetic properties of attraction and repulsion were more metaphysical than physical, both in the Chinese and the Greek cultures. With the widespread use of magnetic compasses in commercial and military boats, the study of the physical properties of magnetic needles became vital to improve the quality of the naval routes. The first scientific report on magnetic properties was written by Peter the Peregrinus de Maricourt in 1269 in the *Epistola de magnete* and marks a break between the superstitious-metaphysical descriptions of magnetic properties and a more scientific approach. Since the XIX century, all descriptions of magnetic properties were only based on the observation of the behaviour of the lodestone needle with respect to the magnetic earth poles.

Despite the widespread use, the principles of magnetism, as we know them today, remained unknown since the description of electromagnetism given by Maxwell’s equations. The atomic description of nature led to the modern vision of magnetic effects. During the last century, the study of magnetic properties always had a deep interconnection between theoretical study and technological application. From the fundamental studies of Louis Néel on magnetic properties of solids, particularly on antiferromagnetic materials, to the discovery of magnetoresistive effect and its application for data storage and recording, the study of magnetic properties had a deep evolution in the last century.

Spintec laboratory and Crocus Technology represent in Grenoble an excellent example of the coexistence of fundamental study and technological application based on magnetic materials. Founded in 2006 from Spintec, Crocus Technology is a start-up that develops Thermally Assisted Magnetic Random Access Memory (TA-MRAM), an evolution of first generation

MRAM which entered the market in 2006 with Freescale Semiconductor. The connection with the original laboratory is kept alive through a joint Research and Development program which finances among other research activities the so-called “thèse CIFRE”, a PhD with an applicative approach, closely connected with a technological application.

It is with this spirit that the study of the present manuscript was carried along the three years of thesis. The functioning principle of TA-MRAM is based on the use of exchange bias properties on both reference and storage layer. Exchange bias is a phenomenon discovered in 1956 by Meiklejohn and Bean describing the shift of the hysteresis loop along one axis due to an interface coupling between a ferromagnetic and an antiferromagnetic layer. As for the lodestone needle in the Middle Ages (without the load of superstition of course), it is intensively exploited in a wide range of technological applications but not yet completely understood.

The objective of the thesis is thus double: improving the performances of exchange biased systems and understanding the fundamental mechanisms that rule this phenomenon. In particular, key parameters for TA-MRAM performance improvements are the control of the dispersion of exchange bias from one bit to another, the tuning of blocking temperature and operating temperature range, as the optimization of exchange bias coupling itself.

Chapter 1 will describe the struggle of the scientific community in the understanding of this fascinating phenomenon, from the first intuitive model of Meiklejohn and Bean to the last models including the influence of grain size in the antiferromagnetic layer and the effects in temperature. The chapter will also show the granular model developed during the thesis. Finally, it will present the state of the art of the experimental studies on exchange bias structures, particularly on patterned systems.

In Chapter 2 the reader will find a description of the most important technological applications of exchange bias, from the milestone of spin valves to the TA-MRAM developed by Crocus Technology.

Chapter 3 will give an exhaustive description of all the steps performed in Spintec laboratory to fabricate and characterize the exchange biased systems, from the sputtering deposition to the patterning of the dots by electron-beam lithography. The chapter will also present the different techniques used to characterize the samples, both physically and magnetically. The chapter will finally describe the model of the atomistic simulations developed in collaboration with L\_Sim laboratory, used in Chapter 4.

Chapter 4 is devoted to the study of exchange bias patterned systems with IrMn/Co bilayers. Three main parameters were considered in the study: the thickness of the Co layer, the thickness of the IrMn layer and the influence of the buffer layer. The study on patterned system was performed with a focussed Kerr system that allowed analysing the magnetic behaviour of few dots per measurements, thus giving a direct qualitative evaluation of exchange bias variability, a very important parameter for MRAM reliability. Together with the description of the results on patterned systems, the chapter will present the analysis of the physical properties of full sheet samples, in particular crystallography and grain size distribution as a function of the different parameters. The chapter will also show the results obtained through the atomistic simulations, in particular the study on the reversal mechanisms and magnetic configuration as a function of Co thickness and the stability of IrMn grains.

Chapter 5 describes an improvement of the standard bilayer exchange biased structure, with the introduction of a second ferromagnetic layer with strong out-of-plane anisotropy. This trilayer structure resulted in a reduced critical thickness of the IrMn layer and an increase of blocking temperature compared to equivalent bilayer structures. These characteristics are an improvement of the performance of exchange biased systems, with possible direct application on TA-MRAM storage layer. The two effects are explained through the granular model of exchange bias exposed in Chapter 1.

In the last Chapter 6, a second way to improve exchange bias performances is presented, with the introduction of a non-magnetic Cu dusting layer at the IrMn/Co interface. The behaviour in temperature is also analysed. The non-magnetic layer is finally implemented in the trilayer structure. The combination of trilayer structure and Cu dusting layer led to an exchange bias field three times larger than the original bilayer structure, with improved thermal properties.



# Chapter 1

## Exchange bias: physical principles and state of the art

In 1922 Stern and Gerlach experimentally found that the electron is defined not only by its charge  $e$  but also by two possible magnetic states. The beam of silver atoms, deflected by a gradient applied magnetic field, split into two distinct populations [1], proving the space quantization of the magnetic moments [2]. In 1925, Uhlenbeck and Goudsmit postulated that the electron possesses an intrinsic angular momentum, named spin [3], with two possible states  $\uparrow$  and  $\downarrow$ , which gives rise to a magnetic moment in the electron when interacting with a magnetic field, giving a theoretical explanation to the experiment of Stern and Gerlach.

From these starting points we can define the spin of an electron as:

$$\mathbf{m}_s = \pm \mu_B \mathbf{z} \quad (1.1)$$

with  $z$  being the axis of the moment and  $\mu_B$  being the Bohr magnetron. The sum of the spins of the electrons in an atom gives the total spin magnetic moment  $\mathbf{S}$ . Its value depends on the number of energy shells and subshells are filled according to Hund's rule and Pauli's exclusion principle. Filled subshells do not contribute to magnetism, having all the magnetic moments compensated; only unfilled subshells contribute to magnetism.

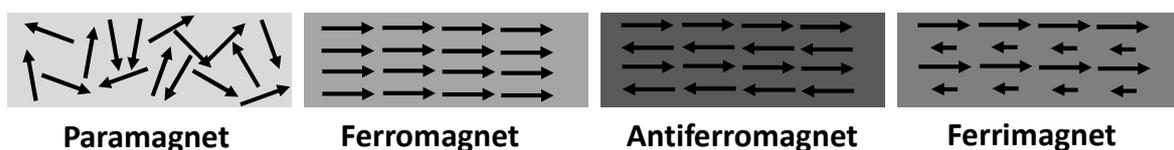


**Fig. 1.1** – Schematic of the spin configurations for paramagnetic, ferromagnetic, antiferromagnetic and ferrimagnetic materials.

On the periodic table, 79 out of 103 elements carry a non-zero magnetic moment at the fundamental atomic state. On a macroscopic scale, the coupling between magnetic moments

determines the type of magnetic order present in the considered material. The coupling energy is defined as:

$$E_{ij} = -J_{ij} \mathbf{m}_i \mathbf{m}_j \quad (1.2)$$

with  $J_{ij}$  the coupling constant and  $i$  and  $j$  are the indexes of first neighbours spins. If the coupling constant is positive, the magnetic moments align in the same direction and the material is defined as ferromagnetic (F). If  $J_{ij} < 0$ , the spins align in opposite directions. If the net moment is equal to zero, the material is named antiferromagnetic (AF), otherwise, in case of unbalance, it is named ferromagnetic. The coupling energy is an ordering energy: when thermal energy overpasses it, the magnetic order is lost and the material becomes paramagnetic (Fig.1.1). The temperature at which a F material passes to the paramagnetic state is named Curie temperature ( $T_C$ ); for the AF case, it is named Néel temperature ( $T_N$ ) [4]. Examples of strongly F materials are iron (Fe), cobalt (Co) and nickel (Ni); ferromagnetism may also present in form of alloys, like CoFe or NiFe. Antiferromagnetic materials can be single elements like manganese (Mn) or chromium (Cr), oxides (NiO, FeO, CoO, MnO) or alloys (IrMn, PtMn, FeMn, CrMn).

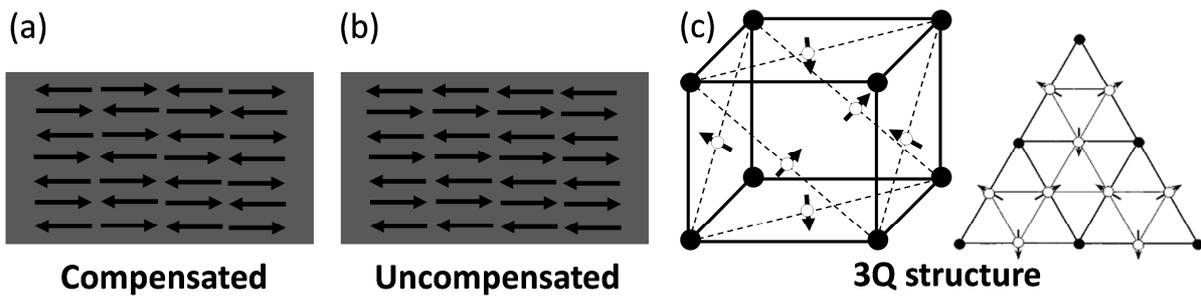


**Fig. 1.2** – Schematics of AF spin configurations: compensated (a), uncompensated (b) and 3Q structure [6] (c).

In the case of AF materials, the spin configuration present in order to have a zero net moment may be present in many different forms. On a two-dimension level, the AF can be modelled as compensated or uncompensated. In the first case each atomic plane presents spins with opposite directions, giving a net moment equal to zero. For the uncompensated configuration, each plane has a zero net moment with alternating spin directions (Fig.1.2a,b). Considering a three dimensional case, things get more complex, namely because of the crystallographic structure of the material which has to be taken into account [5]. In the case of (111) fcc systems, as it is the case for IrMn [6,7] and FeMn [5,8,9], the minimum of energy is obtained with the spins pointing in a so-called non collinear 3Q spin structure, shown in Fig.1.2c, with the AF structure on the left and the (111) surface spin structure on the right [6].

# 1.1 Magnetism in a ferromagnetic layer

## 1.1.1 Magnetic energies

Considering a single domain F layer, its equilibrium status is determined by a compromise between four competing energies. The total energy of a homogeneous F energy is given by:

$$E_{TOT} = E_{ex} + E_{dip} + E_{anis} + E_H \quad (1.3)$$

being respectively the exchange energy, the anisotropy energy, the dipolar energy and the Zeeman energy (see Fig.1.3).

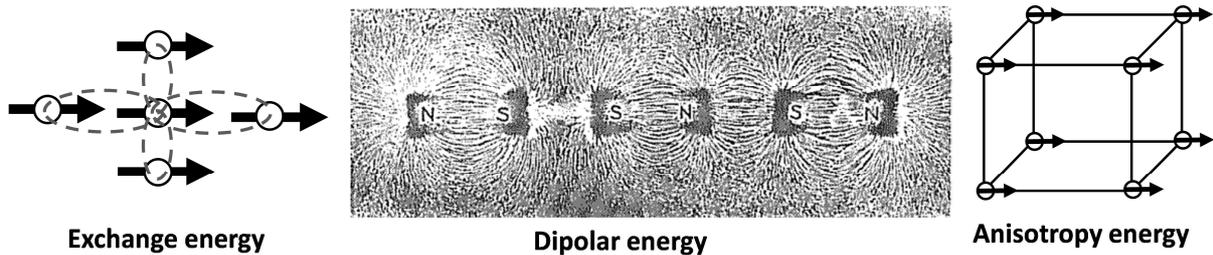


Fig. 1.3 – Schematic of the effects of the exchange, dipolar (from [10]) and anisotropy energy.

**Exchange energy:** it is a short range electrostatic coupling, involving first neighbouring spins. For a F material, the coupling is positive and tends to align all the spins along the same direction (Eq.1.2).

**Dipolar energy:** it is a long term interaction, describing the influence on each spin of the magnetic field generated by all the other spins in the material. This coupling energy decreases as the cube of the distance and depends on the magnetization of the material; its value is small compared to the exchange coupling at atomic distance, but becomes dominating at long distance. The effect of dipolar energy is to reduce the energy due to the presence of poles in the material. It tends to “close” the magnetic flux lines, with the creation of a demagnetizing field antiparallel to the direction of the magnetization. The magnetic field due to the flux lines outside the material is named dipolar field. Exchange energy and dipolar energy play two opposite functions, and the resulting magnetic configuration is a compromise between the two. This aspect becomes particularly important at the nanoscale, both for the micromagnetic configuration of a dot and for the interdot coupling (see Paragraph 1.3).

**Anisotropy energy:** it is an energy acting individually on each spin, due to the crystallographic characteristics of the material. Because of the symmetry of the crystal, a F (or AF) material tends to align along one favourite axis, defined as the easy axis. If only the first order term is considered, the anisotropy energy can be written as:

$$E_{anis} = -K_{anis} V \cos^2 \theta \quad (1.4)$$

with  $K_{anis}$  being the anisotropy constant,  $V$  the volume of the F material and  $\theta$  the angle between the magnetization direction and the axis anisotropy, dependent on the crystallographic structure of the material. The intensity of  $K_{anis}$  strongly depends on the material, and according to the crystalline structure Eq.1.4 may take more complex forms. The anisotropy constant contains two contributions, a volumetric one and a surface one. The latter can become dominant on ultrathin magnetic layers. Its value is temperature dependent, and goes to zero at  $T_C$ .

**Zeeman energy:** it is the energy spent by the system to align the spins along the direction of the applied magnetic field. It is defined as:

$$E_{ij} = -V M_S \cdot H \quad (1.5)$$

with  $M_S$  the saturation magnetization of the material and  $H$  the applied field vectors.

### 1.1.2 The hysteresis loop: Stoner-Wohlfarth model

The behaviour of a F material under an applied field can be described with the Stoner-Wohlfarth model [11]. The authors of this model considered the case of an ellipsoid F material (shape chosen to have a uniformly magnetized material [12]) with a dimension small enough to be modelled as a macrospin. Under an applied magnetic field, it reverses coherently on the field plane. By considering a total energy:

$$E = -K_{anis} V \sin^2 \theta - VM_S H \cos(\theta - \phi) \quad (1.6)$$

with  $\theta$  the magnetization angle and  $\phi$  the field angle, the system presents two equilibrium states at  $\theta = 0^\circ$  and  $\theta = 180^\circ$ , being  $\theta$  along the easy axis (see Fig.1.4a). The two states are separated by an energy barrier:

$$\Delta E_{\pm} = K_{anis} V \left( 1 \pm \frac{M_S H}{2K_{anis}} \right)^2 \quad (1.7)$$

as represented in Fig.1.4b. For a  $H$  large enough the barrier is overpassed and the magnetization is reversed, switching from one equilibrium state to the other. The field at which the switching takes place is called coercive field and it is defined as:

$$H_C = \frac{2K_{anis}}{M_S} \quad (1.8)$$

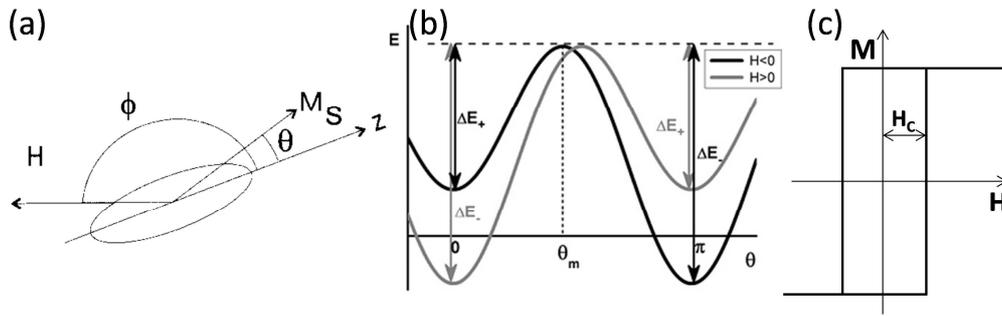


**Fig. 1.4** – (a) Scheme of the F ellipsoid with magnetization  $M_S$  under a field  $H$ , with  $z$  the easy axis [13]. (b) Energy diagram of the under a positive (black line) and negative (grey line) field [14]. (c) Example of hysteresis loop along the easy axis.

When a field larger than  $H_C$  is applied back and forth along the axis, a full loop is performed. The magnetization curve as a function of the applied field takes the name of hysteresis loop (Fig.1.4c).

If the field is applied with an angle  $\phi$  with respect to the easy axis of magnetization, the field necessary to reverse the magnetization is given by  $H_C^\phi = H_{||}^{2/3} + H_{\perp}^{2/3} = (2K_{anis}/M_S)^{2/3}$ , with  $H_{||}$  and  $H_{\perp}$  being the two components of the applied field with respect to the easy axis [15]. From the combination of the two it results that the minimum field necessary to reverse the magnetization is for  $\phi = 45^\circ$ . This principle was used in the first generation MRAM, as it will be shown in Paragraph 2.2.2.

If temperature is taken into account, thermal fluctuations help in overcoming the energy barrier. Néel's model [16], later refined by Brown [17], defined a switching rate:

$$\tau_{\pm} = f_0 \exp\left(\frac{\Delta E_{\pm}}{k_B T}\right) \quad (1.9)$$

with  $f_0$  being the thermal attempt frequency ( $10^9$  Hz) and  $k_B$  the Boltzmann constant.

If at a temperature  $T$  the switching rate  $\tau_{\pm}$  is shorter than the measuring time, the F layer continuously passes the energy barrier and is defined as superparamagnetic. The same definition applies to antiferromagnetic materials [18].

The following paragraph will show what happens when an AF layer is added in contact with the F one, which are the effects on the hysteresis loop and which additional energies have to be taken into account. This phenomenon is known as exchange bias coupling.

## 1.2 Exchange bias phenomenon

Exchange bias is a physical phenomenon first experimentally observed in 1956 by Meiklejohn and Bean, who described the presence of a “new magnetic anisotropy” due to the interaction between a F and an AF layer. In their first brief letter [19] they described the experimental procedure that is still nowadays used to fix the exchange bias coupling. The material was composed of a Co body (F layer) surface oxidized to form a CoO shell (AF layer). When the system was over the Néel temperature of CoO (i.e. at room temperature, being  $T_N = 293\text{K}$ ), the AF layer behaved as a paramagnetic layer and the magnetic properties of the bilayer were the same that for a simple Co layer. When the material was cooled down to  $77\text{K}$  under a saturating field, the AF layer passed from paramagnetic to antiferromagnetic state, coupling with the F layer. It resulted in a shift of the hysteresis loop along the axis of the applied magnetic field, defined as easy axis. This shift was later named exchange bias field. The setting of exchange bias coupling and its effect on the hysteresis loop can be schematized as shown in Fig.1.5, which gives an intuitive description of exchange bias coupling for a generic F/AF bilayer.

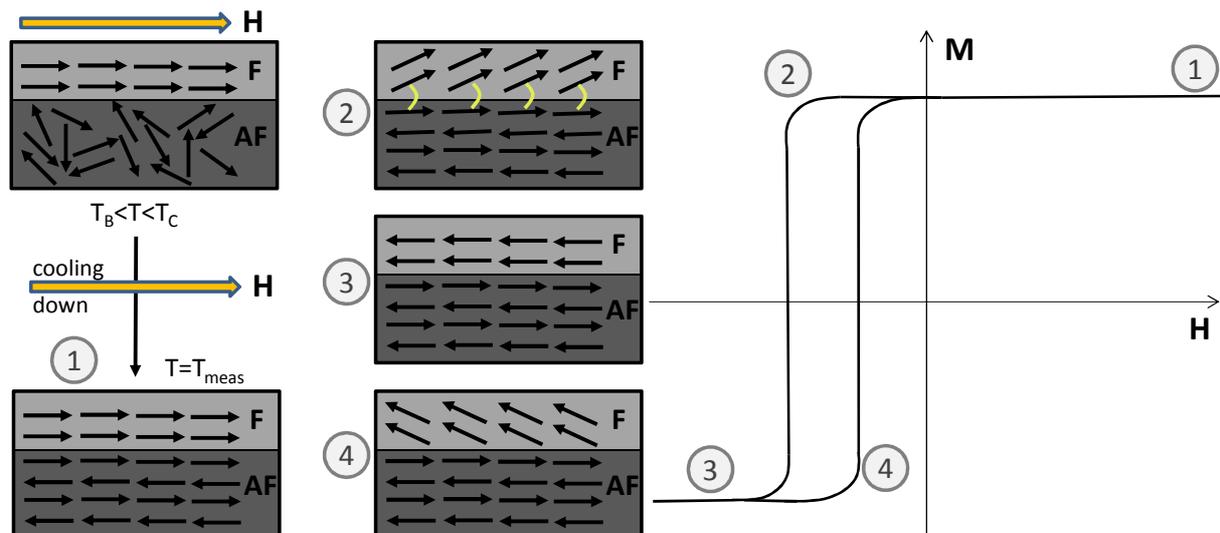


Fig. 1.5 – Schematic of exchange bias coupling.

First, the system is heated up to a temperature  $T$  large enough to unblock the spins in the AF layer. The critical temperature at which the AF spins start unblocking is named blocking temperature  $T_B$  and is usually lower than the bulk Néel temperature of the AF for polycrystalline structures [20]. The system is then cooled down under a saturating field  $H$  to a measuring temperature  $T_{meas} < T_B$ . When the AF orders antiferromagnetically, it couples at the interface with the F layer (a coupling that is conventionally considered ferromagnetic) along the direction of the applied setting field, the easy axis (phase 1 of Fig.1.5). This is valid if the

blocking temperature is lower than the Curie temperature of the F ( $T_B < T_C$ ), because the F layer has to maintain its ferromagnetic order during the cooling down procedure. Whereas a hysteresis loop is measured along the easy axis at  $T_{meas}$ , the interface coupling pins the F layer along the direction of the cooling field. The field necessary to reverse the F magnetization becomes larger than for a single F layer (phase 2). For large enough applied field, the F layer is saturated (phase 3). When the field is reduced, the coupling of the AF spins, which did not move during the loop, forces the F spins to reverse earlier (phase 4), giving a shift of the hysteresis loop. Together with the shift of the hysteresis loops, exchange biased systems usually present an increase of the coercivity.

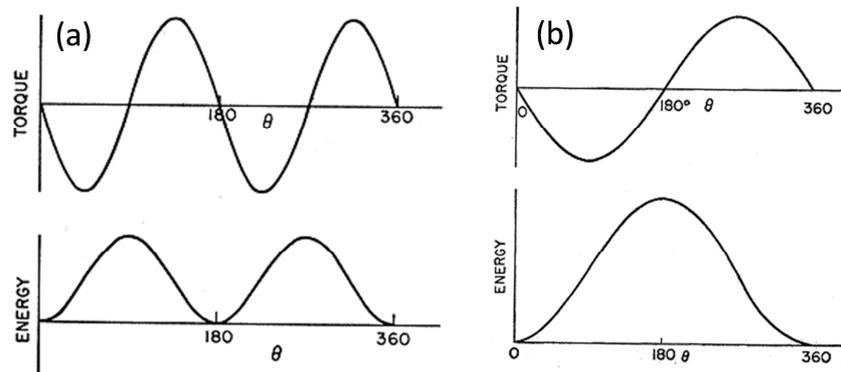


Fig. 1.6 – Torque and energy curves for single Co layer (a) and Co/CoO bilayer below  $T_N$  [16].

Meiklejohn and Bean analysed this effect by torque measurements, with torque being the derivative of the energy as a function of the angle  $\theta$  ( $T = \partial E / \partial \theta$ ) on the anisotropy plane. Whereas the uncoupled Co layer with uniaxial anisotropy showed a torque curve proportional to  $\sin 2\theta$ , Co/CoO system presented along the easy axis a  $\sin \theta$  dependence. This means that, while uniaxial systems are stable (i.e. has energy minima) at both  $\theta = 0^\circ$  and  $\theta = 180^\circ$ , the unidirectional anisotropy at the F/AF interface gives rise to a single energy minimum at  $\theta = 0^\circ$  (See Fig.1.6). A direct consequence is the shift of the hysteresis loop along the  $H$ -axis, compared to the usual symmetrical hysteresis loop of single F layers.

Now, how to quantitatively describe the loop shift and which parameters play a role in the quality of the coupling? In the following paragraphs a series of models, grouped by theoretical approach, will be described, giving an overview on the possible explanations of the exchange bias phenomenon.

## 1.2.1 First model: order of magnitude issue

In their following articles [21,22] Meiklejohn and Bean gave a first model of exchange bias exclusively based on the presence of the additional unidirectional anisotropy, like in the scheme of Fig.1.5, based on the Stoner-Wohlfarth description of magnetization reversal.

First, they considered a single domain spherical particle at 0 K with uniaxial anisotropy. Defining  $\theta$  as the angle between the easy axis of magnetization and the applied field, the free energy is equal to:

$$F = HM_s \cos \theta + K_{anis} \sin^2 \theta \quad (1.10)$$

Taking the derivative  $\partial F / \partial \theta$  and searching for maxima and minima, the coercive force of the resulting hysteresis loop is defined as  $H_c = \frac{2K_{anis}}{M_s}$ .

If to Eq.1.10 a unidirectional anisotropy (as observed from torque measurements) of the form  $-K_U \cos \theta$  is introduced, with  $K_U$  the unidirectional anisotropy, the resulting free energy:

$$F = HM_s \cos \theta + K_{anis} \sin^2 \theta - K_U \cos \theta \quad (1.11)$$

gives a solution to  $\partial F / \partial \theta$  similar to the previous one, with an additional “effective field” [21] which shifts the hysteresis loop:

$$H^1 = H - K_U / M_s \quad (1.12)$$

The additional term can be rewritten with an explicit definition of the thickness of the F layer  $t_F$  [20], so that the exchange bias field is defined as:

$$H_{ex} = \frac{J_{ex}}{M_s t_F} \quad (1.13)$$

where  $J_{ex}$  is the interface exchange coupling. This gives a linear dependence between the loop shift and the inverse of the thickness of the F layer, sign that the exchange bias is, in first approximation, an interfacial phenomenon. Experimentally, the tendency  $H_{ex} \propto t_F^{-1}$  has always been observed, holding for F thicknesses smaller than the F domain wall size.

Meiklejohn later redefined the equation [22], considering independently the angles of the different vectors (see Fig.1.7b) and ascribing the uniaxial anisotropy of an exchange biased system to the only AF layer ( $K_{anis} \cong K_{AF}$ ):

$$F = HM_s \cos(\theta - \beta) + K_{AF} \sin^2 \alpha - K_U \cos(\beta - \alpha) \quad (1.14)$$

which can be rewritten as an energy per unit area:

$$E = HM_s t_F \cos(\theta - \beta) + K_{AF} t_{AF} \sin^2 \alpha - J_{ex} \cos(\beta - \alpha) \quad (1.15)$$

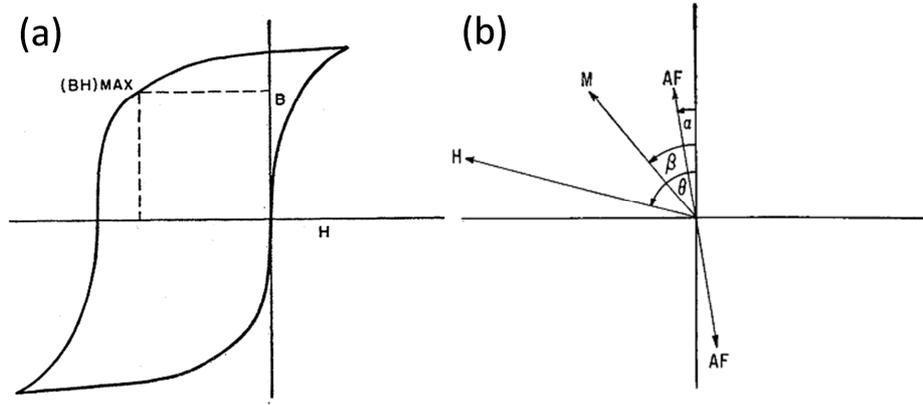


Fig. 1.7 – (a) Schematic of an exchange biased hysteresis loop [21]. (b) Vector diagram of Eq.1.14 [22].

Minimizing Eq.1.15 as a function of  $\alpha$  and  $\beta$ , the equilibrium positions of the F and the AF spins are obtained for:

$$\begin{cases} \frac{\partial E}{\partial \alpha} = 0 \Rightarrow \sin 2\alpha = \frac{J_{ex}}{K_{AF} t_{AF}} \sin(\beta - \alpha) \\ \frac{\partial E}{\partial \beta} = 0 \Rightarrow \sin(\beta - \alpha) = \frac{HM_S}{J_{ex}} \sin(\theta - \beta) \end{cases} \quad (1.16)$$

From the first term of Eq.1.16 it results that the necessary condition in order to have exchange bias is that  $K_{AF} t_{AF} \gg J_{ex}$ , i.e. the anisotropy energy of the antiferromagnet is much larger than the exchange coupling. If this is true, it means that  $\alpha$  remains small independently of  $\beta$ . If  $K_{AF} t_{AF} \ll J_{ex}$ , then it is energetically more convenient to keep  $(\beta - \alpha)$  small, i.e. F and AF spins rotate together. A numerical simulation of the two regimes can be found in Ernult's thesis [23].

This first model has the great quality of giving a first simple picture of the effects of the F/AF coupling. Unfortunately, if  $J_{ex}$  is taken with values close to the F coupling, the resulting exchange bias shift has values two orders of magnitude larger than the experimental one. For this reason, more parameters have to be taken into account to model the exchange bias phenomenon [24].

## 1.2.2 Domain wall model

Chronologically, the second model of exchange bias was proposed by Louis Néel in 1967 [25]. He considered an uncompensated AF layer interface coupled with a F layer. In his article, together with a first explanation to the training effect, i.e. the tendency of exchange bias to reduce its value after the first hysteresis loop, discovered the previous year by Paccard [26], he proposed a domain wall model of exchange bias coupling. The domain wall is formed in the F or AF materials, according to which is the most energetically

favourable solution, parallel to the F/AF interface. Let's take the case of domain wall in the AF layer. Néel considered the interface no more composed by fixed spins; when a magnetic field is applied in the direction opposite to the one of the cooling field, the spin structure of the AF is deformed, following the reversal of the F layer. The resulting exchange field  $H_{ex}$  and coercivity  $H_C$  are thus the result of the changes occurring along the thickness of the AF layer during reversal. If the domain wall remains stable, the loop shows a shift due to the maintained interface coupling. If the domain wall reverses, the irreversible changes of magnetization in the AF layer give a contribution to the coercivity of the loop, which sums up to the intrinsic coercivity component of the F layer.

The domain wall model was later proposed by Mauri *et al.* [27] in 1987. In the following, the formalism of their paper is used.

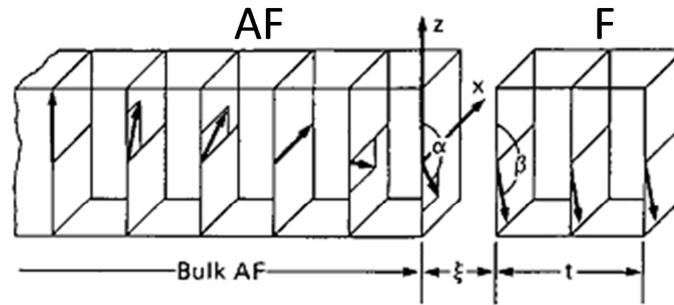


Fig. 1.8 – Magnetic configuration at the F/AF interface [27]. Only one AF spin direction is represented for clarity reasons. Unidirectional anisotropy along the  $z$  axis, applied field along the opposite direction.

The paper considers a F/AF system composed by an uncompensated infinitely thick AF layer and a F layer of thickness  $t$ , with  $t$  much smaller than a F domain wall width. In this way, the creation of the domain wall takes place only in the AF layer. The interface is taken without any roughness effect, i.e. the AF spins are totally uncompensated also at the F/AF interface. During the reversal of the F layer, because of the interfacial coupling, the AF spins begin to rotate as well, leading to a planar domain wall in the AF layer, as shown in Fig.1.8. The energy cost per unit area  $\sigma$  of the domain wall is:

$$\sigma = 2\sqrt{A_{AF} K_{AF}} \quad (1.17)$$

with  $A_{AF}$  and  $K_{AF}$  being the AF exchange stiffness and the AF crystalline anisotropy respectively.

This energy term has to be added to the total energy of interface  $\delta$ , which results equal to:

$$\delta = HM_s t_F (1 - \cos \beta) + K_F t_F \cos^2 \beta + A_{ex} / \xi [1 - \cos(\alpha - \beta)] + 2\sqrt{A_{AF} K_{AF}} (1 - \cos \alpha) \quad (1.18)$$

which has a similar structure compared to Eq.1.15, having the Zeeman term, the anisotropy and the exchange terms plus the domain wall term at the bottom. The equation contains the anisotropy of the F layer  $K_F$ , the exchange energy  $A_{ex}$  and the interface distance  $\xi$ . By

normalizing Eq.1.18 in units of  $2\sqrt{A_{AF}K_{AF}}$ , and substituting  $A_{ex} \propto J_{ex}/a$ , with  $a$  the AF lattice parameter [20], the interface term becomes:

$$\lambda = \frac{J_{ex}}{2a\sqrt{A_{AF}K_{AF}}} \quad (1.19)$$

which is a ratio between the interface coupling and the stiffness of the AF layer, i.e. the “torque” done by the F layer on the interface AF spins during magnetization reversal and the resistance of the AF spin structure to it.

Two extreme cases can be taken into account: strong coupling and weak coupling. For strong coupling ( $\lambda \gg 1$ ) the reversal of the F layer is accompanied by the creation of a  $180^\circ$  domain wall in the thickness of the AF layer. Because of the infinite thickness of the AF layer, no irreversible process takes place in the AF layer, and the resulting exchange bias is equal to:

$$H_{ex} = \frac{2\sqrt{A_{AF}K_{AF}}}{M_S t_F} \quad (1.20)$$

The domain wall term in the nominator of Eq.1.20 reduces the value of  $H_{ex}$ , compared to Eq.1.13, to values close to the experimental one.

For weak coupling ( $\lambda \ll 1$ ), the interface coupling is so weak that no domain wall is created. The resulting exchange bias in this case is:

$$H_{ex} = \frac{J_{ex}}{M_S t_F}. \quad (1.21)$$

with  $J_{ex}$  small enough to give values of  $H_{ex}$  close to the experimental one.

Mauri’s model describes the limit for the formation of a domain wall in the AF layer as the ratio between interface coupling  $J_{ex}$  and AF anisotropy  $K_{AF}$ . Nonetheless, because of the infinitely thick AF layer, it does not give any explanation on the contribution of the AF to the coercivity of the loop and it considers the interface completely flat.

Other models have described exchange bias coupling through domain wall models. Kiwi *et al.* [28] proposed a model for a fully compensated AF structure, with the formation of a domain wall due to the interface canting of the AF spins coupled with the F spins. Kim *et al.* [29] proposed, on the basis of Mauri’s model, a description of the enhancement of coercivity due to the magnetic defects at the interface, which causes the pinning of AF domains.

### 1.2.3 Random field theory

Contemporaneously to Mauri's model, Malozemoff [30] presented a random field model based on the effects of interface roughness. The description of exchange bias is based on the Random Field Ising Model first proposed by Imry and Ma [31]. In their paper they described the influence of random impurities and disorder in the phase transition of systems, adding a random field term to the Hamiltonian of the system. Malozemoff applied their model for a F/AF interface. The AF layer is considered as a fully compensated single crystal. In an ideal, flat surface, no net moment would be present at the interface, thus no loop shift would appear. The AF moment imbalances at the interface, responsible of the exchange coupling, are given by atomic steps of interfacial roughness and defects.

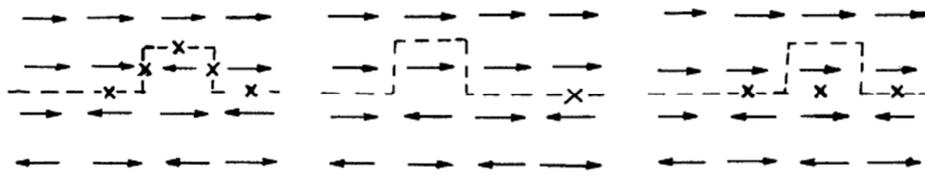


Fig. 1.9 – Examples of spin configuration for an AF atomic step [30].

A monoatomic step at the interface causes a change in the sign of the interactions, deviating from the perfect compensated configuration. This deviation depends on the location of the irregularity (see Fig.1.9). Considering a random distribution of atomic bumps, the random field model argues that the average interfacial energy is different from zero. With this spin configuration in the AF layer, and a single domain F layer, it is energetically convenient for the system to divide the AF film into domain-like regions to minimize the net random unidirectional anisotropy. Contrary to the domain wall models, these domains would have their domain walls perpendicular to the interface, as firstly proposed by Kouvel [32], with semispherical shape (Fig.1.10).

The dimension of the domains is given by the balance between the AF uniaxial anisotropy and exchange anisotropy, with a size of the order of  $\pi\sqrt{A_{AF}/K_{AF}}$ .

The exchange bias field is then determined as the ratio between the interfacial energy difference due to the AF domain  $\Delta\sigma$  and the applied field pressure:

$$H_E = \frac{\Delta\sigma}{2M_F t_F} \quad (1.22)$$

Quantitatively, this equation approaches to the experimental values as Mauri's one, despite the different hypothesis taken into account.

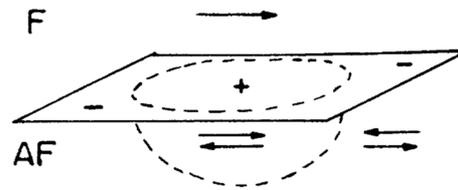


Fig. 1.10 – Examples of spin configuration for an AF atomic step [30].

After Malozemoff's paper, other models have implemented the random model approach, like Morosof *et al.* [33] and Zang *et al.* [34], which examined the role of random field interaction on coercivity.

### 1.2.4 Polycrystalline structures: structural model

The previously presented models consider the AF and F layers in their limit of single crystal structure. For technological applications, most of the exchange biased systems are however deposited by sputtering deposition (see Paragraph 3.1.1). This deposition technique gives polycrystalline structure instead of monocrystalline one. For this reason, it is important to take into account the role of the crystallographic structure in exchange biased systems, particularly for the AF layer.

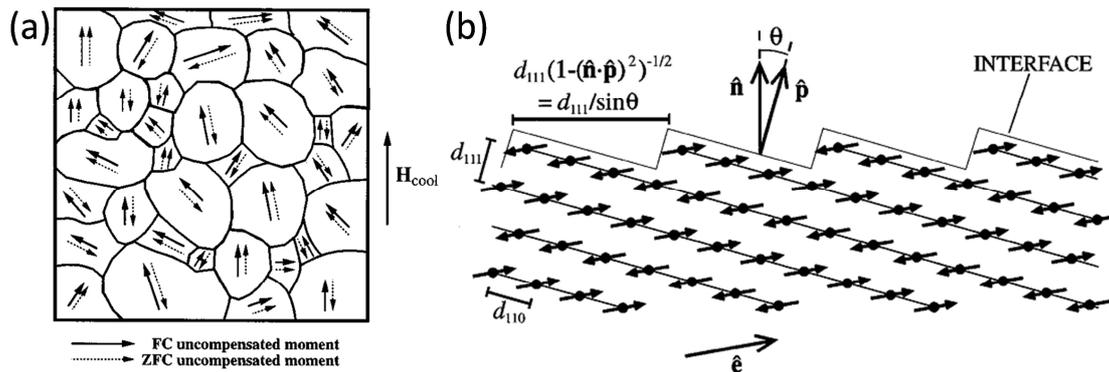


Fig. 1.11 – (a) Polycrystalline structure of AF grains. After field cooling, the AF spins of each grain align along their uniaxial direction with the interfacial spins following the cooling field direction [36]. (b) Interface configuration for compensated AF spin with rough interface [35].

This approach was first theoretically developed by Takano *et al.* [35,36]. They considered a compensated AF structure. Because of the crystalline structure of the AF layer, the interfacial layer of spin will consist on a rough surface with alternate spin directions; at each atomic step, the spin orientation in the AF layer changes of 180°. In this way, considering a polycrystalline structure with grains of different dimensions, each grain contributes to the exchange bias with a total non-zero moment at the F/AF interface. Through a series of Monte Carlo simulation for different level of grain superpositions and roughnesses, they evaluated that on such a compensated structure, only ~ 1% of the interfacial spins, i.e. the uncompensated ones, contributes to the exchange. The low percentage of involved AF

spins in the coupling would justify the low values of exchange bias experimentally observed. Moreover, the simulation proved a correlation between exchange and grain size (for a stable grain) on the form  $H_E \propto L^{-1}$ , with  $L$  the lateral size of the grain, experimentally measured on polycrystalline exchange biased systems.

### 1.2.5 Polycrystalline structures: behaviour in temperature

Most of the models on polycrystalline structures take into account the role of temperature and its impact on the stability of the AF grains. Studies of the evolution of exchange bias in temperature go back to the very first experiments of Meiklejohn and Bean [16], who observed a quasi-linear decrease of  $H_{ex}$  with temperature. When the exchange bias approaches to zero, i.e. the blocking temperature is reached, a corresponding peak in coercivity was soon observed [37].

The first model in temperature for polycrystalline structures the one proposed by Fulcomer and Charap in 1972 [38]. In their fundamental work, they considered a distribution of non-interacting AF grain size volumes coupled with the F layer. The model takes into account the thermal fluctuation effects on the grain volumes, on a Stoner-Wohlfarth model, with an energy barrier  $\Delta E = K_{AF}V$ , being  $V$  the volume of the AF grain. According to its volume, the contribution of each grain to the hysteresis loop changes.

Considering a wide distribution of grain size and shapes, at a fixed temperature they defined three contributions from the AF grains. One population is composed by grains which, because of thermal fluctuations, are superparamagnetic and reverse continuously, contributing partially to the coercivity. The second is composed by grains with weak anisotropy and strong coupling; they are trained during the hysteresis loop and contribute to the coercivity. The last one is composed by “frozen” grains, which maintain their coupling with the F layer during the loop and contribute to the exchange bias. According to the model, ideally at 0 K all grains are blocked and frozen, so no coercivity contribution would come from the AF grains (actually, things get more complicated at very low temperature [39]). When temperature is increased, the thermal fluctuations become more important and the fraction of frozen grains reduces, with an increase of the superparamagnetic and trained ones. At blocking temperature, all grains contribute to the coercivity. For higher temperatures, the AF grains totally uncouple from the F layer and the resulting loop is the one of the single F layer.

This first model describes with good accuracy the behaviour in temperature of exchange biased polycrystalline structures and it is generally considered correct.

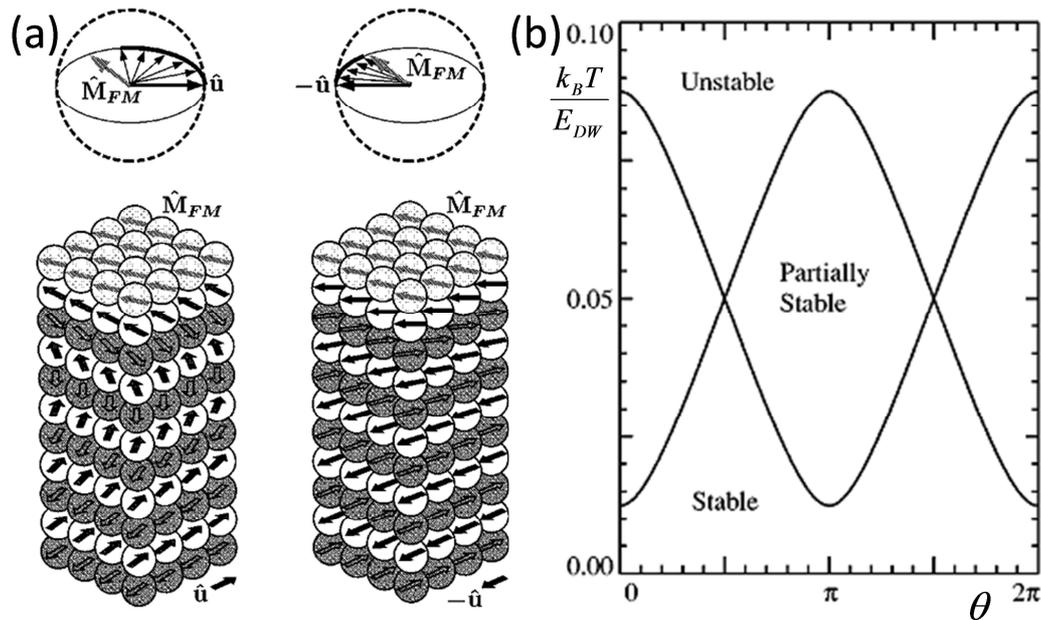


**Fig. 1.12** – (a) Partial wall domain in the AF during F reversal. The left structure represents a stable domain wall, whereas the right one a switched domain wall [42]. (b) Stability graph as a function of angular applied field and ratio between thermal energy and AF domain wall energy.

Stiles and McMichael later developed this model [40-42]. They considered a system with AF grains with no intergrain coupling, coupled with the F layer through direct coupling and partial domain wall in the AF, like in Néel's model. Each grain contributes to the exchange bias shift if it remains stable during the rotation of the F layer; if the AF grain becomes thermally unstable, it undergoes an irreversible transition, contributing to the coercivity (Fig.1.12a). An additional parameter in the stability of the AF grain is the angle of its uniaxial anisotropy with respect to the field cooling direction. For small angles, the partial domain wall does not easily reverse, contributing to  $H_{ex}$ ; above a critical angle, the AF partial wall becomes unstable and switches together with the F layer, contributing to  $H_C$  [40]. In temperature, each grain may pass through three states: stable, contributing to the unidirectional anisotropy; partially stable, following the F reversal, thus dissipating energy; unstable, i.e. switching from one state to the other during the measurement time (Fig.1.12b) [41]. Together with the irreversible transitions in the AF layer, a contribution to the coercivity comes from the inhomogeneous reversal of the F layer due to the interfacial irregular coupling with the AF layer [42].

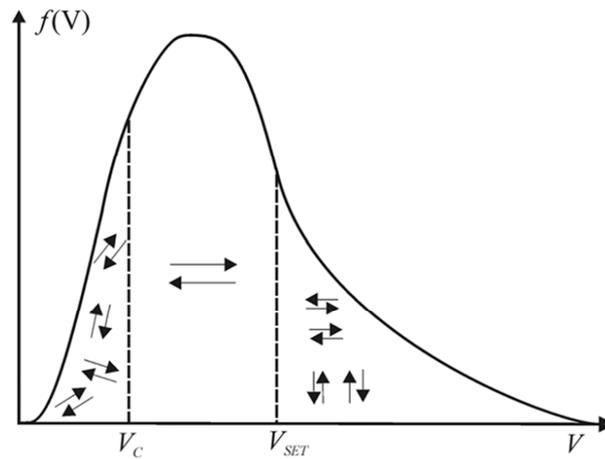


Fig. 1.13 – AF grain size distribution after field cooling [44].

Recently, O’Grady proposed an experimentally based polycrystalline model on AF grain size distributions [43]. By considering a lognormal distribution of AF grain volumes (Fig.1.13), the stability of the grains and their contribution to the hysteresis loop is defined by their volume and by the setting temperature. The ratio of grains that take part in the hysteresis loop shift, for a given volume distribution  $f(V)$ , is given by the integral over  $V$  in the range between two critical volumes  $V_{SET}$  and  $V_C$ :

$$H_E \propto \int_{V_C}^{V_{SET}} f(V) dV \quad (1.23)$$

with  $V_C$  being the critical volume under which grains are thermally unstable at the measuring temperature and  $V_{SET}$  is the setting volume over which grains were not coupled during the annealing process. A series of measurements for different grain volume distributions for different setting and measuring temperatures validated the polycrystalline approach for sputtering exchange biased systems. More details on the temperature measurement protocol used during the thesis will be given in Chapter 5.

## 1.2.6 Granular model of exchange biased polycrystalline systems

During the thesis, the following granular model of exchange biased polycrystalline systems has been developed, based on the models presented in the previous paragraphs. A schematic of the considered grain populations is presented in Fig.1.14.

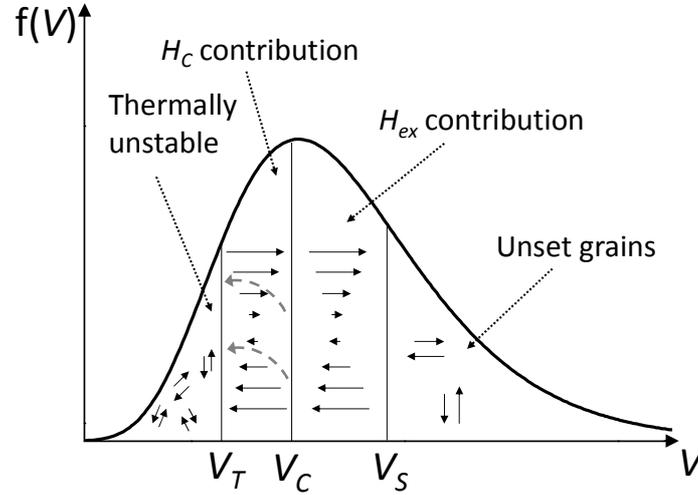


Fig. 1.14 – Schematic representation of the AF grain distribution in a polycrystalline system.

The volume distribution of non-interacting AF grains gives rise to four grain populations whose distribution depends on temperature. During the hysteresis loop, the AF grains can be either: i) thermally unstable and not coupled to F; ii) coupled to F but switchable, thus contributing to the coercivity  $H_C$  [40]; iii) stable, thus contributing to the loop shift; iv) finally, a part of the AF grain population can remain unset after field cooling depending on the annealing temperature  $T_{ann}$ . It has been experimentally shown [43] that, by controlling  $T_{ann}$  and annealing time, the proportion of set grains can be adjusted for a given AF grain size distribution.

Considering the volume distribution due to grain size variations, a temperature-dependent critical volume  $V_c \cong t_c d_c^2$ , with  $d_c$  being the critical grain diameter, can be defined by considering that a AF grain can contribute to the exchange bias field only if, in a Meiklejohn model, the pinning torque due to the AF anisotropy on the grain spin lattice ( $K_{AF} t_{AF} d_c^2$ ) is larger than the dragging torque  $J_{ex} d_c^2$  exerted by the F magnetization during reversal:

$$K_{AF} t_{AF} \gg J_{ex} \quad (1.24)$$

This yields an effective barrier for AF grain magnetic switching given by:

$$\Delta E = d_C^2 K_{AF} t_{AF} \left( 1 - \frac{J_{ex}}{2K_{AF} t_{AF}} \right)^2 \quad (1.25)$$

This barrier has to be compared with the thermal activation factor  $\text{Log}\left(\frac{\tau_{measure}}{\tau_0}\right) k_B T$  where

$\tau_{measure}$  is the characteristic measurement time and  $\tau_0 \approx 10^{-9}$  s the attempt time. This yields:

$$V_C = \frac{\text{Log}\left(\frac{\tau_{measure}}{\tau_0}\right) k_B T}{K_{AF} \left( 1 - \frac{J_{ex}}{2K_{AF} t_{AF}} \right)^2} \quad (1.26)$$

The critical volume under which grains become thermally unstable is defined by the activation energy barrier  $\Delta E = K_{AF} V_T$ , with  $\Delta E$  being the thermal activation factor, thus:

$$V_T = \frac{\text{Log}\left(\frac{\tau_{measure}}{\tau_0}\right) k_B T}{K_{AF}} \quad (1.27)$$

As a result, grains with  $V < V_T$  are thermally unstable, whereas those in the range  $V_T < V < V_C$  contribute to coercivity. Over  $V_C$ , AF grains are stable and contribute to the loop shift, for volumes up to a critical setting value  $V_S$ , over which the annealing procedure was not able to couple the AF grains with the F layer.

When an exchange biased system is heated up,  $H_{ex}$  decreases because of the increasing proportion of unstable grains. When the loop shift vanishes ( $H_{ex} = 0$  Oe), the blocking temperature  $T_B$  is reached. At this temperature, a corresponding peak in  $H_C$  is usually observed, and it is attributed to instabilities in the AF grains [42]. For higher temperatures,  $H_C$  decreases since F and AF layers become more and more decoupled and the anisotropy decreases both in the AF and F layers [45].

### 1.3 Exchange bias in patterned nanodots

During the last decades the improvement in patterning structures at the micro and nanoscale, plus the use of patterned thin magnetic layers for technological applications (see Chapter 2) led to an increasing interest of magnetic properties on the nanostructures. In fact, the behaviour of the magnetic layers substantially changes from a macroscopic, continuous layer to a system with two or three dimensions of micro or nanometric size [46]. In particular, whereas the reversal takes place through domain nucleation close to defects and singularities and its propagation under increasing field, the magnetization reversal mechanism on

nanometric structures is completely different. If the lateral size is too small to allow the formation of a domain wall, the reversal may take place through coherent rotation, curling or bucking. The micromagnetic configuration itself changes according to the lateral size and the thickness of the magnetic layer [47]. The equilibrium between dipolar and exchange energies determines the magnetic state at remanence, which can be single domain or complex flux closure configurations. Moreover, shape effects may have a crucial role in the anisotropy term for determining the magnetic state (see Fig.1.15). Effects like interdot coupling through dipolar field, structural changes due to fabrication steps or dot shape variability may affect the magnetic behaviour of the dots [48].

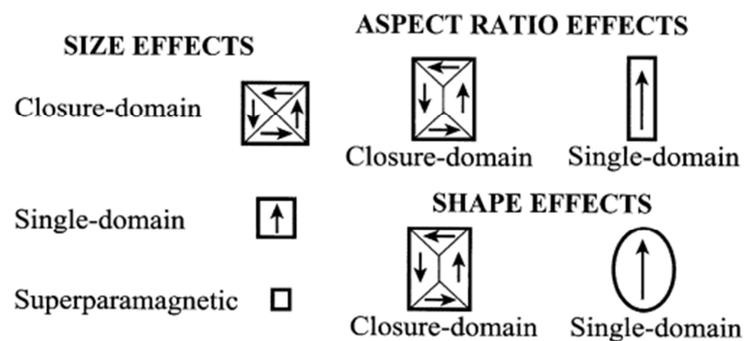


Fig. 1.15 – Typical effects present on nanopatterned magnetic layers [47].

The variety of possible geometries (dots, antidots, wires, rings), shapes and other parameters (lateral size, interdot distance, patterning process, deposition technique...) make nanomagnetism a wide field of research, with numerous challenges from both the fabrication and the characterization points of view [49].

In this field, an important branch is taken by exchange bias properties. Being an interfacial phenomenon, its characteristics may be importantly changed by the dimension of the system, together with the different behaviour of the F layer itself. Together with the fundamental aspect, the study of exchange bias properties on the nanoscale is particularly important for technological applications. As it will be shown in the following chapter, exchange bias is nowadays used in Magnetic Random Access Memories and hard disk read head.



Fig. 1.16 – Sketches of possible nanopatterned configurations for exchange biased dots.

On exchange biased nanosystems, the interfacial anisotropy adds to the energy equilibrium of the system. Together with the shape and geometry ranges of choice, additional

parameters like F and AF materials, layer thicknesses, substrate and buffer layer, deposition ordering and etching (see Fig.1.16), annealing process, field cooling direction with respect to the dot geometry and others make the possibilities of study theoretically endless. To make things easier, as for exchange biased continuous layers, results of different publications are often contradictory and it is difficult to observe clear tendencies, because very different results can be obtained by varying just one of the parameters listed above [50].

Among the wide variety of studies on the subject, the following table gives few experimental results on the behaviour variability of exchange bias patterned dots. In particular the case with a F/AF bilayer, with the F layer on the top (as in Fig.1.16 on the left), is taken into account. More punctual references will be given along Chapter 4.

Ref.	materials	geometry	dimensions	effects
[51]	NiFe/IrMn	square dots	1x1 $\mu\text{m}^2$	Reduction of exchange bias compared to full sheet
[52]	Fe/FeF <sub>2</sub>	circular dots	300; 600 nm diameter	coherent reversal
[53]	NiFe/Hf	circular dots	2 $\mu\text{m}$ diameter	closure domain structure
[53]	NiFe/Hf	circular annular dots	2 $\mu\text{m}$ diameter	closure domain structure; higher coercivity than circular dots
[53]	NiFe/Hf	square dots	2x2 $\mu\text{m}^2$	closure domain structure
[53]	NiFe/Hf	square annular dots	2x2 $\mu\text{m}^2$	Coexistence of domain walls; higher coercivity
[53]	NiFe/Hf	triangular dots	2 $\mu\text{m}$ lateral size	Central domain wall
[53]	NiFe/Hf	triangular annular dots	2 $\mu\text{m}$ lateral size	Presence of a hard axis along one side and easy axis at opposite vertex
[54]	NiFe/FeMn	elliptical ring arrays	3x1.8 $\mu\text{m}^2$ . 400 nm and 750nm widths	Shifted hysteresis loops. Passage from vortex state to onion state
[55]	NiO/NiFe on Si	circular and rectangular shapes	2, 5, 10 $\mu\text{m}$ (diameter); 2x10, 5x10 $\mu\text{m}^2$ (rectangle)	Larger dependence of exchange bias on aspect ratio than on lateral size
[56]	NiO/NiFe on MgO	circular and rectangular shapes	2, 5, 10 $\mu\text{m}$ (diameter); 2x10, 5x10 $\mu\text{m}^2$ (rectangle)	Larger dependence of exchange bias on lateral size
[57]	NiFe/IrMn	circular dots	130nm diameter	Increase of exchange bias compared to continuous layer; smoother magnetization reversal
[58]	NiFe/IrMn	elliptical dots	0.5x0.75; 0.5x1; 0.5x1.5 $\mu\text{m}^2$	Magnetization reversal mechanism dependent on field cooling direction compared to ellipse
[59]	NiFe/IrMn	square dots	90x90 nm <sup>2</sup>	Exchange bias reduced or increased compared to full sheet depending on IrMn thickness
[60]	NiFe/IrMn	circular disk	1 $\mu\text{m}$ diameter	Vortex state when zero field cooled. Shifted multidomain behaviour when field cooled ; fixed chirality
[60]	CoFe/IrMn	circular disk	1 $\mu\text{m}$ diameter	Finite coercivity; magnetization reversal through domain walls
[61]	NiFe/FeMn	square dots	520 and 220 nm lateral size	Reduction of lateral size lowers exchange bias field and blocking temperature

**Table 1.1** – List of experimental results on patterned exchange biased dots.

# Bibliography

- [1] Gerlach W and Stern O 1922 *Zeitschrift für Physik* **9** 353
- [2] Friedrich B and Herschbach D 2003 *Phys. Today* **56** 53
- [3] G E Uhlenbeck and S Goudsmit 1925 *Naturwissenschaften* **13** 953
- [4] Du Trémolet de Lacheisserie E *Magnétisme, Tome 1: Fondements* (EDP Sciences, Grenoble) 2000
- [5] Jungblut R, Coehoorn E, Johnson M T, aans de Stegge J and Reinders A 1994 *J. Appl. Phys.* **75** 6659
- [6] Tomeno I, Fuke I N, Iwasaki H, Sahashi M and Tsunoda Y 1999 *J. Appl. Phys.* **86** 3853
- [7] Sakuma A, Fukamichi K, Sasao K and Umetsu R Y 2003 *Phys. Rev. B* **67** 024420
- [8] Schulthess T C, Butler W H, Stocks G M, Maat S and Mankery G J 1999 *J. Appl. Phys.* **85** 4842
- [9] Stocks G M, Shelton W A, Schulthess T C, Ujfalussy B, Butler W H and Canning A 2002 *J. Appl. Phys.* **91** 7355
- [10] Chen C W *Magnetism and metallurgy of soft magnetic materials* (North-Holland Publishing Company, Amsterdam) 1977
- [11] Stones E C and Wohlfarth E P 1948 *Phil. Trans. R. Soc. Lond. A* **240** 599
- [12] Osborn J A 1945 *Phys. Rev.* **67** 351
- [13] Weller D and Moser A 1999 *IEEE Trans. Magn.* **35** 4423
- [14] Rotarescu C, Petrila I and Stancu A 2011 *Physica B* **406** 2177
- [15] Prejbeanu I L, Kerekes M, Sousa R C, Sibuet H, Redon O, Dieny B and Nozieres J P 2007 *J. Phys.: Condens. Matter* **19** 165218
- [16] Néel L 1949 *Ann. Geophys.* **5** 99
- [17] Brown W F 1963 *Phys. Rev.* **130** 1677
- [18] Néel L *Compt. Rend.* 1961 **252** 4075
- [19] Meiklejohn W H and Bean C P 1956 *Phys. Rev.* **102** 1413
- [20] Nogués J and Schuller I K 1999 *J. Magn. Magn. Mat.* **192** 203
- [21] Meiklejohn W H and Bean C P 1957 *Phys. Rev.* **105** 904
- [22] Meiklejohn W H 1962 *J. Appl. Phys.* **33** 1328
- [23] Ernult F 2002 *Thèse Université Joseph Fourier*
- [24] Berkowitz A and Takano K 1999 *J. Magn. Magn. Mat.* **200** 552
- [25] Néel L 1967 *Ann. Phys. (Paris)* **2** 61
- English translation: Néel L *Selected Works of Luis Néel* 469 (Gordon and Breach, New York, 1988)
- [26] Paccard D, Schlenker C, Massenet O, Montmory R and Yelon A 1966 *Phys. Status Solidi* **16** 301
- [27] Mauri D, Siegmann H C, Bagus P S and Key E 1987 *J. Appl. Phys.* **62** 3047
- [28] Kiwi M, Mejía-López J, Portugal R D and Ramírez R 1999 *Appl. Phys. Lett.* **75** 3995
- [29] Kim J V, Stamps R L, McGrath B V and Camley R E 2000 *Phys. Rev. B* **61** 8888

- [30] Malozemoff A P 1987 *Phys. Rev. B* **35** 3679
- [31] Imry Y and Ma S K 1975 *Phys. Rev. Lett.* **35** 1399
- [32] Kouvel J S 1961 *J. Phys. Chem. Solids* **21** 57
- [33] Morosov A I and Sigov A S 2002 *J. Magn. Magn. Mater.* **242–245** 1012
- [34] Zhang S, Dimitrov D V, Hadjipanayis G C, Cai J W and Chien C L 1999 *J. Magn. Magn. Mater.* **198–199** 468
- [35] Takano K, Kodama R H, Berkowitz A E, Cao W and Thomas G 1997 *Phys. Rev. Lett.* **79** 1130
- [36] Takano K, Kodama R H, Berkowitz A E, Cao W and Thomas G 1998 *J. Appl. Phys.* **83** 6888
- [37] Hagedorn F B 1967 *J. Appl. Phys.* **38** 3641
- [38] Fulcomer E and Charap S H 1972 *J. Appl. Phys.* **43** 4190
- [39] Baltz V, Rodmacq B, Zarefy A, Lechevallier L and Dieny B 2010 *Phys. Rev. B* **81** 052404
- [40] Stiles M D and McMichael R D 1999 *Phys. Rev. B* **59** 3722
- [41] Stiles M D and McMichael R D 1999 *Phys. Rev. B* **60** 12950
- [42] Stiles M D and McMichael R D 2001 *Phys. Rev. B* **63** 064405
- [43] O’Grady K, Fernandez-Outon L E and Vallejo-Fernandez G 2010 *J. Magn. Magn. Mat.* **322** 883
- [44] Vallejo-Fernandez G, Fernandez-Outon L E and O’Grady K 2008 *J. Phys. D: Appl. Phys.* **41** 112001
- [45] Ali M, Marrows C H, Al-Jawad M, Hickey B, Misra A, Nowak U and Usadel K D 2003 *Phys. Rev. B* **68** 214420
- [46] Skomski R 2003 *J. Phys.: Condens. Matter* **15** R841
- [47] Cowburn R P, Koltsov K, Adeyeye O, Welland M E and Tricker O M *Phys. Rev. Lett.* **83** 1042
- [48] Martin J I, Nogués J, Lui K, Vicent J L and Schuller I K 2003 *J. Magn. Magn. Mater.* **256** 449
- [49] Lau J W and Shaw J M 2011 *J. Phys. D.: Appl. Phys.* **44** 303001
- [50] Nogués J, Sort J, Langlais V, Skumryev V, Suriñach S, Muñoz J S and Baró M D 2005 *Phys. Rep.* **422** 65
- [51] Shen Y, Wu Y, Li K, Qiu J and Guo Z 2002 *J. Appl. Phys.* **91** 8001
- [52] Li Z, Petravic O, Eisenmenger J and Schuller I K 2005 *Appl. Phys. Lett.* **86** 072501
- [53] Nakatani R, Takahashi N, Yoshida T and Yamamoto M 2002 *Jpn. J. Appl. Phys.* **41** 7359
- [54] Jung W, Castaño F J, Morecroft D, Ross C A, Menon R and Smith H I 2005 *J. Appl. Phys.* **97** 10K113
- [55] Wang Y J and Lai C H 2001 *J. Appl. Phys.* **89** 7537
- [56] Sort J, Glaczyńska H, Ebels U, Dieny B, Giersig M and Rybczynski J 2004 *J. Appl. Phys.* **95** 7516
- [57] Yu J, Kent A D and Parkin S S P 2000 *J. Appl. Phys.* **87** 5049
- [58] Sort J, Buchanan K S, Pearson J E, Hoffmann A, Menéndez E, Salazar-Alvarez G, Baró M D, Miron M, Rodmacq B, Dieny B and Nogués J 2008 *J. Appl. Phys.* **103** 07C109
- [59] Baltz V, Sort J, Landis S, Rodmacq B and Dieny B *Phys. Rev. Lett.* **94** 117201

[60] Tanase M, Petford-Long A K, Heinonen O, Buchanan K S, Sort J and Nogues J 2009 *Phys. Rev. B* **79** 014436

[61] Sasaki I, Nakatani R, Ishimoto K, Endo Y, Shiratsuchi Y, Kawamura Y and Yamamoto M 2007 *J. Magn. Magn. Mat.* **310** 2677



# Chapter 2

## Exchange bias: technological applications

We are nowadays living in the information era, an historical period in which everyday life is regulated by high-technological devices. Since the spread of the internet, and the diffusion of high speed connections, with portable devices like tablets and smartphones always connected, the quantity of digital information that everyday is exchanged around the world is exponentially increasing.

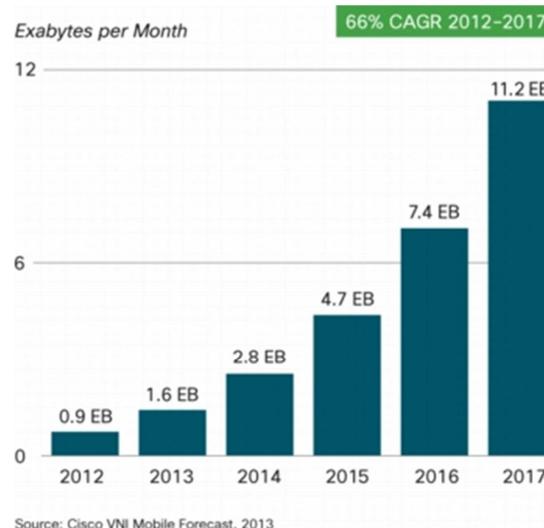


**Fig. 2.1** - Cisco Forecasts 11.2 Exabytes per Month of Mobile Data Traffic by 2017 [1].

As shown in Fig.2.1, mobile data traffic is forecasted to increase from 0.9 Exabytes in 2012 to 11 in 2017, mainly due to the explosion of the Asian market and a widespread diffusion of smartphones. How to face this increase of the information demand?

The technology roadmap of semiconductors proposed by Intel cofounder George Moore in 1965 [2] announced a doubling of chip performances every 18 months. This bold

prediction, given at the first steps of transistor computers, was like a sword of Damocles hanging over the head of R&D engineers. Indeed Moore's law requires a continuous improvement of chip performances, including processing speed, memory capacity, energy consumption and cost. Moore's law is nowadays still, for most of these parameters, valid. This has been made possible by reducing the size of semiconductor transistor, from the 10  $\mu\text{m}$  node of 1971 to the 22 nm one in 2012. This allowed a (roughly) exponential growth of chip performances. The predictions of the International Technology Roadmap for Semiconductors to further decrease the transistor size to down to 15 nm in 2015 [3] are inducing researchers to shift from transitional transistors to more exotic structures like nanowires.

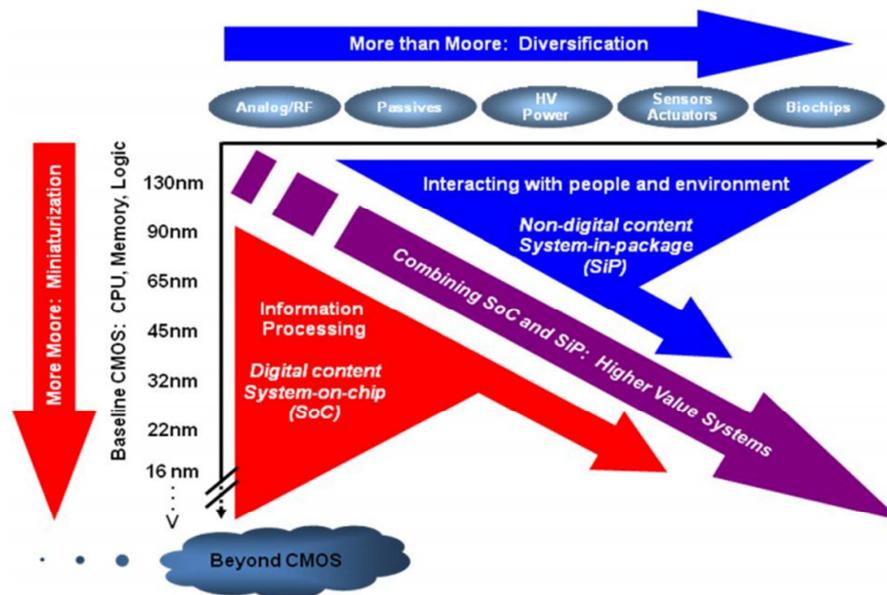


Fig. 2.2 – Tendency of Moore's and More than Moore's laws evolution [3].

However, Moore's law will eventually face its ultimate physical limitations. Together with this, the cost to build a manufacturing facility keeps increasing from node to node. Therefore, parallel to the semiconductor development, a series of diversified technologies were started to be developed in order to obtain similar performances without the scaling node issue, approach known as "More than Moore" (Fig.2.2) [4]. In this big family a large number of technologies are included, from Micro Electro Mechanical Systems (MEMS) to biosensors. Spintronic is part of this large family.

Classical electronic devices are based on the properties of the electrical charge of the electron in conductors and semiconductors. In spintronic devices, the magnetic momentum of the electron, the spin, is exploited as a second degree of freedom to manipulate the properties of electrical current. Magnetic Random Access Memory (MRAM) is one of the main applications of the spintronic group. Contrary to hard disk sequential memory, RAM devices

allow the data reading and storage in any random order. Whereas transistor-based RAMs like Static-RAM (SRAM) or Dynamic-RAM (DRAM) are volatile, i.e. the information is lost when the power is switched off, MRAM is intrinsically non-volatile and can guarantee a long data retention (typically of 10 years). It is the result of a long process of research in the field of magnetic thin films, starting from the discovery of the magnetoresistive effect to its implementation into spin valves. One fundamental physical property necessary for the correct working of MRAM is exchange bias. In the following paragraphs, it will be shown how exchange bias coupling is implemented in data storage devices, starting from spin valve and its application in hard disk head drives down to TA-MRAM (Thermally Assisted – MRAM), Crocus Technology improved implementation of standard MRAM.

## 2.1 Spin Valve

Spin valve was the first technological application of exchange bias [5]. In the following paragraph, the concept of Magnetoresistance, the other fundamental physical phenomenon present in spin valves, is described, starting from the anisotropic magnetoresistance first and going to the giant magnetoresistance later. After the presentation of the spin valve structure, its application on hard disk read heads will be described.

### 2.1.1 From Anisotropic Magnetoresistance to Giant Magnetoresistance

Magnetoresistance defines the property of a conducting material to change its electrical resistance under an applied magnetic field. The effect was first discovered by W. Thompson (Lord Kelvin) on iron and nickel [6]. He noticed how the resistance of the material changed according to the direction of the applied magnetic field with respect to the current: resistivity increased if they were parallel ( $\rho_{//}$ ), it decreased if they were crossed ( $\rho_{\perp}$ ). The difference  $\Delta\rho = \rho_{//} - \rho_{\perp}$  is called Anisotropic Magnetoresistance (AMR). It originates from the electron spin-orbit coupling: the electron cloud about the nucleus is slightly deformed as the direction of magnetization rotates. This changes the number of scattering undergone by the conduction electrons when an electric potential is applied. If the magnetic field is perpendicular to the current, the scattering cross-section is reduced and reciprocally. Since the discovery of Lord Kelvin few improvements in the performances of AMR have been reported, remaining in the order of few per cents [7]. This small resistance variation was nevertheless large enough for technological applications in magnetic sensors and readout head.

The discovery of Giant Magnetoresistance (GMR) in 1988 has signed an important improvement in a field of research that seemed exhausted. Baibich *et al.* (Fert's group) [8]

and Binash *et al.* (Grünberg's group) [9] reported independently a large increase of magnetoresistance in magnetic multilayers, i.e. layers of ferromagnetic (F) metals separated by non-ferromagnetic (NF) metals of nanometric thickness. According the non-magnetic spacer thickness, the F layers are coupled in a ferromagnetic or antiferromagnetic configuration at zero external field.

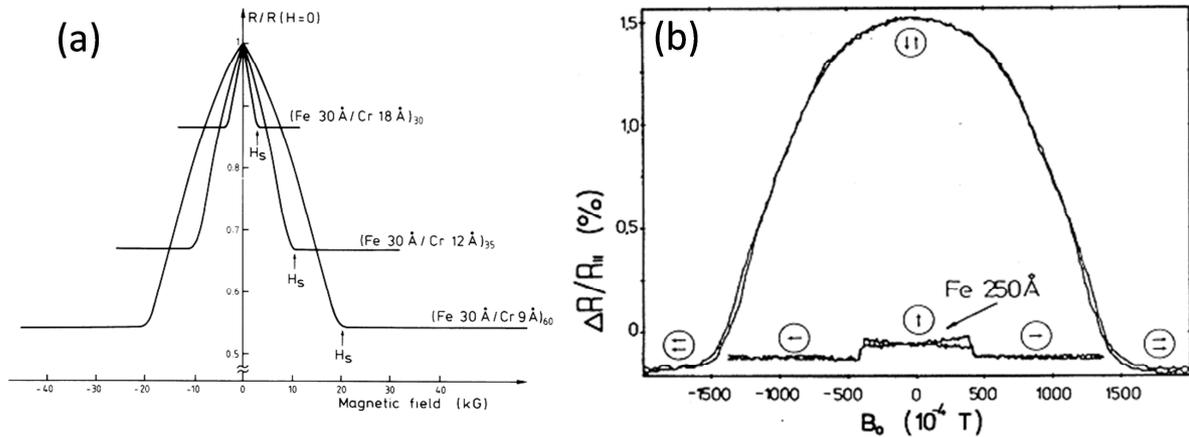
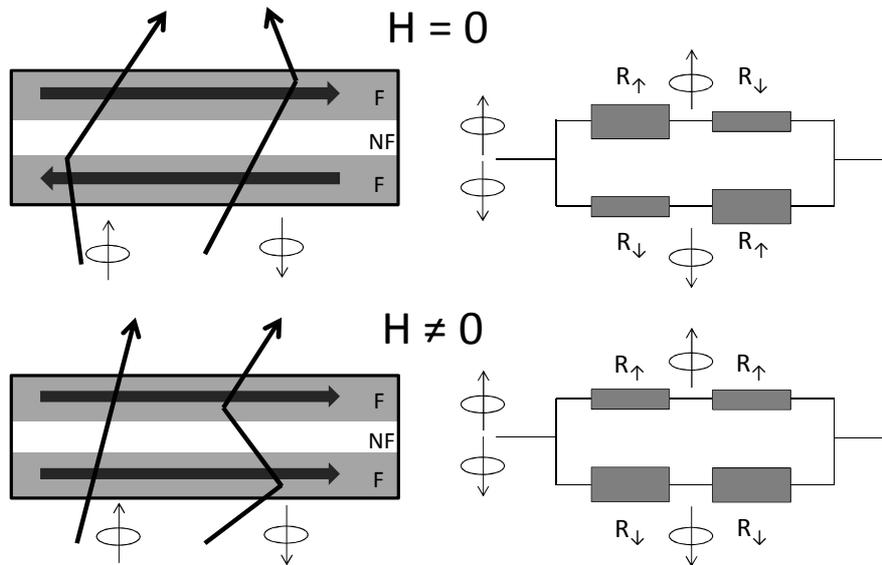


Fig. 2.3 – GMR measurement of (a) Fert's [8] and (b) Grünberg's [9] groups.

Fig.2.3 reports the magnetic measurements of the two papers. When the magnetic field is increased, the resistance decreases until the magnetizations of the Fe layers are parallel to the applied field, giving rise to a MR of a factor of 2.

This phenomenon can be modelled by considering the band structure of a F material [10]. 3d transition F metals (i.e. Fe, Co, Ni and Mn) the density of states at the Fermi level is different for spin  $\uparrow$  and spin  $\downarrow$  populations. When an electric field is applied to the material, the conduction electrons will undergo diffusions, larger is the density of state at the Fermi level, larger are the number of diffusion events. Consequently, the majority-spin electrons will scatter less than the minority one [11]. It is important to notice that in this scheme the spin of the electron is conserved after a scattering event. In addition, the resistance contribution of the NF layer is small and spin-compensated and it can be neglected.

Let's now take into account the trilayer structure of Binash's paper. At zero applied field the two F layers are antiferromagnetically coupled; i.e. if the first F layer has spin-down as majority-spin population, the one of the second F layer will be spin-up (see Fig.2.4). When the current is sent through the trilayer, the spin-down electrons of the current will have a weak scattering with the first F and a strong one with the second one; the opposite for the spin-up population. When a large magnetic field is applied, both F layers are aligned along the direction of the applied field. In this case, one of the two spin current population is weakly scattered and the other one highly scattered.



**Fig. 2.4** – Schematic illustration of the electron transport in F/NF/F structures, with the ferromagnetic layer magnetization with and without applied field, with equivalent resistor network.

This can be modelled with an equivalent resistor scheme, with  $R$  for strong scattering and  $r$  for weak scattering. In the two cases the final resistances are:

$$R_{H=0} = \frac{R+r}{2} \quad R_{H\neq 0} = \frac{2rR}{R+r} \quad (2.1)$$

GMR is then defined as the relative difference of the two resistances:

$$GMR = \frac{R_{H=0} - R_{H\neq 0}}{R_{H\neq 0}} = \frac{(R-r)^2}{4rR} \quad (2.2)$$

The higher the resistance difference, the higher the GMR.

In contrast with AMR, GMR does not depend on the direction of the current but on the relative orientation of the magnetization of the two F layers. Nonetheless, it requires high magnetic fields to align the magnetizations of the different F layers, making it difficult to implement onto magnetic recording devices. The step further that could overcome this limitation was the proposed of the spin valve structure.

### 2.1.2 The role of exchange bias coupling in spin valve structures

Spin valve structure was first proposed by Dieny *et al.* [5] in 1991. The relative orientation of the magnetization of two F layers embedded between a non-magnetic one is still field dependent, but the saturation field is considerably reduced by the using of the exchange bias coupling. They consist in a stack of a pinned electrode (an AF/F bilayer as depicted in Fig.2.5b), a non-magnetic metal and of a free electrode made of a soft ferromagnet. The NM layer magnetically decouples the two F magnetizations and maximizes

the transmission of polarized electrons [12]. The different switching fields of the two F layer are due to the presence of exchange bias coupling. This can be noticed from the magnetization curve of Fig.2.5a.

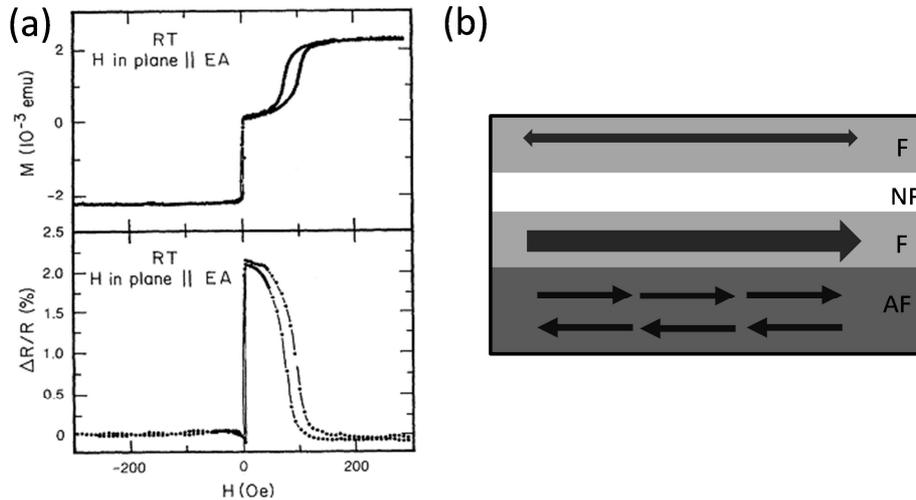


**Fig. 2.5** – (a) Magnetization curve and relative change in resistance of a spin valve [10]. (b) Schematic view of the layer composition of a spin valve.

In Fig.2.5a, the uncoupled (free) NiFe layer, being a soft ferromagnet, reverses at very low applied fields. On the other hand, the interface coupling at the AF-F interface creates a unidirectional anisotropy in the bilayer that stabilizes the magnetization along the easy axis direction. This results in a shift of the hysteresis loop of the bilayer as shown in Fig.2.5a. The magnetoresistive effect can be better understood from Fig.2.5b. Under a negative field, the two layers have parallel magnetizations (i.e. small magnetoresistance). When a small positive field is applied, the magnetization of the NiFe layer is reversed: the two F layers are now antiparallel and the magnetoresistance is maximal. When the field is further increased, the pinned F layer gets its magnetization aligned with the applied field too and the resistance becomes minimal. The difference in the resistance values is due to the relative angle between the free and the pinned layers. The  $\Delta R$  response is linear with the cosine of the difference of the magnetization angle of the two layers. For a small applied field, the pinned layer stay aligned with the easy axis, so that the resistance variation is linearly dependent on the free layer.

The fundamental improvement from GMR multilayer is the possibility to observe the resistance difference at low fields, compared to the high fields otherwise required. In the paper, the spin valve structure presented a magnetoresistance of maximum 5% at room temperature (RT). Further improvements of the spin valve stack allowed more recently reaching 24% GMR at RT [13]. Its main technological application, still present in nowadays devices, is for MR read heads for hard disks.

### 2.1.3 Technological application: hard disk read head

The time necessary to pass from the physical discovery to the technological application was of around 5 years for the spin valve, for hard disk read heads. The linear resistance variation response was used in magnetic sensors to measure the stray field of a magnetic medium since 1994 [14], and is implemented in MR read heads devices since 1997.

A hard disk drive (HDD) is a data storage device present in any personal computer since the early '60s. It is composed by a rotating disk with a magnetic layer as recording media. Up to 2005, the magnetic media was composed by a longitudinally magnetized magnetic layer like CoCrPtTa [15]. Each bit recorded corresponded to a magnetic domain with a magnetic orientation along the plane induced by the hard disk head which determined the value of the bit, '0' or '1'. To have 10 year data stability, the energy barrier between the two magnetic states has satisfy the equation  $K_{eff} V > 67 k_B T$  for 32 Mb, with  $K_{eff} V$  being the anisotropy energy, where  $K_{eff}$  is the effective anisotropy and  $V$  the grain volume,  $k_B$  the Boltzmann constant and  $T$  the temperature. Being the anisotropy fixed by the material, the continuous reduction of bit size (i.e. of  $V$ ) led to the limit of superparamagnetism of longitudinal memory media, which could not progress beyond an areal density of 40 Gbits/in<sup>2</sup>. This led to the introduction of perpendicular media [16]. In this case, the reduction of lateral dimension causes a reduction of demagnetizing field, whereas it was the opposite for longitudinal media. This demagnetizing field reduction pushes further the limit of superparamagnetism, allowing increasing the data density up to 750 Gbits/in<sup>2</sup>.

Considering hard disk heads, they are composed by two functionalities, a writing one and a reading one. The writing part is performed by exploiting the dipolar field between two poles emitted by the inductive current in the head [17].

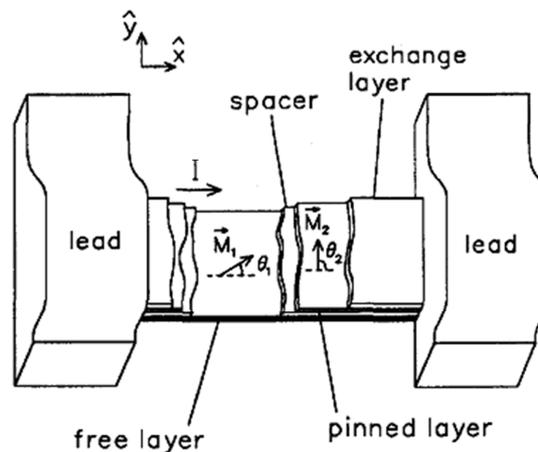


Fig. 2.6 – Schematic view of a spin valve sensor [14].

The reading process is based on spin valve sensor. As shown in the previous paragraph, the free F layer of the spin valve reverses under a low applied field; this causes a change in the resistance value along the thickness of the spin valve, proportional to the relative angle between the free and the pinned layers. In spin valve sensors, the pinned layer is exchange biased along the perpendicular direction with respect to the anisotropy axis of the free layer, as shown in Fig.2.6. In this way the resultant resistance variation is given by  $\Delta R \propto \cos(\theta_1 - \theta_2) \propto \sin \theta_1$ . The response becomes linear ( $\sin \theta_1 \propto H$ ) if the anisotropy hard axis of the free layer is along the transverse signal field direction and the angle variation due to the interaction with the medium is of around  $10^\circ$ .

In case of longitudinal media, the stray field comes from the domain walls of bits with different magnetization direction, which give an increase or a decrease of the resistance value according to the polarity. In case of perpendicular media, it is the bit itself which causes the increase or decrease of resistance. Under some points of view, the phenomenon is similar to the magnetic imaging of Magnetic Force Microscope, as it will be described in Chapter 3.

## 2.2 Magnetic Random Access Memory (MRAM)

Magnetic Random Access Memory (MRAM) is a memory device that has attracted a lot of interest from the fundamental and applicative point of view in the last ten years. In one single memory bit of few hundreds of  $\text{nm}^3$  of volume, plenty of fundamental magnetic properties are condensed. In particular, together with the exchange bias property (on patterned systems), it involves the Tunnel Magnetoresistance (TMR), the magnetoresistive effect that occurs in a magnetic tunnel junction (MTJ). This paragraph will give a description of this physical phenomenon, together with an overview of the MRAM working principles, from the first generation to the last advances in the field. In particular, some stress will be put on the implementation proposed by Crocus Technology, the Thermally Assisted – MRAM (TA-RAM).

### 2.2.1 Tunnel Magnetoresistance

In comparison with GMR, Tunnel Magnetoresistance (TMR) takes place when two ferromagnetic layers are separated by an insulating thin layer instead of a conductive one. For TMR, the difference in resistance depends on the relative angle between the two ferromagnetic layers. In this case, the insulating layer acts as a tunnel barrier; if sufficiently thin, electrons have a significant probability to quantum mechanically tunnel through it. As for the GMR, the spin is conserved after tunnelling the insulating layer, so the two spin

currents ( $\uparrow$  and  $\downarrow$ ) can be considered as independent channels. With these hypotheses the TMR is calculated in a similar way as shown in Paragraph 2.1.1.

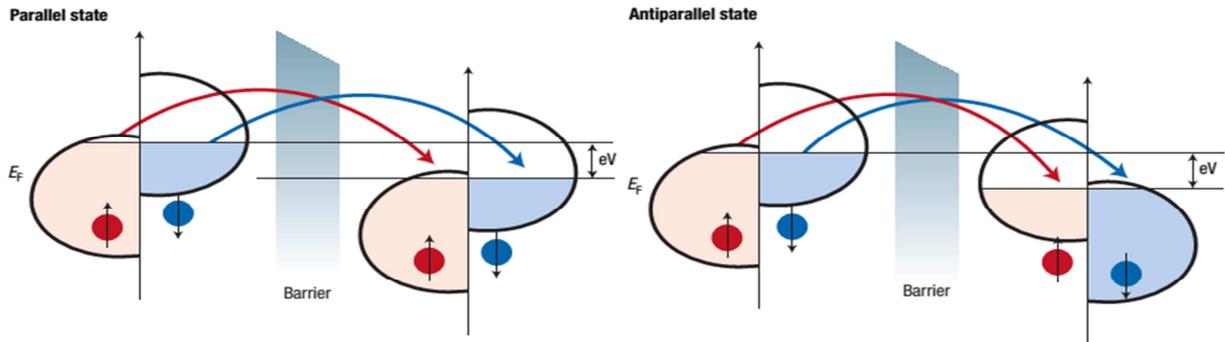


Fig. 2.7 – Schematic representation of the spin tunneling through an insulating barrier [18].

In Fig.2.7, the band structure of the two spin channels at the two sides of the barrier is represented. If the magnetization of the two F layers is parallel, minority spin will find more free state to tunnel to than in an antiparallel configuration, giving a lower resistance value compared to the antiparallel configuration.

TMR is thus defined as:

$$TMR = \frac{R_{H=0} - R_{H \neq 0}}{R_{H \neq 0}} = \frac{2P_1P_2}{1 - P_1P_2} \quad (2.3)$$

where  $P_i$  is the polarization of the electrode  $i$ , defined as the normalized difference of density

$$P_i = \frac{D_i^\uparrow - D_i^\downarrow}{D_i^\uparrow + D_i^\downarrow}$$

of states  $D_i$  for the two spin states up and down:

This phenomenon was first observed by Jullière in 1975 [19] on a Fe/Ge/Co trilayer junction at 4.2 K, which presented a TMR of 14%. Its interest for applications was renewed with the work of Moodera *et al.* [20] and Miyazaki *et al.* [21], which first showed in 1995 the possibility of having significant TMR at room temperature. An example of TMR measurement is shown in Fig.2.8.

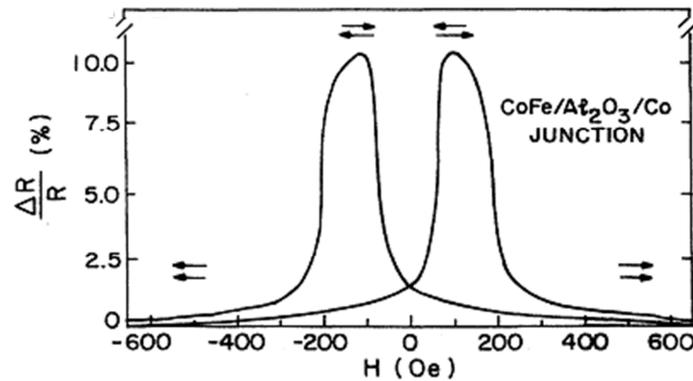


Fig. 2.8 – TMR measurement of CoFe/Al<sub>2</sub>O<sub>3</sub>/Co junction at room temperature [20].

In their work, amorphous alumina ( $\text{Al}_2\text{O}_3$ ) was used as insulating layer and sandwiched between CoFe and Co electrodes. With this structure, they reached TMR values up to 24% at 4.2 K and 12% at RT. Since then, a huge development in the performances of TMR structure has been achieved, particularly with the choice of MgO as insulating material [22-23]. The huge increase in performances, up to 200% at RT, is due to the crystallographic properties of MgO [24-25]. For an amorphous barrier, the TMR only originates from the difference of the density of states at the Fermi level of the two spin populations. If the barrier is crystalline, the tunnelling electrons are filtered according to the symmetry of their wave function. The symmetry of the Bloch states at the Fermi energy becomes a key parameter in electron tunnelling. The band structure of the F layers has different energy values according to the spin state of the electron. If the symmetry of the majority energy band is the same of the barrier, the electrons are efficiently filtered. This additional filtering led to a huge increase of TMR performances, with a record of 600% for highly optimized stacks [26].

Many parameters play a role in the quality of TMR junctions, like quality of the interfaces, crystallographic growth, quantity of defects and spin polarization. The continuous optimization of TMR stacks led to a series of recipes that are nowadays considered standard, like the annealing temperature for an optimized MgO barrier texture [27] or the crystallographic growth of the electrodes [28]. The large variation of resistance between the two states at low applied magnetic fields made TMR a dominant structure compared to GMR multilayers, whose maximal performance does not overpass 40% at room temperature [29]. These high performances are exploited in hard disk read heads since 2005 and in Magnetic Random Access Memory systems since 2000.

### 2.2.2 First generation MRAM

With its integration of magnetic stacks in a semiconductor environment, MRAM is a primary example of More-Than-Moore spintronic device. Each bit is based on a MTJ of submicron lateral size; the two values ('0' and '1') are given by the relative orientation of the magnetization of two F layers. The first magnetization is fixed by the exchange bias coupling and it is named reference layer. The second magnetization is free to switch and it is named storage layer (see Fig.2.9). The spacer, an insulating layer, magnetically decouples the two F layers. When the current passes through the stack, the relative magnetization direction of the two magnetic layers gives two possible resistance states which determine the value of the bit. In order to distinguish the two values, a TMR of at least 100% is usually required. Other

specifications required for a working device are ten years of data retention, thermal stability (up to 90°C for automobile devices), reduced current consumption and correct bit writing.

During the last fifteen years, MRAM showed a large number of technological evolutions based on the discovery and applications of different physical phenomena. All the implementations involve the storage layer part of the stack, which is the most critical because it is the one that has to change its magnetization direction during the writing part and to maintain it when reading.

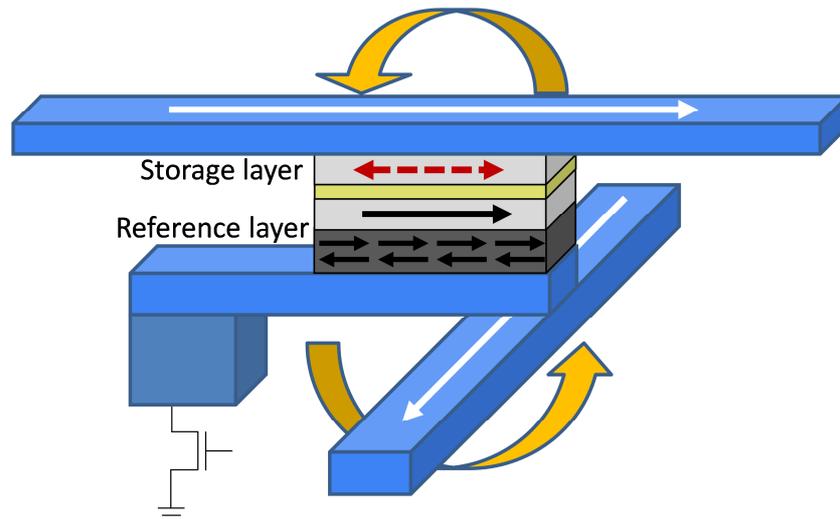


**Fig. 2.9** – Scheme of the writing process in the first generation MRAM.

The reference layer is composed a F/AF bilayer, with PtMn or IrMn layer as AF layer, chosen for their high Néel Temperature (or more precisely blocking temperature) that guarantees the stability in the working temperature range. The F layer is exchange coupled with the AF layer, thus pinning the reference layer in a fixed magnetization direction.

The first MRAM generation is known as Stoner-Wohlfarth MRAM (SW-MRAM). In this structure the F layer in the reference part is constituted by a single F layer, as for the storage layer. The writing is done by two magnetic fields perpendicular one to the other and created by the current passing through two orthogonal metallic lines close to the MTJ (see Fig.2.9). The magnetic field created is proportional to the current injected in the field lines. Each line passes close to a series of MTJ, but only the combination of the two lines assures the writing of the bit. This is possible because the magnetic field produced by the current passing through the line is not large enough to reverse the magnetization of the storage layer alone, i.e. its magnetic field is lower than the coercive field of the layer. According to Stoner-Wohlfarth's model [30] the field necessary to reverse the magnetization when the field is applied at 45° is minimal (see Paragraph 1.1.2). If the two currents generate two equivalent

perpendicular magnetic fields, whose sum overpasses the coercive field at  $45^\circ$  of the F layer, the magnetization is reversed (see Fig.2.10).

This process has the great disadvantage in term of power consumption of having two current lines passing through a large number of MTJ. The magnetic properties of the storage layer are intrinsically different from one dot to another (as it will be largely discussed in Chapter 4). The resulting switching field distribution along the different lines may cause undesired writing by one single current line on dots with lower coercivity. This is even more degraded when the lateral size is reduced.

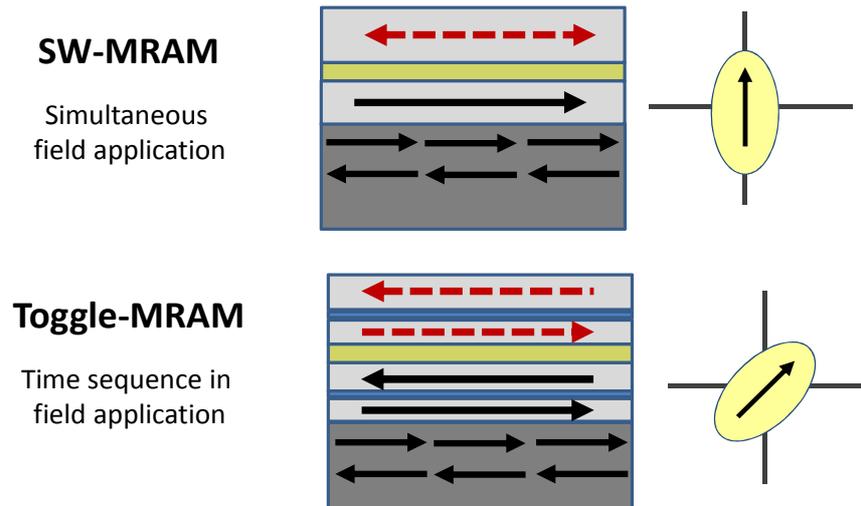


**Fig. 2.10** – Schematic view of SW and Toggle-MRAM stacks and their ellipses orientation with respect to the current lines.

For this reason SW-MRAM never entered the market but was first improved by substituting the simple F layer of the storage layer with a synthetic ferrimagnet (see Fig.2.10). This improvement is known as Toggle-MRAM [31] and entered the market in 2006 with Freescale Semiconductor (nowadays its spin out Everspin Technologies). The advantage of such structure lays in the complexity required to reverse the magnetization of the bilayer, decreasing the field sensitivity and increasing thermal stability [32]. The two F layers, under a sufficiently large applied field, do not maintain their  $180^\circ$  opposite magnetization direction but perform a so called spin flop [33], i.e. they lose their collinear direction and tend to align along the direction of the applied field. The coupling between the two layers does not allow reversing the magnetization with a single combination of currents. With a sequence of magnetic fields applied along different axis [34], the two magnetizations turn along the astroid since when the total magnetization is reversed (see Fig.2.11). Moreover, also in the reference layer the single F layer was substituted with a synthetic antiferromagnet. It is composed by two F layers separated by a thin non-magnetic one that couples

antiferromagnetically both F layers. This choice is to reduce the emitted stray field, which could couple different MTJs among them, and to avoid micromagnetic effects.

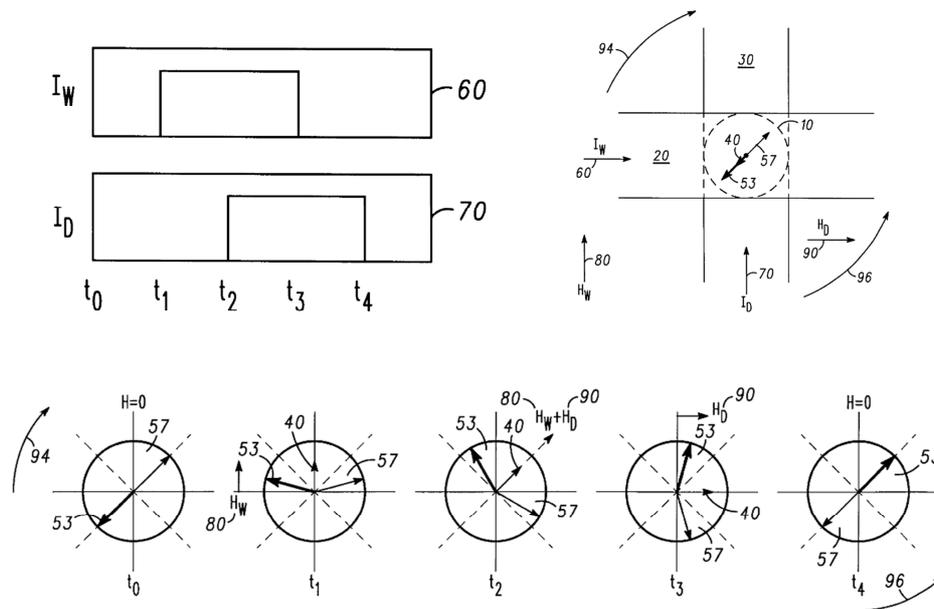


**Fig. 2.11** – Scheme of writing steps on Toggle-MRAM [33]. The two currents  $I_W$  and  $I_D$  are not sent simultaneously, in order to reverse step by step the magnetization of the coupled F bilayer.

This kind of MRAM has been commercialized by Motorola and Everspin from 256 kb to 16Mb MRAM. However, its performances are limited in scalability. MRAM bits have to guarantee a 10 year data reliability. As for hard disk drives, data retention is closely related to the effective anisotropy and the volume of the magnetic storage layer ( $K_{eff} V > 67 k_B T$  for 32 Mb). The reduction of lateral bits dimension leads to an increase of the total thickness to maintain  $V$  constant or to an increase of  $K_{eff}$ . In both cases, this implies an increase of the switching field, which means higher currents, an increase of energy consumption and electromigration problems. Moreover, current stripes would have to be larger, making the effort of reducing the MTJ lateral size useless. For these reasons, nowadays two main evolutions of MRAM are on the way to the market [35]: Thermally Assisted MRAM (TA-MRAM) and Spin Transfer Torque MRAM (STT-MRAM).

### 2.2.3 Thermally Assisted MRAM (TA-MRAM)

One possible solution to improve the scalability, the thermal stability and the writing selectivity of MRAM is the so-called Thermally Assisted Switching MRAM (TA-MRAM) [36], an implementation of standard MRAM that uses the properties of exchange bias not only in the reference layer but also in the storage one, allowing to reduce the number of current lines per bit from two to one.

The presence of a unidirectional coupling in the storage layer has the aim to assure the data retention: if the coercivity of the hysteresis loop is lower than the loop shift, the storage layer presents only one possible value at zero field, guarantee good reliability under field disturbance as well.

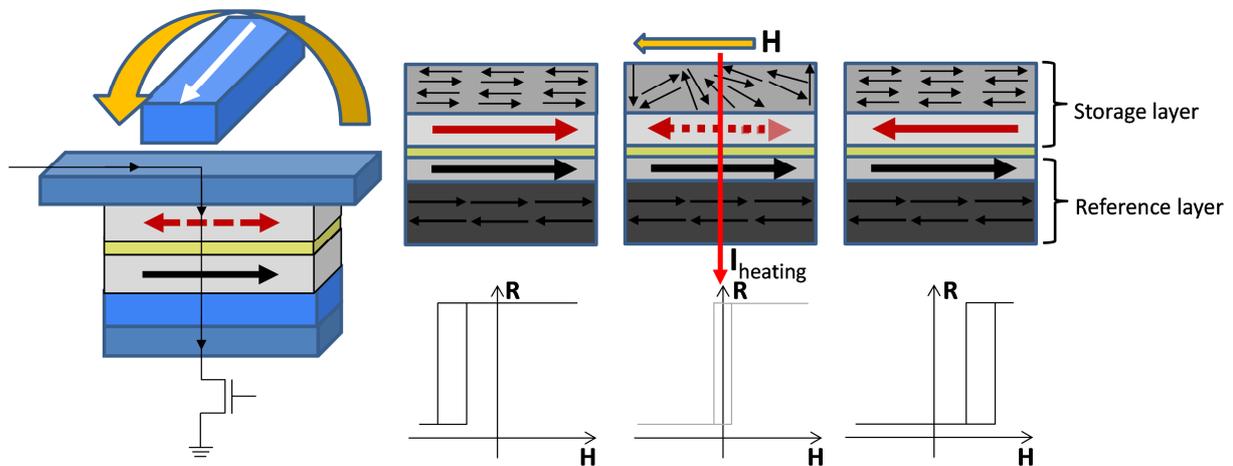


**Fig. 2.12** – Sketch of the writing process for TA-MRAM. When the heating current passes through the MTJ, the AF layer of the storage layer becomes unblocked. The magnetic field emitted by the current line reverses the magnetization of the F layer. During the cooling down, the exchange bias is re-established in the new direction, pinning the magnetization.

The writing process is based on the different thermal properties of the AF layer used in the storage layer compared to the one present in the reference layer. Indeed, the writing takes place through a thermal annealing of the storage exchange biased layer by a pulsed current. A current pulse (down to 1-5 ns [37]) passing through the MTJ causes the heating of the junction [38]. If the current is large enough, the temperature in the MTJ overpasses the blocking temperature of the AF layer in the storage layer (lower than the one of the reference layer). Whereas PtMn has a large blocking temperature (up to 380°C [39]) that guarantees its stability during the heating process, IrMn and FeMn [40,41] are preferred materials for the storage layer, with blocking temperatures in the range 100-230°C (For an overview on blocking temperature values for FeMn and IrMn, see [42]).

The writing process is described in Fig.2.12. When the AF layer is heated above  $T_B$ , the exchange bias coupling is cancelled, so the F layer remains uncoupled. With the application of a magnetic field by a current line, the F magnetization is switched. After the current pulse, the temperature is cooled down in 10-20 ns [34] and the AF layer is coupled again with the F storage layer, along the direction of the cooling field.

Reading is performed by passing a current sufficiently small not to unblock the storage layer. This implementation has been proposed in a patent of 2002 [43] which led to the creation of the start-up Crocus Technology in 2004. The advantages compared to first generation MRAM are the presence of a single current line and a higher selectivity in writing, together with the

possibility of scaling down the dot size without losing the thermal stability of the storage layer.

Nonetheless, many parameters play a role in the correct functioning of a TA-MRAM memory. Being the storage layer the main actor in writing a reading, the blocking temperature of the storage layer has to be optimized, presenting a small dispersion from cell to cell and no overlap with the blocking temperature distribution of the reference layer. The exchange bias field of the storage layer has to be large enough to guarantee one single stable state at zero field, i.e. large hysteresis field shift and reduced coercivity. The data retention at room temperature is improved by the increased effective anisotropy of the storage layer given by coupling of the F layer with the AF one, thus largely increasing the thermal stability factor for equivalent volumes.

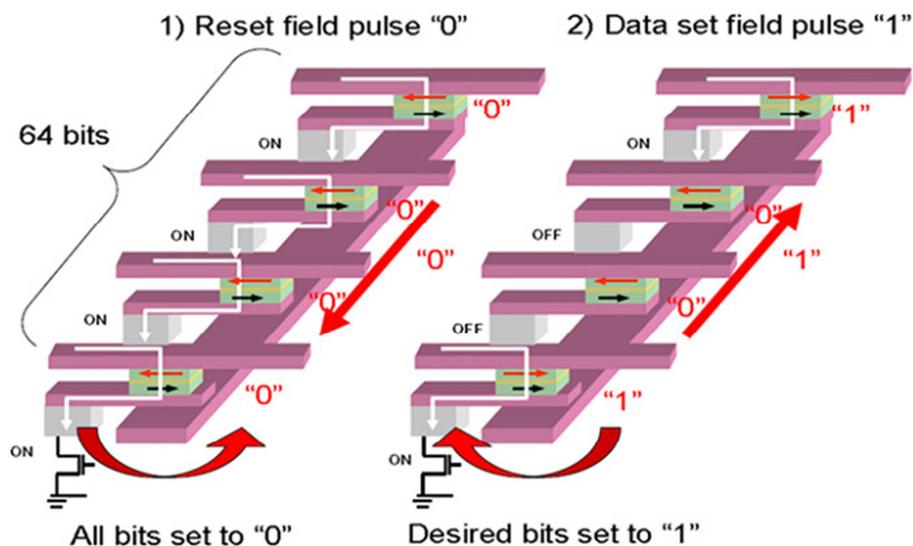


Fig. 2.13 – Writing selectivity of TA-MRAM on a 64bit memory [35].

Among these critical points, each MTJ has to guarantee that the field emitted by the current line passing through a series of junction during the writing of one bit is not sufficient to reverse the magnetization of the storage layer of the bits where no current is injected (See Fig.2.13). For this reason, the exchange bias properties of the storage layer have to be controlled and optimized, with reduced variability from one bit to another. If these conditions are satisfied, the writing of a "word" (i.e. multiple bits at the same time) can be done with a single current line, reducing power consumption.

## 2.2.4 Spin Transfer Torque MRAM (STT-MRAM)

Spin Transfer Torque (STT) is a physical phenomenon first predicted by Slonczewski [44] and Berger [45]. As in GMR and TMR the different magnetization of F layers causes a variation in the behaviour of the current passing through them, STT describes the possibility

of a current to be polarized by the magnetization of a F layer and to excite a torque on the spins of the second F layer.

This phenomenon can be described considering two F layers (i.e. Co) separated by a non-magnetic one [46], as shown in Fig.2.14. When current flows through the sandwich structure, its conducting electrons are polarized through the spin-transfer scattering against the lattice of the first F layer (named polarizer). The spin polarized electrons cross the non-magnetic spacer conserving their spin. At the interface with the second F layer (free layer), the conducting spins are partially reflected and transmitted. The transmitted ones precess for a short distance ( $\sim 1$  nm) along the magnetization direction of the second F layer, since when it align along its direction. This precession generates a flow of angular momentum. This torque is transmitted to the spins of the second F layer, and takes the name of Spin Transfer Torque.

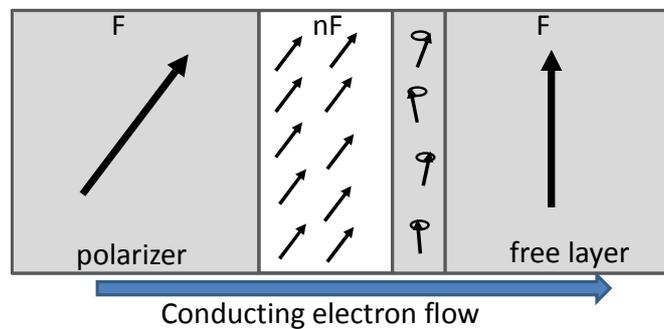


Fig. 2.14 – Schematic view of Spin Transfer Torque principle.

If the current passing through the layers is sufficiently large, i.e. above a threshold value called critical current (usually around  $10^6$  A/cm<sup>2</sup>), the polarization at the second interface induces a torque on the spins of the free layer whose intensity is large enough to reverse the magnetization of the layer. The torque is given by the vectorial product of the spin magnetization of the free layer with the current polarization.

The theoretical predictions were first verified with Co/Cu/Co trilayer structures [47] and later implemented in MTJ systems [48], with the reference layer as polarizer and the storage one as free layer. The parallel configuration is obtained by sending a conducting electron flow from the pinned to the storage layer. The antiparallel state is achieved with a current pulse of opposite polarity. In a MRAM memory cell, STT allows to reduce the number of current lines to zero, because the writing process is performed by passing a current through the single MTJ. Reading is performed at a lower current to avoid STT switching. The critical current necessary to reverse the magnetization is determined by a critical current density [36]. As a consequence, for fixed free layer thickness and effective anisotropy the current scales as the area of the cell.

First STT-MRAM had the F layers with in-plane magnetization. MTJ were processed on an elliptical shape to fix the magnetization along the long axis of the ellipses, induced by the shape anisotropy of the dot. A maximum aspect ratio of the order of 2 was used to avoid micromagnetic states. Nonetheless, this shape anisotropy is not sufficient to guarantee thermal stability for lateral dimensions below 45 nm [35].

For this reason, perpendicular STT-MRAM structures were proposed to overcome the superparamagnetic limit [49]. F layers with out-of-plane magnetization present very large effective anisotropy that provides good thermal stability at small dimensions. The two magnetic states are clearly defined without adding any shape effect, thus simplifying the fabrication process. Moreover, perpendicular storage layer presents very large coercivity at room temperature, thus guaranteeing good data retention. Finally, the current density necessary to reverse the magnetization is lower than for in-plane structures. Whereas for in-plane magnetization the precession takes place passing through an out-of-plane oscillation, for the perpendicular case this energy consumption is not present [50].

One of the most critical parameters in STT-MRAM is the separation between the writing, reading and breakdown distributions, i.e. the data retention in low current condition and the breakdown voltage limit during the writing step.

Recently, the possibility of including the advantages of Thermally Assisted switching in STT-MRAM systems has been proposed. As a matter of fact, in TA-MRAM the data retention at room temperature of the storage layer is improved by the presence of an AF layer. Typically, the F/AF bilayer behaves like a hard ferromagnet with respect to the thermal activation because of the large anisotropy of the AF material. In fact, the increased anisotropy of the storage layer due to exchange bias coupling allows the reduction of the lateral dimension of the memory point without facing the superparamagnetic limit. This can be implemented in STT based MRAM structures. In TA-STT-MRAM, the current passing through the MTJ heats up the storage layer to a temperature large enough to unpin the storage layer, and at the same time its polarized conduction electrons transfer enough torque (i.e. the current density is large enough) to induce STT switching. After the current pulse, the AF layer in the storage layer couples again with the F layer, setting the magnetization direction. This implementation allows improving the scalability of in-plane STT-MRAM without adding any current lines to the system. For further details, see Hérault's thesis [51].

# Bibliography

- [1] [http://www.cisco.com/en/US/solutions/collateral/ns341/ns525/ns537/ns705/ns827/white\\_paper\\_c11-520862.html](http://www.cisco.com/en/US/solutions/collateral/ns341/ns525/ns537/ns705/ns827/white_paper_c11-520862.html)
- [2] Moore, Gordon E. 1965 *Electronics* **38 (8)** 4
- [3] The International Technology Roadmap for Semiconductors: 2012 Update, p.17
- [4] Kent J P and Prasad J 2008 *IEEE 2008 Custom Integrated Circuits Conference* 395
- [5] Dieny B, Speriosu V S, Parkin S S P, Gurney B A, Wilhoit D R and Mauri D 1991 *Phys. Rev. B* **43** 1297
- [6] W Thompson 1857 *Proc. Roy. Soc.* **8** 546
- [7] McGuire T R and Potter R I 1975 *IEEE Trans. Magn.* **4** 1018
- [8] Baibich M N, Broto J M, Fert A, Nguyen Van Dau F, Petroff F, Etienne P, Creuzet G, Friederich A and Chazelas J 1988 *Phys. Rev. Lett.* **61** 2472
- [9] Binasch G, Grünberg P, Saurenbach F and Zinn W 1989 *Phys Rev. B* **39** 4828
- [10] Tang D D and Lee Y-J 2010 *Magnetic Memory*
- [11] Fert A and Campbell I A 1968 *Phys. Rev. Lett.* **21** 1190
- [12] Dieny B, Speriosu V S, Metin S, Parkin S S P, Gurney B A, Baumgart P and Wilhoit D R 1991 *J. Appl. Phys.* **69** 4774
- [13] Egelhoff W F, Chen P J, Powell C J, Stiles M D, McMichael R D, Judy J H, Takano K and Berkowitz A E 1997 *J. Appl. Phys.* **82** 6142
- [14] Heim D E, Fontana R E, Tsang C, Speriosu V S, Gurney B A and Williams M L 1994 *IEEE Trans. Magn.* **30** 316; Tsang C, Fontana R E, Lin T, Heim D, Speriosu V S, Gurney B A and Williams M L 1994 *IEEE Trans. Magn.* **30** 3801
- [15] Utsumi K, Inase T and Kondo A 1993 *J. Appl. Phys.* **73** 6680
- [16] Piramanayagam S N 2007 *J. Appl. Phys.* **102** 011301
- [17] Khizroev S and Litvinov D 2004 *J. Appl. Phys.* **95** 4521
- [18] Chappert C, Fert A, Nguyen Van Dau F 2007 *Nature Mat.* **6** 813
- [19] Julliere M 1975 *Physics Letters A* **54** 225
- [20] Moodera J S, Kinder L R, Wong T M and Meservey R 1995 *Phys. Rev. Lett.* **74** 3273
- [21] Miyazaki T and Tezuka N 1995 *J. Magn. Magn. Mater.* **139** L231
- [22] Parkin SSP, Kaiser C, Panchula A, Rise P M, Hughes B, Samant M and Yang S-H 2004 *Nature Mater.* **3** 862
- [23] Yuasa S, Nagahama T, Fukushima A, Suzuki Y and Ando K 2004 *Nature Mater.* **3** 868
- [24] Butler W H, Whang X G, Schulthess T C and MacMaren J M 2001 *Phys. Rev. B* **63** 054416
- [25] Mathon J and Umerski A 2001 *Phys. Rev. B* **63** 220403

- [26] Ikeda S, Hayakawa J, Ashizawa Y, Lee Y M, Miura K, Hasegawa H, Tsunoda M, Matsukura H and Ohno H 2008 *Appl. Phys. Lett.* **93** 082508
- [27] Djayaprawira D D, Tsunekawa K, Nagai M, Maehara H, Yamagata S, Watanabe N, Yuasa S, Suzuki Y and Ando K 2005 *Appl. Phys. Lett.* **86** 092502
- [28] Yuasa S and Djayaprawira D D 2007 *J. Phys. D: Appl. Phys.* **40** R337
- [29] Parkin S S P, Roche K P, Samant M G, Rice P M, Beyers R B, Scheuerlein R E, O'Sullivan E J, Brown S L, Bucchigano J, Abraham D W, Lu Yu, Rooks M, Trouilloud P L, Wanner R A and Gallagher W J 1999 *J. Appl. Phys.* **85** 5828
- [30] Stoner E C and Wohlfarth E P 1948 *Phil. Trans. Roy. Soc. A* **240** 599
- [31] Savtchenko L, Engel B N, Rizzo N D, DeHerrera M F and Janesky J A 2003 US Patent 6 545 906 B1
- [32] Abarra E N, Inomata A, Okamoto I and Mizoshita Y 2000 *Appl. Phys. Lett.* **77** 2581
- [33] Worledge D C 2004 *Appl. Phys. Lett.* **84** 4559
- [34] Savtchenko L, Engel B N, Rizzo N D, DeHerrera M F and Janesky J A 2003 US Patent 6,545,906 B1
- [35] Prejbeanu I L, Bandiera S, Alvarez-Hérault J, Sousa R C, Dieny B and Nozières J P 2013 *J. Phys. D: Appl. Phys.* **46** 074002
- [36] Prejbeanu I L, Kerekes M, Sousa R C, Sibuet H, Redon O, Dieny B and Nozières J P 2007 *J. Phys.: Condens. Matter* **19** 165218
- [37] Hérault J, Sousa R C, Ducruet C, Dieny B, Conraux Y, Portemont C, Mackay K, Prejbeanu I L, Delaët B, Cyrille M C and Redon O 2009 *J. Appl. Phys.* **106** 014505
- [38] Kerekes M, Sousa R C, Prejbeanu I L, Redon O, Ebels U, Baraduc C, Dieny B, Nozières J P, Freitas P P and Xavier P 2005 *J. Appl. Phys.* **97** 10P501
- [39] Saito M, Hasegawa N, Koike F, Seki H and Kuriyama T 1999 *J. Appl. Phys.* **85** 4928
- [40] Gapihan E, Sousa R C, Hérault J, Papisoi C, Delaye M T, Dieny B, Prejbeanu I E, Ducruet C, Portemont C, Mackay K and Nozieres J P 2010 *IEEE Trans. Magn.* **46** 2486
- [41] Lombard L, Gapihan E, Sousa R C, Dahmane Y, Conraux Y, Portemont C, Ducruet C, Papisoi C, Prejbeanu I L, Nozieres J P, Dieny B and Schuhl A 2010 *J. Appl. Phys.* **107** 09D728
- [42] R. Coehoorn 2003 *Novel Magnetoelectric Materials and Devices* p.171-179
- [43] Dieny B and Redon O 2002 US Patent App. 10/495,637.
- [44] Slonczewski J C 1996 *J. Magn. Magn. Mater.* **159** 1
- [45] Berger L 1996 *Phys. Rev. B* **54** 9353
- [46] Dieny B, Sousa R C, Hérault J, Papisoi C, Prenat G, Ebels U, Houssameddine D, Rodmacq B, Auffret S and Buda-Prejbeanu L D 2010 *Int. J. Nanotechnol.* **7** 591
- [47] Grollier J, Cros V, Hamzic A, George J M, Jaffrès H, Fert A, Faini G, Ben Youssef J and Legall H 2001 *Appl. Phys. Lett.* **78** 3663
- [48] Huai Y, Albert F, Nguyen P, Pakala M and Valet T 2004 *Appl. Phys. Lett.* **84** 3118

- [49] Nakayama M, Kai T, Shimomura N, Amano M, Kitagawa E, Nagase T, Yoshikawa M, Kishi T, Ikegawa S and Yoda H 2008 *J. Appl. Phys.* **103** 07A710
- [50] Mangin S, Ravelosona D, Katine J A, Carey M J, Terris B D and Fullerton E E 2005 *Nature Mat.* **5** 210
- [51] Hérault J 2010 *Thèse Université Joseph Fourier*

# Chapter 3

## Samples preparation, experimental analysis and atomistic simulation

This chapter will present a brief description of the instrumentation and measurement techniques used during the three years of thesis, with a glimpse of the physical principles ruling them. Concerning the process part, this chapter will give the deposition conditions and the cleanroom procedure followed to obtain the patterned systems. Finally, the atomistic simulation model implemented in collaboration with L\_Sim will be described, from the energy model to the F/AF bilayer modelling.

### 3.1 Sample preparation

#### 3.1.1 Sputtering deposition and annealing process

During the thesis, all samples were deposited with a Plassys sputtering deposition machine, present in Spintec laboratory. This kind of deposition technique is mainly used for technological applications (and in the MRAM domain too) for the reduced cost and higher throughput compared to other deposition techniques like epitaxial evaporation or chemical vapour deposition. Fig.3.1 shows the working principle of a typical sputtering system.

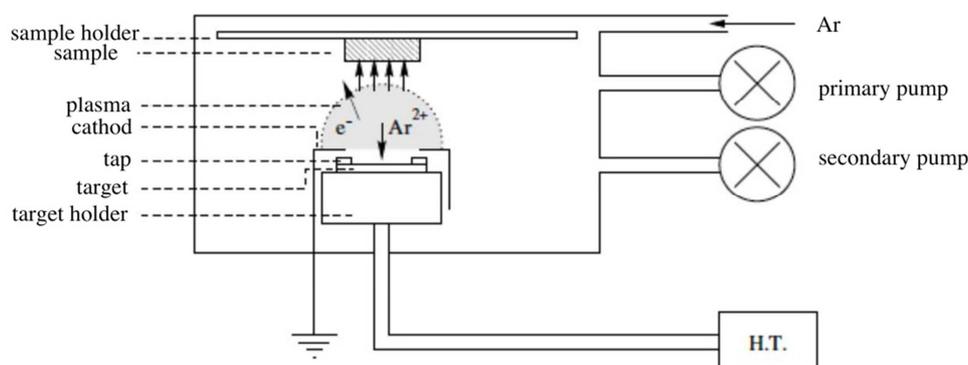


Fig. 3.1 – Schematic view of the sputtering system [1].

Samples are introduced into an isolated chamber, in which a vacuum of around  $3 \cdot 10^{-7}$  mbar is kept constant by a secondary pump. All the samples used are deposited on to (100) Si small squares or stripes, covered by a layer of native oxide of around 100 nm thick. The chamber contains several targets, covered by a sliding tap. Materials deposited during the thesis were all on targets pointing perpendicularly to the sample during the depositions. For this reason, no particular shadowing effects or deposition angular direction had to be taken into account for the experimental results. In order to start the deposition, a controlled flux of Ar (81 standard cubic centimetres per minute (sccm)) is introduced. When the pressure reaches  $2.5 \cdot 10^{-3}$  mbar, if a cathode (i.e. the cylinder containing the selected target) is set to a negative voltage of around (ranging from 50 to 150 V according to the material and the desired deposition rate), the gas gets ionized, creating plasma. Positive ions are attracted to the cathode. This collision causes atoms of the target to isotropically leave the surface, depositing on the sample placed above the selected cathode by a mechanical system. Plasma is kept in the chamber by the emission of secondary electrons during the ionic bombardment, repulsed by the negative potential of the target. The negative voltage is obtained by DC current for conducting targets and RF current for isolating ones in order to maintain the emission of electrons. To start and end the deposition of a material on the sample, a shutter is mechanically moved to cover and uncover the sample. During the thesis, all the deposited materials were conducting. The sputtering deposition rate of each material is obtained from the ratio between the thickness of a deposited layer and the time of deposition. The thickness calibration is performed by X-ray reflectometry on very thick reference layers at the installation of a new target. The total deposition time has to take into account the time spent to open and close the shutter covering the sample of few fraction of second; this time may become important for ultrathin layers.

After deposition, in order to set the exchange bias coupling, samples were annealed and field cooled under a constant applied field of 2000 Oe. The annealing was performed in a vacuum chamber at around  $10^{-6}$  mbar pressure to avoid sample oxidation and the diffusion of external impurities. Typical parameters were a heating temperature of 473 K (200°C) for 30' to overpass IrMn blocking temperature [2]. In case of patterned samples, the annealing was also performed after the cleanroom processes, in order to re-set the coupling after the thermal processes spent by the sample in the fabrication steps.

### 3.1.2 Patterning samples: from spin coating to SEM imaging

Patterned samples were prepared in the PTA (Plateforme Technologique Amont), a cleanroom shared by CEA and CNRS users. It is a 350 m<sup>2</sup> cleanroom of class 1000 (or ISO 6), where 4" wafer and smaller samples can undergo several technological processes. Among them, resist deposition and removal, optical and e-beam lithography, etching processes, Scanning Electron Microscopy (SEM) and optical microscopy. The patterned samples studied during the thesis experienced:

- electron beam lithography, to have the a quality patterning geometry at very low dimensions;
- ion beam etching, to have the magnetic signal only on the patterned dots and not on the surrounding trenches and substrate.

There are many different technological approaches in order to obtain a patterned sample. The most commonly used is based on the concept of lithography. Two possible lithographical processes are possible: optical lithography or electron beam lithography. Both techniques require the deposition of a particular polymeric layer, called resist, on the sample. The resist is usually baked at fixed temperatures in order to optimize its chemical and physical characteristics. The exposure of the resist to UV light (if optical lithography) or to an electron beam (e-beam lithography) changes its characteristics. If it is a so-called “positive resist”, the exposed part becomes more soluble in the following development solution. If it is a “negative resist”, the atoms of the exposed zones crosslink, resulting less soluble. After the exposure, the sample is developed: a chemical bath removes the undesired resist, leaving the desired geometry on the resist for a successive etching process (Fig.3.2).

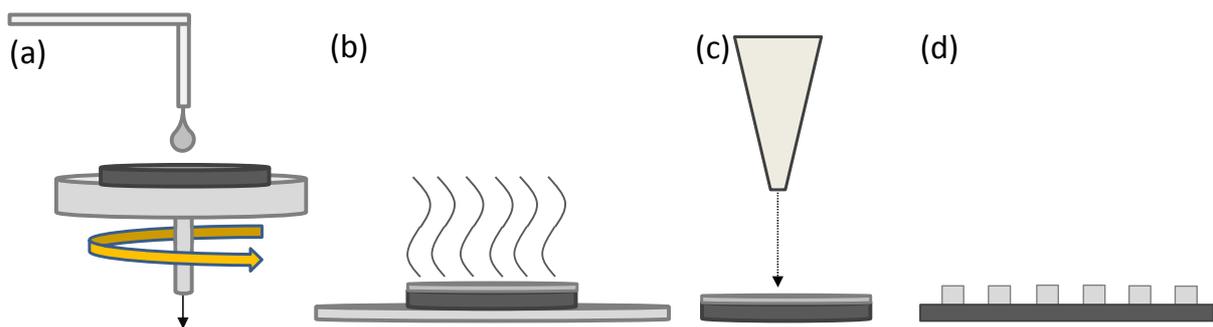


**Fig. 3.2** – Steps for an e-beam lithography process: (a) resist spin-on, (b) resist heating (baking), (c) e-beam lithography process on the resist and (d) resist profile after development. The remaining resist will protect the deposited layers from ion beam etching.

Optical lithography is widely used in industrial production namely for its high throughput. In fact, the geometry is transferred in one single shot on the whole surface by the use of a mask.

E-beam lithography is a scanning lithography technique. A focused electron beam is emitted by an electron gun. This beam is then focused by a system of lenses in order to reduce aberrations and defocusing. Ultra-high vacuum is kept in the e-beam cannon in order to avoid electron collisions. No mask is required. The sample is scanned line by line, following a pattern prepared by external software. According to the pattern, some zones of each line are exposed to the beam, while the beam is blanked in case of non-exposed zones. E-beam lithography has a higher resolution (according to the resist and etching process, it can go down to around 10 nm) than optical lithography, resulting ideal for nanotechnological research. On the other hand, its high writing time compared to optical lithography technique makes its use in massive production less diffuse.

During the thesis, e-beam lithography was chosen because of the higher versatility in the patterning geometry (no mask had to be prepared) and higher resolution; moreover, all samples had small patterned regions (below the  $\text{mm}^2$ ), so total exposure time was not excessive.

The resist used was FOX, a HSQ (Hydrogen silsesquioxane) negative resist. A 150 nm thick layer was deposited on the samples with a standard spin-coating process, with 4000 rpm for 60 s. The sample was then baked at 150 and 200°C for 120 s and 120 s each to guarantee an evaporation of the solvents and a proper adhesion of the resist to the surface. Prepared samples were then inserted into the e-beam system. Once the samples have been patterned following the desired geometry, a development bath of 120 s is performed in an acid solution based on AZ developer in order to remove the unexposed resist. The preparation of the software program of the patterning and the e-beam focalization were performed in collaboration with Gilles Gaudin at SPINTEC. The quality of the process before the etching step was verified by SEM, see Fig.3.3.

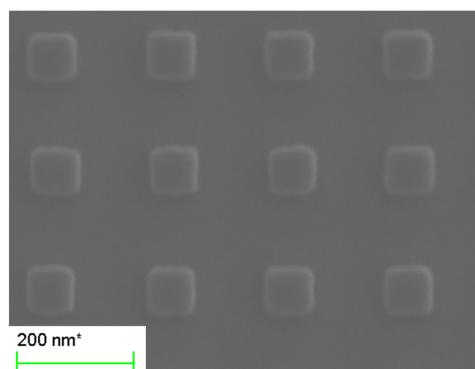


**Fig. 3.3** – SEM image of 100 nm dots before etching.

In order to remove the deposited layers from the unpatterned parts of the samples, Ion Beam Etching (IBE) was performed. This technique is based on physical etching, obtained by

ion milling the surface, without chemical reaction. Each material has a different etching rate. The resist requires a long etching time to be completely removed. Its thickness and material properties protect the underlying magnetic layers that are removed only from the unprotected zones. On the other hand, after the etching process the resist layer results thinner than before, and its removal problematic for the underlying layers. For this reasons, the resist layer was kept for the Kerr effect measurements. The etching was stopped at the detection of the buffer layer, i.e. the unpatterned regions still present the Ta and Cu layers. The quality of the etching process was then verified by SEM.

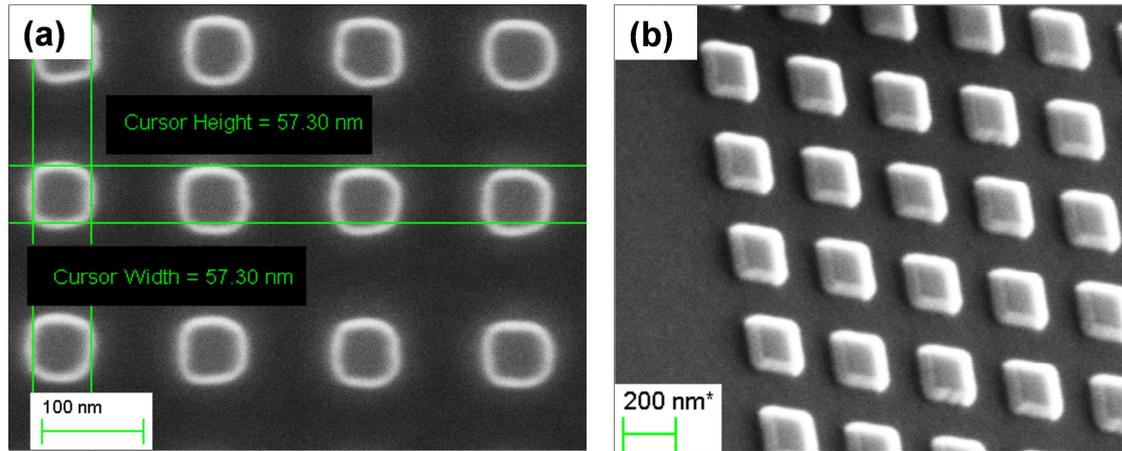


**Fig. 3.4** – (a) SEM image of 50 nm dots after etching. (b) Tilted image of 200 nm dots after etching.

In Fig.3.4, the example of SEM image after etching is given. The white border of the dots marks the border between the patterned part and the etched one, as it can be observed from the tilted image of Fig.3.4b.

## 3.2 Sample characterization

### 3.2.1 Atomic Force Microscopy and Magnetic Force Microscopy

Magnetic Force Microscopy (MFM) imaging is a useful technique to locally study the magnetic state of nanostructures. For nanometric devices, few techniques can give information about the local magnetic domain structure. Among them, the one who gives one of the highest resolutions, providing both magnetic and topographic information, is the MFM [3]. The MFM is essentially a modified Atomic Force Microscopy (AFM).

The AFM allows nanoscopic resolution of the topography of a sample. It is based on the measure of the interaction force between the sample and the tip of a cantilever. This interaction force causes a deflection of the cantilever. The measurement is performed through the reflection of a diode laser on the back of the cantilever. When the cantilever is deflected,

also the reflected laser beam is deflected (Fig.3.5). The surface of the sample is scanned line by line.

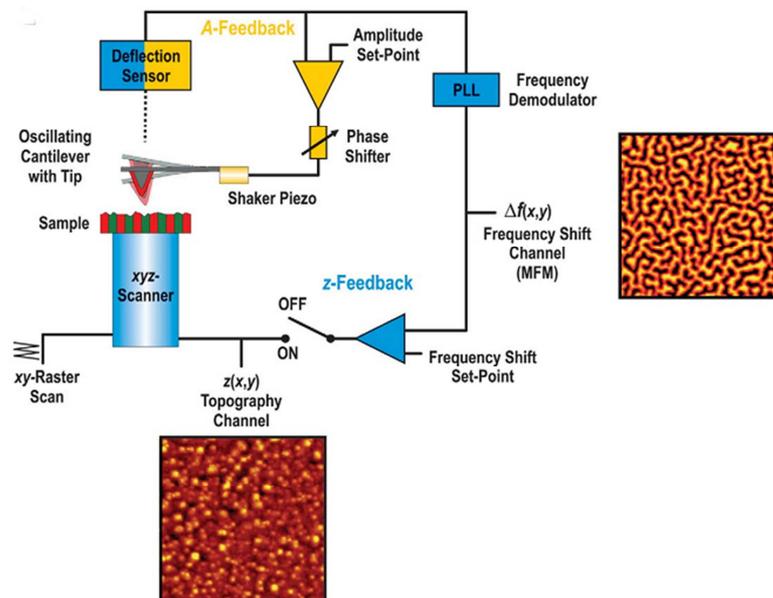


Fig. 3.5 – Schematic of the MFM working principle [3].

There are three different AFM measurement techniques:

- *contact mode*: the tip is kept in contact during the scanning of the surface of the sample. It can be performed in two possible configurations: *variable deflection*: the topography is obtained by the variation of the position of the reflected laser beam, due to the deflection of the cantilever; *constant force*: the deflection of the cantilever is kept constant through a feedback system, that varies the height of the cantilever with respect to the surface of the sample.
- *non-contact mode*: the tip scans the surface at a certain height with respect to the sample. Non-contact forces (like Van der Waals forces) are detected.
- *tapping mode*: the cantilever is put in vibration next to its resonant frequency (usually the first mode). The variation of the resonant frequency due to the interaction with the surface reveals the topography of the sample. The typical resonant frequency of an AFM tip is between 100 and 500 kHz, while the MFM tip has resonant frequency between 10 and 100 kHz because of the use of a longer cantilever.

In the case of MFM measurement, the tip scans twice each line, first in tapping mode, then in non-contact mode. The first scan gives the topography of the surface, while the second, also known as magnetic scanning, reproduces the topography of the sample at a fixed height, in order to detect only the long range magnetic interaction. This procedure is defined as lift mode. The magnetic measurement is performed measuring the gradient of the force, through the phase shift of the oscillating cantilever.

The phase variation is given by:

$$\Delta\Phi = -\frac{Q}{k} \left( \frac{\partial F}{\partial z} \right) \quad (3.1)$$

where  $Q$  is the quality factor,  $k$  the spring constant and  $F$  is the interacting magnetic force, whose value along the  $z$  axis (vertical displacement of the tip respect to the sample) is:

$$F_z = -q_{mag}^2 H_z + m_{mag}^x \frac{\partial H_x}{\partial z} + m_{mag}^y \frac{\partial H_y}{\partial z} + m_{mag}^z \frac{\partial H_z}{\partial z} \quad (3.2)$$

Usually, the magnetic tip is saturated only along the  $z$ -axis. In this case only  $m_{mag}^z \neq 0$ ; so we obtain:

$$\Delta\Phi = -\frac{Q}{k} \left( -q_{mag}^z \frac{\partial H_z}{\partial z} + m_{mag}^z \frac{\partial^2 H_z}{\partial z^2} \right) \quad (3.3)$$

with the two terms being respectively the monopole and the dipole contributions.

As a result, the MFM images the force gradient acting on the magnetic tip.

This means that (Fig.3.6):

- for the out-of-plane magnetization case, the contrast of the MFM images represents the different magnetic domains;
- for the in-plane magnetization case, the tip is sensible only to the stray field entering into or going out of the magnetic domain wall. As a result, the MFM image shows the boundaries between different planar magnetic domains.

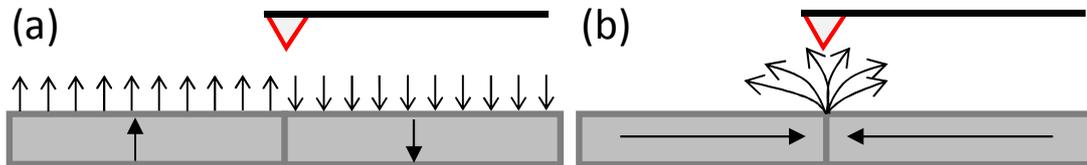


Fig. 3.6 – Interaction between the MFM tip and the perpendicular (a) or planar (b) stray field.

Tip interaction with the sample may influence the measurement, both topographically (geometry of the tip) or magnetically (magnetization reversal of the tip or of the sample because of interaction forces). Because of the necessity to know the magnetic characteristics of the tip by particular calibration techniques in order to have quantitative measurements [4-6], MFM remains in most cases a qualitative instrument.

During the thesis all MFM measurements were performed with a Digital Instrument Nanoscope IIIa with standard magnetic tips of Si with a hard magnetic coating.

### 3.2.2 Focalized Magneto-optic Kerr effect

Magneto-optic Kerr effect (MOKE) is a measurement technique based on the effects on the polarization or intensity of focused light reflected from a magnetized material. There are three possible MOKE configurations (Fig.3.7) [7]:

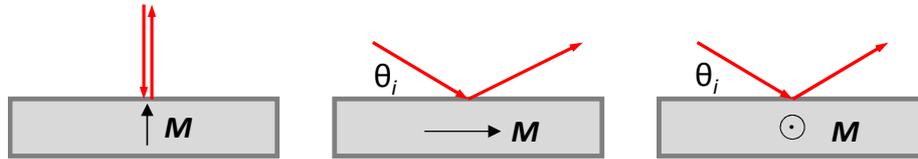


Fig. 3.7 – Schematic representation of polar (a), longitudinal (b) and transversal (c) MOKE.

- *Polar Kerr effect*: used for samples with out-of-plane magnetization. Linearly polarized light impinges the sample with normal incidence. Reflected light has an angular rotation  $\varphi_r$  of its polarization proportional to the magnetization;
- *Longitudinal Kerr effect*: used for samples with an in-plane magnetization parallel to the light plane of incidence. Linearly polarized light, with  $E$  parallel or perpendicular to the plane of incidence, impinges the surface with an angle  $\theta_i$ . Reflected light results elliptically polarized, with the change in polarization proportional to the sample magnetization.
- *Transversal Kerr effect*: used for samples with an in-plane magnetization perpendicular to the light plane of incidence. Also in this case light impinges with an angle  $\theta_i$ , but the magnetization is measured by the variations of reflectivity  $r$ . Light does not require to be polarized.

During the thesis, this kind of hysteresis loop characterization was used on a highly focused system to allow measuring few dots at time. The instrumentation, developed at Institut Néel CNRS Grenoble by Jan Vogel and Manlio Bonfim, consisted in a longitudinal focalized-MOKE, whose schematic is presented in Fig.3.8.

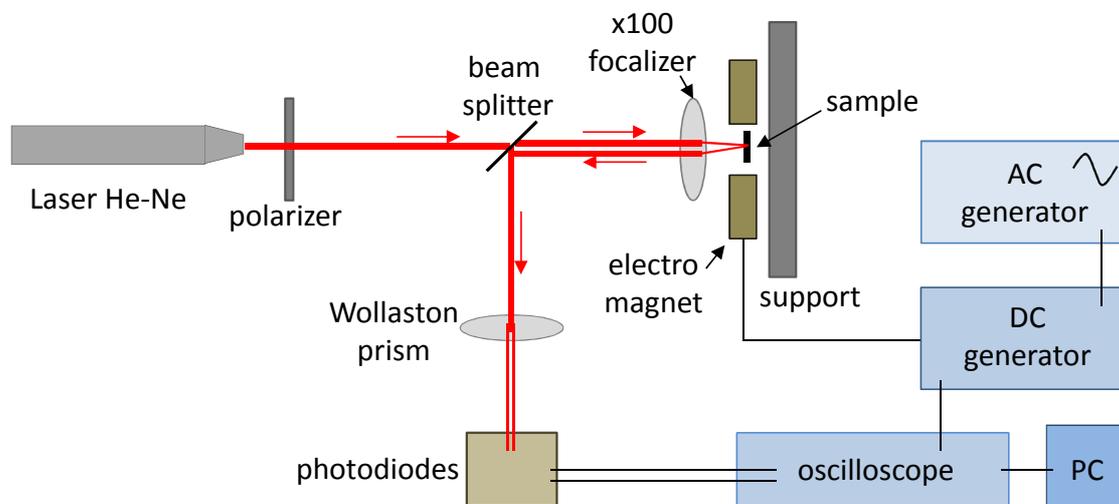
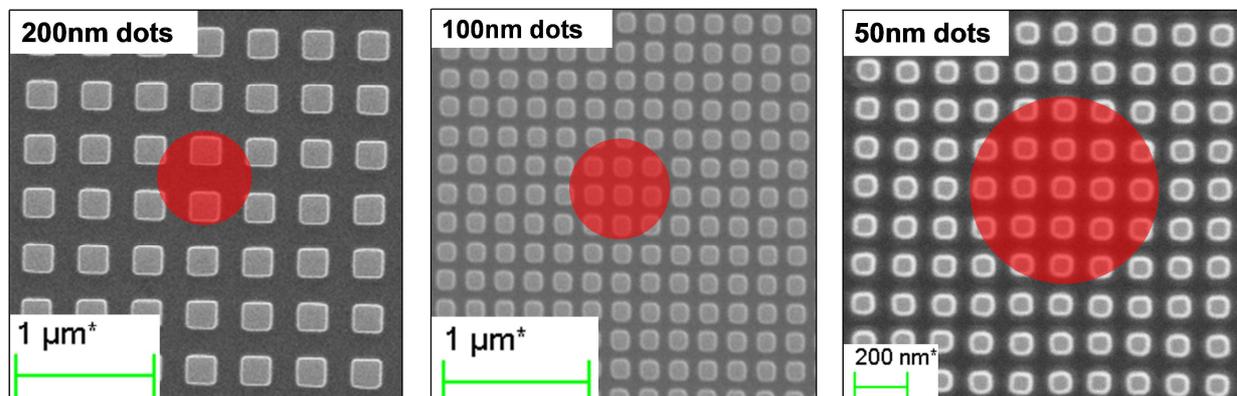


Fig. 3.8 – Schematic representation of the Focalized-MOKE setup.

A He-Ne laser (wavelength 632 nm) beam of 7 mW power was polarized and focused with a system of lenses. A 100x focalization lens focused the laser beam to a spot of around 600 nm diameter. This allows measuring about 2-3 dots for the 200 nm dot size, 9-10 dots for the 100 nm dot size and 14-15 for the 50 nm cases (Fig.3.9). The samples were fixed on a ScanPod© support. This system allows moving the sample both in translation and rotation, providing high accuracy in the focalization and in the dot localization. The reflected signal was separated by a Wollaston prism into two beams with orthogonal polarizations and then analysed by two photodiodes, allowing determining the polarization of the reflected beam and thus the magnetic signal of the sample.

The samples were positioned inside the gap of an electromagnet. To obtain reasonable statistics on  $H_{ex}$  distributions, fifty measurements were performed on each sample along the easy axis (defined as the direction of the setting field during annealing) for all dot sizes plus the sheet films. A sinusoidal signal was sent to the electromagnet for sweep rates going from 1.2 to 33 T/s. In this range of variation, the sweep rate had no significant influence on the magnetic behaviour. For simplicity reasons, the measurements presented in the following chapters have all been performed at 3.3 T/s. Each measurement was the result of an average of hundred individual hysteresis loops on the same spot. All measurements were performed at room temperature.



**Fig. 3.9** – SEM images of two chosen patterned geometries after e-beam lithography and IBE. The red circle represents the laser spot area during focalized-MOKE measurements indicating the number of dots probed by the laser spot.

### 3.2.3 X-ray diffraction (XRD)

X-ray diffraction is a technique that allows obtaining information on the crystallographic structure of a material. This happens through the detection of plane waves generated by the constructive interference of the spherical waves due to the interaction between the incident x-ray plane waves and the atomic crystalline structure. This phenomenon is described by Bragg's law  $n\lambda = 2d \sin\theta$ , with  $\lambda$  being the incident wavelength,  $\theta$  the angle between the scattering planes of the crystal and the incident x-ray, and  $d$  is the interplane distance. During the thesis, a Co radiation source with  $\lambda = 1.789$  Angstrom has been used. Peaks are observed for values of  $\theta$  which give constructive interferences (i.e. verify Bragg's law) for the considered value of  $d$ , characteristic of the studied crystal. The measurement of  $\theta$  values corresponding to diffraction peaks allows the determination of the  $d$  interreular distances, which are directly related to the unit cell, thus to the lattice parameters. This kind of scan allows determining the crystallographic structure and the lattice parameter of the considered material (or series of layers). The technique used to cover the diffraction spectrum is the Bragg-Brentano  $\theta$ - $2\theta$ , shown in Fig.3.10.

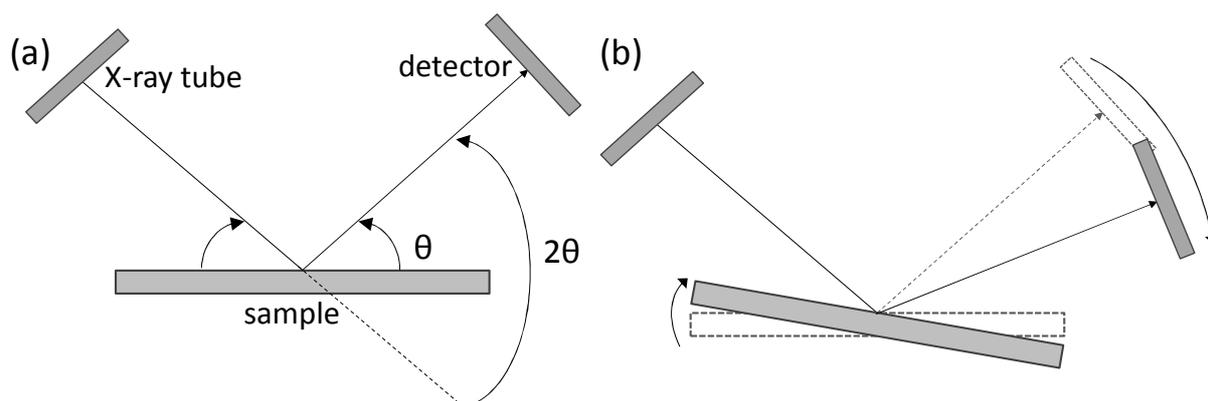


**Fig. 3.10** – Schematic representation of the  $\theta$ - $2\theta$  method: (a) definition of  $\theta$  and  $2\theta$  angles; (b) movement of sample and detector during a  $\theta$ - $2\theta$  scan for a fixed x-ray tube.

According to the x-ray diffraction machine, different mechanical movements are possible to perform a  $\theta$ - $2\theta$  scan. During the thesis, the machine presented a fixed x-ray tube. In this case, during the scan the sample and the detector move together, maintaining a  $2\theta$  angle between the incident and the reflected beam and a  $\theta$  angle between the reflected beam and the sample. In this way, the planes with a component normal to the sample are detected. The position of the diffraction peak of a material may shift from its bulk position because of strain due to interface lattice parameter mismatch with neighbour materials.

### 3.3 Atomistic simulation

In parallel with the experimental study, a simulation approach has been considered during the three years of thesis, based on the implementation of a code for atomistic simulations developed by L\_Sim laboratory of CEA Grenoble. Micromagnetic simulations consider magnetic behaviour in sub-micrometre length scale. An atomic approach considers singularly each spin of the magnetic system. Thus the effects of an interface coupling like the exchange bias one can be taken account with a direct interaction of the spins, instead of having to add an extra magnetic field to mimic this effect in micromagnetic simulations. Effects like domain formation and dipolar effect could be observed during the simulations of the hysteresis loop of F/AF dots.

On all the studied systems, a hysteresis loop was calculated along the easy axis direction. The spin configurations at each point of the loop were obtained by minimizing the total magnetic energy for all the values of the applied field, starting at each step from the spin configuration of the previous step.

The different models, with different sizes, shapes and layer stackings, were created by programming in Python language. They allowed the definition of the interactions, dot size and geometry, spin direction and energy parameters. Once the structure was set, a series of energy minimizations under applied field allowed simulating a hysteresis loop. The software used for these calculations was Mi\_Magnet, developed by Frédéric Lançon, Luc Billard and Thomas Jourdan from the L\_Sim laboratory [8-10]. Mi\_Magnet is a Fortran code based on the Heisenberg model that allows the minimization of the energy of a magnetic system, starting from an initial atomic spin configuration, and giving at the end the equilibrium state, as well as information on the energy values of the system. It allows the simulation of systems with up to a million of atoms. The resulting spin configurations were then observed by V\_Sim, software which allows the visualization of the atomic and spin structures of a crystalline system from different points of view, with the possibility of displaying the physical parameters obtained by Mi\_Magnet or selecting atomic planes or sections.

#### 3.3.1 Heisenberg model and physical parameters

Mi\_Magnet is a global energy minimization code based on the classical Heisenberg model. The model describes each spin as  $s = s \mathbf{u}$ , with  $\mathbf{u}$  a 3D unit vector and  $s$  its spin modulus. The total energy of the system is defined as [1,11]:

$$\begin{aligned}
E = E_{Zeeman} + E_{dip} + E_{ex\_coupl} + E_{anis} = \\
- \sum_{i=1}^N \mathbf{H}_{ext} \mathbf{s}_i + \sum_{i,j < i}^{N,N} \frac{\mu_0}{4\pi} \frac{\mathbf{s}_i \cdot \mathbf{s}_j - 3(\mathbf{s}_i \cdot \mathbf{n}_{ij})(\mathbf{s}_j \cdot \mathbf{n}_{ij})}{r_{ij}^3} - \sum_{i,j < i}^{N,n_i} J_{ij} \mathbf{s}_i \cdot \mathbf{s}_j - \sum_{i=1}^N K_i (\mathbf{n}_i \cdot \mathbf{u}_i)^2
\end{aligned} \quad (3.4)$$

The energy terms are respectively:

- *Zeeman energy*, calculated as the interaction between each of the N spins and the external field  $\mathbf{H}_{ext}$ ;
- *Dipolar energy*, calculated by a fast multipole method [8-9] as the interaction between each spin and all the other spins. The vector  $\mathbf{n}_{ij}$  is the unit vector pointing from spin  $i$  to spin  $j$ , and  $r_{ij}$  is the distance between these two spins;
- *Exchange coupling energy*, calculated as the interaction of each spin with its  $n_i$  nearest neighbours. Different exchange coupling constants  $J$  were defined for F-F, AF-AF and AF-F spin interactions, both in-plane and out-of-plane;
- *Anisotropy energy*, calculated on each spin. The modulus  $K$  and direction  $\mathbf{n}$  of the anisotropy term were set independently for both F and AF spins.

The energy minimization process of Mi\_Magnet is a FORTRAN implementation [12] of the conjugate gradient method [13-14]. To understand its working principle, let's compare it with another classic minimization method, the steepest descent (see Fig.3.11).

The steepest descent is a first order optimization algorithm. The minimum of a function  $f$  is reached with a zig-zag like path by moving from a point  $\mathbf{P}_i$  to the minimum by gradually sliding down the gradient  $-\nabla f(\mathbf{P}_i)$  [15]. It's a very simple method but quite inefficient because of the many small steps necessary to reach the minimum.

On the other hand, the conjugate gradient method generates a path in the configuration space by taking account of the quadratic part of  $f$ , as  $f(\mathbf{x}) \approx c - \mathbf{b} \cdot \mathbf{x} + \frac{1}{2} \mathbf{x} \cdot \mathbf{A} \cdot \mathbf{x}$ . If for configurations  $\mathbf{P}_i$  a sequence of vectors  $\mathbf{g}_i = -\nabla f(\mathbf{P}_i)$  and a corresponding sequence of conjugate vectors  $\mathbf{h}_i$  are defined, these two sequences lead to the minimum of the quadratic form through successively conjugate directions  $\mathbf{h}_i$ , passing from  $\mathbf{g}_i = -\nabla f(\mathbf{P}_i)$  to  $\mathbf{g}_{i+1} = -\nabla f(\mathbf{P}_{i+1})$ . The method is effective because function  $f$  is getting better represented by its quadratic part as configurations  $\mathbf{P}_i$  approach the minimum.

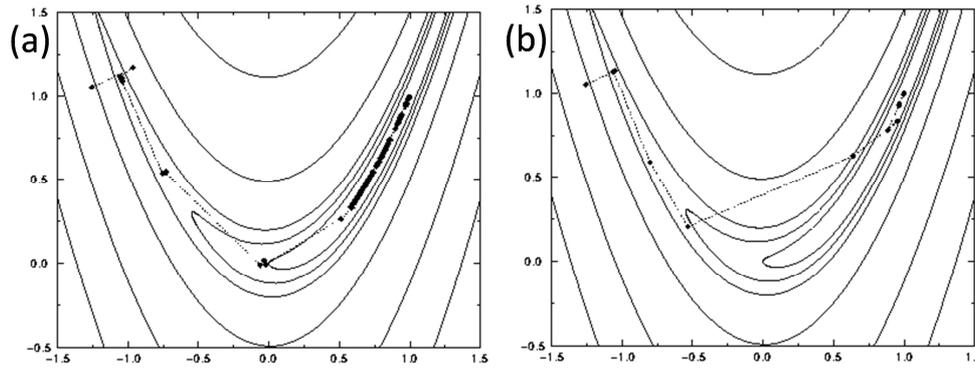


**Fig. 3.11** –Steepest descent (a) and conjugate gradient (b) minimization paths on a 2D function. Each black point represents a step [12].

In the case of Mi\_Magnet, the function  $f$  to be minimized is the total energy  $E$  of the system, which takes into account the whole spin population. Each spin  $i$  has its orientation defined by two angles  $\theta_i$  and  $\varphi_i$ , and all these angles are the variables of  $f$  to optimize with the conjugate gradient method. The successive steps are repeated until all the torques acting the spins are below a given threshold.

The micromagnetic values of exchange coupling, spin modulus and in-plane magnetocrystalline anisotropy of Co and IrMn [16-18] were:

$$\begin{aligned}
 \mu_B(\text{Co}) &= 2.2 \mu_B \\
 \mu_B(\text{IrMn}) &= 1.6 \mu_B \\
 K_{anis}(\text{Co}) &= 1000 \text{ J} / \text{m}^3 \\
 K_{anis}(\text{IrMn}) &= 5.5 \cdot 10^5 \text{ J} / \text{m}^3 \\
 A(\text{Co}) &= 10^{-11} \text{ J} / \text{m}
 \end{aligned} \tag{3.5}$$

It has to be noticed that, for simplicity, the system had a simple cubic (SC) crystalline structure with an interatomic distance of 0.2 nm (as for bulk Co) for both the F and the AF layers. In this way the crystalline model of the system is much simplified since the crystalline structure of IrMn is composed of two sublattices as shown in Chapter 1, and both Co and IrMn have an fcc structure. The aim of the simulations is to observe the effects of F/AF coupling on systems with reduced lateral size, in particular the domain wall formation in the AF layer during magnetization reversal. This aspect cannot be simulated with standard micromagnetic models, which usually represent the exchange bias coupling as an additional field to the system.

For each spin of the system, a spin modulus (in  $\mu_B$ ) and an anisotropy value (in meV) were given, together with the values of the exchange coupling with its neighbours. For F-F neighbours, the coupling was set positive ( $J_{F-F} > 0$ ). The AF layer consists of atomic planes parallel to the interface with a F in-plane coupling ( $J_{x,AF-AF}, J_{y,AF-AF} > 0$ ) and an AF coupling

perpendicular to them ( $J_{zAF-AF} < 0$ ). This setting corresponds to the uncompensated AF scheme of Fig.1.2. The F/AF interface is parallel to the  $x$  and  $y$  axes. The thickness is the size along  $z$ . The F/AF interface was arbitrary set with a F coupling ( $J_{F-AF} > 0$ ). Since no roughness is introduced at the interface, the system is fully uncompensated. The  $x$ -axis was chosen as the easy axis of anisotropy in the system. For each initial condition, all the F spins and the AF spins in the first atomic plane at the interface were set in the same  $x$ -direction. This mimics the result of a cooling with an applied field along the easy axis of the system.

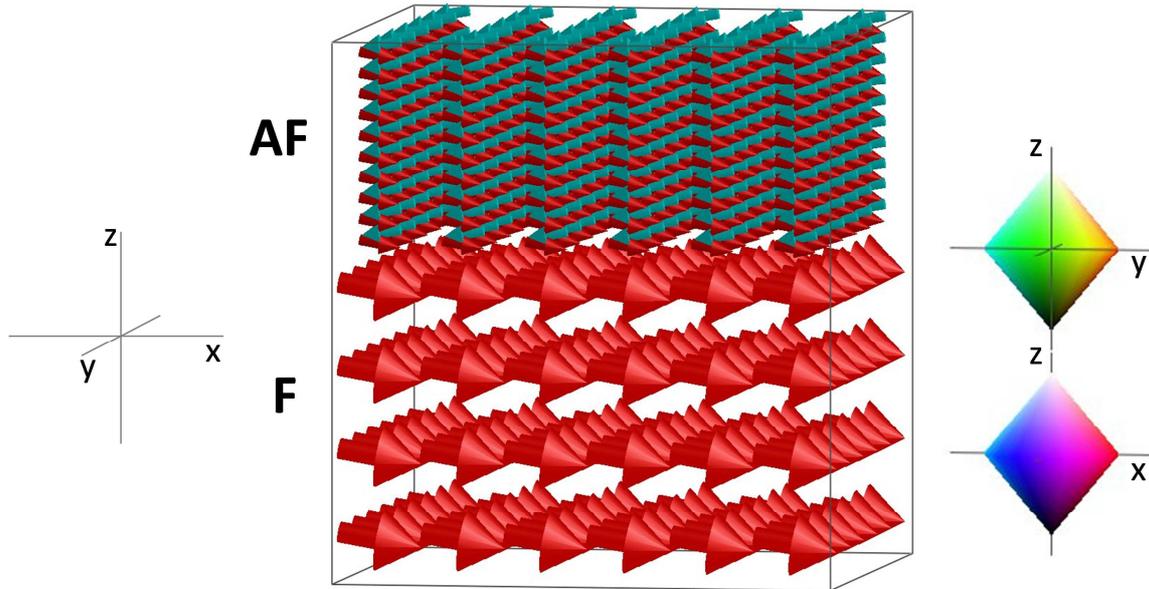


**Fig. 3.12** –V\_Sim visualization of an example of small F/AF system. Big red arrows represent  $8 \times 8 \times 8$  F macrospins, blue and red small arrows represent  $8 \times 8 \times 1$  uncompensated AF macrospins. On the right, the legend colour for the chosen visualization angle.

To achieve system sizes comparable to those of experimental patterned dots while keeping reasonable calculation times, spins were locally grouped into “macrospins” and interactions were rescaled. The F macrospins were formed by  $8 \times 8 \times 8$  ( $x \times y \times z$ ) spins, while to preserve the alternating orientations along  $z$  of the AF layers, the AF macrospins were formed by  $8 \times 8 \times 1$  spins (Fig.3.12). The Co exchange stiffness  $A$  was used to obtain the equivalent exchange coupling through the equivalence valid for a simple cubic structure:

$$J = \frac{2a}{\mu_B^2} A \quad (3.6)$$

where  $a$  is the interatomic distance (equal to 0.2 nm) for both the AF and F crystals.  $J_{F-F}$  was directly obtained through this equivalence.

$J_{AF-AF}$  was obtained through the equivalence:

$$\frac{J_{F-F} \mu_F^2}{J_{AF-AF} \mu_{AF}^2} = \frac{T_C}{T_N} \quad (3.7)$$

where  $T_C$  is the Curie temperature of F (1400 K for Co) and  $T_N$  the Néel temperature of AF (690 K for IrMn).

Concerning the F/AF interface coupling, two different cases were taken into account. In one case, the value was obtained from Eq.3.5 with  $\mu_B^2 = \mu_F \mu_{AF}$  where  $\mu_F$  and  $\mu_{AF}$  are the spin modulus, respectively in the F and AF layers. This strong interface coupling was used to observe the creation of domain walls parallel to the interface and in the AF layer during the F magnetization reversal. In the second case, the interface coupling was reduced by two orders of magnitude to consider a reduced effective coupling due to structural defects like roughness or grain boundaries.

The presence of macrospins with different sizes and shapes required a further renormalization of the  $J$  couplings. With a coupling energy defined for single spin interaction as:

$$E_{coupling} = J \mathbf{s}_1 \cdot \mathbf{s}_2 = J s_1 s_2 \cos \theta \cong J s_1 s_2 \left( 1 - \frac{\theta^2}{2} \right) \quad (3.8)$$

the macrospin defined as  $\mathbf{S} = n_x n_y n_z \mathbf{s}$  (in our case with  $n_x$  and  $n_y$  equal to 8 and  $n_z$  equal to 8 for the F and 1 for the AF) requires the definition of two angles for the F/AF interface, one for the internal spins of the F macrospin along  $z$ , another for the F-AF spins at the interface. The generalized coupling energy formula for macrospins is:

$$\begin{aligned} E_{Macrospin} &= J_M \mathbf{S}_1 \cdot \mathbf{S}_2 = J_M S_1 S_2 \cos \theta_M = J_M (n_x n_y n_z)^2 s_1 s_2 \cos \theta_M \cong \\ &\cong J_M (n_x n_y n_z)^2 s_1 s_2 \left( 1 - \frac{\theta_M^2}{2} \right) \end{aligned} \quad (3.9)$$

with corrective terms according to the kind of macrospins involved in the interaction. More details can be found in Appendix I. The consistency of the model was checked comparing the energies and the hysteresis loops of a macrospin system ( $8 \times 8 \times 8$  for F macrospins and  $8 \times 8 \times 1$  for AF macrospins) with a  $1 \times 1 \times 1$  system.

Finally, F and AF layers were subdivided into grains of equal dimension to take into account the polycrystalline state of the materials. A lateral grain size of 9.6 nm was chosen, close to the typically measured size in IrMn sputtered layers (see Chapter 4). The lateral coupling between the crystalline grains could be adjusted. In most of our simulations, the F grains were considered fully coupled, while AF grains were assumed uncoupled corresponding to the averaging out of the exchange energy across the disordered grain boundaries.

To reproduce a hysteresis loop, the system is first saturated by a positive field along the easy axis  $x$  and then decreasing fields are applied. The field is applied with  $1^\circ$  from the anisotropy axis of the F and AF layers to favour the magnetization reversal. For each field value, the energy is minimized starting from the spin configuration calculated for the previous field. When the opposite saturation field is reached, the second part of the loop is achieved by increasing back the magnetic field.

In this model, no thermal effects were taken into account, except for the initial state seen as the result of a thermal annealing under applied field.

## Bibliography

- [1] Ernult F 2002 *Thèse Université Joseph Fourier*
- [2] Ali M, Marrows C H, Al-Jawad M, Hickey B, Misra A, Nowak U and Usadel K D 2003 *Phys. Rev. B* **68** 214420
- [3] Schwarz A and Wiesendanger R 2008 *Nano Today* **3** 28
- [4] Lohau J 1999 *J. Appl. Phys.* **86** 3411
- [5] Lohau J 2000 *J. Appl. Phys.* **76** 3094
- [6] Khizroev S K, Jayasekara W, Bain J A, Jones R E and Kryder 1998 *IEEE Trans. Magn.* **34** 2030
- [7] Du Trémolet de Lacheisserie E 2000 *Magnétisme, Tome 1: Fondements* EDP Sciences, Grenoble
- [8] Jourdan T, Lançon F and Marty A 2007 *Phys. Rev. B* **75** 094422
- [9] Jourdan T, Marty A and Lançon F 2008 *Phys. Rev. B* **77** 224428
- [10] Ernult F, Dieny B, Billard L, Lançon F and Regnard J R 2003 *J. Appl. Phys.* **94** 6678
- [11] Jourdan T 2008 *Thèse Université Joseph Fourier*
- [12] Press W H, Flannery B P, Teukolsky S A and Vetterling W T 1990 *Numerical recipes (FORTRAN)* Cambridge University Press
- [13] Hestenes M R and Stiefel E 1952 *J. Reas. Nat. Bur. Stand.* **49** 409
- [14] Hager W W and Zhang H 2006 *Pac. J. Optim.* **2** 35
- [15] Wang Xu 2008 *Method of steepest Descent and its applications* University of Tennessee
- [16] Yamaoka T, Mekata M and Takaki H 1971 *J. Phy. SOC Japan* **31** 391
- [17] Buda L D 2001 *Thèse Université de Strasbourg*
- [18] Vallejo-Fernandez G, Fernandez-Outon L E and O'Grady K 2007 *Appl. Phys. Lett* **91** 212503



# Chapter 4

## **Exchange bias variability on patterned arrays of IrMn/Co square dots**

As shown in Chapter 2, exchange bias is exploited in MRAM systems for pinning the reference layer and, in case of Thermally Assisted MRAM, for stabilizing the magnetization direction of the storage layer at operational temperature. In this kind of systems, as in spin valves for hard disk read heads, lateral sizes are on the order of few hundreds of nm. At these lateral dimensions, micromagnetic effects like shape effects, size effects and layers thicknesses affect the behaviour of the F layer. At the same time, the reduced dot dimensions affect also the properties of the AF layer. In particular, for a sputtered system the number of AF grains present on a single dot is reduced to few hundreds down to few tens. When the number of AF grains is so low, the dot population is not large enough to reproduce the average population of a full sheet sample, like the one presented in Chapter 1.

This chapter will present the study performed on IrMn/Co square dots, patterned with the fabrication process described in Chapter 3. The main focus of the study has been centered on the variability of exchange bias properties, i.e. the variation of hysteresis loop shape and shift from one small group of dots to another. Three parameters have been changed: the thickness of the F layer, the thickness of the AF layer and the thickness of the buffer layer. Each change of parameter focuses corresponds to a change of magnetic properties on the dot. In the first case, the micromagnetic configuration of the F layer is affected; changing the AF thickness involves the AF grain lateral size and volume, with consequences on the thermal stability of exchange bias. For the last case, the different thickness of the buffer layer changes the AF grain diameter and its distribution without varying its thickness.

## 4.1 Aim of the study

### 4.1.1 Finite size effects on exchange patterned dots

In 1999 Cowburn *et al.* [1] showed how the micromagnetic properties of a F layer changes according to the lateral size of the dot and the thickness of the layer. Later MFM measurements on Co circular dots [2] and micromagnetic simulations [3] confirmed the presence of three regimes as a function of lateral size and Co thickness: single domain (SD) for thin F layer and small lateral size, out-of-plane magnetization for thick F layer and small lateral size and vortex state elsewhere. For an equivalent F thickness, the transition from circular to elliptical dot may change the micromagnetic behaviour and the magnetization reversal, passing from vortex to SD reversal for an increasing aspect ratio [4] or change the annihilation field [5].

When adding an AF layer to the dot, the hysteresis loop is shifted compared to an equivalent unbiased dot; the micromagnetic behaviour of the dot may differ from the unbiased case according to the field cooling conditions [6]. NiFe/IrMn square dots showed a larger or smaller exchange bias compared to equivalent full sheet samples according to IrMn thickness, together with an enhancement of coercivity and a reduction of blocking temperature [7]. Similar structures presented different values of blocking temperature, exchange and coercivity according to the lateral size [8] or differences in  $H_{ex}$  and  $H_C$  trends as a function of IrMn thickness as a function of the measuring temperature [9]. IrMn/NiFe square dots showed a decrease in exchange bias compared to continuous layer [10] whereas needle-shaped and rectangular IrMn/CoFe dots presented increased coercivity compared to equivalent CoFe dots and similar exchange values compared to full sheet samples [11].

As it appears quite clearly, the range of possible behaviours that an exchange biased dot system may present is quite large. In our study the attention will be focused on IrMn/Co dots of fixed geometry (square shape) for three different lateral sizes (200x200, 100x100 and 50x50 nm<sup>2</sup>), changing different parameters (Co thickness, IrMn thickness and buffer layer thickness). Co dots are known to present a coherent reversal for thin F values and vortex nucleation and annihilation for thick F values [2,12,13]; our study will confirm similar micromagnetic configurations when exchange coupled with IrMn.

In this study, the micromagnetic properties of the selected geometry have been verified by MFM measurements. The analysis was then centred on the variability of exchange bias properties of the dots through focalized-MOKE and on the spin configurations through atomistic simulations.

### 4.1.2 Variability of magnetic properties on patterned systems

One of the most important issues in MRAM systems is the reliability and reproducibility of magnetic behaviour from one memory point to another. Indeed, magnetic nanostructures intrinsically have variability of magnetic properties [14]. Nominally identical magnetic stacks present different magnetic field reversal from dot to dot, giving a so called switching field distribution (SFD). This phenomenon occurs both on perpendicular [15-17] and in-plane [18,19] magnetized dots. The evaluation of SFD can be obtained qualitatively by Magnetic Force Microscopy (MFM) by scanning a large number of dots under an in-situ applied magnetic field. This variability is usually attributed to dot-to-dot variations of anisotropy, number of nucleation centres for perpendicular media, or by the presence of defects or shape variability. This variability directly reflects on MTJ structures reproducibility. For those structures, the SFD is observed through memory tests like the switching probability as a function of write current [20-21]. Similar distributions have been observed on exchange biased systems, like IrMn/NiFe circular dots [22].

In the study, the possibility of focussing the MOKE measurements on few dots will give a qualitative evaluation of the SFD on exchange biased systems, allowing to compare hysteresis loops of few identical dots one with the other, instead of having an average measurement on the whole patterned systems, as it usually appears in literature.

## 4.2 Micromagnetic effects of Co thickness on IrMn/Co square dots

### 4.2.1 Full sheet samples

The composition of the considered multilayered exchange biased samples was (units in nm): Ta<sub>3</sub>/Cu<sub>3</sub>/IrMn<sub>6</sub>/Co<sub>x</sub>/Pt<sub>2</sub>, with x = 2.5, 3.7, 5, 10, 15, 20 and 25 nm. Ta and Cu were used as buffer layers in order to improve the growth of the F and AF layers (see the following paragraph) [23]. The IrMn alloy composition is Ir<sub>20</sub>Mn<sub>80</sub>. A thickness of 6nm was chosen because IrMn/Co full sheet samples show a maximum of exchange bias around this value [24] (also confirmed by full sheet samples in the IrMn thickness effect study, see Fig. 4.25). Pt was used as capping layer to avoid Co oxidation. All layers were deposited by dc magnetron sputtering on thermally oxidized (100) Si wafers. The base pressure was 3·10<sup>-7</sup> mbar, whereas the Ar pressure during deposition was 2.5·10<sup>-3</sup> mbar. The targets were facing the substrates during deposition, so that neither shadowing nor oblique deposition effects have to be considered. The samples were subsequently annealed at 473 K (200°C), above the IrMn

blocking temperature for the considered thickness [25], for 30' in vacuum at about  $10^{-5}$  mbar, with a setting planar field of around 2000 Oe. This deposition and annealing steps have been maintained unchanged for all the samples presented in the chapter.

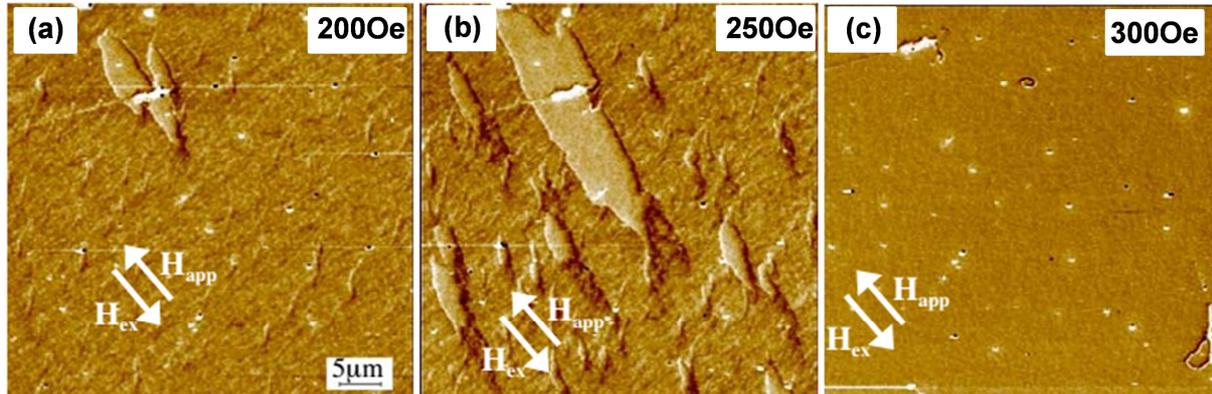


**Fig. 4.1** – MFM images of magnetization reversal with in-situ applied field for the IrMn<sub>6</sub>/Co<sub>5</sub> continuous layer. From (a) to (b) the formation and propagation of domain walls is observed, since total magnetization reversal (c) is reached.

MFM measurements on IrMn<sub>6</sub>/Co<sub>5</sub> continuous layer were performed under in-situ applied planar field to observe the magnetization reversal. Fig.4.1 shows a series of MFM scans on the same zone of the samples, at different applied fields. Images show the nucleation and propagation of domain walls at structural defects, since complete magnetization reversal, typical of continuous films. The shape of the domains and the contrast at the domain walls confirm similar measurements performed on Co/IrMn bilayers [26]. In Fig.4.2,  $H_{ex}$  marks the cooling field direction set during annealing, whereas  $H_{app}$  is the direction of the in situ applied field. It is important to underline that the direction of the applied field along the easy axis always had an experimental deviation with respect to the setting field. For this reason, the resulting magnetization direction of the system should be directed along the sum of the two vectors (applied field and unidirectional anisotropy), in a model similar to the one of Meiklejohn, as shown in Fig.1.7b (Fig.4.2). For this reason, the values of the in-situ applied field present in the MFM images have to be considered as qualitative.

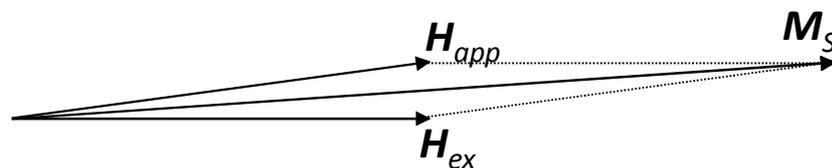


**Fig. 4.2** – Model of experimental tilt between exchange anisotropy and applied field, and the resulting sample magnetization.

Full sheet samples were then measured with focalized-MOKE. Samples were characterized with fifty measurements on different spots of the surface. Variability of full sheet samples resulted negligible, with a standard deviation from the mean value always smaller than 10 Oe. Hysteresis loop measurements at room measurement along the field cooling direction (easy axis) show a linear decrease of exchange bias as the Co thickness

increases (Fig. 4.3). This confirms the typical behaviour of exchange bias bilayers and is coherent with equivalent system measurements present in the literature [23].

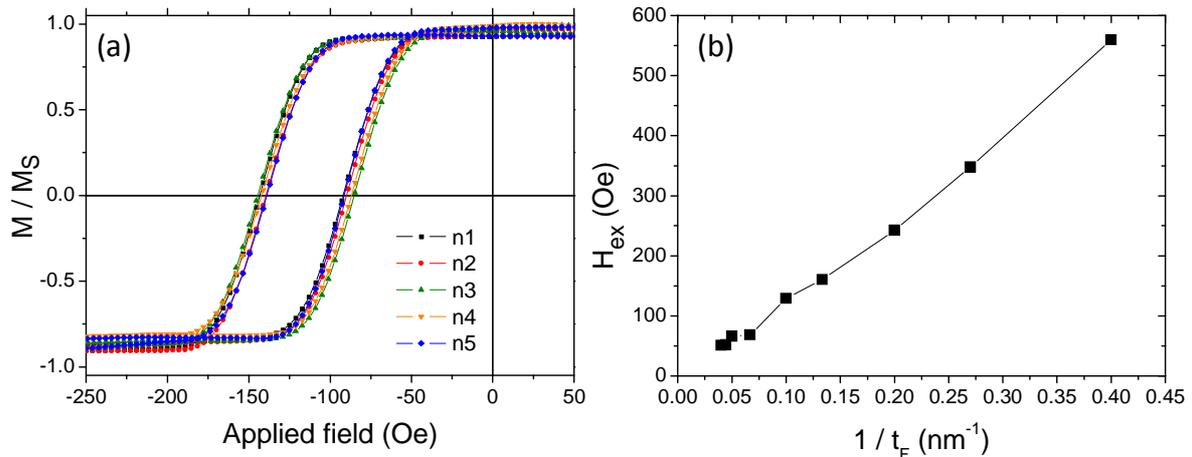


**Fig. 4.3** – (a) Five focused measurements on different spots of IrMn<sub>6</sub>/Co<sub>10</sub> full sheet sample. (b)  $H_{ex}$  curve as a function of the inverse of Co thickness on full sheet samples at room temperature.

#### 4.2.2 Patterned samples – MFM imaging

Two different geometries were considered: square dots  $200 \times 200 \text{ nm}^2$  with an edge to edge spacing of 200 nm and square dots of  $50 \times 50 \text{ nm}^2$  with an edge to edge spacing of 100 nm. This dense geometry was chosen to have a large enough signal for focalized-MOKE measurements. For these interdot spacings, it can be considered from earlier studies that the dots are weakly interacting from a magnetostatic point of view [27]. The size and shape of the dots as well as their spacing were controlled by scanning electron microscopy imaging (see Paragraph 3.1.2).

Patterned samples were first characterized by MFM measurements with in-situ applied field. A half loop was imaged on a group of dots, using the following procedure:

- Saturation of the sample with an external field of 2000 Oe along the setting field direction;
- MFM image at remanence (Fig.4.4a and Fig.4.4c);
- Application of an in-situ planar field along the easy axis, in the direction opposite to the setting field (Fig.4.4b and Fig.4.4d). The applied field was increased up to 400 Oe and then decreased down to 50 Oe, to reproduce a half hysteresis loop. MFM images were performed at different applied fields.
- MFM image at remanence.

According to the Co layer thickness, two different regimes were observed; they will be distinguished as thin F and thick F cases.

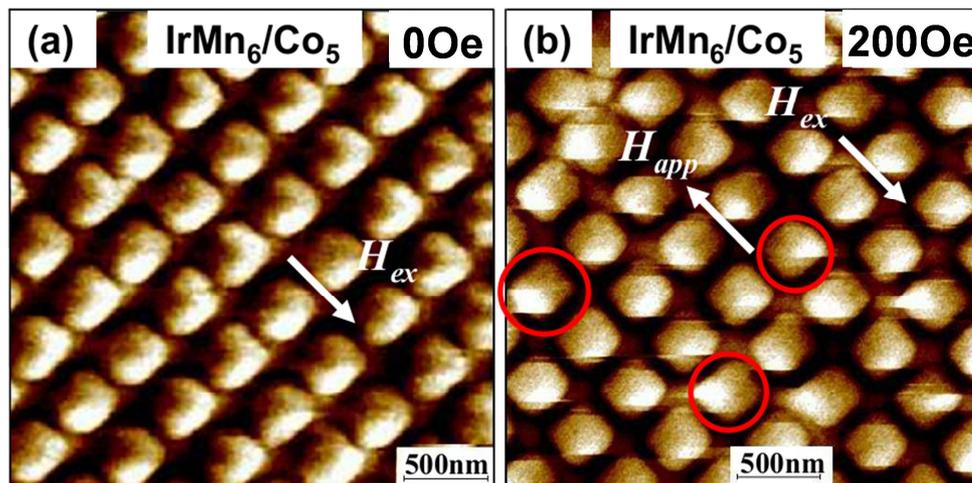


**Fig. 4.4** – MFM image at remanence after field saturation (a) and with in-situ applied field (b) for 200 nm square dots of IrMn<sub>6</sub>/Co<sub>5</sub>.

For the thin Co regime, as shown in Fig.4.4 for the case with 5 nm Co thickness, the dots appeared with a uniform dipolar contrast at zero field along the setting field direction (Fig.4.4a). This indicates the presence of a SD state. When applying the field in opposite direction, SD dots presented coherent magnetization reversal (Fig.4.4b). Red circles emphasise the in-plane reversal of the dots. It has to be noticed that the dots did not reverse at the same time or along the same direction. This result already indicates the presence of SFD, as will be confirmed by focalized-MOKE measurements in the following paragraph. The reversal mechanism is similar to the one observed on comparable Co circular dots [2], meaning that the exchange biasing with IrMn does not affect the magnetization reversal mechanism of the F layer.

For the thick Co regime, starting from a thickness of 20 nm, the magnetization reversal took place through the formation of complex multidomain configurations (Fig.4.5b). The dots with this second configuration has lower stray field compared to the SD ones; for this reason, its contrast appears much weaker and, because of the presence of both states in the image, it becomes difficult to detail its magnetic configuration. Also in this case, the transition from single domain state, present at remanence, to multidomain state did not take place at the same field for all dots.

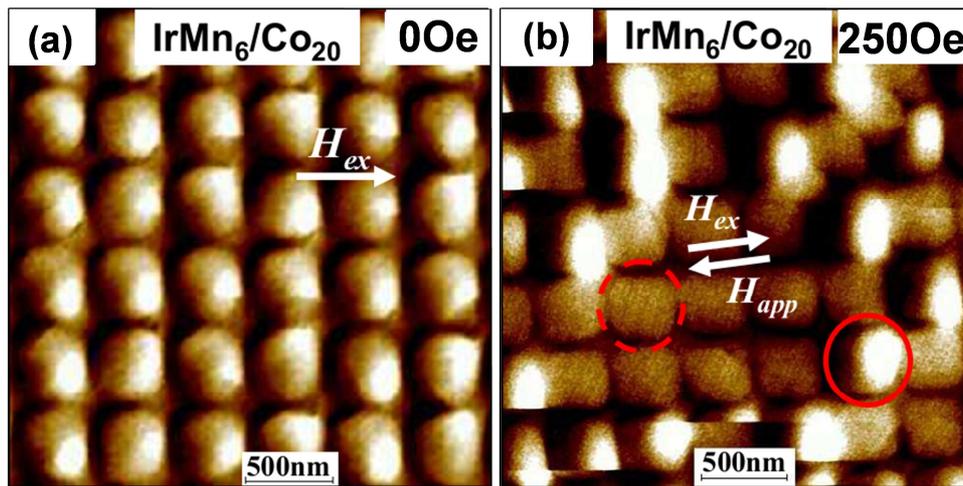


**Fig. 4.5** –MFM image at remanence after field saturation (a) and with in-situ applied field (b) for 200 nm square dots of IrMn<sub>6</sub>/Co<sub>20</sub>. The transition from single domain (continuous circle) to multidomain state (dashed circle) is observed in (b)

For both regimes no apparent correlation, like group reversal for coherent reversal or chains of vortices [27] exists in the magnetization reversal process between neighbouring dots. This indicates that the dots are weakly magnetostatically coupled as previously stated. For these reasons, in the following discussion, they will be considered as independent.

### 4.2.3 Patterned samples – Focalized-MOKE measurements

Focalized-MOKE measurements confirmed the presence of two different reversal behaviours depending on the Co thickness. Samples with thicknesses from 2.5 to 15 nm presented a single shifted hysteresis loop, whereas samples with 20 and 25 nm thicknesses showed double loops, with a general shift along the direction of the setting field (see Fig.4.7). The possibility of having shifted double loops for exchange biased dots was already observed in NiFe/IrMn dots [28]. This configuration was confirmed for both dot sizes, indicating that the micromagnetic behaviour did not change in the selected dot dimensions (see Fig.4.6). It has to be remembered that the measure of Fig.4.6a takes into account 2-3 dots whereas Fig.4.6b is the average on 14-15 dots.

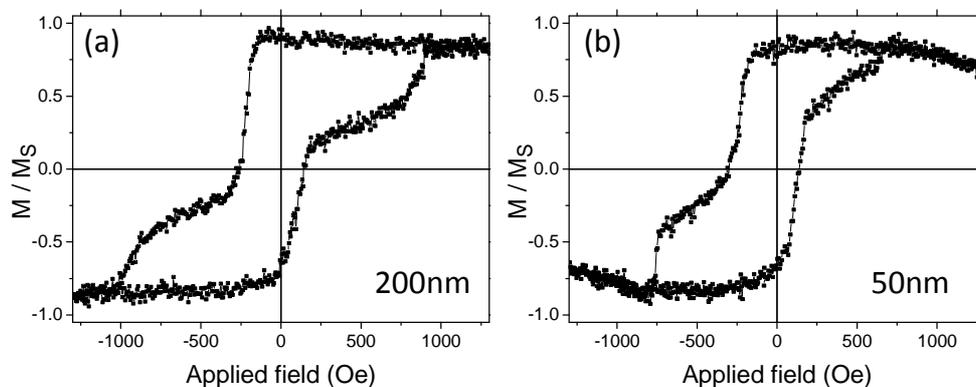


**Fig. 4.6** – Hysteresis loop of a single focused measurement for the 200 nm (a) and 50 nm (b) cases for IrMn<sub>6</sub>/Co<sub>20</sub> sample.

Before getting into the details of exchange bias variability, let's first observe the average behaviour of the patterned systems in comparison with the full sheet one. The averaged hysteresis loops of Fig.4.7 are the result of the normalized sum of fifty measurements performed at different locations on the 200 nm patterned dots and on the sheet film for two Co thicknesses: 10 and 20 nm. The patterned samples clearly show a large increase in coercivity as compared to the continuous film. For both Co thicknesses, the samples exhibit an overall loop shift, slightly reduced compared to the sheet film (see Fig.4.7b). The loop of the thicker Co sample (Fig.4.7a) has a constricted shape likely associated with the formation of a vortex-like intermediate state. Such a shape was already reported in other publications for large arrays of magnetic dots [29,30]. In particular, in Ref. [29] the hysteresis loop of the NiFe/IrMn disk (similar to the one of Fig. 4.7a) is compared to MFM images with in-situ applied field as presented in Paragraph 4.2.1. Also in that case, the contrast fell to zero passing from dipolar to multidomain configuration.

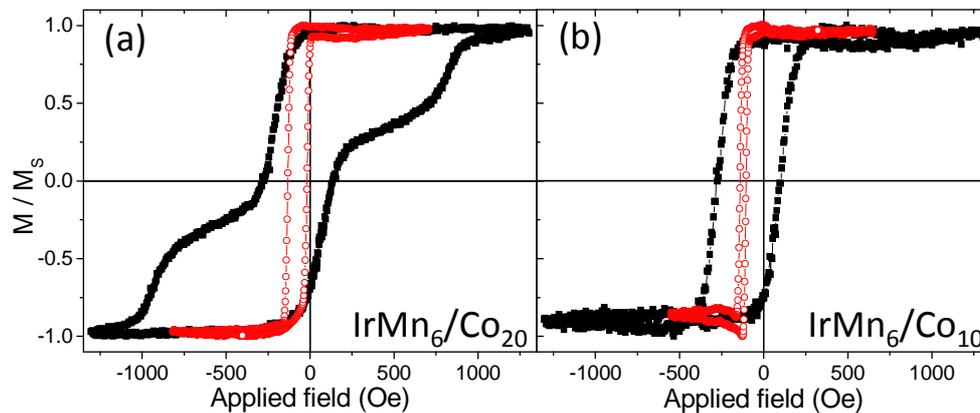


**Fig. 4.7** – Hysteresis loops averaged over 50 measurements on different zones for 200 nm square dots (solid squares) and full sheet samples (open circles) for IrMn<sub>6</sub>/Co<sub>20</sub> and IrMn<sub>6</sub>/Co<sub>10</sub> samples.

Moreover, the loops of patterned samples seem to present a smoother magnetization reversal with respect to sheet films. However, as it will be shown from the local measurements, this smoother magnetization reversal in the patterned samples is due to two coexisting aspects: the distribution of reversal field among the different dots which tends to spread out the averaged loop and an intrinsic smoother magnetization reversal within each individual dot. This second aspect can only be noticed when the measurement is focalized on few dots and not averaged on the whole patterned system.

Indeed, by considering local hysteresis loops, strong variations in the shape of the hysteresis loops were observed on different zones of the same sample with nominally identical dots. This is illustrated in Fig.4.8 which compares the hysteresis loops in two different zones of the same patterned sample, the laser spot enlightening 2 to 3 dots. A smooth magnetization reversal on patterned dots is already observed in the local measurements. In

contrast, local measurements on sheet samples showed small variations in exchange field and coercivity, and a sharp magnetization reversal (Fig.4.3a). This indicates that the different magnetization reversal mechanisms (domain nucleation/propagation in continuous films and coherent reversal or multidomain configuration in dots) cause different slope in the hysteresis loops.

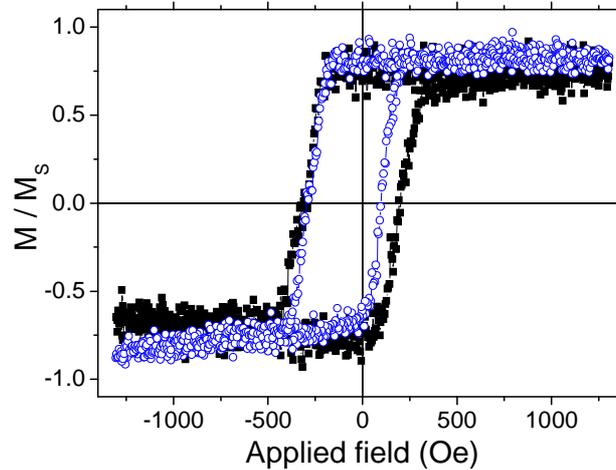


Fig. 4.8 – Comparison between two focused measurements on two different zones for 200 nm IrMn<sub>6</sub>/Co<sub>15</sub> square dots.

From the fifty measurements performed on different areas of the patterned systems, a series of direct information about exchange bias variability could be derived. The average exchange bias of the patterned dots was compared with the corresponding value on full sheet samples. The resulting curve, as a function of the inverse of Co thickness, is shown in Fig.4.9. In the figure, the red background marks the thick F regime (corresponding to the hysteresis loop of Fig.4.7a), whereas the grey one marks the thin one (Fig.4.7b). Error bars on patterned samples take into account the noise of the measurement due to the weakness of the signal.

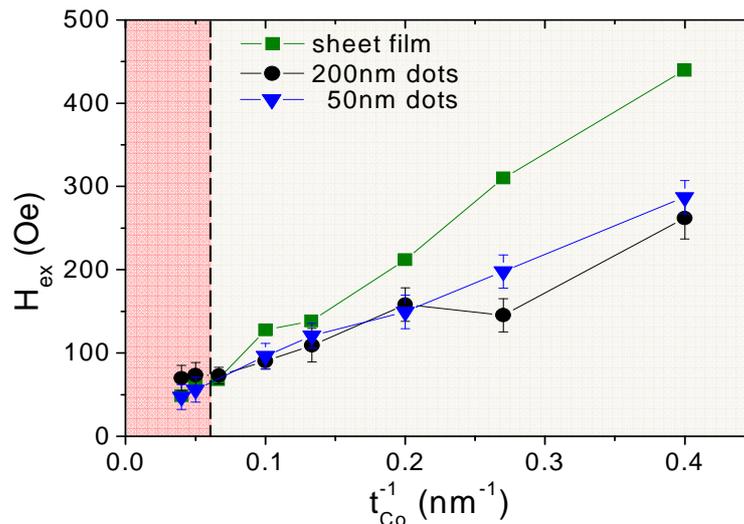


Fig. 4.9 – Average exchange bias field values as a function of the inverse of Co thickness for full sheet samples (green squares), 200 nm (black circles) and 50 nm (blue triangles) square dots.

It appears quite clearly how the average exchange bias amplitude is significantly reduced on patterned dots compared to sheet samples for thin Co layers, whereas for thicker Co layers the average values of  $H_{ex}$  are similar. Moreover, the samples with different dot sizes exhibit similar properties in terms of exchange bias amplitude, at least in the investigated range between 200 nm and 50 nm square dots. Thus, concerning the average behaviour, no relevant size effect is observed. Moreover, both patterned systems maintain a fairly linear behaviour as a function of the inverse of Co thickness. Given this linear tendency, the exchange bias energy  $E_{ex}$  can be obtained from the slope of the average  $H_{ex}$  with respect to the inverse of Co thickness using the following relationship:

$$H_{ex} = \frac{E_{ex}}{M_s t_{Co}} \quad (4.1)$$

where  $M_s$  is the saturation magnetization of Co ( $\sim 1400 \text{ emu/cm}^3$ ),  $t_{Co}$  the Co thickness, and  $H_{ex}$  the average exchange bias field as plotted in Fig.4.8. The linear fit gives a value of around  $0.09 \text{ erg/cm}^2$  for the patterned dots. Full sheet samples present higher exchange energy of around  $0.15 \text{ erg/cm}^2$ , comparable to values reported in the literature for equivalent stacks [23].

In order to correctly evaluate the variability from dot to dot of exchange bias properties, the exchange bias energy has to be considered instead of the exchange bias shift, in order to normalize it to the Co thickness. Variability is obtained from the standard deviation  $\sigma$  of the exchange energy, defined as:

$$\sigma = \sqrt{\frac{1}{N} \sum_{i=1}^N (x_i - \mu)^2}, \text{ with } \mu = \frac{1}{N} \sum_{i=1}^N x_i \quad (4.2)$$

In this case,  $\mu$  corresponds to the average exchange energy,  $x_i$  to the local measurement and  $\sigma$  to the standard deviation of the exchange energy, defined as  $\Delta E_{ex}$ . Fig.4.10 shows its evolution as a function of Co thickness for the 200 nm and 50 nm lateral size cases.

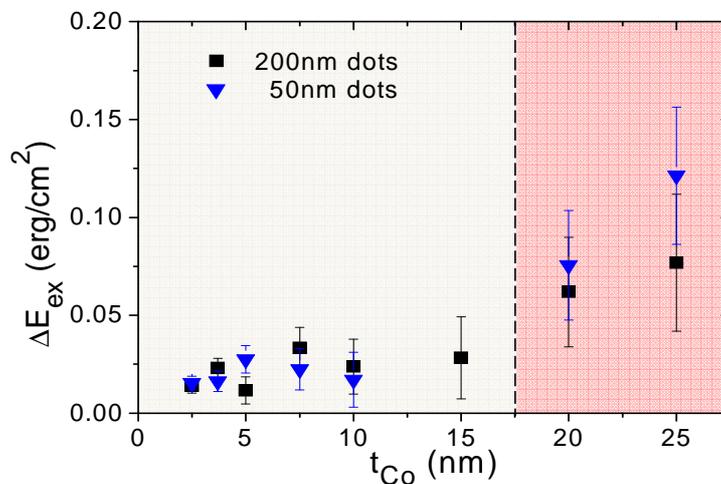


Fig. 4.10 – Width of the zone to zone distribution in exchange energy for patterned dots as a function of the Co thickness.

Despite the difficulty in comparing the results associated with different dot sizes because of the different number of probed dots per measurement (see Fig.3.9), some conclusions can nevertheless be drawn. In the regime of single shifted loops, no clear tendency in  $H_{ex}$  or  $\Delta E_{ex}$  can be observed in Fig.4.10. Similar values of  $\Delta E_{ex}$  are obtained for both 200 and 50 nm dots. Fluctuations in  $\Delta E_{ex}$  are however observed in the Co thickness range between 2.5nm and 10 nm. Since each Co thickness is associated with a different patterning operation, the observation of larger fluctuations in the standard deviation  $\Delta E_{ex}$  for low Co thickness may mean that the distribution in exchange bias properties from dot to dot is more sensitive to process fluctuations for low Co thickness than for large Co thickness. When the magnetization reversal is characterized by a shifted double loop process as in Fig.4.7a, i.e. for thick Co layers, the variations from dot to dot become much more significant compared to situations in which the magnetization reversal is characterized by a single shifted loop (Fig.4.7b). This is particularly true for the 50 nm dots, for which the measured variability is much larger than for the 200 nm dots despite the larger number of dots probed at each measurement due to the smaller pitch between dots.

In fact, if the curve of Fig.4.10 is normalized by the number of measured dots per measurement, the increased variability of the 50 nm dots in the thick Co regime appears clearly (Fig.4.11).

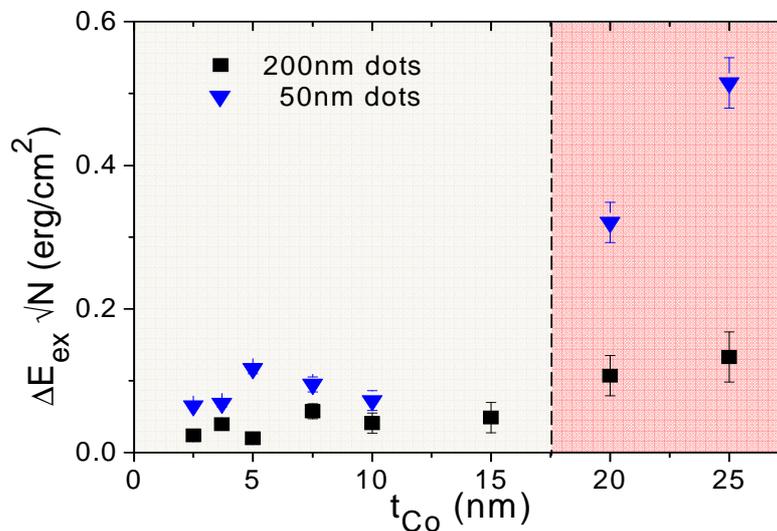


Fig. 4.11 – Normalized exchange energy distribution for patterned dots as a function of the Co thickness.

When considering the normalized curve, it can be observed how the smaller dots present a larger variability compared to the 200 nm case also in the single shifted regime. This aspect will be discussed in detail in the following paragraph.

#### 4.2.4 Patterned samples – Atomistic simulations

Experimental measurements were then compared to atomistic simulations performed with Mi\_Magnet, with the atomic construction and energy parameters presented in Chapter 3.

First, in order to verify the validity of the model, the magnetization processes in unbiased F dots with different lateral sizes  $L$  and thicknesses  $h$  were simulated. The aim was to obtain a graph as a function of these two parameters,  $L$  and  $h$ , which that would correspond to the ones obtained experimentally [1] or by micromagnetic simulation [3].

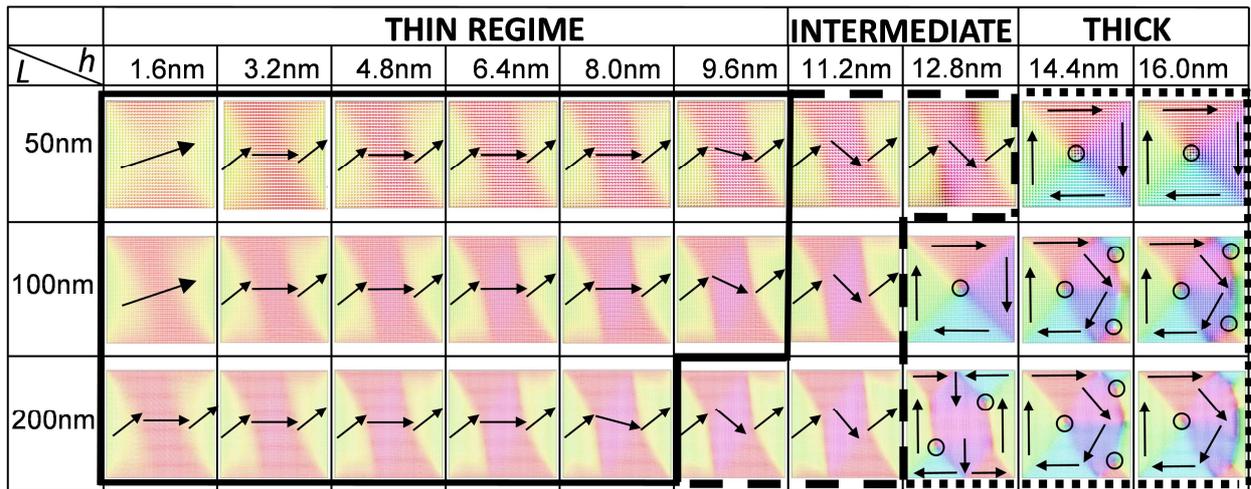


**Fig. 4.12** – Diagram of the spin configurations at remanence, versus the lateral size  $L$  and the thickness  $h$ , for single-F square dots obtained by atomistic simulations. Arrows indicate the local magnetization direction and small circles indicate the vortex locations. Continuous line encircles the coherent reversal regime, dashed line the multidomain one and dotted line the vortex regime.

The diagram of Fig.4.12 was obtained considering lateral sizes ranging from 50 to 200 nm and thicknesses from 1.6 to 16 nm. It shows the spin configurations at remanence and three different signatures of the magnetization reversal mechanisms can be recognized in these magnetic configurations. The zone delimited by a continuous line, concerning thin F layers, shows single domains – S state configurations – at remanence. In contrast, the zone delimited by a dotted line corresponds to the thickest dots (thickness  $> 12.8$  nm) and shows vortex spin configurations at remanence. In between these two regimes (dashed region), an intermediate magnetization configuration was obtained, corresponding to an S-state at remanence but with a more complex reversal mode than for thinner dots. To better observe the different magnetization processes associated to each regime, let's analyse their corresponding hysteresis loops.

In Fig.4.13 the hysteresis loop of a thin F case is plotted. The magnetization reversal takes place through a coherent reversal of the spins within the sample plane. The

corresponding simulated MFM images are in good agreement with the dipolar contrast obtained on the patterned samples as shown in Fig.4.4.

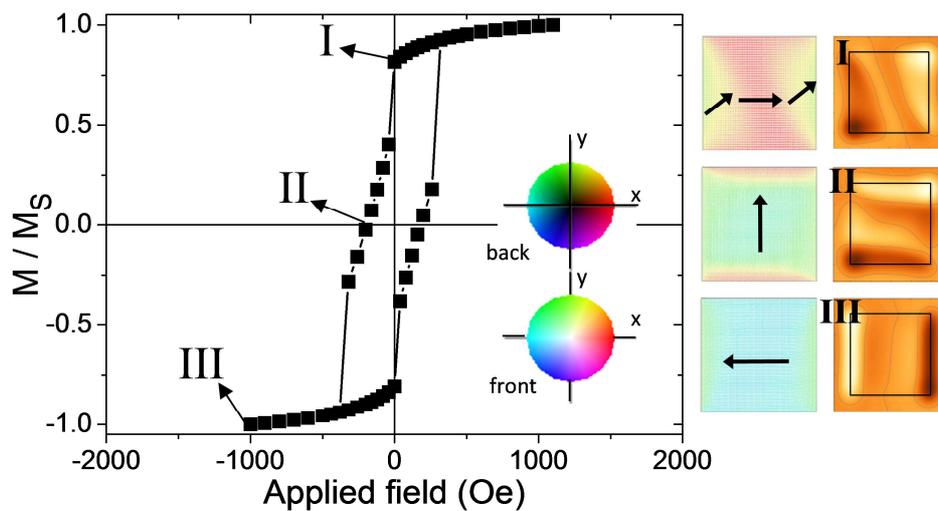


Fig. 4.13 – Hysteresis loop for a F dot of width 200 nm and thickness 1.6 nm. On the right, the characteristic spin configurations and their simulated MFM image.

Fig.4.14 shows the hysteresis loop and the spin configuration during the magnetization reversal for the intermediate case. In this case the magnetic configuration at remanence is still an S-state, but the magnetization reversal takes place through the formation of a multidomain state with two vortices. The two magnetic configurations before (I) and at (II) the creation of the multidomain state are shown. Arrows indicate the local magnetization direction of the different zones. In (II) two circles underline the presence of two vortices. With increasing applied field (III), the vortices move perpendicularly, favouring the central region, until they disappear at the surfaces and leave a new S-state.

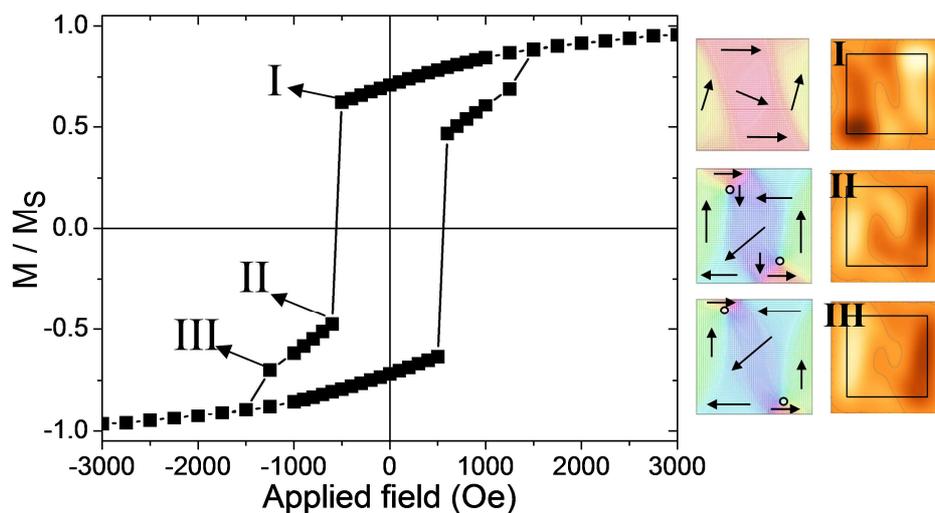
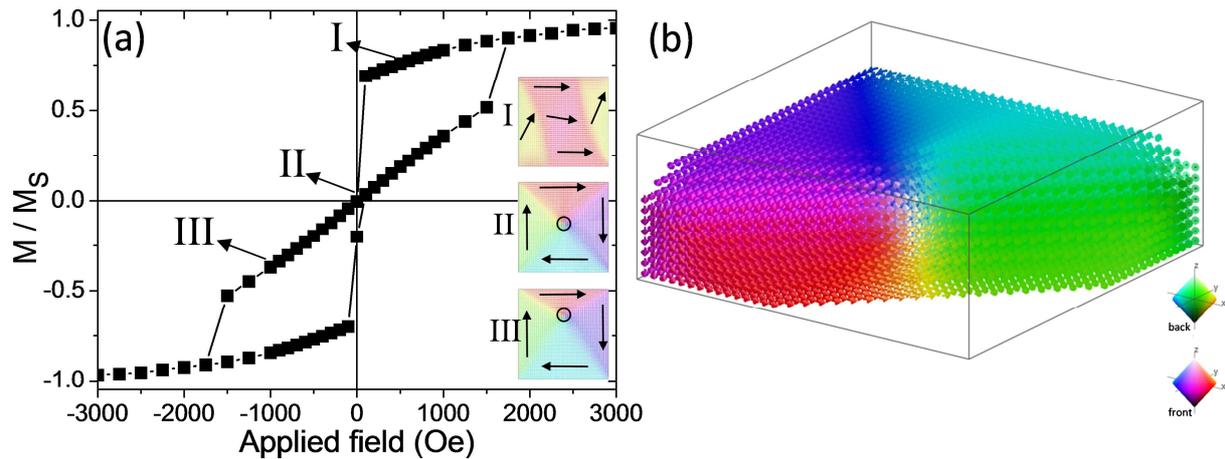


Fig. 4.14 – Hysteresis loop for a F dot of width 100 nm and thickness 11.2 nm. On the right, the characteristic spin configurations and their simulated MFM image.

Fig.4.15a considers the thickest F regime. In this case, during the hysteresis loop, the vortex core moves in the direction perpendicular to the direction of the applied field, increasing in that way the number of spins with positive projection along this direction, up to a critical field for which the vortex is annihilated. This vortex annihilation/nucleation process is irreversible and exhibits some hysteresis. This behaviour is in agreement with previous experimental observations and agrees with the results obtained by other simulation methods [5,31]. A section of the F layer showing the position of the vortex in the spin configuration is shown in Fig.4.15b.



**Fig. 4.15** – (a) Hysteresis loop for 100 nm dot with 12.8 nm F layer with corresponding spin configurations. (b) Section of the F layer at remanence.

After checking the validity of the simulation model on simple F systems, the AF layer was added to the system as described in Paragraph 3.3. Two different conditions were taken into account: weak interface coupling to observe the shift of the hysteresis loop and strong interface coupling to analyse the stability of the AF grain domain walls during F magnetization reversal.

The weak F/AF coupling led to a shift of the hysteresis loop without affecting the shape of the hysteresis loop. In particular, the intermediate case can be taken into account.

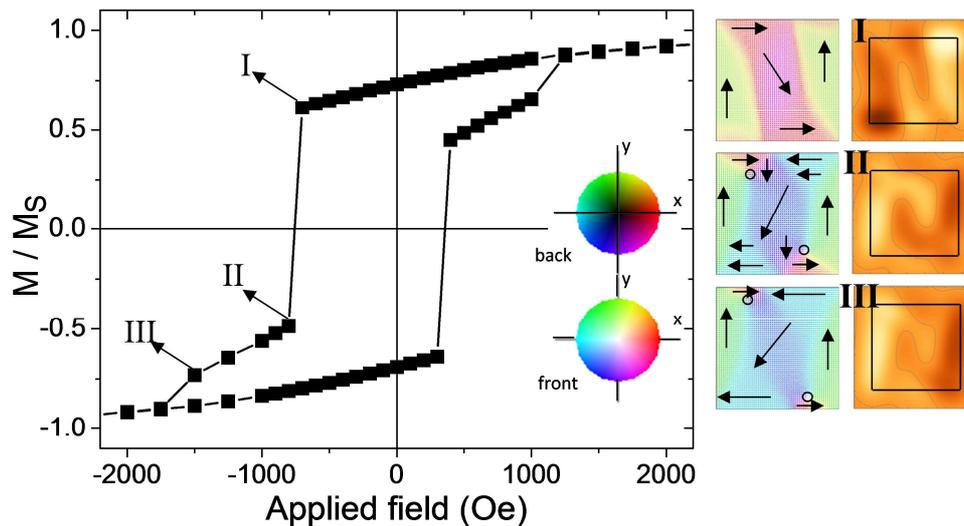


**Fig. 4.16** – Atomistic simulations for a F/AF system in the intermediate regime. On the right, the spin configurations and corresponding simulated MFM images.

As it can be seen in Fig.4.16, the simulated hysteresis loop is in good agreement with the experimental measurements of Fig.4.5a and Fig.4.6a. The simulated MFM images showed a bipolar contrast for the S state configuration. In the multidomain case, the images consist in a complex combination of faint contrasts. The MFM signal resulting from the multidomain state is much weaker than the bipolar one, and confirms the difficulty to have a reasonably high signal to observe it experimentally (see Fig.4.5b). In the range of Co thicknesses used on patterned dots, corresponding to the thickest case of atomistic simulations in Fig.4.15, no pure vortex state was observed. In order to achieve it, a larger thickness of Co would have been necessary.

Subsequently, the F/AF interface coupling was increased to the nominal value to observe the formation of a domain wall parallel to the interface within the AF layer during the F magnetization reversal (see Fig.4.17). The larger anisotropy of the AF layer forces the F spins at the interface to remain along the direction of the interfacial AF spins. During the F magnetization switching, this causes a deformation of the spin configuration along the thickness of the F layer (Fig.4.17b). Reciprocally, the reversal of the F spins causes the AF spins to follow the magnetization reversal, resulting in the formation of a domain wall throughout the AF layer as described by Néel's [32] and Mauri's [33] models. As the F layer approaches its saturation (from Fig.4.17c to Fig.4.17d), the AF spins at the interface keep following the reversal of the interfacial F spins.

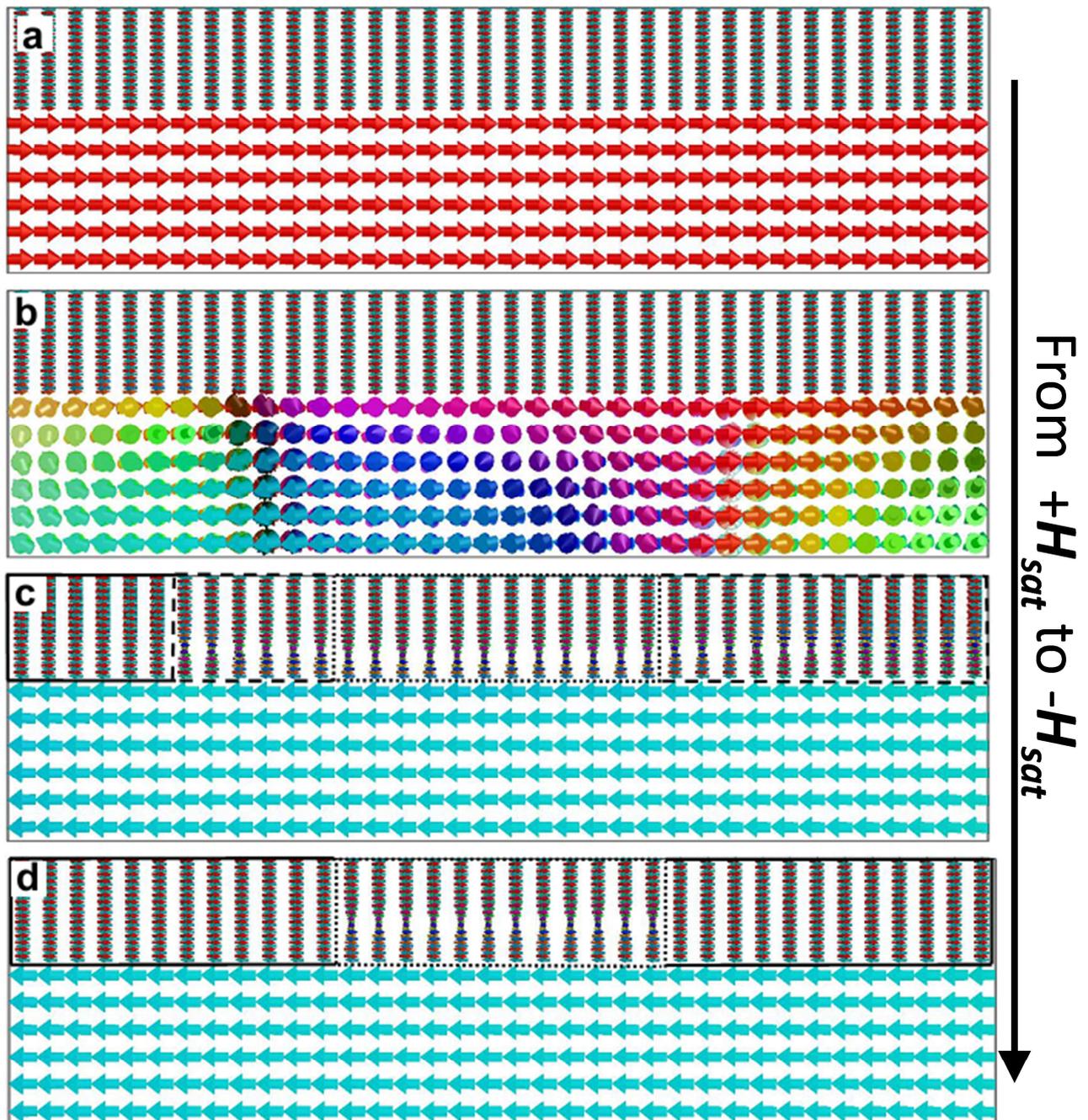


**Fig. 4.17** – Lateral view of the simulated F/AF systems. Large spins represent the  $8 \times 8 \times 8$  macrospins of the F layer, smaller spins the  $8 \times 8 \times 1$  spins in the AF layer. (a) Spin configuration at positive saturation. F and AF spins at the interface are parallel. (b) Under a negative field, magnetization reversal takes place through a complex multidomain state induced by the interfacial coupling with the AF. (c) During the F spin reversal, domain walls appear in the AF layer. The position of the domain wall changes according to the history of the interfacial F spins, leading to a stable domain walls (zone circled by a dotted line) or to a domain wall reversal (zone circles by a continuous line). Grains circled with a dashed line are in an intermediate state that will lead to a grain reversal at larger applied field. The difference in domain wall positions can be noticed between stable grains (dotted line) and these grains. (d) Spin configuration at negative saturation.

The behaviour of AF grains differs depending on the thickness of the F layer. Because of the hysteresis loops experimentally obtained, the interest was focused on thin F systems and on the intermediate state before vortex creation. Fig.4.18 shows the spin configuration of the F layer at remanence for the two cases, for different dot sizes  $L$  ( $50 \times 50 \text{ nm}^2$ ,  $60 \times 60 \text{ nm}^2$  and  $70 \times 70 \text{ nm}^2$ ). At the right of each magnetic image, a view of the dot partition is shown, each cell representing an independent AF grain. The different shades indicate two magnetic behaviours of the AF grains during the field cycling. The cells are represented in white if a domain wall is reversibly formed and annihilated when the field is ramped back and forth between positive and negative saturation of the F layer magnetization. These grains contribute to the shift of the hysteresis loop, because of the F/AF interfacial coupling. In Fig.4.17, they correspond to the grains circled with a dotted line. In contrast, the cells are represented in grey if the domain wall is formed and pushed out of the top surface, resulting in an AF spin lattice in the grain completely reversed during the reversal of the F layer. The torque exerted by the latter on the AF spin lattice is large enough, compared to the torque associated with the AF anisotropy energy, to drag the entire AF spin lattice during the F magnetization reversal. These AF grains primarily contribute to the energy loss, i.e. to the coercivity of the loop. They correspond to the grains circled with a continuous line in Fig.4.17.

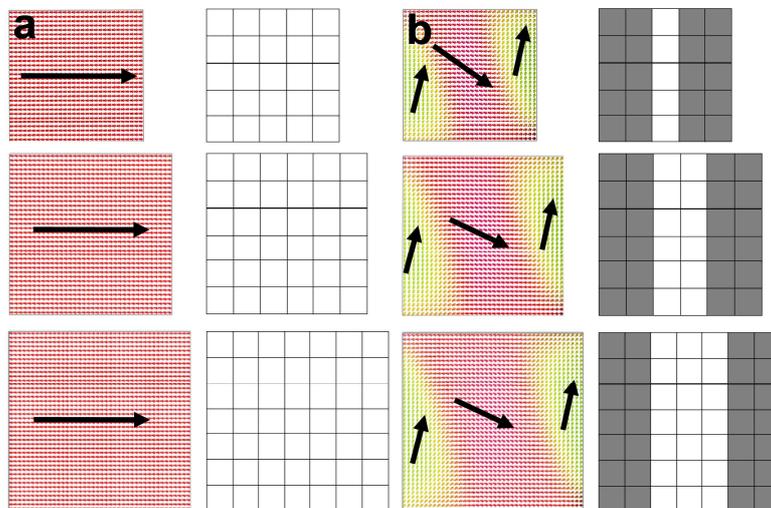


**Fig. 4.18** – Spin configurations at remanence and AF grain states (white or grey) at negative saturation for thin (1.6 nm) (a) and thick (12.8 nm) (b) F layer for three different dot sizes. The different grain shades distinguish their behaviours during magnetization reversal (white: the AF domain walls move reversely; grey: they go through the layer and disappear at the top surface).

Fig.4.18 shows that for thin F layers the domain walls of all the AF grains remain stable, whereas for thicker F layer the spin lattice completely switch during the loop in the AF grains located at the dot edges. As it can be seen from Fig.4.17c, this reversal is due to the different positions of the domain walls along the thickness of the AF grains. During the

magnetization reversal, the grains close to the border present a domain wall that propagates deeper through the AF layer compared to the grains in the center. This is attributed to the different spin configuration in the F layer at remanence. The presence of a strong interface coupling at the F/AF interface tends to align the F spins along the easy axis direction because of the strong AF anisotropy. Whereas for thin F layers, all spins are aligned along the setting directions, this effect becomes less pronounced on thick F layers. In this case, the contribution of the dipolar field on F magnetization becomes more important, particularly along the edges of the dots. Because of the creation of a pronounced S state at remanence, the magnetization at the dot edges is already strongly distorted at remanence. As a result, the F magnetization is locally exerting earlier a torque on the AF spin lattice of the grains located at the edges than on the grains located in the bulk of the dots. The reversal process through the formation of a multidomain configuration as shown in Fig.4.16 and Fig.4.17c and 4.17d further contributes to differentiate the behaviour of AF grains at edges and in the bulk of the dots. Note that these edge effects are only due to the micromagnetic behaviour of the F layer, induced at the surface by the dipolar interactions. From Fig.4.17 it is clear that the edge effects become more and more significant when the size of the dot is reduced, as a result of the increase in the surface/volume dot ratio.

Up to now in the simulations, the applied field has been aligned to the common anisotropy axis (except for a  $1^\circ$  angle set to break the initial symmetry). We will see in the following that it is more precisely the relative orientation of the spins in the F layer with respect to the anisotropy axes of the AF grains that governs the stability or instability of the grains.

#### 4.2.5 Micromagnetic effects: conclusions

IrMn/Co arrays of patterned square dots of  $200 \times 200 \text{ nm}^2$  and  $50 \times 50 \text{ nm}^2$  as lateral size have been investigated by MFM and focalized-MOKE. In the considered range of Co thicknesses, two different micromagnetic behaviours were characterized: single shifted loops with coherent rotation and double-shifted loops with magnetization reversal through the formation of a multidomain state. The support of atomistic simulations led to a definition of the multidomain state as an intermediate configuration between single domain and vortex states, with a magnetization reversal passing through a double vortex state.

Local measurements directly showed that the hysteresis loops of nominally identical stacks and dots strongly vary from dot to dot. The exchange energy variability appears to be more important when the magnetization reversal in the ferromagnetic layer takes place via

multidomain configuration. Atomistic simulations showed that micromagnetic effects in the F layer are responsible for AF grain instabilities on the edges of the dot. These effects, due to the dipolar interactions, are present for thick enough F layers and become more important when the lateral dot size is reduced. This scalability effect is confirmed on the experimental measurements, where the variability of 50 nm dots with thick Co layer was larger than the 200 nm case despite each measurement was the averaging on a larger number of dots.

Fortunately, the variability is less pronounced when thinner magnetic layers are used which corresponds to the situation of practical interest for MR readers or MRAM.

The presented study has been presented at Intermag 2012 and led to the publication of an article on Journal of Physics D: Applied Physics [34].

### **4.3 IrMn grain size effects on exchange bias variability on IrMn/Co square dots**

The previous paragraph showed the consequences of Co thickness variation on exchange-biased IrMn/Co patterned dots. The micromagnetic effects on the Co layer affected the spin configuration and magnetization reversal process; the different reversal mechanism had direct consequences on exchange energy variability.

In this paragraph, the thickness of the Co layer will be fixed at 5 nm, a value at which reversal takes place through coherent reversal (see Fig.4.4 and Fig.4.7b). Instead of studying the micromagnetic effects due to the competition between dipolar and exchange energies, the analysis will be focused on the microstructural properties of the IrMn layer, in particular the crystalline growth and grain size (diameter and volume). Among the different possible choices that could induce these variations, two were selected: the thickness of the IrMn layer and the thickness of the buffer layer.

After a preliminary study by XRD and AFM characterization, samples were patterned and a statistical study of exchange bias variability through focalized-MOKE measurements was performed. The variability was then compared to unbiased Co dots in order to evaluate the influence of IrMn structural variations on the magnetic properties of the bilayer.

#### **4.3.1 How to tailor IrMn grain size?**

During the thesis all samples were deposited by sputtering deposition (see Paragraph 3.1.1). This technique gives thin layer samples with a polycrystalline structure. In case of conducting materials like those deposited on the studied stacks, the growth of the layers

during the deposition and after an annealing process follows a series of steps. At first, the film forms with the nucleation of isolated crystals on the substrate or on the previous thin film. These crystals then grow in thickness and laterally. This lateral growth leads to impingement and coalescence of crystals, creating grain boundaries. After coalescence, subsequent thickening occurs through a quasi-epitaxial growth, giving the grains a columnar structure [35].

In exchange biased systems, the microstructure properties of both AF and F layers become an important parameter in the determination of the quality of the interface coupling and have important consequences on thermal stability in both the AF and F layers. This effect is taken into account in the polycrystalline models presented in Paragraph 1.2. Microstructure properties include interface roughness, crystallographic quality, interfacial diffusion, grain diameter and more. In our study the attention will be focused mainly on grain size and crystallographic quality.

*What is the main effect of changing the grain size?* It has been observed [36-37] that on polycrystalline systems the exchange bias intensity is proportional to the density of uncompensated AF spins at the interface. If a compensated AF spin structure is taken into account (as it is the case of IrMn [38]), uncompensated spins appear mainly at the grain boundaries. As a result, their density is inversely proportional to the AF grain diameter. The influence of the AF grain dimension has to be considered in combination with the thermal stability of the AF grain, which directly depends on its volume [39]. Combining the two aspects, an optimized configuration would be a thick AF layer with small grain diameters [37]. Unfortunately, for IrMn polycrystalline thin layers increasing the thickness causes an increase of the average grain lateral size and a broadening of its distribution [39]. It is important to remember that in our study not only the grain size but also its distribution may play a fundamental role on the exchange bias distribution, which can be modelled with a lognormal function [40,41].

*How can the grain size be modified?* Apart from changing the thickness of the AF layers, there are different ways to tailor the grain size and the crystallographic quality of the AF layer. One way, without changing the stack of the multilayer, is to change the sputtering rate [42,43], the target voltage, the process pressure [44] or the deposition voltage [44,45] during the deposition process. Annealing temperature also plays a role on the crystallization quality and grain diameter of the polycrystalline structure [46-48]. Considering variations on the stack, the buffering layer plays a fundamental role [46-52]. In a first place, its crystallographic structure determines the growth of the following AF layer [50], even to the

point of changing or suppressing the texture of the following layers [51]. When the buffering layer material is not changed, a variation of its thickness is enough to influence the AF microstructure [52].

*How can the grain size be measured?* An indirect way to obtain the average grain size is through x-ray diffraction, via the rocking curve [46,47,50]. Anyway, this method gives good information only about the average value and a good evaluation of the width of the distribution requires high quality crystallization and thick layers, which is not always the case. A more direct method is through TEM grid scans [43,44]. The layers are deposited on a carbon grid and a Transmission Electron Microscopy (TEM) image is taken through the thickness of the stack. This method allows seeing with very high resolution the grains and their crystallographic order, and with a large scan it allows having good statistics on the grain population. On the other hand, the deposition on a grid instead than on a Si/SiO<sub>2</sub> substrate changes the composition of the full stack itself. For this reason during the thesis AFM measurements were preferred to calculate the grain size distribution (as in [49,53]). Careful measuring the surface topography allows the detection of grains and grain boundaries. The volume of the grains is then evaluated through ImageJ software. This technique, as the TEM grids, supposes a columnar growth from the AF to the capping layer, i.e. the observed grains are the same also in the underlying AF layer. For AFM scans, measurements can be compared only if they were performed with the same tip, otherwise the convolution between different tips and the sample surface may affect the measurement. Moreover, the evaluation of the grain size itself is affected by the user [40] (see Fig.4.19). For this reason, all grain size measurements after AFM imaging were performed by me, under similar health conditions. This allows comparing sample to sample distributions, having a relative evaluation of the grain sizes more than an absolute one.

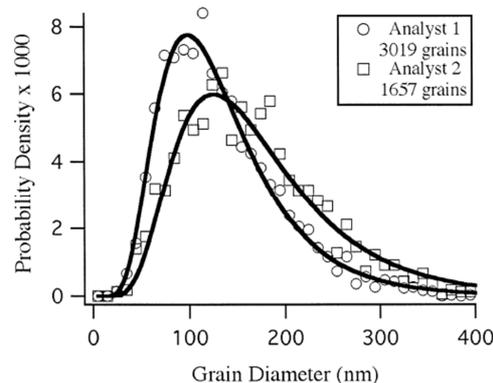


**Fig. 4.19** – Experimental issues due to grain size measurements done by two different analysts [40].

### 4.3.2 Full sheet samples – Structural and magnetic analysis

#### Buffer series

Among the possible materials for buffering layer, different thicknesses of Cu and Ru were selected to be deposited on a Ta layer, which is used as an adherence layer for the following layers. The stacks were (thicknesses in nm): Ta<sub>3</sub>/Cu<sub>x</sub> (Ru<sub>x</sub>)/IrMn<sub>12</sub>/Co<sub>5</sub>/Pt<sub>2</sub>, with x ranging from 1 to 12 nm. A thick IrMn layer was selected to have a maximum signal for XRD. All samples were annealed at 473 K (200°C) for 30' under a planar setting field of 2000 Oe. Samples were analysed magnetically with Kerr measurements and microstructurally with AFM and XRD measurements.

Fig.4.20 shows the exchange bias  $H_{ex}$  and coercivity  $H_C$  values for the different buffer layers, including the case with no Cu or Ru layer.

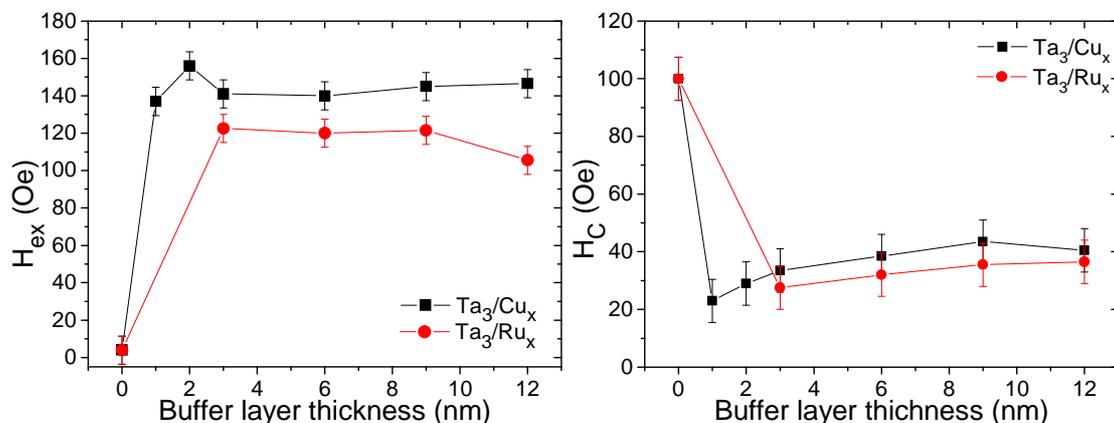


Fig. 4.20 – Exchange bias  $H_{ex}$  and coercivity  $H_C$  as a function of buffer material and thickness for IrMn<sub>12</sub>/Co<sub>5</sub> bilayer.

It can be noticed how the Cu underlayer gives higher loop shift compared to the Ru one, with a slight increase of coercivity. Considering the buffer thickness effect, it appears to have a slight influence on the exchange, apart from a peak at 2 nm for the Cu layer. The  $\Delta H_{ex}$  between different buffer thicknesses is of around 20 Oe for both Cu and Ru. On the other hand, if IrMn is directly deposited on Ta, the sample has no exchange and a large coercivity. Now let's pass to the microstructural analysis.

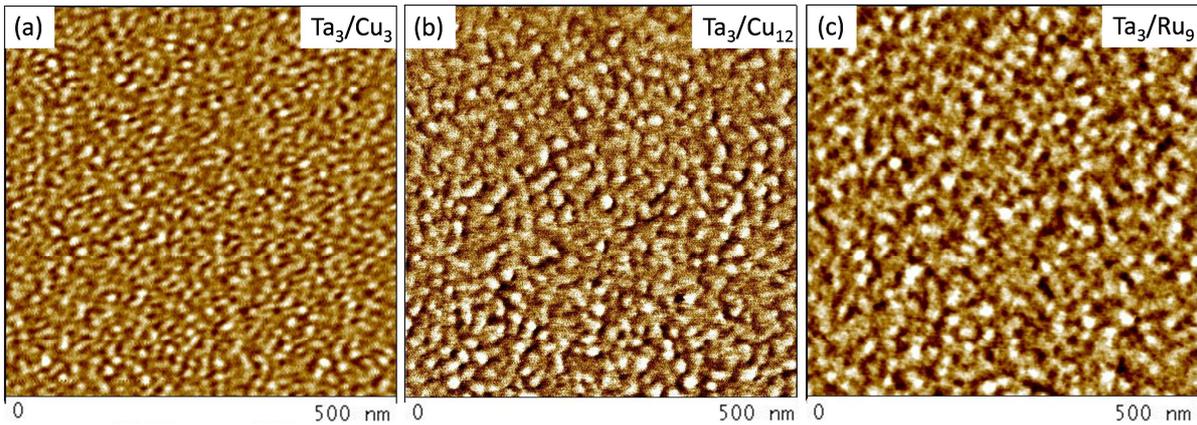


Fig. 4.21 – AFM measurements for three different buffer layers.

Fig.4.21 shows some examples of AFM measurements for different buffer layers. The topographic images, with a z-scale of few nm, allow distinguishing the granular structure of the grains, with white and dark contrasts. On each image, over 200 grains were circled and measured, giving a good statistics of the grain size distribution. This distribution was then plotted both as a frequency distribution (Fig.4.22a and Fig.4.22b) and as a cumulative distribution function (Fig.4.22c and Fig.4.22d), being the former one useful to easily observe the width of the distribution and the latter to mark the average value. A clear tendency can be observed.

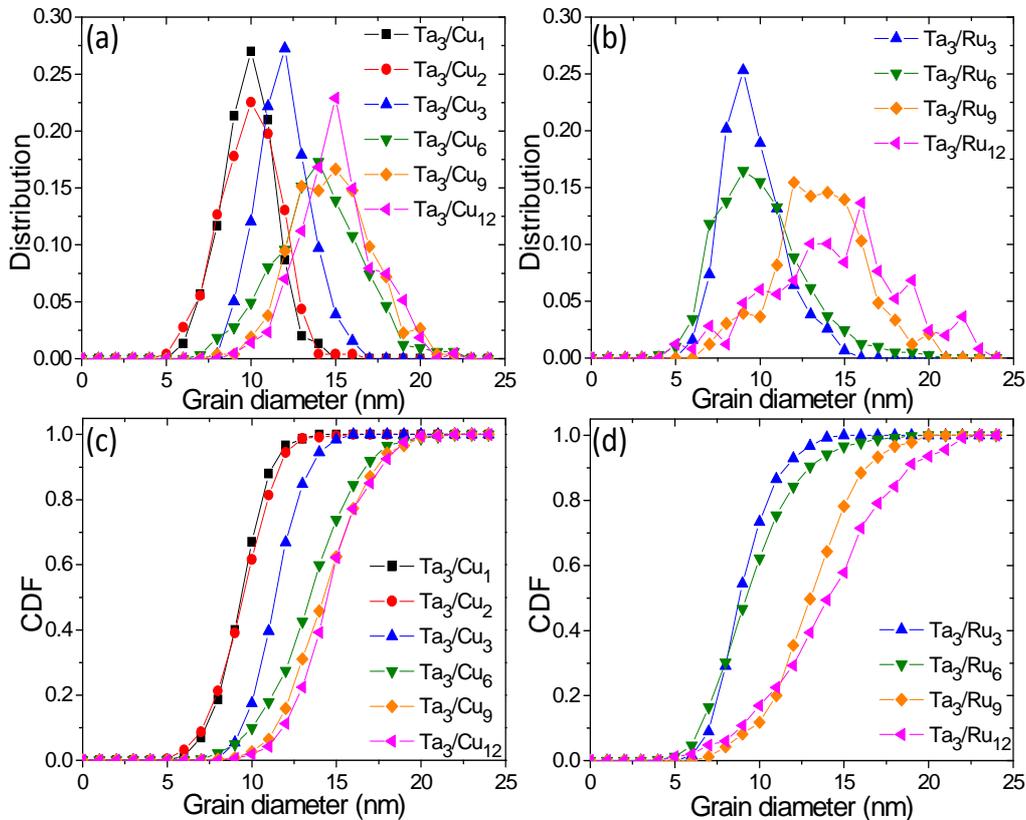


Fig. 4.22 – Normalized frequency distribution (a,b) and cumulative distribution function (c,d) from AFM measurements for Cu (a,c) and Ru (b,d) buffer layers.

With the increase of the buffer thickness, the average grain diameter increases too in a monotonic way for both buffer layers. Concerning the distribution width, higher grain size implies larger grain distribution. It can be observed comparing the AFM measurements of Fig.4.21a and Fig.4.20b. For thin Cu layer, small grains cover quite homogeneously the scanned surface, whereas for thicker Cu the variability of grains, among the large one and considering the presence of with smaller grains in-between them, leads to a broader distribution. When comparing Cu and Ru equivalent thicknesses, the samples with Cu buffer layer present sharper grain distribution than the Ru one; the average grains size overlaps for thick layers, whereas for thin values the grains for the Ru case are in average thinner but still with a large distribution. The fact that this variation of the grain lateral dimension for different buffer thicknesses has no particular influence on the exchange bias value can be attributed to a balance between smaller, thermally unstable grains and larger, unset grains in the total grain population.

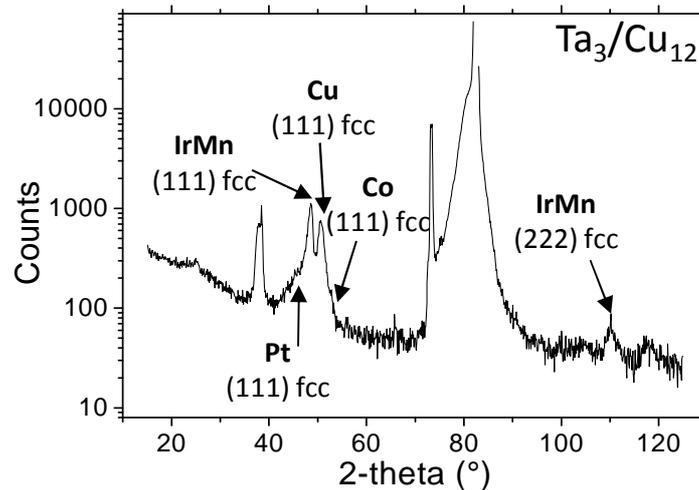


Fig. 4.23 – X-ray diffraction pattern for 12 nm Cu buffer layer

Concerning the X-ray  $\theta$ - $2\theta$  diffraction scans, Fig.4.23, shows an example for one of them. Apart from the strong signal coming from the underlying Si substrate (see the peaks at  $2\theta = 82^\circ$  for Si (100)), the peaks of the 12 nm IrMn layer can be easily detected, matching with an fcc structure of a  $\text{Ir}_{20}\text{Mn}_{80}$  material with the (111) and (222) peaks. Cu shows the (111) peak of its fcc structure. Co (111) peak is broader because of the lower thickness, and is partially covered by the peaks of IrMn and Cu, as it happens for the Pt capping layer. The variation of the thickness of the buffer layer causes some oscillations on the lattice parameter of the IrMn layer, but without any clear tendency and with an average value of  $a = 0.207$  nm.

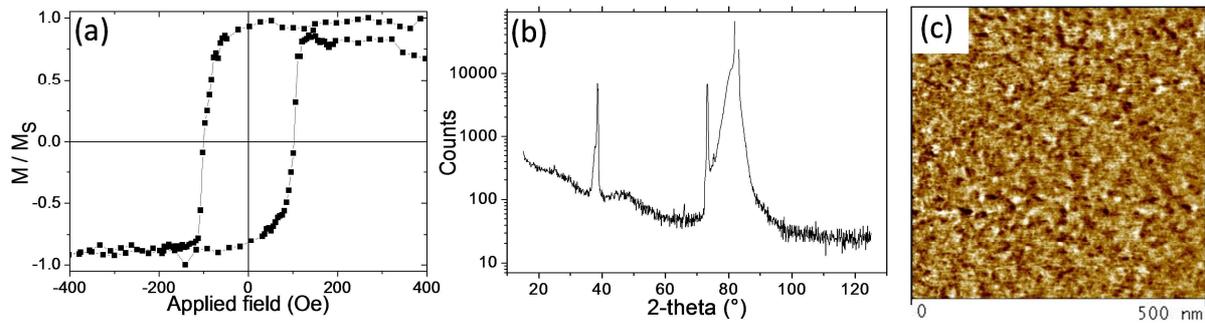


Fig. 4.24 – Hysteresis loop (a),  $\theta$ - $2\theta$  XRD scan (b) and AFM measurement (c) of the  $\text{Ta}_3/\text{IrMn}_{12}/\text{Co}_5/\text{Pt}_2$ .

When studying the microstructure of the sample without Cu or Ru buffer layer, it resulted that the lack of this layer does not allow the IrMn layer to correctly grow in its polycrystalline form (Fig.4.24). The XRD measurement does not show any peak apart from the one due to the substrate; in the AFM images no clear grain structure appears, thus it can be assessed that all the layers of the stack are in an amorphous state. This behaviour for a Ta buffer layer is confirmed in the literature in MTJ structures [51].

To conclude, a Cu or a Ru buffer layers are necessary to allow the polycrystalline growth of the IrMn and Co layers; without crystallization, no exchange appears. When comparing buffer material and thicknesses, it results that Cu is a better buffer layer than Ru giving larger  $H_{ex}$ . From the crystallographic point of view, the properties of the IrMn layer are similar independently on the buffer material or thickness. Nonetheless, Cu grain distribution is sharper than the Ru one. The maximum of exchange bias is observed for a Cu thickness of 2 nm, value at which the grain average dimension is low and the distribution sharp. For this reason, this buffer layer has been selected for the variability study on patterned samples and for the series of full sheet and patterned samples with increasing IrMn thickness.

### ***IrMn thickness series***

With the selected buffer layer  $\text{Ta}_3/\text{Cu}_2$ , the following stacks were deposited (thicknesses in nm):  $\text{Ta}_3/\text{Cu}_2/\text{IrMn}_x/\text{Co}_5/\text{Pt}_2$ , with  $x$  ranging from 1 to 12 nm, and annealed at 473 K (200°C) for 30' under a planar setting field of 2000 Oe. From the hysteresis loops performed along the easy axis the values of  $H_{ex}$  and  $H_C$  presented in Fig.4.25 were obtained.

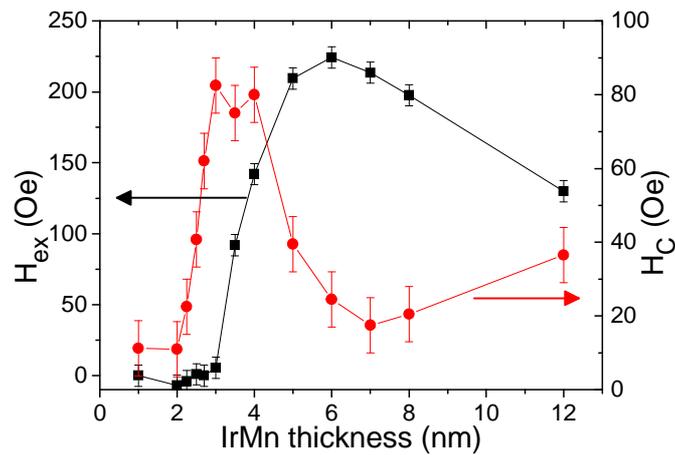


Fig. 4.25 – Exchange bias  $H_{ex}$  and coercivity  $H_C$  as a function of IrMn thickness for the of the  $Ta_3/Cu_2IrMn_x/Co_5/Pt_2$  series.

Exchange bias starts appearing at 3 nm, increasing up to 6 nm; after the peak,  $H_{ex}$  decreases slowly for increasing IrMn thickness. Around 3 nm the coercivity presents a peak; its value then decreases to a minimum at the  $H_{ex}$  peak. This behaviour is coherent with the results obtained on similar IrMn/Co bilayers [25] and it is due to the thermal stability of the IrMn grains at the measuring temperature and during the annealing process. More details on the behaviour in temperature and the grain volume effects will be given in the following chapter (Paragraph 5.2.1) in comparison with trilayer structures. Focalized-MOKE measurements on different spots of full sheet samples gave a maximal exchange variability ratio  $(\Delta H_{ex}/H_{ex})_{max}$  of 0.05.

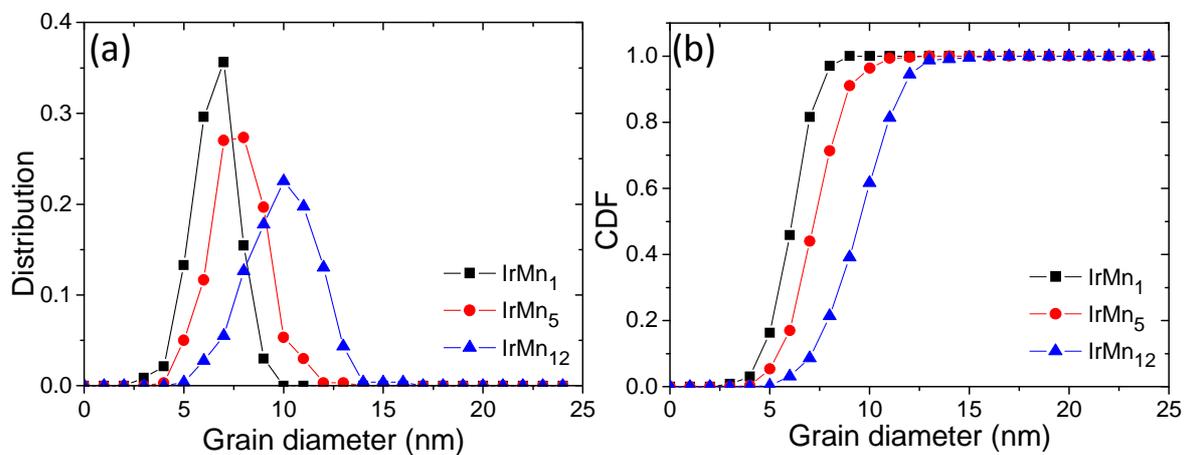


Fig. 4.26 – Normalized frequency distribution (a) and cumulative distribution function (b) for different IrMn thicknesses.

From AFM measurements, the grain population was calculated with the method previously described. Fig.4.26 shows the frequency distribution and CFD for different IrMn thicknesses. The sputtered systems present an increase of the grain lateral size as the IrMn thickness increases, together with a broadening of the distribution. This confirms the tendency observed from the buffer series in Fig.4.22 (the larger the grains, the wider the distribution). Moreover, it is in accordance with the results obtained in the literature [39,41], which showed

how an increase of the IrMn thickness leads to an increase of the grain volume and a broadening of the grain size distribution. The range of measured grain volumes fits well with those presented in the cited studies, thus confirming the validity of the measuring method.

However, in our study the interest is not particularly focused on the volumetric properties of the grains, but on their lateral size, mainly for two reasons. The first one is that the aim of the study on patterned dots is to study the effect of the AF grain distribution on exchange bias variability: in the case of large grains with broad distribution, different dots may present very different IrMn grain populations, whereas for small and homogeneous grains the IrMn microstructure will not be very different from one dot to another. The goal is thus to reduce the grain lateral size so that the average lateral size becomes much smaller than the dot size in an MRAM system. The second aspect is that in this part no temperature dependence is taken into account: all measurements were performed at room temperature. This aspect will be taken into account on full sheet samples in Chapter 5.

### 4.3.3 Patterned samples – MFM and Focalized-MOKE measurements

For patterned systems, the following thicknesses were considered for the two cases:

- Buffer series:  $\text{Ta}_3/\text{Cu}_x/\text{IrMn}_{12}/\text{Co}_5/\text{Pt}_2$  with  $x = 1, 2, 6, 9$  and  $12$  nm;
- IrMn thickness series:  $\text{Ta}_3/\text{Cu}_2/\text{IrMn}_x/\text{Co}_5/\text{Pt}_2$  with  $x = 3, 4, 5, 6.5, 10, 12$  and  $15$  nm.

Three different geometries were processed: square dots  $200 \times 200 \text{ nm}^2$  with an edge to edge spacing of  $200 \text{ nm}$  and square dots of  $100 \times 100 \text{ nm}^2$  and  $50 \times 50 \text{ nm}^2$  with an edge to edge spacing of  $100 \text{ nm}$ . As for the patterned systems of Paragraph 4.2, it can be considered from earlier studies that the dots are weakly interacting from a magnetostatic point of view [27]. With a Co thickness of  $5 \text{ nm}$  for both IrMn and Cu thickness series, all dots presented a single domain state at remanence (Fig.4.27a) and a coherent magnetization reversal within each dot (Fig.4.27b). The dipolar MFM contrasts observed at remanence on the various dots indicate however that the magnetization of the dots is sometimes oriented along the diagonal of the dots (corresponding to the longest dimension) and sometime oriented parallel to the edge of the dots. The coexistence of these two magnetic states (leaf and S states [54]) in small dot groups at remanence is a sign of small dot-to-dot micromagnetic interaction, which is anyway lost during magnetization reversal, as the lack of patterns in Fig.4.27b indicates.

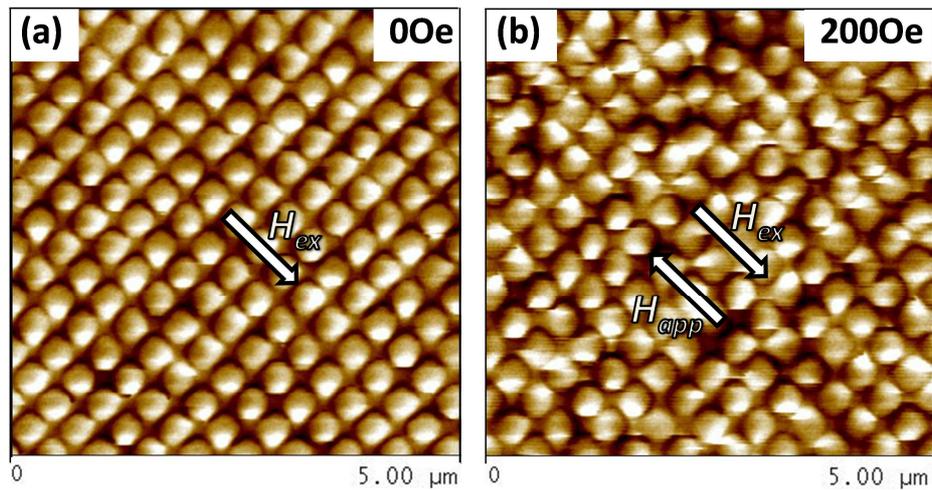


**Fig. 4.27** – MFM image on 200 nm square dots for IrMn<sub>3.5</sub>/Co<sub>5</sub> sample at remanence (a) and under in-situ applied field (b).

Again, MFM images gave a qualitative picture of the switching field variability from dot to dot, as it can be seen in Fig.4.27b. In the picture measured under a 200 Oe applied field, the around two hundred dots present a wide distribution of in-plane angles, marking different steps of the magnetization reversal under the same field with preferred intermediate directions (diagonals or parallel to the edges).

In order to have a more qualitative evaluation of the variability, fifty focused measurements were performed on each sample for all dot dimensions. Coherently with the MFM scans, all loops showed a shifted single loop and variability in coercivity and loop shift (see Fig.4.28) for all the considered lateral dimensions. Moreover, a relevant increase in coercivity was observed on patterned samples compared to full sheet ones, confirming the tendency observed in Paragraph 4.2.

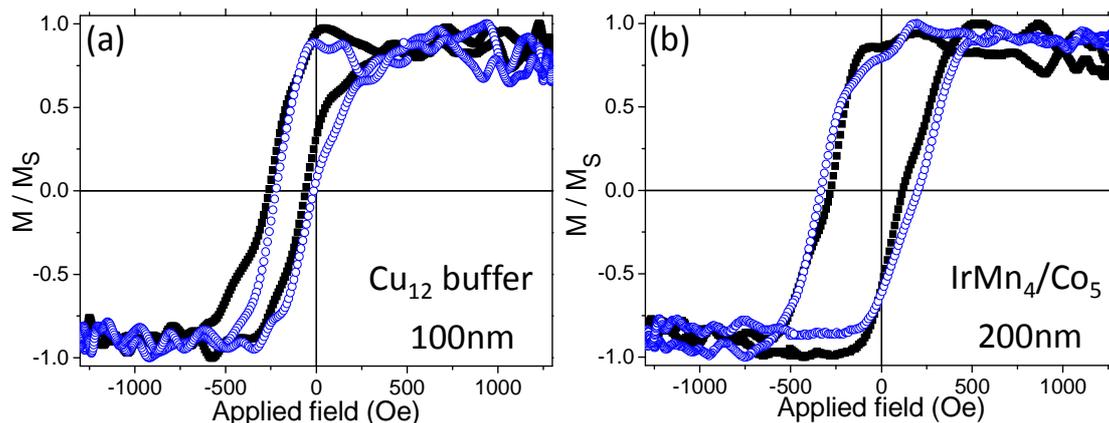


**Fig. 4.28** – Comparison between two focused measurements on two different zones in black and blue for 100 nm Cu<sub>12</sub>/IrMn<sub>12</sub>/Co<sub>5</sub> (a) and 200 nm IrMn<sub>4</sub>/Co<sub>5</sub> (b) square dots.

From the focalized measurements, exchange bias average values were calculated and compared between full sheet and patterned samples. The resulting curves for the two series are plotted on Fig.4.29.

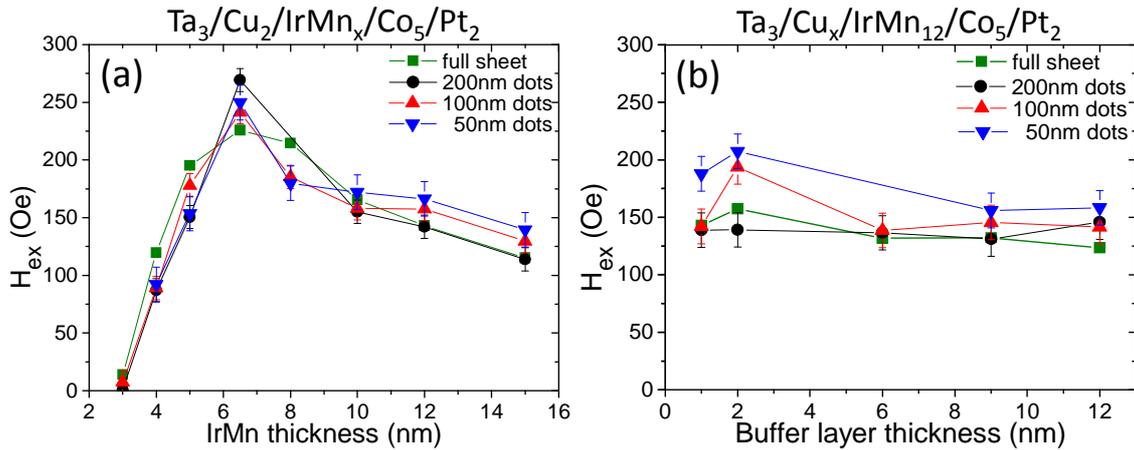


Fig. 4.29 – Average exchange bias values for full sheet and patterned samples as a function of thickness IrMn thickness (a) and buffer thickness (b).

Let's first consider the effect of the IrMn thickness. Fig.4.29a shows that the trend of the  $H_{ex}$  curve does not change from patterned to full sheet samples. This means that in the selected dot geometry and lateral size range, IrMn/Co dots average exchange bias behaviour does not deviate from the full sheet one. In the literature, scalability and thickness effects on patterned systems affect differently the hysteresis loops according to the materials, dot geometry and dimensions or dynamics. For examples, square Co/CoO dots showed enhanced asymmetric loops when reducing the lateral sizes [55], whereas rectangular ones increased  $H_{ex}$  for small dots and thin Co layer [56]. (Pt/Co)/IrMn stacks deposited on small polystyrene particles showed similar  $H_{ex}(t_{IrMn})$  tendencies of the corresponding sheet films, although  $H_{ex}$  increased for the dots [57]. For NiFe<sub>12</sub>/IrMn<sub>x</sub> 90 nm square dots measured in [7] and modelled in [58] in a thicker IrMn regime than ours, almost no variations of  $H_{ex}$  with IrMn thickness were reported. These different behaviours versus antiferromagnetic layer thickness may be associated with various origins. Growth and correlatively interfacial roughness may influence AF domain sizes, in a Malozemoff model (see Paragraph 1.2.3), and thus be the origin of size effects [7]. Moreover, the use of different F layers (which implies different thermal stabilities, magnetizations, F/AF exchange stiffness, anisotropies ...) may affect the reversal mode mechanisms. Finally, magnetic field sweep dynamics may also play a role, since it influences AF grains stability during the F magnetization reversal [59,60] and the dynamic magnetization reversal of the F layer itself [61]. For examples, our measurements were performed at a frequency of 11 Hz, whereas in [7] the frequency was about four orders of magnitude lower [62].

Considering the buffer series of Fig.4.29b, no particular trend is observed. Patterned dots have an average  $H_{ex}$  around the value of the full sheet samples or slightly larger for the 50 nm dots case. It has to be underlined, however, that the differences in exchange due to the

Cu thicknesses are already quite small in full sheet samples, and the uncertainty of the focused measurements covers this variation.

The first conclusion from the averaged behaviour is that changes in the IrMn microstructure (grain volume and lateral size distributions) do not imply differences in the average behaviour between patterned dots and full sheet samples. This is valid for a lateral size range from 200 to 50 nm, where no relevant scalability effects are observed.

Is there any effect of the Cu buffer or IrMn thicknesses on the dot to dot exchange bias variability? Fig.4.30 shows the exchange bias normalized exchange energy variability calculated with Eq.4.2 for the two series.

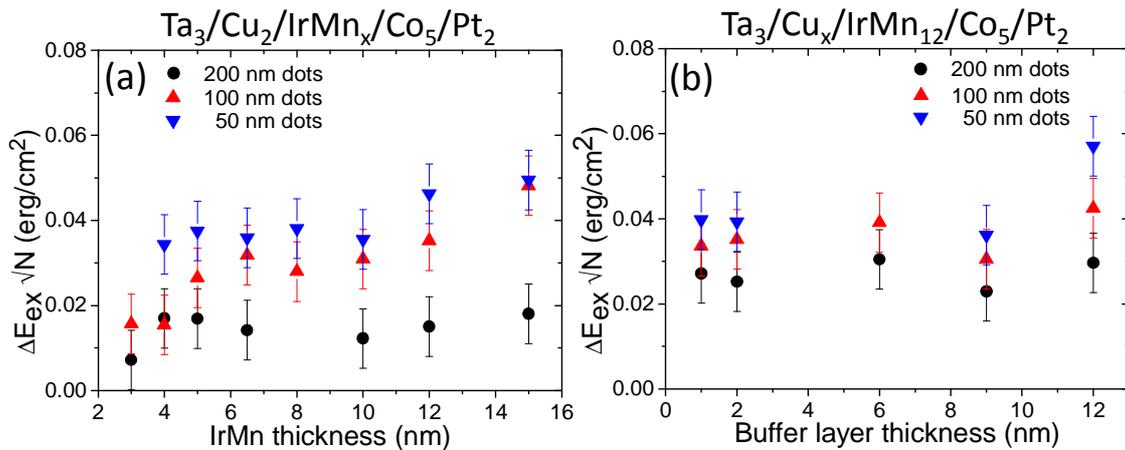


Fig. 4.30 – Normalized exchange bias variability for patterned dots of IrMn thickness (a) and buffer thickness (b) series.

It can be observed that in both series the reduction of the dot lateral size implies an increase of exchange energy variability. This appears quite clearly in Fig.4.30a. This result can be interpreted as follows. When the lateral dimension of the patterned system is reduced, impact of the patterning on the edge of the dots is more and more significant. During the dot etching, AF grains located at the edge of the dots are cut [58]. Consequently, their volume is reduced thus affecting the grain size distribution [63]. This effect has been proven to have consequences on the thermal stability of patterned systems, reducing the blocking temperature compared to equivalent continuous layers [63-65]. In this case, we observe that the instability of the grains at the edges also affects the exchange bias variability.

Concerning the general trends of these curves, it can be noticed in Fig.4.30a that, particularly for the 100 and 50 nm dots, the exchange energy variability increases with the IrMn thickness. As measured from AFM images in Fig.4.26, IrMn grain size increases as its thickness increases, together with a broadening of its volume distribution. When patterning the square dots, systems with 100 and 50 nm as lateral size may contain around 130 and 30 grains respectively (500 for 200 nm dots), a quantity not large enough to cover the whole

grain distribution. If the grain distribution is wide, as it is the case for thick IrMn layer samples, the AF grain population may differ importantly from one dot to another, leading to exchange bias variation larger than in the case of small and uniform grains. A similar trend is observed for the buffer layer series in Fig.4.30b.

#### 4.3.4 IrMn microstructural effects: conclusions

Microstructural properties of IrMn layer have been tailored in order to observe their influence on exchange bias variability in arrays of patterned dots. IrMn grain lateral size and distribution were varied by changing the thickness of the buffer layer (Cu and Ru) or its own thickness. Thickening the buffer layer or IrMn thickness led to an increase of AF grain size and a broadening of its distribution. The variation of the buffer layer thickness had minor influence on exchange bias value on full sheet samples; this is attributed to a compensation of unset and unstable grains populations.

200x200, 100x100 and 50x50 nm<sup>2</sup> square dot arrays were patterned and characterized by MFM and focalized-MOKE measurements. Average exchange bias values showed no scalability effect on both buffer and IrMn thickness series.

Regarding exchange bias variability, two main effects were observed. The first one concerns the scalability effect. When reducing the dot lateral size, exchange bias variability increases. This is due to the grain cutting at dot edges during the etching procedure, which modifies the grain population in the dot (larger number of smaller grains) resulting in grain thermal instability. The effect becomes predominant when the dot size is reduced, because of the larger relative weight of the edges compared to the inner volume of the dots. The second effect is that the exchange variability increases with increasing grain lateral size and distribution, particularly for small dots. In this case, the reduced lateral size leads to a partial representation of the whole grain distribution per dot. As a consequence, different dots may present different grain populations, thus different exchange bias values. This effect becomes more important for large grains and wide distributions.

The study reported in this paragraph has been presented in an oral talk at JEMS 2013.

## 4.4 Atomistic simulations – Influence of IrMn anisotropy axis

This paragraph will present a series of works on exchange variability that we have performed by atomistic simulations. The study was centered on the distribution of the anisotropy axis. This is because the sputtering deposition of polycrystalline layers, not only leads to distribution of grain diameters, but also gives a distribution of anisotropy directions. The simplified model used in Paragraph 4.2 is thus enriched by adding a random anisotropy axis to each AF grain, in order to approach a more realistic picture of the sample structure. More precisely, instead of a fixed anisotropy angle  $\varphi = 1^\circ$  in the anisotropy  $x$ - $y$  plane as previously used in our calculations, an angle between  $-90^\circ$  and  $+90^\circ$  is randomly attributed, with a uniform distribution, to each grain of the AF layer. An example of one configuration with such a distribution of anisotropy directions is shown in Fig.4.31b.

A series of ten different configurations with random anisotropy axis has been created. The statistical dispersion allows us to observe the influence of the AF anisotropy axis distribution on coercivity and exchange, as modelled by Stiles and McMichael [66].

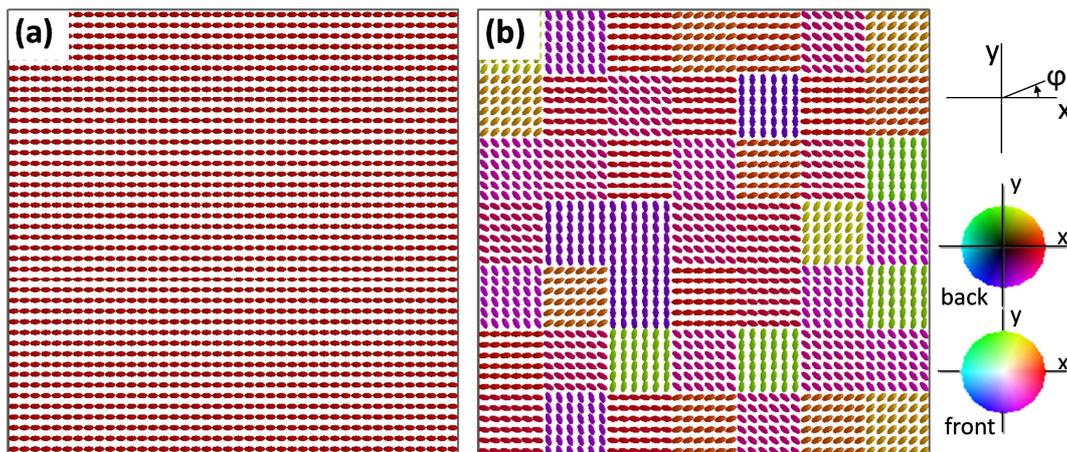


**Fig. 4.31** – Anisotropy axis for the AF spins. (a) Homogeneous axis direction of the AF layer, as used in Paragraph 4.2. (b) Example of a configuration with a random axis distribution. To each grain, the axis is associated to a random angle  $\varphi$  (see graph and colour legend on the right).

### *Influence of the disorientation between the $K_{AF}$ axis and the $H$ direction*

Before getting to the results of the random axis distribution, it is worth to analyse the influence of the angle between the applied field  $H$  and the AF anisotropy axis on the domain wall stability. In the simulations performed in the Paragraph 4.2, all grains presented identical anisotropy direction, with  $\varphi = 1^\circ$  with respect to the  $x$ -axis and also the applied field  $H$  (See Fig.4.31 and relative legends). The small angle was introduced in order to break the initial symmetry, escape the energy saddle point, and allow the minimization calculation to start. If

the angle is increased (as in the case of  $\varphi = 5^\circ$  shown in Fig.4.32), the domain wall that is created in the AF layer during the magnetization reversal results closer to the interface than in the case of  $\varphi = 1^\circ$ . If the AF anisotropy axis direction has a larger angle  $\varphi$ , the domain is stabilized during the magnetization reversal, remaining close to the interface. On the other hand, the larger  $\varphi$ , the smaller the rotation of the AF spins along the thickness of the AF layer when the F layer flips to the negative values of the applied field, thus the smaller the resulting loop shift. On the opposite, when the anisotropy axis and the applied field have a close direction (as  $\varphi = 0.1^\circ$ ), the AF domain wall is pushed far along the thickness of the AF layer at negative saturation and can possibly be expelled at the top surface. This can be observed in Fig.4.32, for a single grain with thick AF layer. The case with  $\varphi = 0.1^\circ$  shows the domain wall deep into the AF layer. In case of a thinner AF layer the domain wall would have been unstable with a reversal of all the AF spins.

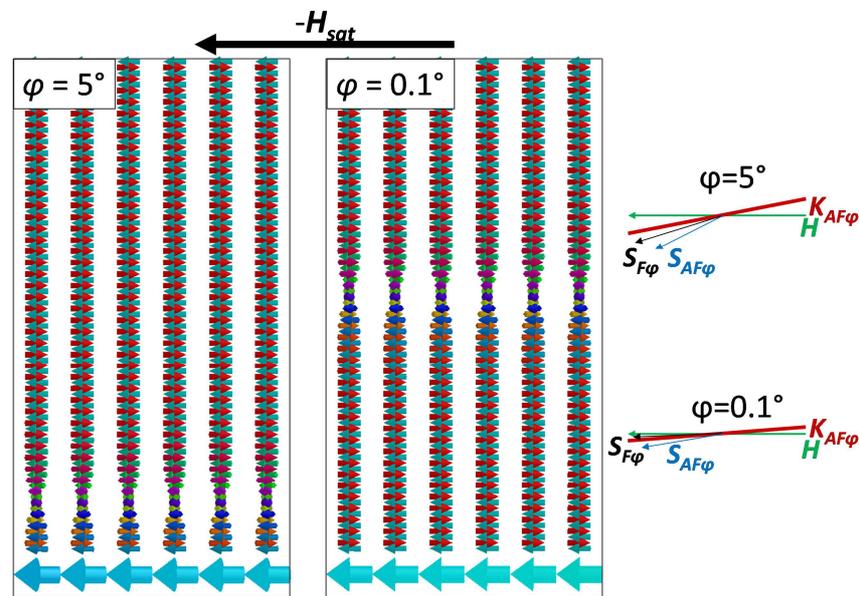


**Fig. 4.32** – AF domain wall profile at negative saturation for two different AF anisotropy angles ( $\varphi = 5^\circ$  on the left and  $\varphi = 0.1^\circ$  on the right). On the far right of the figure, diagrams of the spin directions at negative saturation.

On the right of Fig.4.32, a schematic of the spin diagram, similar to the one proposed by Meiklejohn and Bean (see Fig.1.7) is shown. From the analysis of the spin directions during the different steps along the hysteresis loop, we show that the AF domain reversal (shown on the AF grains at the borders of the dot in Fig.4.17) takes place when the F spins at the interface are directed at an angle  $\varphi$  between the one of the applied field  $\mathbf{H}$  and the one of the anisotropy axis  $\mathbf{K}_{AF}$ . When this takes place, the AF domain wall dramatically shifts toward the top surface of the AF layer, reversing the whole domain as it reaches the proximity of the opposite surface. It has to be underlined that the domain wall width does not change with the angle of the applied field since this depends on the material properties of the AF layer. This

behaviour is demonstrated in Fig.4.33a and Fig.4.33b. In Fig.4.33a, the domain wall profiles  $\Phi(t_{IrMn})$  are shown, versus the distance  $d$  from the interface along the thickness of the AF layer (in the case  $\varphi = 0.1^\circ$  the whole AF domain has reversed). The Fig.4.33b, presents the same data but with a shift of the origins along  $z$ ; their superposition shows that the domain wall profiles, and in particular the widths, are identical. The alignment with the field  $H$  of the F spins at the interface gives the boundary conditions at the interface for the domain-wall profile, while the orientation  $\varphi$  of the anisotropy axis corresponds to the boundary condition far from the interface.

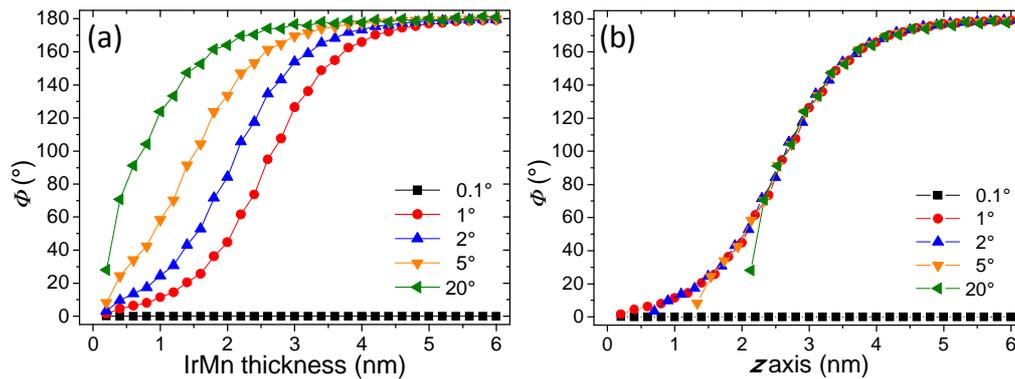


**Fig. 4.33** – (a) Orientation  $\Phi$  of the AF spins along the AF thickness for different angles  $\varphi$  of the anisotropy axis (same  $K_{AF}$ ). (b) Translation of the origins along the  $z$  axis to prove the superposition of the domain wall profiles.

### *Effects of the anisotropy axis distribution on the hysteresis loop*

The effect of a random distribution of the anisotropy axes on the hysteresis loop coercivity and exchange bias values is illustrated in Fig.4.34, where a selection of ten simulations with the random axis distribution are shown. The simulations concerned a case where the F layer has a coherent magnetization reversal and a strong interface coupling that emphasizes the formation of AF domain walls.

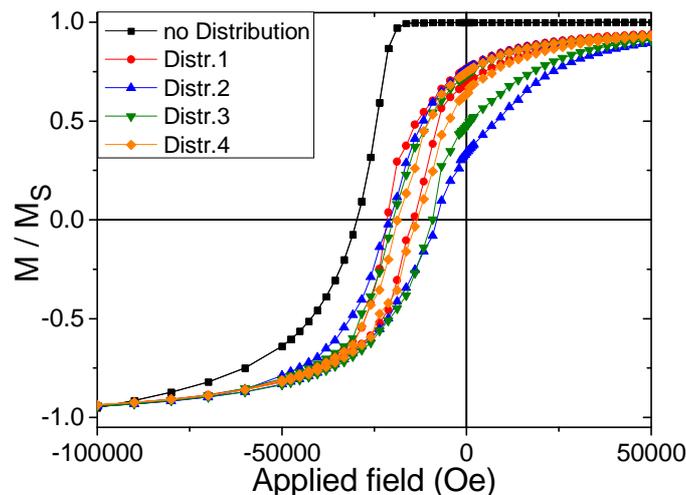


**Fig. 4.34** – Series of hysteresis loops for a coherent reversal of the F layer: one with a uniform AF anisotropy axis orientation (black squares) and four in the case of non-uniform and random distributions (the hysteresis loops of the ten simulated configurations are not all shown to preserve visibility).

Whereas in the case of a uniform axis orientation the hysteresis loop has the classical shape due to the domain wall creation and annihilation back with no hysteresis losses [67], the other distributions present some grains with critical  $\varphi$  angle, contributing to the coercivity. Together with that, grains with large  $\varphi$  angle contribute less to the exchange bias loop shift, thus reducing the final value of  $H_{ex}$ .

### **Summary**

The hysteresis loops obtained in presence of random AF anisotropy axis distribution get closer to those observed experimentally, and confirms the theoretical model of Stiles and McMichael [66]. The variation of  $H_{ex}$  and  $H_C$  for different  $\varphi$  angle distributions shows another possible origin of the exchange bias variability. Despite the difficulty in evaluating the impact of this parameter among those experimentally observed in the previous paragraphs, it appears as another intrinsic characteristic of sputtered exchange biased systems that may affect the exchange bias variability among dots. Moreover, the instability of the AF domain walls in the case of small angles between the applied field  $\mathbf{H}$  and the anisotropy axis  $\mathbf{K}_{AF}$  may be a possible explanation of the observed increased values of  $H_{ex}$  for a small angle with respect to the annealing direction [68].

## **4.5 Conclusions of the chapter**

This chapter showed a study of exchange bias variability in arrays of IrMn/Co patterned square dots. The study was performed by focalized-MOKE measurements, with AFM, MFM and XRD characterizations.

Two main aspects were treated: the micromagnetic effects due to the variation of Co thickness and the microstructural effects of the IrMn grain structure.

In the former case, MFM and Kerr measurements showed two different reversal mechanisms according to Co thickness. For thin F layer, magnetization reversal takes place through coherent reversal of the single domain magnetic state. For thick Co layers magnetization passes through a complex multidomain configuration during magnetization reversal. The spin structure during the reversal was analysed by atomistic simulations. Concerning the exchange bias variability, qualitatively observed by MFM images with in-situ applied field, it was quantitatively evaluated by focalized-MOKE measurements. In the multidomain regime, the variability becomes more important than in the single domain state, with dramatic effects for reduced lateral size dots. This was attributed to AF grain instability on the edges of the dot. This effect, due to dipolar interaction between the thick F layer and

the AF layer and to the earlier torque of F spins at the borders on the AF spins at remanence, causes AF domain training during magnetization reversal, leading to grain instability and domain reversal. The effect becomes particularly important when the lateral dot size is reduced.

The second study concerned the microstructural properties of IrMn layer and their effects on exchange bias variability. IrMn grain size was tailored by varying the buffer layer and IrMn thicknesses and characterized by AFM measurements. Increasing the buffer layer and the IrMn thicknesses leads to an increase of the grain average size and distribution. When patterned, samples presented in both cases no significant scalability effects concerning the average exchange bias behaviour, following the trends of the full sheet samples. Concerning the exchange variability, two main effects were observed. Firstly, a scalability effect: smaller dots always presented larger variability than the larger ones. This is attributed to grain instability on the edges due to grain cutting. Secondly, variability increased with increasing IrMn grain size and distribution, particularly for small dots. Because of the reduced lateral dimensions, small dots do not contain enough IrMn grains to cover the whole population; as a result, different dots may present very different IrMn grain sizes, leading to variations of exchange bias field.

## Bibliography

- [1] Cowburn R P, Koltsov D K, Adeyeye A O, Welland M E and Tricker D M 1999 *Phys. Rev. Lett.* **83** 1042
- [2] Prejbeanu I L, Natali M, Buda L D, Ebels U, Lebib A, Chen Y and Ounadjela K 2002 *J. Appl. Phys.* **91** 7343
- [3] Buda L D, Prejbeanu I L, Ebels U and Ounadjela K 2002 *Comp. Mat. Sci.* **24** 181
- [4] Schneider M, Hoffmann H and Zweck J 2003 *J. Magn. Magn. Mat.* **257** 1
- [5] Schneider M, Hoffmann H, Otto S, Haug Th. and Zweck J 2002 *J. Appl. Phys.* **92** 1466
- [6] Hoffmann A, Sort J, Buchanan K S and Nogués J 2008 *IEEE Trans. Magn.* **44** 1968
- [7] Baltz V, Sort J, Landis S, Rodmacq B and Dieny B 2005 *Phys. Rev. Lett.* **94** 117201
- [8] Sasaki I, Nakatani R, Ishimoto K, Endo Y, Shiratsuchi Y, Kawamura Y and Yamamoto M 2007 *J. Magn. Magn. Mat.* **310** 2677
- [9] Manginas G, Chatzichristidi M, Speliotis Th and Niarchos D 2007 *Microel. Engin.* **84** 1536
- [10] Shen Y, Wu Y, Xie H, Li K, Qiu J and Guo Z J. *J. Appl. Phys.* **91** 8001
- [11] Yu J, Kent A D and Parkin S S P 2000 *J. Appl. Phys.* **87** 5049
- [12] Lebib A, Li S P, Natali M and Chen Y 2001 *J. Appl. Phys.* **89** 3892
- [13] Demand M, Hehn M, Ounadjela K, Stamps R L, Cambril E, Cornette A and Rousseaux F 2000 *J. Appl. Phys.* **87** 5111
- [14] Lau J W and Shaw J M 2001 *J. Phys. D: Appl. Phys.* **44** 303001
- [15] Li S P, Lebib A, Chen Y, Fu Y and Welland M E 2002 *J. Appl. Phys.* **91** 9964
- [16] Hu G, Thomson T, Albrecht M, Best M E, Terris B D, Rettner C T, Raoux S, McClelland G M and Hart M W 2004 *J. Appl. Phys.* **95** 7013
- [17] Thomson T, Hu G and Terris B 2006 *Phys. Rev. Lett.* **96** 257204
- [18] Fernandez A and Cerjan C J 2000 *J. Appl. Phys.* **87** 1395
- [19] Hao Y, Castaño F J, Ross C A, Vögeli B, Walsh M E and Smith H I 2002 *J. Appl. Phys.* **91** 7989
- [20] Katoh Y, Saito S, Honjo H, Nebashi R, Sakimura N, Suzuki T, Miura S and Sugibayashi T 2009 *IEEE Trans. Magn.* **45** 3804
- [21] Jeong W C, Park J H, Koh G H, Jeong G T, Jeong H S and Kim K 2005 *J. Appl. Phys.* **97** 10C905
- [22] Salazar-Alvarez G, Kavich J J, Sort J, Mugarza A, Stepanow S, Potenza A, Marchetto H, Dhesi S S, Baltz V, Dieny B, Weber A, Heyderman L J, Nogués J and Gambardella P 2009 *J. Appl. Phys.* **95** 012510
- [23] Seu K A, Huang H, Lesoine J F, Showman H D, Egelhoff W F, Gan L and Reilly A C 2003 *J. Appl. Phys.* **93** 6611
- [24] Moritz J, **Vinai G** and Dieny B 2012 *IEEE Magn. Lett.* **3** 400024

- [25] Ali M, Marrows C H, Al-Jawad M, Hickey B, Misra A, Nowak U and Usadel K D 2003 *Phys. Rev. B* **68** 214420
- [26] Gornakov V S and Lee C G 2010 *J. Phys.: Conf. Series* **200** 072036
- [27] Natali M, Prejbeanu I L, Lebib A, Buda L D, Ounadjela K and Chen Y 2002 *Phys. Rev. Lett.* **88** 157203
- [28] Sort J, Salazar-Alvarez G, Baro M D, Dieny B, Hoffmann A, Novosad V, Nogues J 2006 *Appl. Phys. Lett.* **88** 042502
- [29] Sort J, Hoffmann A, Chung S H, Buchanan K S, Grimsditch M, Baro M D, Dieny B and Nogués J 2005 *Phys. Rev. Lett.* **95** 067201
- [30] Jung W, Castaño F J, Morecroft D, Ross CA 2005 *J. Appl. Phys.* **97** 10K113
- [31] Guslienko K, Novosad V, Otani Y, Shima H and Fukamuchi K 2001 *Phys. Rev. B* **65** 024414
- [32] Néel L 1967 *Ann. Phys. (Paris)* **2** 61. An English translation is available in *Selected works of Louis Néel* edited by N. Kurti (Gordon and Breach, New York, 1988), p.469
- [33] Mauri D, Siegmund H C, Bagus P S and Key E 1987 *J. Appl. Phys.* **62** 3047
- [34] **Vinai G**, Moritz J, Gaudin G, Vogel J, Bonfim M, Lançon F, Prejbeanu I L, Mackay K and Dieny B 2013 *J. Phys. D: Appl. Phys* **46** 345308
- [35] Thompson C V 2000 *Annu. Rev. Mater. Sci.* **30** 159
- [36] Takano K, Kodama R H, Berkowitz A E, Cao W and Thomas G 1997 *Phys. Rev. Lett.* **79** 1130
- [37] Martien D, Takano K, Berkowitz A E and Smith D J 1999 *Appl. Phys. Lett.* **74** 1314
- [38] Tomeno I, Fuke I N, Iwasaki H, Sahashi M and Tsunoda Y 1999 *J. Appl. Phys.* **86** 3853
- [39] Vallejo-Fernandez G, Fernandez-Outon L E and O'Grady K 2008 *J. Phys. D: Appl. Phys.* **41** 112001
- [40] Carpenter D T, Codner J R, Barmak K and Rickman J M 1999 *Mater. Lett.* **41** 296
- [41] O'Grady K, Fernandez-Outon L E and Vallejo-Fernandez G 2010 *J. Magn. Magn. Mat.* **322** 883
- [42] Manzoor S, Vopsaroiu M, Vallejo-Fernandez G and O'Grady K 2005 *J. Appl. Phys.* **97** 10K118
- [43] Vopsaroiu M, Vallejo-Fernandez G, Thwaites M J, Anguita J, Grundy P J and O'Grady K 2005 *J. Phys. D: Appl. Phys.* **38** 490
- [44] Vopsaroiu M, Thwaites M J, Rand S, Grundy P J and O'Grady K 2004 *IEEE Trans. Magn.* **40** 2443
- [45] Tang L, Laughlin D E and Gangopadhyay 1997 *J. Appl. Phys.* **81** 4906
- [46] Kanak J, Stobicki T, Schebaum O, Reiss G and Brückl H 2006 *Phys. Stat. Sol (b)* **243** 197
- [47] Stobiecki T, Kanak J, Wrona J, Czapkiewicz M, Kim C G, Kim C O, Tsunoda M and Takahashi M 2004 *Mol. Phys. Rep.* **40** 156
- [48] Xu M, Lu Z, Yang T, Liu C, Mai Z and Lai W 2002 *J. Appl. Phys.* **92** 2052
- [49] Li M H, Cai J W, Yu G H, Jiang H W, Lai W Y, Zhu F W 2002 *Mater. Sci. Eng. B* **90** 296
- [50] Pakala M, Huai Y, Anderson G and Miloslavsky L 2000 *J. Appl. Phys.* **87** 6653

- [51] Lacour D, Durand O, Maurice J L, Jaffrès H, Van Dau F N, Petroff F, Etienne P, Humbert J and Vaurès A 2004 *J. Magn. Magn. Mat.* **270** 403
- [52] Nishioka K, Hou C, Fujiwara H and Metzger R D 1996 *J. Appl. Phys.* **80** 4528
- [53] Fecioru-Morariu M, Ali S R, Papusoi C, Sperlich M and Güntherodt G 2007 *Phys. Rev. Lett.* **99** 097206
- [54] Torres L, Martinez E, Lopez-Diaz L and Iñiguez J 2001 *J. Appl. Phys.* **89** 7585
- [55] Girgis E, Portugal R D, Loosvelt H, Van Bael M J, Gordon I, Malfait M, Temst K, Van Haesendonck C, Leunissen L H A and Jonckheere R 2003 *Phys. Rev. Lett.* **91** 187202
- [56] Laureti S, Suck S Y, Haas H, Prestat E, Bourgeois O and Givord D 2012 *Phys. Rev. Lett.* **108** 077205
- [57] Malinowski G, Albrecht M, Guhr I L, Coey J M D and van Dijken S 2007 *Phys. Rev. B* **75** 012413
- [58] Vallejo-Fernandez G and Chapman J N 2009 *Appl. Phys. Lett.* **94** 262508
- [59] Xi H, White R H, Mao S, Gao Z, Yang Z, Murdock E 2001 *Phys. Rev. B* **64** 184416
- [60] Garcia F, Moritz J, Ernult F, Auffret S, Rodmacq B, Dieny B, Camarero J, Penneç Y, Pizzini S and Vogel J 2002 *IEEE Trans. Magn.* **38** 2730
- [61] Moritz J 2003 *Thèse Université Joseph Fourier de Grenoble*
- [62] Private communication
- [63] Baltz V, Sort J, Rodmacq B and Dieny B 2005 *Phys. Rev. B* **72** 104419
- [64] Baltz V, Gaudin G, Somani P and Dieny B 2010 *Appl. Phys. Lett.* **96** 262505
- [65] Vallejo-Fernandez G and Chapman J N 2010 *J. Appl. Phys.* **107** 09D704
- [66] Stiles M D and McMichael R D 1999 *Phys. Rev. B* **59** 3722
- [67] Kim J V and Stamps R L 2005 *Phys. Rev. B* **71** 094405
- [68] Camarero J, Sort J, Hoffmann A, García-Martín J M, Dieny B, Miranda R and Nogués J 2005 *Phys. Rev. Lett.* **95** 057204



# Chapter 5

## **Exchange bias enhancement: (Pt(Pd)/Co)<sub>3</sub>/IrMn/Co trilayer structures**

This chapter will present the possibility of improving exchange bias properties in IrMn/Co structures through an additional out-of plane layer coupled with IrMn at the other interface. It will be shown how this second coupling reduces the critical AF thickness for which the exchange is set and increases the blocking temperature compared to equivalent IrMn/Co bilayers. These effects will be interpreted with the granular model of exchange bias exposed in Paragraph 1.2.6. In particular, the crossed-axis coupling in the trilayer structure causes an indirect IrMn grain coupling and a spin canting due to the out-of-plane magnetized layer.

In the previous chapter, the study of exchange bias variability was performed on samples with different buffer layer thickness and IrMn thickness. In that case, the purpose was to observe the effects of different grain size population on dot to dot variability. In this chapter, we will describe the origin of the dependence of exchange bias on AF thickness through the granular model of Paragraph 1.2.6. The same model will be used when considering the thermal effects on the AF grain stability. The effects of the trilayer structure and its crossed-axis coupling in the IrMn layer will be described on the basis of this model.

## 5.1 Out-of-plane anisotropy: (Pt/Co), (Pd/Co) multilayers

In 1985 Carcia *et al.* [1] discovered that, by alternating layers of Pd and Co, for Co thicknesses below 0.8nm the easy axis of magnetization was oriented along the direction normal to the surface. The same phenomenon was then observed on (Pt/Co) [2] and (Au/Co) [3] multilayers. As presented in Chapter 2, multilayers with perpendicular magnetization are important in technological applications because of their very strong out-of-plane anisotropy, necessary to reduce the lateral size without overcoming the superparamagnetic limit, together with the practical advantage of being deposited by sputtering.

The out-of-plane magnetization, theoretically predicted by Néel [4], is due to a series of coexisting phenomena. The Co layer being ultrathin (thickness of a few Angstroms), the interface and surface energies become of the same order of magnitude that the bulk ones. If we take into consideration the energy equation of the Stoner-Wohlfarth model of Eq.1.6, the anisotropy term  $K_{anis}$  can be decomposed into three terms: the demagnetizing part ( $-2\pi \mathbf{H}_d \mathbf{M}_S$ ), the volume term  $K_V$  (i.e. the magnetocrystalline anisotropy) and the interface anisotropy  $K_S$  [5,6]:

$$K_{anis} = -2\pi \mathbf{H}_d \mathbf{M}_S + K_V + \frac{2K_S}{t_F} \quad (5.1)$$

The first term may induce the magnetization to go out-of-plane in patterned systems with very thick F layer [7,8] because of its tendency to put the magnetization along the longest axis. In multilayer structures the interfacial term may become predominant and induce perpendicular anisotropy. Constraints, roughness, interdiffusion and orbital hybridization are examples of parameters important for the interfacial term.

In the case of (Pt/Co) and (Pd/Co) multilayers, the lattice parameter mismatch between Co and its neighbour layers leads to strains. This variation of lattice parameter along the F layer thickness influences the magnetic properties of the material, up to leading the magnetization axis to the out-of-plane direction; these effects are described by a magnetoelastic energy. Interface roughness may also play a role, reducing the effective out-of-plane anisotropy. Co orbital hybridization with non-magnetic materials at the interfaces modified the filling of the Co band structure, leading to an additional out-of-plane anisotropy. Finally, annealing processes may cause interdiffusion of Pt and Pd into the Co layers, (they are both miscible with Co [9-11]) creating CoPt and CoPd alloys which degrade the quality of the perpendicular anisotropy.

### 5.1.1 (Pt(Pd)/Co)/IrMn systems

If (Pt/Co) or (Pd/Co) multilayers are coupled to an AF layer and field cooled with an out-of-plane applied field, shifted hysteresis loops are obtained when applying a field perpendicular to the substrate. A wide literature [12-18] allows us to precisely tailor (Pt(Pd)/Co) multilayer thicknesses [12,13,16,18], number of repetitions [14,16], interfacial properties [16,17] to optimize exchange bias properties. This large interest is in part due to the technological implications on perpendicular STT-MRAM systems and spin valves, as mentioned in Chapter 2.

In our multilayer structures, the (Pt(Pd)/Co) multilayers will be of the type (thickness in nm): (Pt<sub>1.8</sub>/Co<sub>0.6</sub>)<sub>3</sub> and (Pd<sub>1.8</sub>/Co<sub>0.6</sub>)<sub>3</sub>, thicknesses at which a good perpendicular exchange has been observed [13,14]. In our case, anyway, we are mainly interested not on optimizing the out-of-plane exchange field, but into having a stable, fully remanent out-of-plane magnetic state during the in-plane hysteresis loops. This is dependent, among other parameters, on the number of multilayer repetitions. Samples with the stack Ta<sub>3</sub>/(Pt<sub>1.8</sub>/Co<sub>0.6</sub>)<sub>N</sub>/IrMn<sub>4</sub>/Pt<sub>2</sub> and Ta<sub>3</sub>/(Pd<sub>1.8</sub>/Co<sub>0.6</sub>)<sub>N</sub>/IrMn<sub>4</sub>/Pt<sub>2</sub>, with N going from 3 up to 30, were deposited and annealed at 200°C for 30' with an in-plane setting field of 2000 Oe.

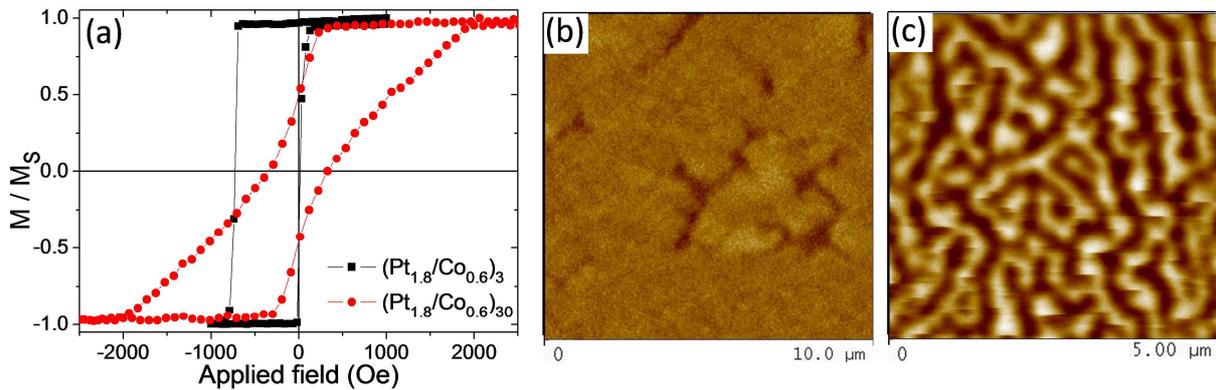


**Fig. 5.1** – (a) Out-of-plane hysteresis loops for Ta<sub>3</sub>/(Pt<sub>1.8</sub>/Co<sub>0.6</sub>)<sub>N</sub>/IrMn<sub>4</sub>/Pt<sub>2</sub> samples for 3 and 30 multilayer repetitions, with corresponding MFM images at remanence for N = 3 (b) and N = 30 (c).

As it can be observed from the out-of-plane hysteresis loops of Fig.5.1a, the sample with three multilayer repetitions has a square loop, whereas the sample with 30 repetitions has a large loop with out-of-plane domains, as it can be observed from the MFM images at remanence of Fig.5.1b and Fig.5.1c. The MFM scans shows that, whereas (Pt<sub>1.8</sub>/Co<sub>0.6</sub>)<sub>3</sub> sample does not show domains, from 15 repetitions the magnetic state at remanence presents domains, whose size reduces with the increase of number of repetitions, up to the domain pattern observed for the (Pt<sub>1.8</sub>/Co<sub>0.6</sub>)<sub>30</sub> sample. A similar behaviour was observed for the (Pd<sub>1.8</sub>/Co<sub>0.6</sub>)<sub>N</sub> samples. These results are coherent with those present in the literature on

similar multilayer stacks [19,20]. For a few multilayer repetitions, the magnetic switching is sharp because of the quick magnetization nucleation and domain wall motion in the sample. For larger  $N$ , due to the larger demagnetizing energy, multidomain state is more stable at remanence; the application of a field smoothly favours one domain polarity, until the sample is saturated.

## 5.2 Effects of trilayer structures on IrMn critical thickness

### 5.2.1 Hysteresis loops at room temperature

#### Bilayer series

As anticipated in Paragraph 4.3, IrMn/Co bilayers start presenting a hysteresis loop shift over a critical AF thickness  $t_C$  [21] of  $3 \pm 0.5$  nm, as shown in Fig.5.2a.

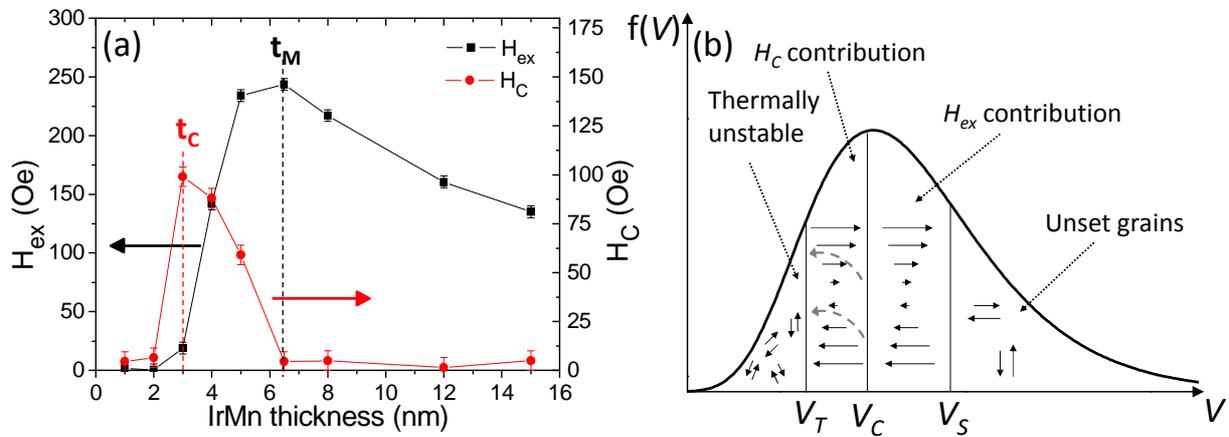


**Fig. 5.2** – (a) Exchange bias and coercivity for  $Ta_3/Cu_2/IrMn_x/Co_5/Pt_2$ . Vertical dashed lines indicate the critical thickness  $t_C$  in red and the maximum thickness  $t_M$  in black. (b) Schematic representation of the AF grain distribution in a polycrystalline system.

Around the critical thickness  $t_C$ , a peak in coercivity is observed. Exchange bias then increases reaching a maximum for a thickness  $t_M$  of  $6.5 \pm 0.5$  nm, after which a decrease of exchange field is observed. This behaviour is widely reported in the literature for Mn based AF layers [21-24]. The critical thickness, in a domain wall model [21], is defined as the ratio between the interface coupling  $J_{ex}$  and the AF anisotropy  $K_{AF}$ :

$$t_C = \frac{J_{ex}}{K_{AF}} \quad (5.2)$$

whereas the decrease in exchange after  $t_M$  is usually attributed, in a random field model, to the presence of domain in the AF layer [25].

By taking into account the correspondences between critical thicknesses and critical volumes, three different regimes can be determined by comparing the exchange curve of Fig.5.2a with the granular model, reproposed in Fig.5.2b. For  $t < t_C$ , most of the IrMn grains

are thermally unstable, no coupling is set with the Co layer, so no loop shift is observed. Around  $t_C$  most of the grain volume population is in the “ $H_C$  contribution” range, thus the samples present large coercivity but low exchange. The ratio of grain in the stable range increases when increasing the IrMn thickness, reaching the maximum at  $t_M$ . After the peak, for  $t > t_M$ , two phenomena take place. On one size, domains in the AF layer are created [25]. In parallel with that, the increasing thickness and lateral size of the grains lead to an increase of the portion of grains with  $V > V_S$ . Those grains are so large that they remain unset during the annealing procedure and thus they do not contribute to the exchange anymore, reducing  $H_{ex}$ . The same description is valid for the  $H_{ex}$  curves presented in Paragraph 4.3.2 for the buffer and IrMn thickness series at room temperature.

### Trilayer series

If we consider the trilayer structures with the stacks  $Ta_3/(Pt_{1.8}/Co_{0.6})_3/IrMn_x/Co_5/Pt_2$  and  $Ta_3/(Pd_{1.8}/Co_{0.6})_3/IrMn_x/Co_5/Pt_2$ , for  $x$  ranging from 2 to 15 nm, the evolution of exchange field and coercivity as a function of IrMn thickness is the one presented in Fig.5.3.

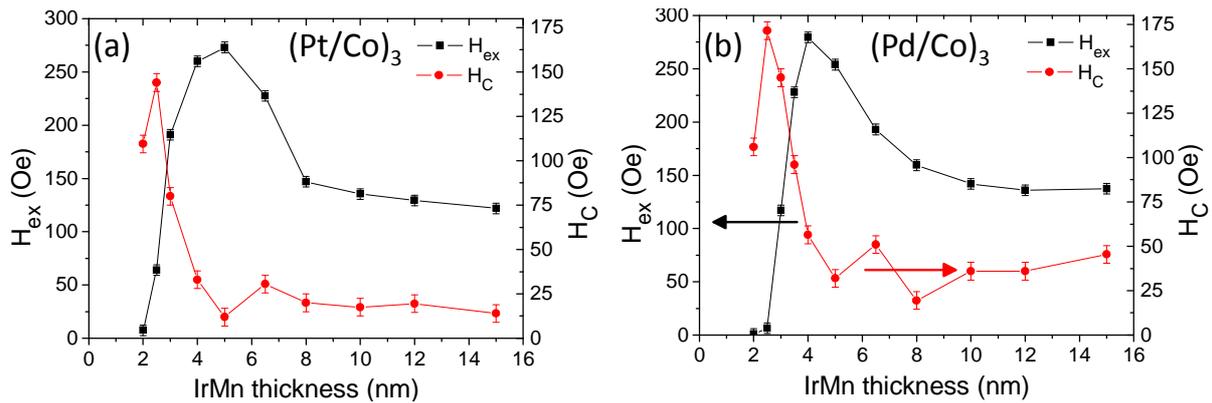
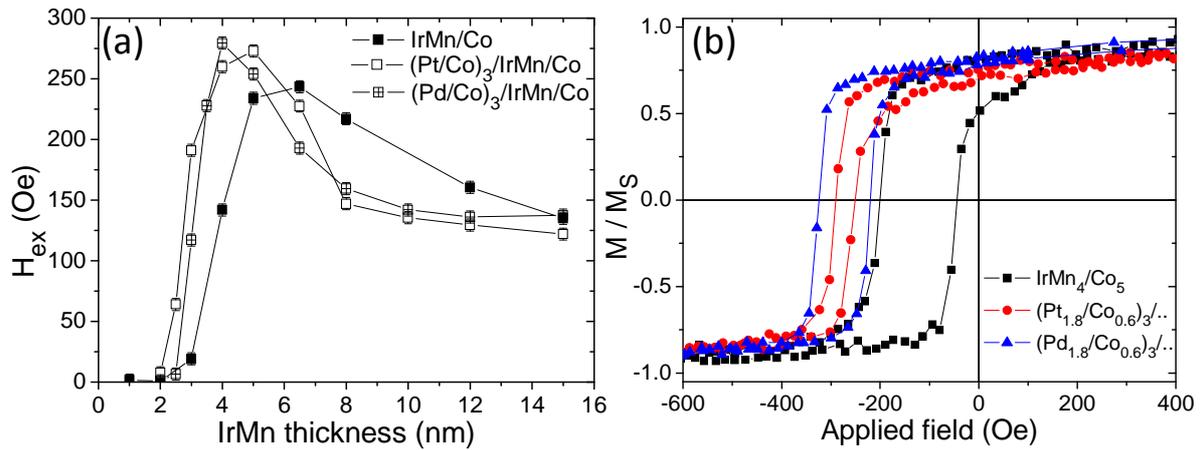


Fig. 5.3 – Exchange bias and coercivity for (a)  $Ta_3/(Pt_{1.8}/Co_{0.6})_3/IrMn_x/Co_5/Pt_2$  and (b)  $Ta_3/(Pd_{1.8}/Co_{0.6})_3/IrMn_x/Co_5/Pt_2$ .

Two main aspects can be observed from the graphs of Fig.5.3. Firstly, the critical thickness  $t_C$  appears at  $2 \pm 0.5$  nm for both (Pt/Co)<sub>3</sub> and (Pd/Co)<sub>3</sub> trilayer series, a lower value compared to the one of the bilayer series. Secondly, the peak of exchange  $t_M$  is present for lower IrMn thicknesses ( $5 \pm 0.5$  nm for (Pt/Co)<sub>3</sub>/IrMn/Co trilayer and  $4 \pm 0.5$  nm for (Pd/Co)<sub>3</sub>/IrMn/Co trilayer), reaching higher values of exchange compared to the corresponding maximum exchange of the bilayer series, as it can be noticed from Fig.5.4a.



**Fig. 5.4** – (a) Comparison of  $H_{ex}$  curves as a function of IrMn thickness for the three structures. (b) Hysteresis loops at 300 K for the three structures for 4 nm IrMn thickness.

A similar trend has also been observed for Ta<sub>3</sub>/Co<sub>5</sub>/IrMn<sub>x</sub>/Co<sub>5</sub>/Pt<sub>2</sub> samples [26], with a reduction of the critical thickness  $t_C$  and its corresponding peak in coercivity, as it can be seen in Fig.5.5, where a larger number of samples is considered in the range of IrMn thicknesses around  $t_C$ .

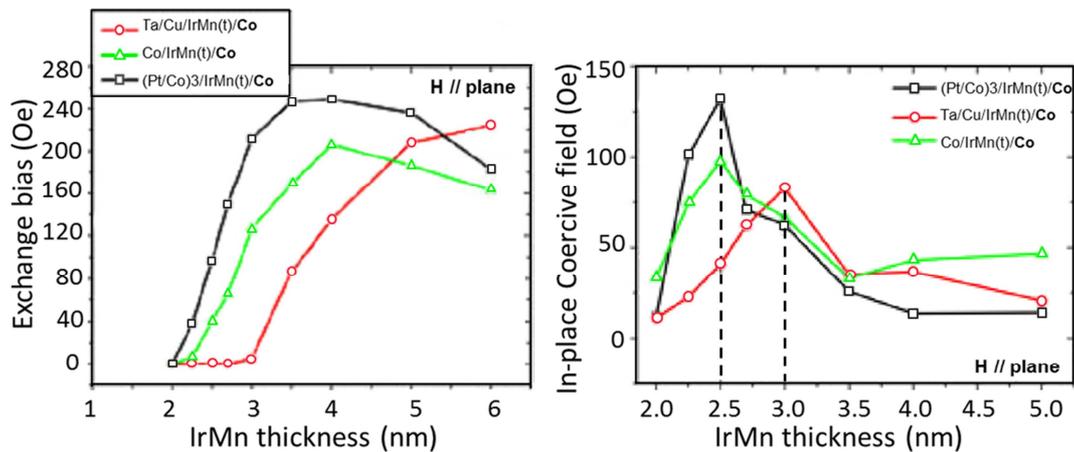


**Fig. 5.5** – Exchange bias field and coercivity for bilayer and trilayer structures [26]. Dotted lines denote the  $H_C$  peak corresponding to  $t_C$ .

## 5.3 Effects of trilayer structures on IrMn/Co blocking temperature

Does the variation of exchange bias properties at room temperature affect its thermal behaviour? To investigate this, a series of hysteresis loop measurements in temperature have been performed on bilayer and trilayer structures, with the aim of determining the blocking temperature  $T_B$  of the system and the thermal behaviour of  $H_{ex}$ . As described in Chapter 1,  $T_B$  is defined as the temperature at which loop shift falls to zero, and in polycrystalline systems with metallic AF layers is generally lower than the Néel temperature [27]. Two AF thermal properties have been extracted here from the temperature dependent measurements. The first one is the maximum  $T_B$ , the second one is the  $T_B$  distribution among the AF grains.

In the first case, the sample, after having being annealed at a temperature  $T_a$ , is field cooled to a temperature  $T_l$ , at which a first hysteresis loop is performed. The temperature is subsequently increased, and a hysteresis loop is performed at each temperature step. In our case, samples were field cooled down to 5 K with a field cooling of 10 kOe and heated up to 400 K with 10 K steps. This measuring method has the advantage of being relatively quick and allows observing the decrease of exchange bias with temperature due to the progressive thermal activation of the grains. In the literature this method is widely used since the very first papers of Meiklejohn and Bean (Fig.5.6) [28]. On the other hand, the different hysteresis loops are measured at different temperatures. As a consequence, parameters like anisotropy and exchange coupling, which are temperature dependent, may vary from one hysteresis loop to another one.

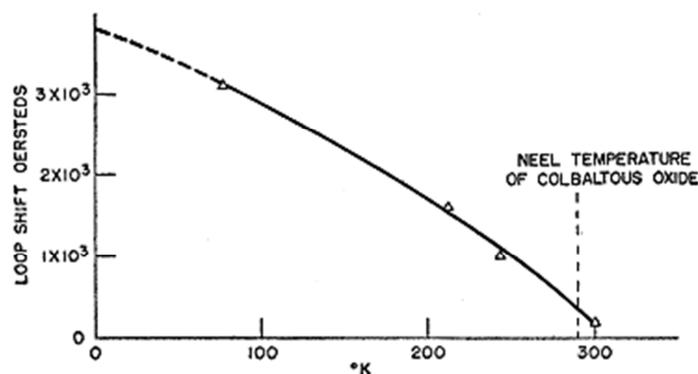


Fig. 5.6 – Historical example of exchange bias measurement in temperature [28].

For this reason, the blocking temperature distribution was measured [29,30] (see Fig.5.7). Samples were field-cooled from 400 to 5 K under a 10 kOe positive field. The temperature was then increased up to an intermediate temperature  $T_a$  under a field in the

opposite direction with respect to the initial field cooling one, and then decreased to 5 K, temperature at which a new hysteresis loop is measured. The applied reverse field was large enough (10 kOe) to saturate the Co layer magnetization in the direction opposite to the initial exchange bias direction. With this procedure, the grain population that becomes thermally unstable below  $T_a$  is field cooled and set in the opposite direction compared to the initial setting direction. The procedure is then repeated for increasing  $T_a$  values, up to 400 K. The higher  $T_a$ , the more grains are reversely set. If all grains are reversed, the exchange bias measured at 5 K has the same value but the opposite sign than the one measured after the initial field cooling in positive field. The advantage of this procedure is that all measurements are performed at the same temperature, so all physical parameters present in the stack are comparable from one loop to another one [31].

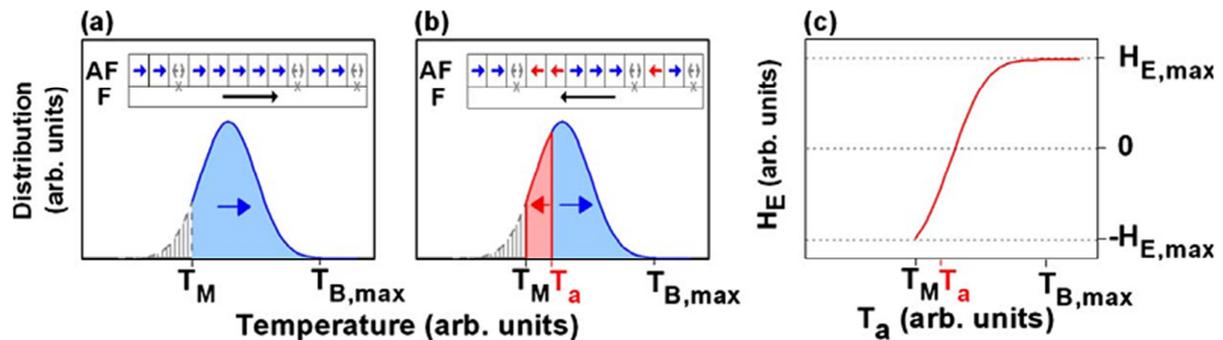
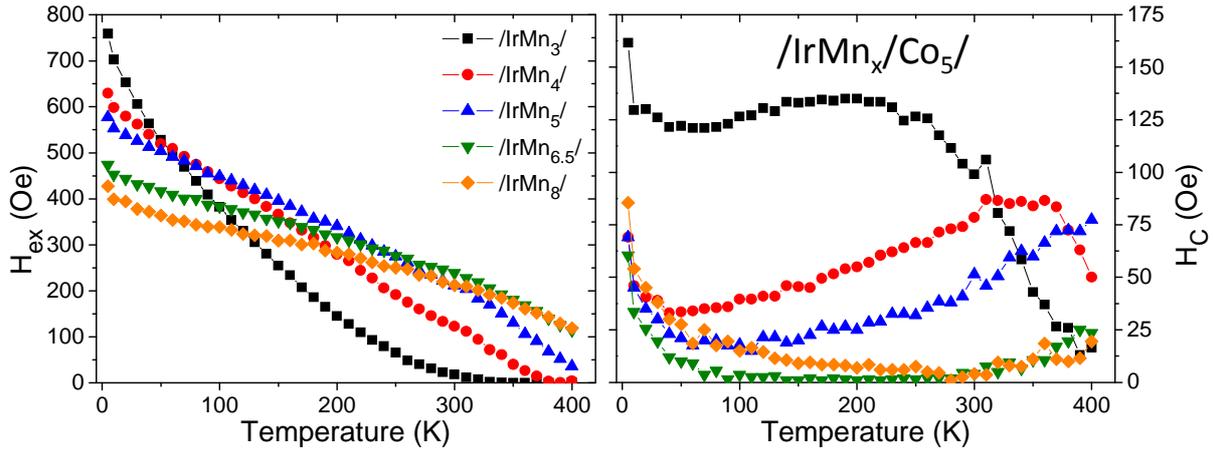


Fig. 5.7 – Sketch of the AF grain orientation during blocking temperature distribution [31]. (a) AF grain population after initial field cooling; (b) partial grain reorientation after heating at temperature  $T_a$  and field cooling with opposite field; (c) temperature dependence of exchange bias with this procedure.

### 5.3.1 Measurements in temperature

Among the samples presented in the previous paragraph, those with an IrMn thickness between 3 and 8 nm were measured in temperature with the “maximum blocking temperature” procedure, for all the three structures. Let’s start the description from the simple bilayer case, shown in Fig.5.8. As a reminder, the considered stacks are the following:

- $Ta_3/Cu_2/IrMn_x/Co_5/Pt_2$ , with  $x$  going from 3 to 8 nm for the bilayer case;
- $Ta_3/(Pt_{1.8}(Pd_{1.8})/Co_{0.6})_3/IrMn_x/Co_5/Pt_2$ , with  $x$  going from 3 to 8 nm for the trilayer cases.

**Bilayer series**

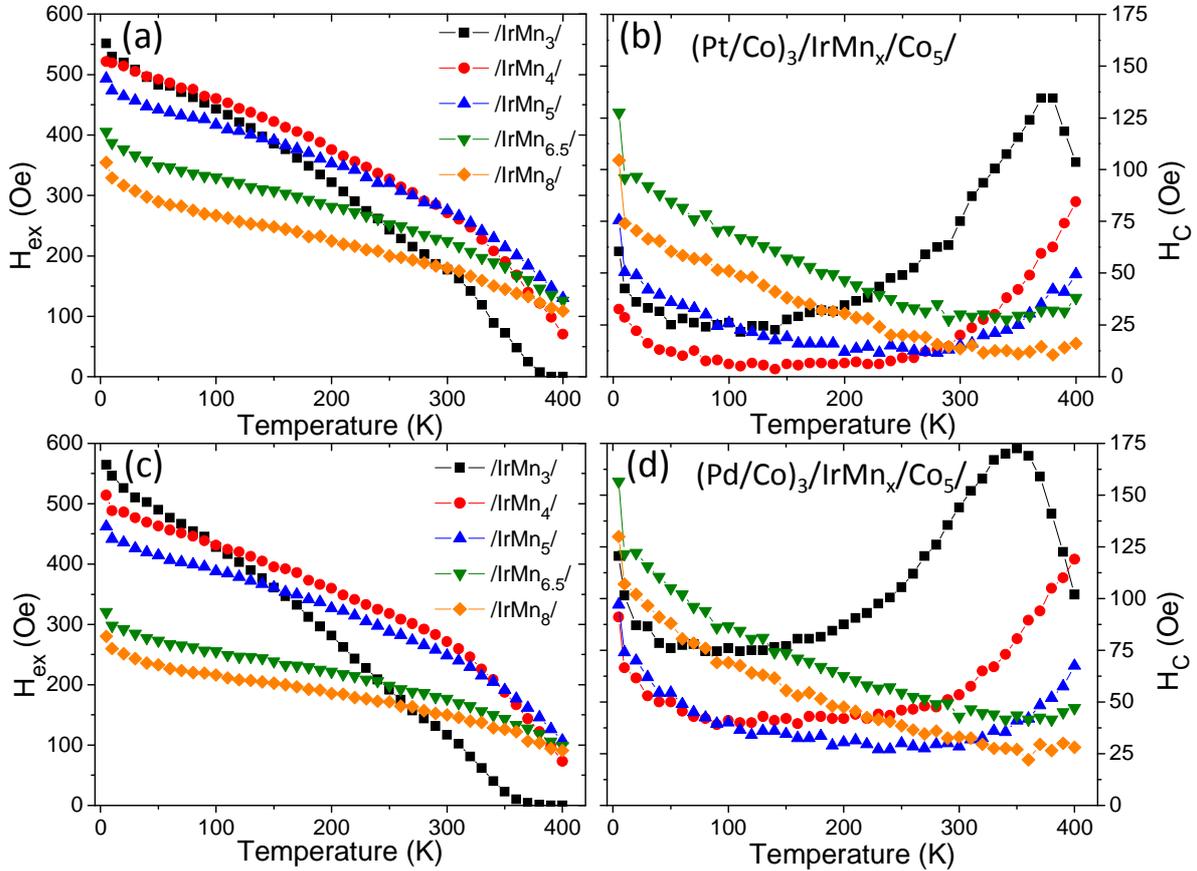
**Fig. 5.8** – Temperature dependence of exchange bias and coercive field for the Ta<sub>3</sub>/Cu<sub>2</sub>/IrMn<sub>x</sub>/Co<sub>5</sub>/Pt<sub>2</sub> bilayer structure.

In the bilayer series, it can be observed from Fig.5.8 that the blocking temperature increases with IrMn thickness and the average slope of the  $H_{ex}(T)$  curves gradually decreases when increasing IrMn thickness. In case of very thin IrMn layer,  $H_{ex}$  is very large at low temperature but rapidly decreases as the temperature increases. These observations can be interpreted with the granular model as follows. As described in the previous chapter, the average AF grain size increases with AF thickness [32]. The density of uncompensated spins at the F/AF interface for compensated AF spin structures (as it is the case for IrMn [33]) increases with the reduction of grain size. Thus, if an AF grain with small size is thermally stable, its contribution to  $H_{ex}$  is larger than the one given by a bigger grain [34,35]. This is consistent with the observation of a larger value of  $H_{ex}$  for 3 nm IrMn layer compared to the 8nm one at low temperatures. When the temperature is increased, the smaller grains (thin AF case) soon become thermally unstable, thereby losing their contribution to the loop shift and increasing their contribution to the coercivity (see, for example, the 4nm IrMn thickness case). In contrast, the bigger grains (thick AF case) remain thermally stable to higher temperatures, causing  $H_{ex}(T)$  to decrease more slowly with temperature and yielding a higher  $T_B$ . It can be noticed that in the 3 nm IrMn bilayer case,  $H_C$  is already large at low temperature, and partially covers the peak at  $T_B$ . We attribute this to the fact that some AF grains in the grain size distribution are so small that even at low temperature their spin lattice is dragged during the F layer magnetization reversal so that they contribute to the coercivity of the loop. For all thicknesses, the  $H_{ex}$  curves follow a quasi-linear dependency on temperature. This is coherent with the results presented in the literature for similar systems [22,36].

*Trilayer series*

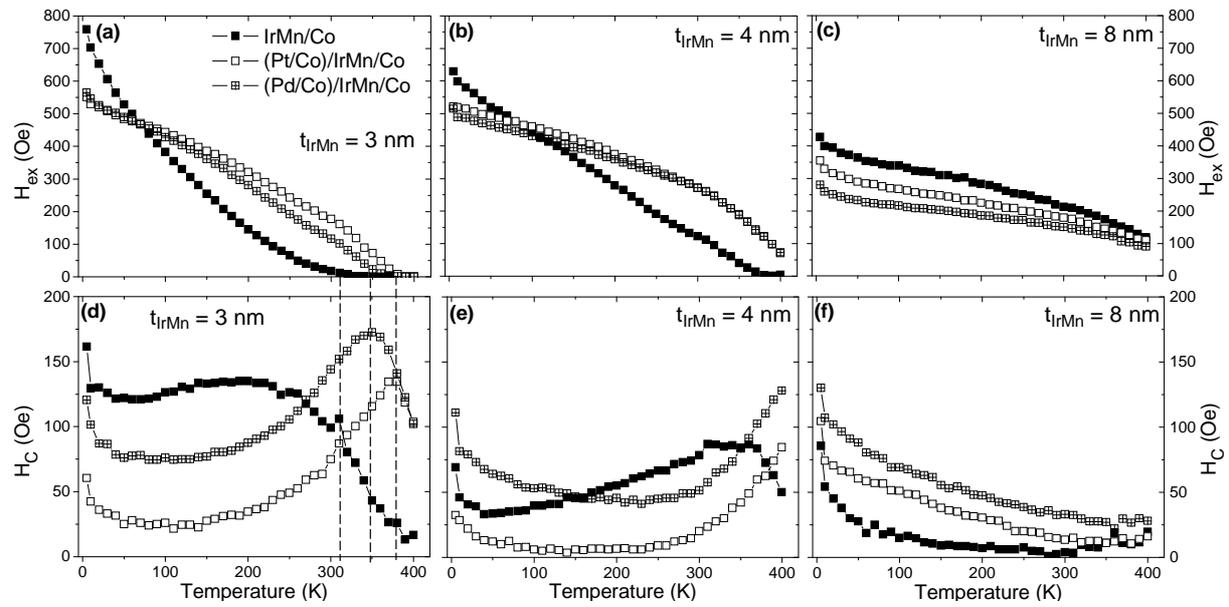
We want to show now the impact of using the trilayer system on the thermal dependence of magnetic properties.

Fig.5.9 shows the temperature dependence of  $H_{ex}$  and  $H_C$  for the two trilayer structures, (Pt/Co)<sub>3</sub>/IrMn/Co in Fig.5.10(a) and (b) and (Pd/Co)<sub>3</sub>/IrMn/Co in Fig.5.10(c) and (d).



**Fig. 5.9** – Temperature dependence of exchange bias  $H_{ex}$  (a,c) and coercive field  $H_C$  (b,d) for the Ta<sub>3</sub>/(Pt<sub>1.8</sub>/Co<sub>0.6</sub>)<sub>3</sub>/IrMn<sub>x</sub>/Co<sub>5</sub>/Pt<sub>2</sub> (a,b) and Ta<sub>3</sub>/(Pd<sub>1.8</sub>/Co<sub>0.6</sub>)<sub>3</sub>/IrMn<sub>x</sub>/Co<sub>5</sub>/Pt<sub>2</sub> (c,d) structures, for x going from 3 to 8 nm.

It can be observed, by comparing the  $H_{ex}(T)$  curves of Fig.5.9a and Fig.5.9d with the one of Fig.5.8, that in the case of thin IrMn layer, the blocking temperature is reached for higher temperatures than the ones obtained of the bilayer case. This difference appears more clearly when comparing together the three samples for a given IrMn value, as it is in Fig.5.10 for different IrMn thicknesses.



**Fig. 5.10** – Temperature dependence of  $H_{ex}$  (a-c) and  $H_C$  (d-f) of bilayer and trilayer structures for different IrMn thicknesses. Vertical dashed lines from (a) to (d) indicate the blocking temperature  $T_B$  of the different stacks for a 3 nm IrMn thickness.

In Fig.5.10a and Fig.5.10d, for a 3 nm IrMn thick, the vertical dashed lines indicate the  $T_B$  values of the three systems. For the bilayer case,  $T_B$  is reached around  $310 \pm 5$  K, whereas for (Pt/Co)<sub>3</sub>/IrMn/Co and (Pd/Co)<sub>3</sub>/IrMn/Co trilayers  $T_B$  is found to be  $380 \pm 5$  and  $350 \pm 5$  K respectively. The shift in temperature is also present for an IrMn thickness of 4 nm, whereas the effect tends to vanish for thicker AF (see Fig.5.10c and Fig.5.10f). Moreover, in this thin IrMn regime,  $H_{ex}(T)$  curves for the trilayer systems show a concave (negative curvature) shape compare to the convex, quasi-linear of the bilayer case. The difference in slope between bilayer and trilayer samples can be better observed by plotting the derivative of  $H_{ex}$  as a function of temperature, as shown in Fig.5.11 for the 4 nm IrMn thick case.

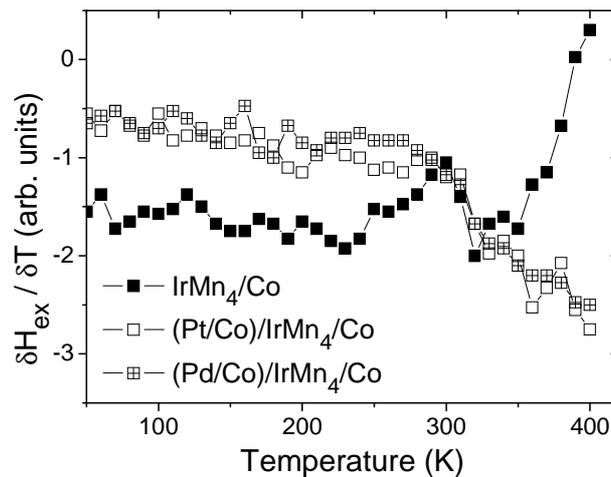


**Fig. 5.11** – Derivative of exchange bias as a function of temperature for the three structures, for 4 nm IrMn thickness.

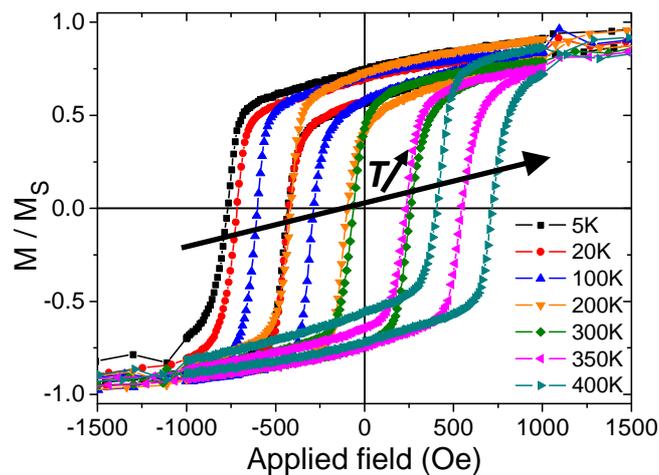
In the temperature regime up to 300 K, the IrMn/Co sample presents a steeper slope than the trilayer ones; a similar slope is maintained up to the blocking temperature at 380 K, when then  $H_{ex}$  falls to zero, as its derivative. The trilayer samples, after the large range in temperature with a smoother slope compared to the bilayer sample, show a sharper slope when approaching  $T_B$ , starting from 300 K.

By correlating the results of the measurements in temperature with those at room temperature, it appears that in the regime of thin IrMn layer an enhancement of exchange bias properties, with increased maximum value of loop shift and reduction of critical thickness, together with an increase of the blocking temperature, takes place.

### 5.3.2 Blocking temperature distribution

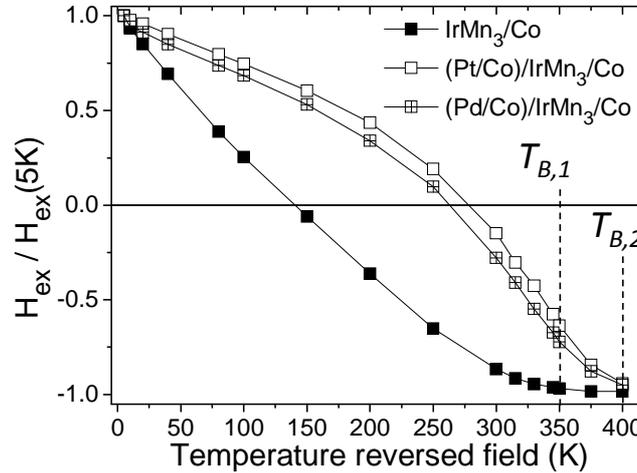
The measurements showed in the previous paragraph showed the temperature dependence of exchange bias field for the bilayer and trilayer structures. In this paragraph, blocking temperature distributions measurements have been performed on the three structures, for the 3 nm IrMn thickness case. This kind of measurement allows evaluating the distribution of the blocking temperature  $\Delta T_B$  and, by measuring all hysteresis loops at 5 K, removes any dependency of exchange coupling and anisotropy on temperature.

Fig.5.12 shows a selection of hysteresis loops after annealing at different increasing temperatures and field cooling at 5 K with opposite field, for the (Pt/Co)<sub>3</sub>/IrMn/Co case. It can be observed how the exchange bias shifts from negative to positive values because of the progressive reversal of the IrMn grains, approaching to the maximum positive exchange bias, which is reached when all grains are reversed at the annealing temperature  $T_a$ .



**Fig. 5.12** – Hysteresis loops of the  $Ta_3/(Pt_{1.8}/Co_{0.6})_3/IrMn_3/Co_5/Pt_2$  sample after heating at different temperatures  $T_a$ , whose values are shown in the legend. The slope is due to the paramagnetic contribution of the sample support and Si/SiO<sub>2</sub> substrate.

By measuring the exchange bias values for each curve for the three samples, the temperature dependences were obtained, as shown in Fig.5.13. The exchange bias is defined as positive at the initial state cooled down at 5 K, and normalized to its value. The exchange bias field changes its sign when more than half of the initial grain population is field cooled in the opposite direction after heating at  $T_a$ . Full grain reversal takes place when the normalized exchange goes to -1.



**Fig. 5.13** – Temperature dependence of normalized exchange bias on  $T_a$  through blocking temperature distribution measurement. Vertical dashed lines indicate the maximum blocking temperature for the bilayer ( $T_{B,1}$ ) and trilayer ( $T_{B,2}$ ) samples.

The difference in shape of the thermal variations of  $H_{ex}(T)$  between the bilayer and the trilayer structures is confirmed. Whereas IrMn/Co bilayer shows a convex, quasi-linear exchange bias reversal, both trilayer structures show a concave reversal, together with an increase of the maximum blocking temperature, reached around 350 K ( $T_{B,1}$  on the graph) for the bilayer case and around 400 K ( $T_{B,2}$  on the graph) for the trilayer ones. As a result, the temperature effects on anisotropy and exchange coupling can be considered negligible in the economy of the exchange bias temperature dependence. Concerning the coercivity values obtained through  $T_B$  distribution,  $H_C$  remains constant in temperature for the three samples, in coherence with what observed in the literature [37].

It is possible to extract the portion of grains reversed during the heating for different temperatures  $T_a$  by deriving the  $H_{ex}(T)$  curves as a function of temperature, thus giving the blocking temperature distribution of the grain population. The resulting curve is plotted in Fig.5.14. Because of the not sufficiently large number of measurements at very low temperature, where spin glass contribution takes place [31], the curve is mainly focused on grain distribution at high temperature.

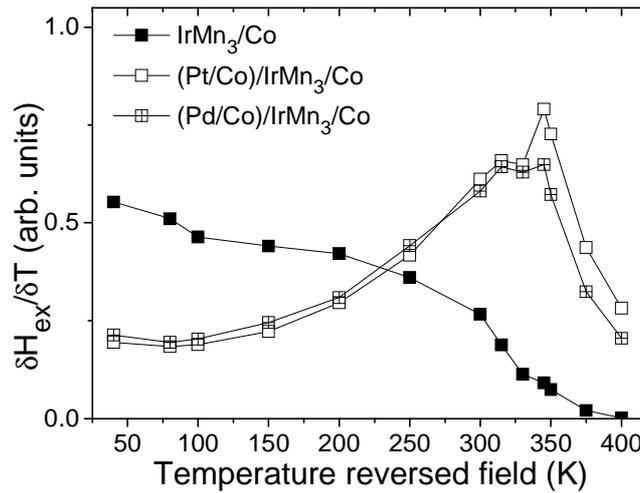


Fig. 5.14 – Temperature dependence of  $\delta H_{ex}/\delta T$  on  $T_a$  for 3 nm IrMn thickness for bilayer and trilayer structures.

Considering the bilayer case, the blocking temperature distribution is very broad, extending all over the temperature range between low  $T$  and 400 K. By correlating the distribution of blocking temperature with the IrMn grain size distribution, it means that part of the grains starts being unstable at very low temperatures; this uncoupling continues taking place since when  $T_B$  is reached. In contrast, the distribution of blocking temperature in the trilayer shows a clear peak between 250 and 400 K, which confirms the coercivity peak observed in Fig.5.9.

## 5.4 Discussion

The presence of a second out-of-plane F layer in contact with IrMn on the other interface of the trilayer structure has shown to have three important consequences on the exchange bias properties at the IrMn/Co interface: a reduction of IrMn critical thickness  $t_C$ , an enhancement of  $H_{ex}$  at  $t_M$  and an increase of blocking temperature  $T_B$  for thin IrMn layers.

In the following paragraph, these effects will be analysed with the granular model exposed in Paragraph 1.2.6 and represented in Fig.5.2.

Firstly, the consequences of the underlayer change on the IrMn growth has to be investigated. A variation of grain population would namely vary the ratio between the four populations, thus affecting the exchange bias behaviour, as the variation of crystallographic properties.

### 5.4.1 Structural analysis

In order to verify the influence of the growth conditions on the magnetic properties, XRD scans and AFM scans for grain counting measurements were performed both on bilayer and trilayer structures.

#### Morphology

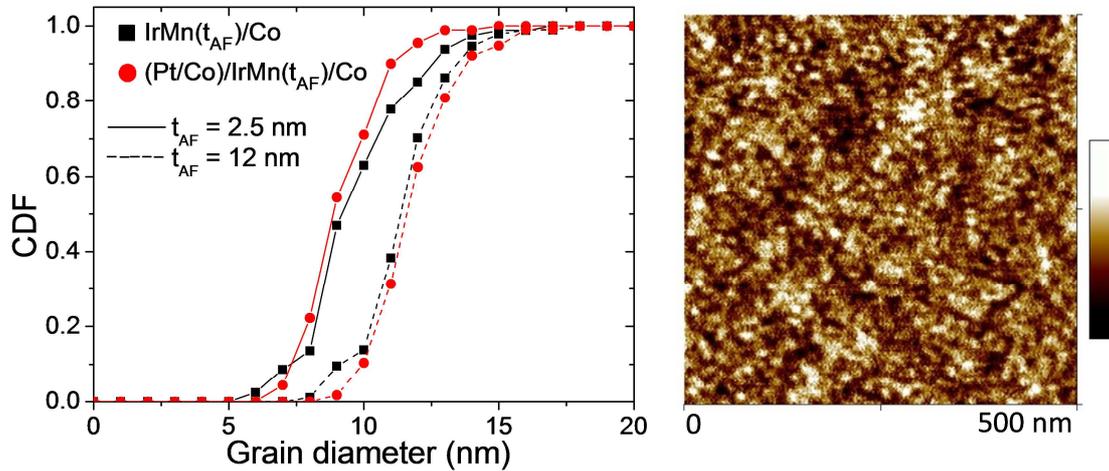


**Fig. 5.15** – Cumulative distribution functions for bilayer (black squares) and trilayer (red circles) structures, and an example of AFM scan for the (Pt/Co)<sub>3</sub>/IrMn<sub>12</sub>/Co sample.

Fig.5.15 shows the cumulative distribution function of the bilayer and the trilayer structures for two different IrMn thicknesses (thin case 2.5 nm, close to the range of thicknesses where the exchange properties are improved in the trilayer structures, and thick case 12 nm because of the larger grain size). About 200 grains have been measured per each sample. From these graphs, it appears that the grain size distributions are comparable between the bilayer and trilayer samples. The increasing grain size with increasing IrMn thickness is thus confirmed also for the trilayer structure. This means that the grain population in the trilayer structure is comparable with the one present in the bilayer one. As a result, no changes in the ratio of grains contributing to the exchange can be considered as the reason of exchange enhancement or  $t_C$  reduction. Moreover, AFM scans do not indicate any significant changes in the interfacial roughness from series to series, thus  $J_{ex}$  should not vary much from samples to samples.

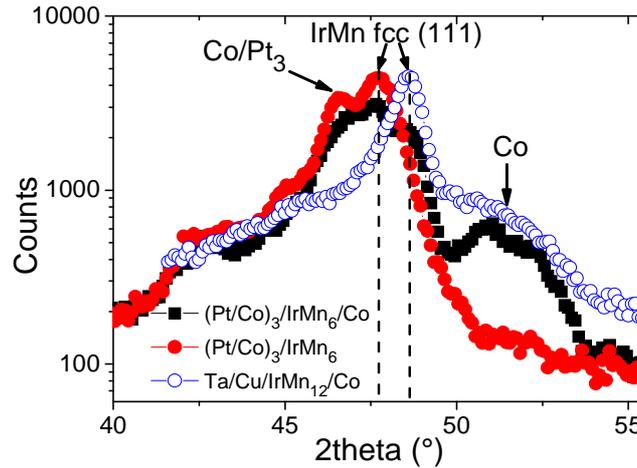
*Crystalline structure*

Fig. 5.16 – X ray diffraction for three different samples with different IrMn underlayers.

Concerning the x-ray characterization, the IrMn/Co bilayer structure was compared with the (Pt/Co)<sub>3</sub>/IrMn/Co one and with (Pt/Co)<sub>3</sub>/IrMn samples, which allowed to observe the IrMn peak without the Co layer, for 6 and 12 nm thicknesses of IrMn, as shown in Fig.5.16. For samples deposited on the (Pt/Co)<sub>3</sub> layer, the IrMn diffraction peaks have very similar (111) fcc texture, independently on the presence of the Co layer. Samples grown on Cu buffer layer, on the other hand, present a peak at higher  $2\theta$  angle, corresponding to a more compact (111) texture, being the lattice parameter  $a$  equal to 2.093 Å for the (Pt/Co)<sub>3</sub> underlayer case and to 2.065 Å for the bilayer one. The shift of IrMn diffraction peak is reported in the literature for bottom and top spin valve structures [38]. A more compact (111) fcc structure has influences on the IrMn anisotropy  $K_{AF}$ , thus varying the values of  $V_T$  and  $V_C$  of Eq.1.27 and Eq.1.26. Whereas this effect has to be taken into account, it cannot explain alone the reduction of critical thickness and the increase of blocking temperature.

For this reason, two effects due to the additional out-of-plane coupling have to be taken into account: the spin canting and the indirect IrMn intergrain coupling.

### 5.4.2 Granular model: effects of the out-of-plane layer on IrMn/Co coupling

We will discuss in this paragraph about two possible interpretations of the improved magnetic properties of the trilayer structures.

#### *Indirect intergrain coupling*

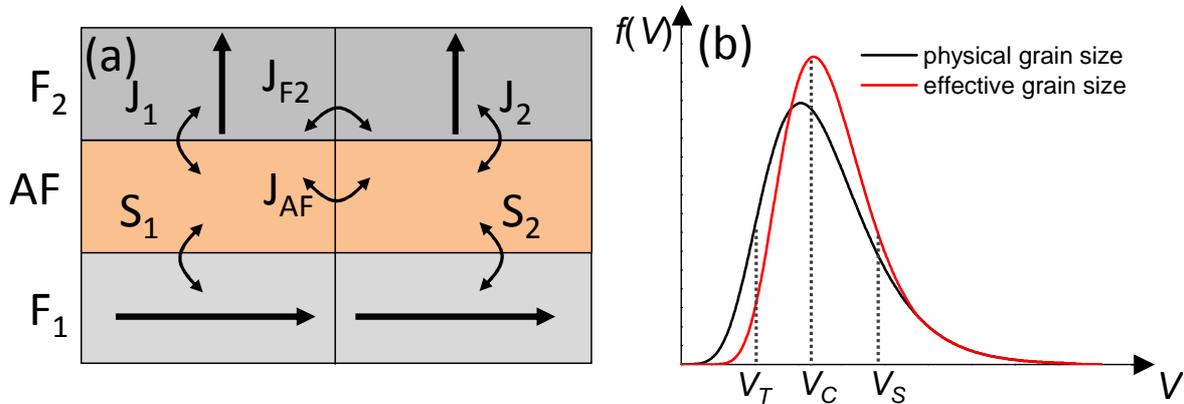


**Fig. 5.17** – (a) Sketch of the AF intergrain coupling through the additional out-of-plane layer  $F_2$ . (b) Schematics of the effect of indirect coupling on the effective IrMn grain size.

In this model, IrMn grains are considered independent one with respect to the other, i.e. uncoupled, because of the disordered atom positioning along the grain boundaries [39,40]. On the other hand, F layers have strong intergrain coupling. Therefore, the spin lattice in neighbouring AF grains is indirectly coupled via the F-layer magnetization. Because of the reversal of the F layer during the hysteresis loop, this effect in bilayer structure is considered not large enough to stabilize the AF grains, because the coupling takes place through a layer that is following the applied field. Let's now consider the case of the trilayer structure case, where a second F layer is added on the other side with a perpendicular magnetization, as depicted in Fig.5.17a. The anisotropy field  $H_K$ , defined as the in-plane field at which the magnetization of the multilayer is put into plane, was measured on the trilayer samples. Its values were respectively 6 kOe for the (Pt/Co)<sub>3</sub> series and 5 kOe for the (Pd/Co)<sub>3</sub> one. This means that the magnetization of the additional out-of-plane layer remains almost fixed during the in-plane hysteresis loop. This is valid for all our field range of interest [41]. As a result, the IrMn intergrain coupling mediated by the additional F layer is maintained all along the hysteresis loop. The increased intergrain coupling due to the interface interaction of out-of-plane spins with IrMn ones creates an effective grain size larger than the physical one, stabilizing otherwise thermally unstable grains. This variation of the effective grain population can be schematized as shown in Fig.5.17b.

## Spin canting

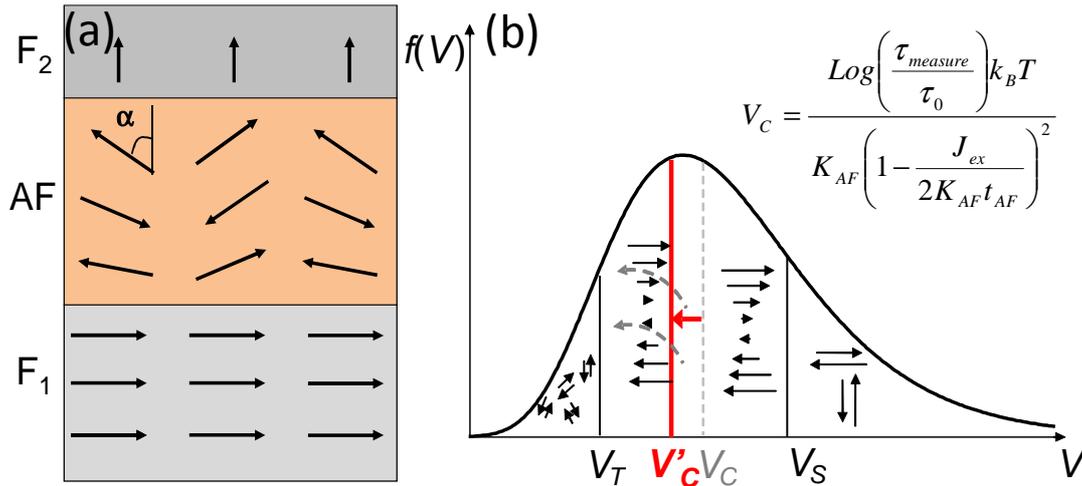


**Fig. 5.18** – (a) Sketch of the spin canting due to F<sub>2</sub>/AF interface coupling. (b) Schematics of the effect of IrMn spin canting at the IrMn/Co interface on the grain contribution to exchange bias; on the right, Eq.1.26.

IrMn, because of its fcc (111) compensated structure, is known to exchange couple with both in-plane and out-of-plane F layers. In the IrMn/Co bilayer, the spins in the IrMn AF tend to lie in the (111) planes along a triangular lattice. In the (Pt/Co)/IrMn/Co and (Pd/Co)/IrMn/Co trilayers, due to the exchange interaction with the out-of-plane magnetized (Pt/Co) - (Pd/Co) multilayers, they tend to be pulled out-of the (111) plane [42]. In a trilayer structure, this out-of-plane canting of AF spins tends to propagate throughout the AF layer, with a gradual damping, from the interface with the out-of-plane multilayer towards the opposite interface, as depicted in the sketch of Fig.5.18a. For sufficiently thin IrMn layer, this propagation induces a change of the spin angle at the IrMn/Co interface, which reduces the interfacial exchange stiffness  $J_{ex}$ . From Eq.1.26, this reduction decreases the value of the critical volume  $V_C$ , as schematized in Fig.5.18b.

By considering a single AF thickness, part of the grain distribution which would have contributed to the coercivity of the loop with a larger  $J_{ex}$  can now resist the torque exerted by the F magnetization on the AF spin lattice during magnetization reversal, thus contributing to  $H_{ex}$ . As a result, the exchange bias increases despite a reduction in the interfacial coupling because more AF grains remain stable and the smallest ones have the largest uncompensated spins [35].

***Effects on  $t_C$  and  $H_{ex}(t_M)$*** 

AFM grain counting measurements of Fig.5.15 showed that bilayer and trilayer structures have, for equivalent IrMn thicknesses, similar grain populations. The reduction of IrMn critical thickness  $t_C$  in trilayer structures can be explained as a combination of the two effects previously described. Spin canting, by reducing  $J_{ex}$ , allows small grains to start contributing to the exchange at lower thicknesses than in the bilayer case. On the other hand, the effective population itself is modified by the indirect coupling through the out-of-plane layer, which artificially increases the “effective” size of the grains. This combination may also explain the higher value of  $H_{ex}$  at  $t_M$  compared to the equivalent one for the bilayer sample, due to a larger portion of grain population contributing to the loop shift, and the lower values of exchange for thick IrMn layer, where intergrain coupling may increase the effective grain size to values too large to be set during annealing.

***Effects on  $T_B$*** 

From the temperature study it appears how both phenomena of spin canting and intergrain coupling are needed to be considered in order to explain the different behaviours observed in the trilayer structures compared to the bilayer one.

Firstly, the increase of  $T_B$  at low IrMn thicknesses can be attributed to the propagation of the canting of IrMn spins from (Pt/Co)<sub>3</sub>/IrMn and (Pd/Co)<sub>3</sub>/IrMn interface to the IrMn/Co one. This canting reduces the dragging torque on the AF spin lattice and therefore increases the ability of the AF grains to contribute to the exchange bias up to higher temperatures. The shift in temperature is present for low IrMn thicknesses, whereas the effect tends to vanish for thicker AF (see Fig.5.10). This indicates that the canting of IrMn spins gets damped on a length of the order of 5 nm. For thin IrMn values, the reduction of interfacial exchange stiffness  $J_{ex}$  reduces the value of the critical volume  $V_C$ . Considering the same grain population in the trilayers as in the bilayer, the shift in temperature of  $V_C$ , i.e. the transition of grain population from switching behaviour to stable domain during field reversal, is delayed compared to the bilayer structure, thus increasing the blocking temperature  $T_B$ . Moreover, the reduction of exchange at very low temperature observed in Fig.5.10 can be explained by spin canting. In that regime of temperature most of the AF grains are coupled to the F layer in the bilayer system. In that case the decrease of interface coupling due to spin canting leads to a reduction of exchange because of a reduced torque exerted by the AF spins on the F layer.

Together with the canting influence, the indirect AF grain coupling is also observed, particularly in the shape of the temperature dependence of  $H_{ex}$ . Whereas bilayer samples have

a quasi linear decrease in  $T$ , the concave shape of the trilayer samples, with a delay in the decrease of exchange at low temperatures, can be attributed to the artificial increase of the grain size. Indirect coupling stabilizes in temperature the smaller grains by increasing their effective size. This effect can be better observed through Fig.5.19.

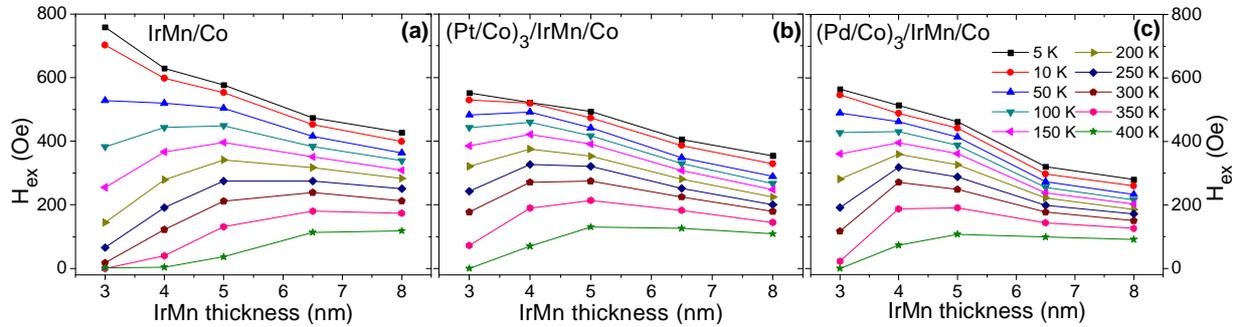


**Fig. 5.19** – Exchange bias as a function of IrMn thickness for different selected temperatures for the three different stacks studied.

Fig.5.19 shows the evolution of  $H_{ex}$  with IrMn thickness for different measurement temperatures, for the three cases. For the IrMn/Co bilayer stack (Fig.5.19a) the maximum of  $H_{ex}$  markedly shifts from 3 to 8 nm as the temperature is increased with significant variations in  $H_{ex}(t_{AF})$ . In contrast, in the trilayer cases (Fig.5.19b and Fig.5.19c), the  $H_{ex}$  variation in temperature remains in a smaller envelope, with smaller variations in  $H_{ex}$  values versus IrMn thicknesses between 4 and 8 nm in the wide range of investigated temperatures.

This homogenized grain behaviour is also evident from the temperature dependence of the coercive field in Fig.5.10d and the blocking temperature distribution of Fig.5.14. Whereas in IrMn/Co bilayer the  $H_C$  peak is preceded by a large smooth increase in coercivity (i.e. part of the IrMn grains start switching at low temperature), the  $H_C$  peak of the trilayer structures appears much more pronounced and sharp. The indirect IrMn grain coupling tends to homogenize the thermal behaviour of the grains. As a result, the transition from stable to switchable grains happens more uniformly all over the grain size distribution. From the exchange bias point of view, the effective grain size distribution in the trilayer structures for thin IrMn thickness is sharper than the grain size distribution of the bilayer despite they present comparable physical sizes. The same behaviour is observed in Fig.5.16. The distribution of blocking temperature in the IrMn/Co bilayer is very broad extending all over the range between low temperature and 400 K whereas those of the trilayer stacks present a clear peak between 250 and 400 K. By correlating the distribution of blocking temperature with the IrMn grain size distribution, this confirms the homogenized behaviour of IrMn grains by the indirect grain coupling through the perpendicularly magnetized (Pt/Co) or (Pd/Co) multilayers.

## 5.5 Interest of trilayer structures for technological applications

The possibility of increasing the blocking temperature in ultrathin AF layers and of enhancing the exchange bias field is of technological interest for TA-MRAM applications [43], in particular for the retention and writing properties of the storage layer (see Paragraph 2.2.3). In the range of temperature from 300 to 400 K (interesting from the application point of view), the investigated trilayer structures present, together with larger  $H_{ex}$ , a larger  $H_{ex}/H_C$  ratio compared to the corresponding bilayer. From Fig.5.5, for 4 nm IrMn thickness at 300 K,  $H_{ex}/H_C$  ratio is 1.6 for IrMn/Co bilayer, versus 13.6 and 5.3 for (Pt/Co)<sub>3</sub>/IrMn/Co and (Pd/Co)<sub>3</sub>/IrMn/Co trilayers. This ratio is an important quality factor for data retention and writing reliability in TA-MRAM systems: a large exchange bias with low coercivity means a hysteresis loop with both switching field far from zero field, avoiding intermediate state issues during the writing or reading processes. Another important advantage of the trilayer structures compared to the bilayer one is the shape of the  $H_{ex}(T)$  variation, concave (negative curvature) instead of convex or almost linear for the bilayer stack. A concave variation is more appropriate for TA-MRAM application since it means that the memory retention is less degraded on the whole operating range than in the case of a linear variation and that the storage layer pinning energy sharply decreases as the writing temperature is approached. For these reasons, this kind of trilayer structures is an excellent candidate to improve storage layer performances and reliability in TA-MRAM.

Moreover, these trilayer structures can be very interesting in magnetoresistive TMR heads for hard disk drives since they may allow reducing the total thickness of the pinning layer and thereby reduce the shield to shield spacing in the reader. This is particularly true in (Pt/Co) or (Pd/Co) are used wherein strong out-of-plane anisotropy can be obtained with very ultrathin (Pt(Pd)/Co) repeats [44].

### 5.5.1 Annealing effects on bilayer and trilayer thermal properties

In order to verify the applicability of the trilayer structures to MTJ based devices (TA-MRAM systems or TMR heads), as-deposited stacks were heated up to 613 K (340°C) for 90', typical annealing parameters used to optimize the MgO barrier texture in MTJ stacks [45], as shown in Paragraph 2.2.1. This annealing was performed on the three structures for the 4nm thick IrMn case. Fig.5.20 shows the hysteresis loops at 300K after annealing, compared with the equivalent samples annealed at 473 K (200°C) for 30'.

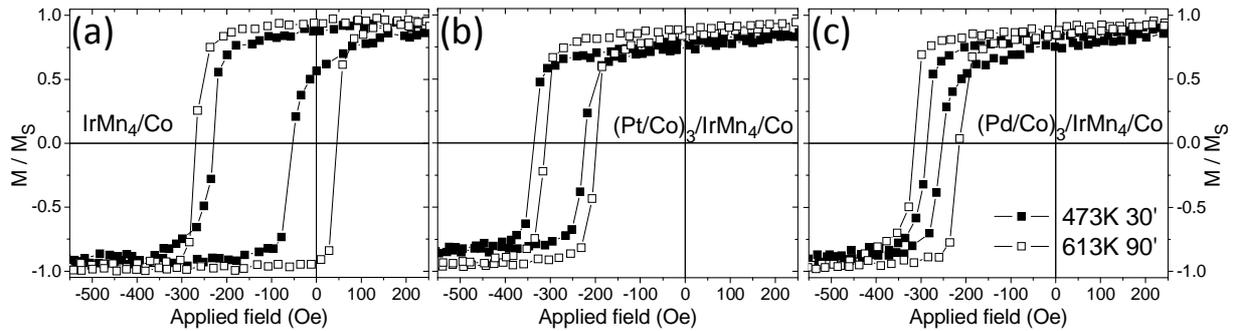


**Fig. 5.20** – Hysteresis loops at 300 K for the IrMn<sub>4</sub>/Co (a), (Pt/Co)<sub>3</sub>/IrMn<sub>4</sub>/Co (b) and (Pd/Co)<sub>3</sub>/IrMn<sub>4</sub>/Co (c) structures for 4 nm IrMn thickness in the two annealing process cases.

In the bilayer case (Fig.5.20a), an increase of coercivity is observed. It can be explained by the longer annealing at higher temperatures, which may induce Mn interdiffusion of into Co layer, thus varying the interfacial properties and material compositions. In the trilayer cases (Fig.5.20b and Fig.5.20c), both stacks maintain a large  $H_{ex}$  also after the higher annealing process, comparable to the one obtained at 200°C. In presence of (Pt/Co) and (Pd/Co) multilayers, the annealing process is responsible of diffusion of Pt and Pd into Co layers. This mixing can lead to the dissolution of the multilayer structure, creating a CoPt or CoPd alloy, thus losing the perpendicular magnetization properties [11]. For this reason, Extraordinary Hall Effect measurements have been performed on the trilayer structures to verify that the multilayers still present a perpendicular magnetization.

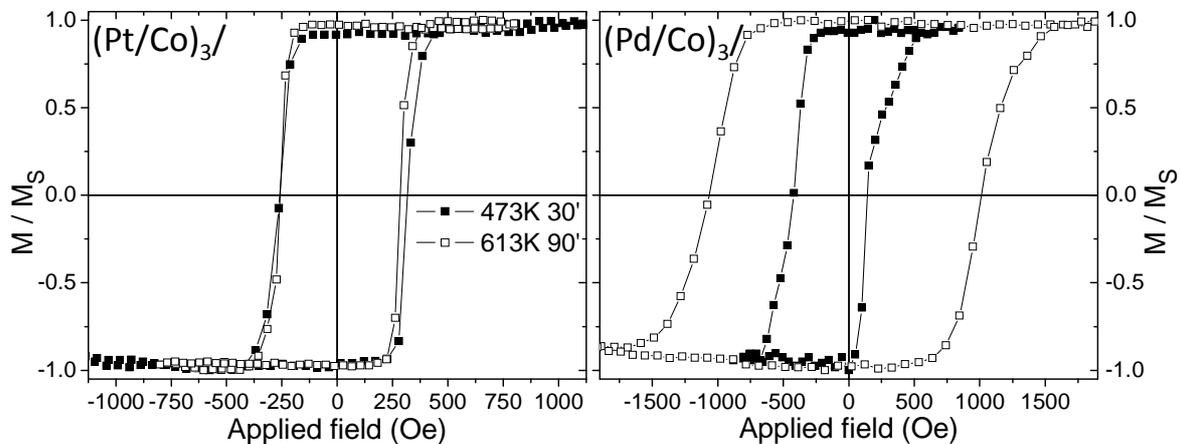


**Fig. 5.21** – Out-of-plane hysteresis loops for the two trilayer structures in the two annealing process cases.

As it can be observed from Fig.5.21, the magnetic properties of the (Pt/Co)<sub>3</sub>/IrMn<sub>4</sub>/Co sample are maintained unchanged after the annealing at higher temperature, whereas the (Pd/Co)<sub>3</sub> one shows an increase in coercivity, but still presents a perpendicular magnetization.

Thermal properties were then verified with the maximum blocking temperature procedure, in the same range of temperatures as the samples annealed at 200°C. The resulting temperature dependences are plotted in Fig.5.22.

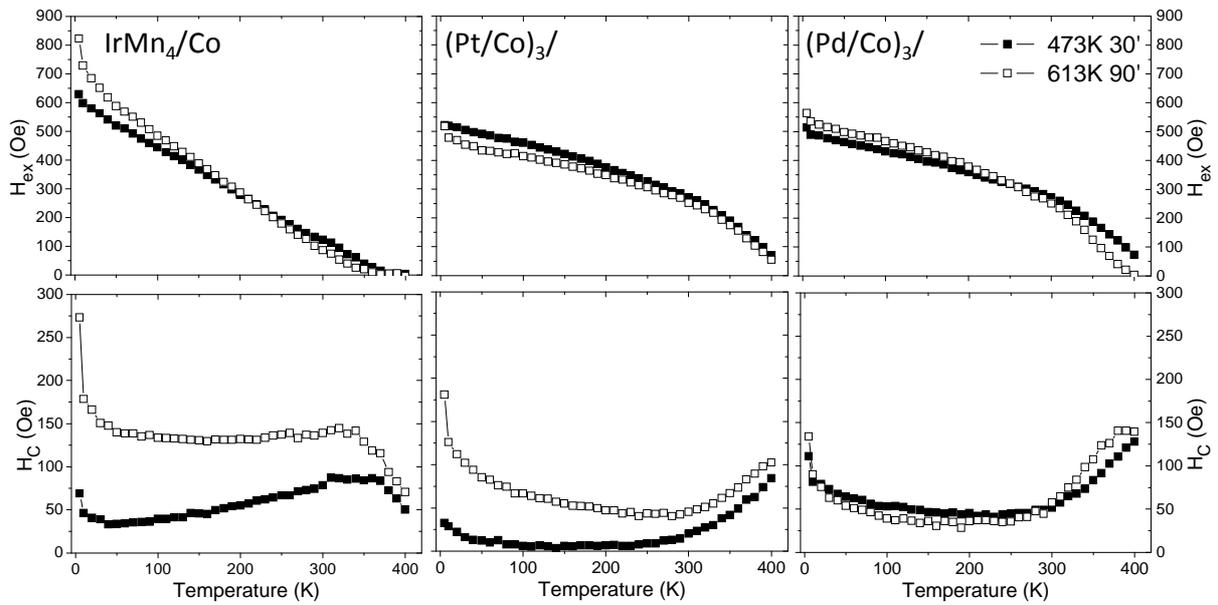


Fig. 5.22 – Temperature dependences of  $H_{ex}$  and  $H_C$  of bilayer and trilayer structures for the two annealing process cases.

$H_{ex}$  curves of the three stacks preserve comparable slopes after annealing at higher temperature. The increase of  $T_B$  in the trilayer stacks compared to the IrMn/Co bilayer is preserved, as the sharpness of the  $H_C$  peak close to  $T_B$  and the larger  $H_{ex}/H_C$  ratios. From Fig.5.19, the ratio at 300 K for the samples annealed at 340°C is 0.6 for the bilayer case, 5.5 for (Pt/Co)<sub>3</sub> trilayer and 4.3 for (Pd/Co)<sub>3</sub> trilayer.

These results confirm that the two investigated trilayer structures maintain their enhanced properties also after annealing at high temperature. For this reason, they are valuable candidates to improve the data retention and writing reliability of TA-MRAM cells.

## 5.6 Conclusions of the chapter

This chapter showed a study on trilayer structures composed by an IrMn layer coupled from one side with a Co layer and on the other side with (Pt/Co) or (Pd/Co) multilayers, having the two F layers crossed-axis magnetic orientation. Trilayer structures were exchange biased with an in-plane setting field and compared with IrMn/Co bilayers.

The proposed trilayer structure show a series of improvements compared to the bilayer one. Firstly, the critical IrMn thickness  $t_C$  is reduced, as well as the exchange peak value  $t_M$  in the  $H_{ex}(t_{IrMn})$  curve. The maximum value of exchange obtained for both trilayers is larger than the one on the IrMn/Co stack. These enhancements at room temperature go together with improved thermal properties. In the thin IrMn range, i.e. where these enhancements take place, an increase of the blocking temperature is observed. In addition, the trilayer structures

present a concave variation of  $H_{ex}(T)$  instead of the usual linear or convex behaviour observed in bilayer structures.

These properties have been discussed through a granular model of exchange bias. Together with a variation of the IrMn lattice parameter on the trilayer structures compared to the bilayer one, which affects its anisotropy, the additional out-of-plane layer is responsible for two effects. The first effect is an indirect grain coupling, which homogenized the behaviour in temperature and stabilized otherwise thermally unstable grains. The second effect is a canting effect of the IrMn spins from one interface to the other, which reduced the IrMn/Co interface coupling thus reducing the IrMn spin reversal critical volume.

The presented trilayer structures show properties that are interesting for technological application. The homogenized blocking temperature distribution and the concave  $H_{ex}(T)$  variation make them suitable for TA-MRAM application. They also offer a number of advantages in TMR heads in terms of total stack thickness and stability of pinning at very small dimensions. These properties are maintained after an annealing at temperatures compatible with the annealing required for proper crystallization of MgO based magnetic tunnel junctions. For these reasons, (Pt/Co)<sub>3</sub>/IrMn/Co and (Pd/Co)<sub>3</sub>/IrMn/Co trilayers are very good candidates for technological applications as storage layer in TA-MRAM systems and pinning layer in TMR heads.

The presented study led to the publication of two articles, respectively on IEEE Magnetic Letters [26] and Journal of Physics D: Applied Physics [46].

## Bibliography

- [1] Carcia P F, Meinhaldt A D and Suna A 1985 *Appl. Phys. Lett.* **47** 178
- [2] Carcia P F 1988 *J. Appl. Phys.* **63** 5066
- [3] den Broeder F J A, Kuiper D, van de Mosselaar A P and Hoving W 1988 *Phys. Rev. Lett.* **60** 2769
- [4] Néel L 1954 *J. Phys. Rad.* **15** 225
- [5] Johnson M T, Bloemen P J H, den Broeder F J A and de Vries J J E 1996 *Rep. Prog. Phys.* **59** 1409
- [6] Bandiera S 2011 *Thèse Université de Grenoble*
- [7] Buda L D, Prejbeanu I L, Ebels U and Ounadjela K 2002 *Comp. Mat. Sci.* **24** 181
- [8] Miramond C, Fermon C, Rousseaux F, Decanini D and Carcenac F 1997 *J. Magn. Magn. Mat.* **165** 500
- [9] Draaisma H J G, den Broeder F J A and de Jonge W J M 1988 *J. Appl. Phys.* **63** 3479
- [10] Hashimoto S, Ochiai Y and Aso K 1989 *J. Appl. Phys.* **66** 4909
- [11] Lechevallier L, Zarefy A, Letellier F, Lardé R, Blavette D, Le Breton J, Baltz V, Rodmacq B and Dieny B 2012 *J. Appl. Phys.* **112** 043904
- [12] Rhee J R 2007 *J. Appl. Phys.* **101** 09E523
- [13] Sort J, Baltz V, Garcia F, Rodmacq B and Dieny B 2005 *Phys. Rev. B* **71** 054411
- [14] van Dijken S, Moritz J, Coey J M D 2005 *J. Appl. Phys.* **97** 063907
- [15] Lin L, Thiyagaraiah N, Joo H W, Heo J, Lee K A and Bae S 2010 *Appl. Phys. Lett.* **97** 242514
- [16] Zarefy A, Lechevallier L, Lardé R, Chiron H, Le Breton J M, Baltz V, Rodmacq B and Dieny B 2010 *J. Phys. D: Appl. Phys.* **43** 215004
- [17] Garcia F, Sort J, Rodmacq B, Auffret S and Dieny B 2003 *Appl. Phys. Lett.* **83** 3537
- [18] Liu Y F, Cai J W and He S L 2009 *J. Phys. D: Appl. Phys.* **42** 115002
- [19] Knepper J W and Yang F Y 2005 *Phys. Rev. B* **71** 224403
- [20] Sbiaa R, Bili Z, Ranjbar M, Tan H K, Wong S J, Piramanayagam S N and Chong T C 2010 *J. Appl. Phys.* **107** 103901
- [21] Mauri D, Kay E, Scholl D and Howard J K 1987 *J. Appl. Phys.* **62** 2929
- [22] Ali M, Marrows C H, Al-Jaward M, Hickey B J, Misra A, Nowak U and Usadel K D 2003 *Phys. Rev. B* **68** 214420
- [23] Xi H and White R M 2000 *Phys. Rev. B* **61** 1318
- [24] Jungblut R, Coehoorn R, Johnson M T, aan de Stegge J and Reinders A 1994 *J. Appl. Phys.* **75** 6659
- [25] Malozemoff A P 1987 *Phys. Rev. B* **37** 7673
- [26] Moritz J, **Vinai G** and Dieny B 2012 *IEEE Magn. Lett.* **3** 4000244
- [27] Nogués J and Schuller I K 1999 *J. Magn. Magn. Mat.* **192** 203

- [28] Meiklejohn W H and Bean C P 1957 *Phys. Rev.* **105** 904
- [29] Tsang C and Lee K 1982 *J. Appl. Phys.* **53** 2605
- [30] Soeya S, Imagawa T, Mitsuoka S and Narishige S 1994 *J. Appl. Phys.* **76** 5356
- [31] Baltz V, Rodmacq B, Zarefy A, Lechevallier L and Dieny B 2010 *Phys. Rev. B* **81** 052404
- [32] Vallejo-Fernandez G, Fernandez-Outon L E and O'Grady K 2008 *J. Phys. D: Appl. Phys.* **41** 112001
- [33] Tomeno I, Fuke H N, Iwasaki H, Sahashi M and Tsunoda Y 1999 *J. Appl. Phys.* **86** 3853
- [34] Martien D, Takano K, Berkowitz A E and Smith D J 1999 *Appl. Phys. Lett.* **74** 1314
- [35] Takano K, Kodama R H, Berkowitz A E, Cao W and Thomas G 1997 *Phys. Rev. Lett.* **79** 1130
- [36] Nozières J P, Jaren S, Zhang Y B, Zeltser A, Pentek K and Speriosu V S 2000 *J. Appl. Phys.* **87** 3920
- [37] Baltz V 2013 *Appl. Phys. Lett.* **102** 062410
- [38] Anderson G, Huai Y and Milosawsky L 2000 *J. Appl. Phys.* **87** 6989
- [39] O'Grady K, Fernandez-Outon L E and Vallejo-Fernandez G 2010 *J. Magn. Magn. Mat.* **322** 883
- [40] Fulcomer E and Charap S H 1972 *J. Appl. Phys.* **43** 4190
- [41] Nogués J, Stepanow S, Bollero A, Sort J, Dieny B, Nolting F and Gambardella P 2009 *Appl. Phys. Lett.* **95** 152515
- [42] Moritz J, Bacher P, Auffret S and Dieny B 2011 *J. Magn. Magn. Mater.* **323** 2391
- [43] Prejbeanu I L, Bandiera S, Alvarez-Hérault J, Sousa R C, Dieny B and Nozières J P 2013 *J. Phys. D: Appl. Phys.* **46** 074002
- [44] Yakushiji K, Saruya T, Kubota H, Fukushima A, Nagahama T, Yuasa S and Ando K 2010 *Appl. Phys. Lett.* **97**, 232508
- [45] Djayaprawira D D, Tsunekawa K, Nagai M, Maehara H, Yamagata S, Watanabe N, Yuasa S, Suzuki Y and Ando K 2005 *Appl. Phys. Lett.* **86** 092502
- [46] **Vinai G**, Moritz J, Bandiera S, Prejbeanu I L and Dieny B 2013 *J. Phys. D: Appl. Phys.* **46** 322001

# Chapter 6

## Cu dusting at IrMn/Co interface in bilayer and trilayer structures

This chapter will present the study of the effects of the insertion of a Cu ultrathin layer at the IrMn/Co interface. In contrast to what it is usually done in the literature, instead of analysing the long-range effects of a thin interlayer, the study is focused on the effects of a few Angstrom thick interlayer on exchange bias field, in order to observe if the reduced interface coupling could have some beneficial effects. The study is performed on IrMn/Co bilayers and on the (Pt(Pd)/Co)/IrMn/Co trilayer structures presented in the previous chapter. A model based on the reduction of interface coupling is proposed.

### 6.1 Long range exchange bias: an open question

In 1997 Gökemeijer *et al.* [1] studied the exchange bias properties of NiFe/CoO layers in presence of a noble metal spacer (Cu, Au and Ag). Quite surprisingly, the loop shift was maintained even in presence of a few nm thick spacer at the interface (see Fig. 6.1a). The  $H_{ex}$  evolution as a function of the interlayer thickness fitted with an exponential decrease of the interface coupling, whose decay was spacer dependent. This result was the first evidence that exchange bias can be a long range interaction.

Since then, numerous experiments have been carried out to analyse the long range effect of exchange coupling, with contradictory results. Thomas *et al.* [2] measured a vanishing of  $H_{ex}$  for 1nm thick spacers. Because of the reduced interlayer thickness, they asserted that exchange bias is not a long range coupling, and the loop shift persistence for few Angstrom interlayer was due to pinholes. Wang *et al.* [3] measured a blocking temperature decrease in FeMn/Cu/Co with increasing Cu thickness, and a non-monotonic bias dependence of spacer thickness at low temperature. Yanson *et al.* [4] confirmed the  $H_{ex}$  exponential

decrease for Cr interlayer together with a coercivity drop, but no blocking temperature dependence on the spacer thickness. Oscillatory exchange interaction for thick interlayer has been reported for FeNi/Cu(Cr)/FeMn structures [5] and when Cu is inserted in the FeMn layer [6].

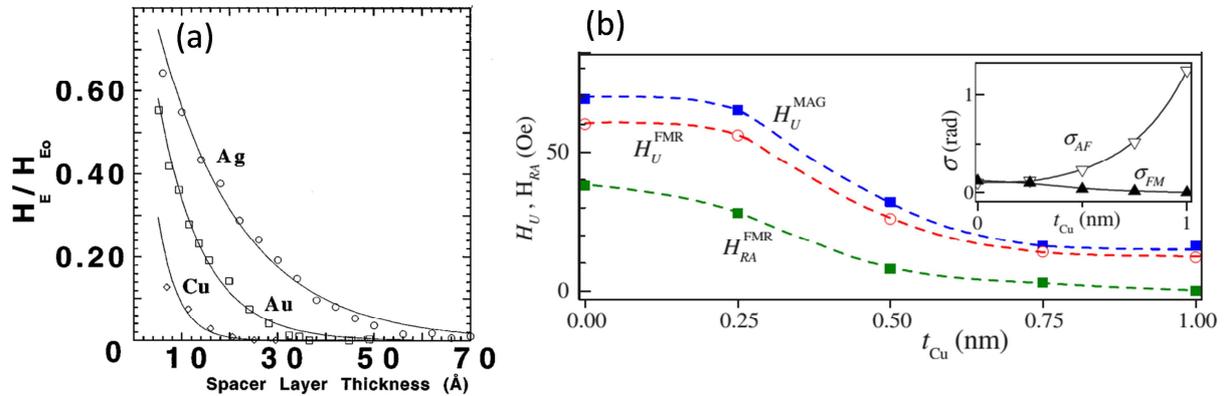


Fig. 6.1 – Exchange bias curves as a function of interlayer thickness in [1] and [9].

All the cited articles are focused on the exchange bias properties in presence of a (relatively) thick interlayer, in order to study the long range behaviour of exchange bias. Nonetheless, some studies analysed the exchange bias properties in presence of an ultrathin interlayer ( $< 1$  nm), showing an enhancement of the hysteresis loop. Ali *et al.* [7] measured it for Pt and Cu ultrathin interlayers in IrMn/Co based spin valve structures; Liu *et al.* [8] for Pt spacer in NiFe/FeMn layers. Whereas Pt may form PtMn at the interface, the effect of Cu was not clear, also because other studies [1,9,10] showed a bias drop (see Fig. 6.1b). An ultrathin Ta interlayer is sufficient to drop the exchange coupling to zero [7,11]. By combining Pt and Cu interlayer, it has been observed that exchange bias could persist for an interlayer thickness up to 6 nm [12]. Finally, an  $H_{ex}$  enhancement has been observed by doping the IrMn/CoFe interface with Mn [13,14].

In our study, a Cu interlayer at the IrMn/Co interface has been inserted for thicknesses ranging from 0.1 to 1 nm, in different conditions. Main attention will be focused on the ultrathin spacer regime, when the Cu layer is not yet continuous but simply a dusting layer.

## 6.2 Cu interlayer in IrMn/Co bilayers

Cu interlayer effect was first studied on IrMn/Co bilayers, for different buffering layer thicknesses and IrMn thicknesses. In this chapter, the microstructural analysis, the effects on exchange bias and on blocking temperature will be described.

### 6.2.1 Effects on exchange bias

The stacks considered were:  $\text{Ta}_3/\text{Cu}_x/\text{IrMn}_{12}/\text{Cu}_y/\text{Co}_5/\text{Pt}_2$ , for a 2 and 12 nm thick Cu buffer layer and  $\text{Ta}_3/\text{Cu}_2/\text{IrMn}_4/\text{Cu}_x/\text{Co}_5/\text{Pt}_2$  with a Cu interlayer thickness ranging from 0 to 1 nm. Thick IrMn layer was chosen to facilitate the microstructural analysis by AFM, whereas 4nm IrMn layer was chosen to be compared with (Pt(Pd)/Co)/IrMn/Co trilayer structures in the exchange bias enhancement regime. All samples were annealed at 200°C for 30' under 2000 Oe applied in-plane field.

Fig.6.2 shows the evolution of exchange bias and coercivity as a function of Cu interlayer thickness in the thick IrMn regime at room temperature. Error bars on the  $x$  axis take into account the uncertainty due to the opening and closing of the shutter during the Cu deposition. It can be observed how, for Cu interlayer thicknesses below 0.3 nm,  $H_{ex}$  increases up to 50%, with a maximum reached at 0.1 nm. This regime of exchange bias enhancement takes place for Cu thicknesses so low that the spacer cannot be considered yet a continuous layer [7] (since a Cu monolayer is around 0.2 nm thick), but simply a dusting layer. For this reason, it will be defined as the *dusting regime*.

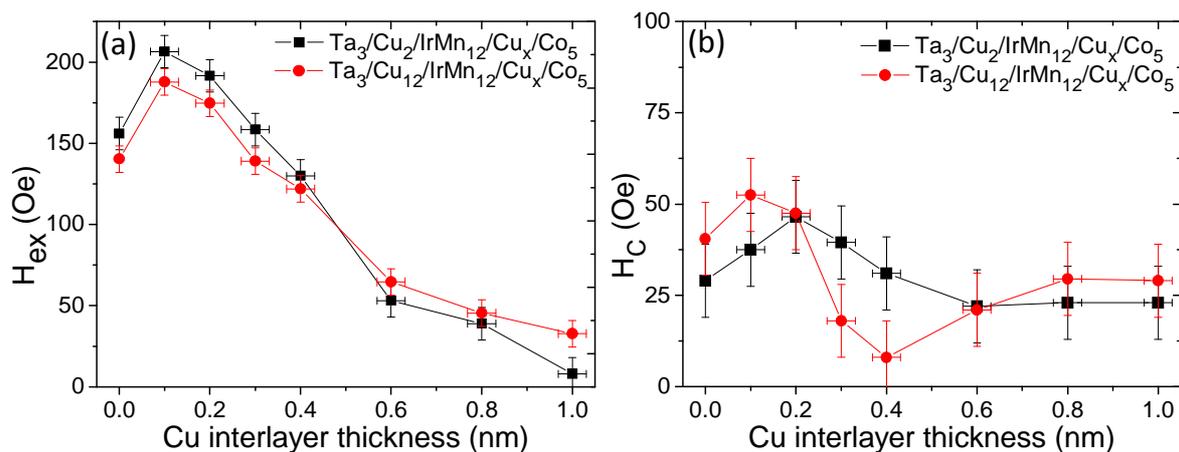


**Fig. 6.2** – Exchange bias  $H_{ex}$  (a) and coercivity  $H_C$  (b) as a function of Cu interlayer thickness for 12 nm IrMn layer, for two Cu buffer layer thicknesses (2 nm in square black and 12 nm in round red).

Compared to the study of [9] shown in Fig.6.1b, which presents a very similar stack with 15nm thick IrMn layer, our samples include thinner Cu interlayers (between 0 and 0.3 nm), allowing observing the exchange bias enhancement in the dusting regime. Once the Cu thickness is increased, exchange bias drops, going close to zero at 1nm thickness. No buffer layer effect is observed, as well as no trend in coercivity.

In Fig.6.3a, the exchange bias and coercivity curves are shown as a function of Cu interlayer thickness for the 4 nm IrMn case, at room temperature.  $H_{ex}$  follows the same trend, with an enhancement in the dusting regime and a drop in the continuous regime. On the other

hand, coercivity has a similar behaviour compared to the exchange bias, with an important decrease in the continuous regime (see Fig.6.3b).

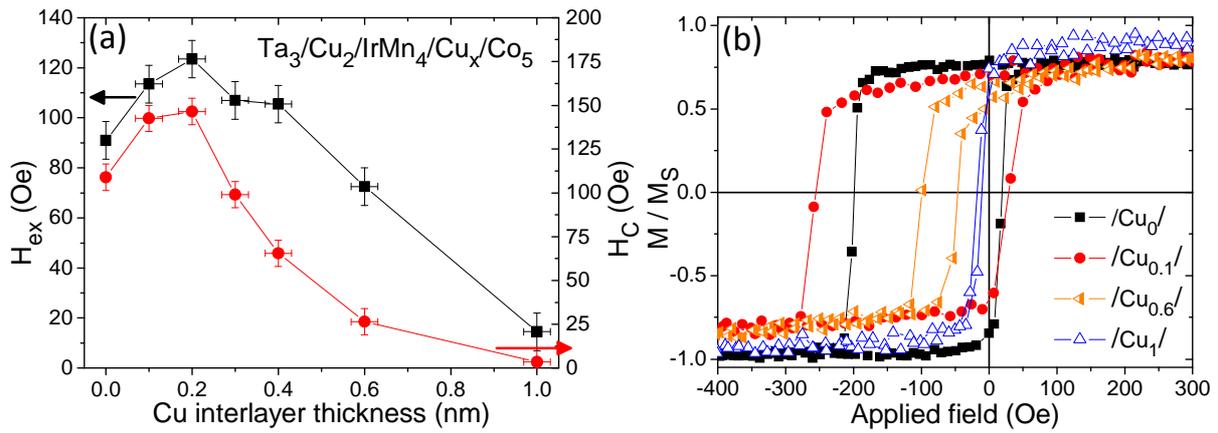


**Fig. 6.3** – (a) Exchange bias  $H_{ex}$  and coercivity  $H_C$  as a function of Cu interlayer thickness for a 4 nm thick IrMn layer. (b) Corresponding hysteresis loops for different Cu interlayer thicknesses measured at room temperature.

Samples with thick IrMn layer were measured in the as deposited state, in order to observe the influence of the Cu spacer on the IrMn/Co interface before pinning the F layer through the annealing field cooling procedure. Fig.6.4 shows the hysteresis loops for three different Cu interlayer thicknesses. For the case with no interlayer and in the dusting regime (Fig.6.4a and Fig.6.4b), the loops present the typical shape of biased IrMn/Co bilayers before annealing: the AF domains, oppositely oriented, imprint on the F layer during the deposition [15]. On the other hand, in the continuous regime (Fig.6.4c, black squares) the loops become more and more rectangular. In this continuous regime, the measured loops become similar to the loops measured on a single Co layer ( $Ta_3/Cu_2/Co_5/Pt_2$ ) (in red in Fig.6.4c), thus marking a progressive decoupling between IrMn and Co layers because of the increased Cu thickness.

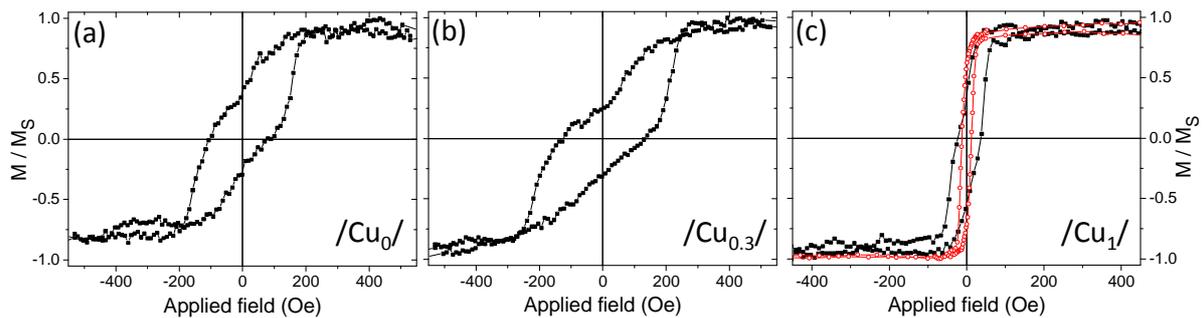


**Fig. 6.4** – Hysteresis loops of as deposited samples for no interlayer (a), 0.3 nm (b) and 1 nm (c) Cu interlayer. In (c) the  $M(H)$  loop of a sample without IrMn layer is shown in open red circles.

### 6.2.2 Microstructural analysis

In order to understand the variation of exchange bias in presence of Cu interlayer, the effect of the Cu insertion on the microstructural properties of the AF layer has to be investigated. Whereas its presence has no reason to affect the IrMn crystallographic growth, its effect on the grain size population and distribution is not known and has to be investigated. In order to do that, Atomic Force Microscope (AFM) scans were taken on IrMn/Cu/Co structures, for two extreme cases: no interlayer and 1nm thick Cu spacer. Measurements were performed on samples with 12 nm thick IrMn, after annealing. The same technique used in Chapters 4 and 5 has been followed for these measurements. Fig.6.5 shows the normalized grain distribution after measuring over 200 grains per sample. It can be observed how, despite the large thickness of the Cu interlayer the IrMn average grain size is not particularly affected ( $10.1 \pm 0.1$  nm for 0 nm Cu,  $10.5 \pm 0.1$  nm for 1 nm Cu), neither is the distribution width.

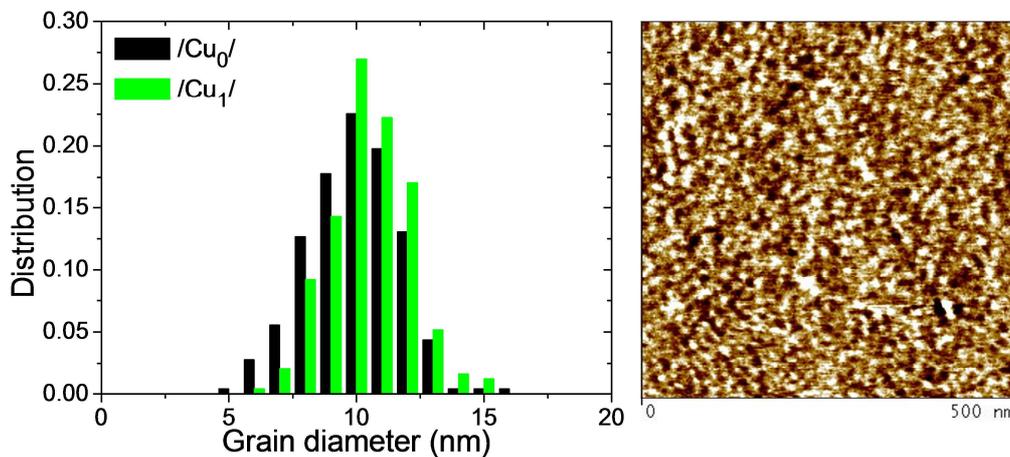


**Fig. 6.5** – Normalized grain distribution for IrMn<sub>12</sub>/Cu<sub>x</sub>/Co<sub>5</sub> bilayers for x = 0 and 1 nm (on the left), with the AFM scan for the Cu<sub>1</sub> sample (on the right).

It results that the presence of a thin Cu layer at the IrMn/Co interface has minor effects on the grain size population in the AF layer. This result is coherent with the one published in [16], where the distribution of sputtered IrMn grains in presence of different Cu impurity percentages appeared unchanged.

### 6.2.3 Effects on blocking temperature

As for the exchange enhancement of Chapter 5, it is interesting to observe the consequences of the  $H_{ex}$  variation at room temperature on the thermal stability at higher temperature, in particular on the blocking temperature. Moreover, this is a controversial subject in the long range exchange bias domain, where oscillations in temperature or  $T_B$  variations in presence of a spacer have been observed.

Samples were measured in temperature with the maximum blocking temperature procedure, as already described in Paragraph 5.3. In case of samples with 12 nm thick IrMn layer, because of their higher blocking temperature compared to thinner IrMn layers, we expected values of  $T_B$  too high to be measured by the VSM used in Chapter 5. Thus, measurements were performed with an ADE VSM, which allowed reaching a maximum temperature of around 250°C under an Ar gas flow, starting from a room temperature measurement. Fig.6.6 shows the evolution of exchange bias and coercivity as function of temperature for the  $Ta_3/Cu_2/IrMn_{12}/Cu_x/Co_5/Pt_2$  series, for different Cu interlayer thicknesses. It can be observed how, in the dusting regime ( $x < 0.4$  nm), the exchange bias decrease in temperature follows a slope similar to the one present for the case with no spacer. The larger exchange bias at room temperature gives thus an increased blocking temperature increases. It can be observed quite clearly from Fig.6.6b, where the coercivity peak for the samples with Cu dusting is shifted at higher temperatures, for a  $T_B$  variation of about 50°C.

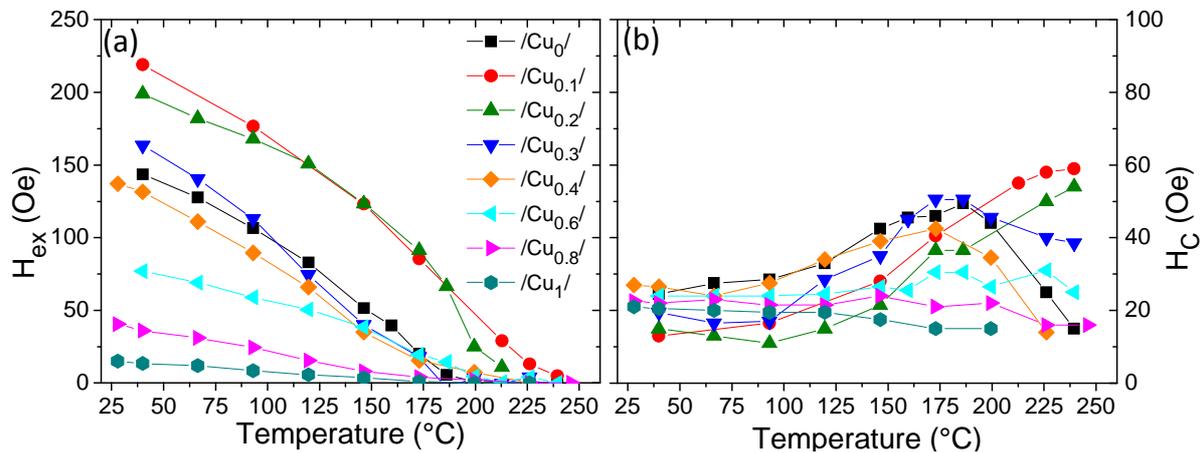


**Fig. 6.6** – Exchange bias (a) and coercivity (b) evolution as a function of temperature for  $IrMn_{12}/Cu_x/Co_5$  bilayers at high temperature.

On the other hand, when the continuous regime is reached ( $x > 0.4$  nm), the  $H_{ex}$  decrease in temperature is much smoother. As a consequence, despite the lower  $H_{ex}$  at room temperature, the  $T_B$  in this range is close to the one of the case with no interlayer.

When considering the temperature range from 5 to 400 K, this tendency is confirmed in the whole curve. From Fig.6.7 it appears that in the dusting range the  $H_{ex}$  decrease in temperature follows the same slope of the simple bilayer case, whereas in the continuous regime a slow reduction of exchange bias takes place. Because of the large values of  $T_B$ , this temperature range is not large enough to observe the coercivity peak, which would help determining the maximum blocking temperature.

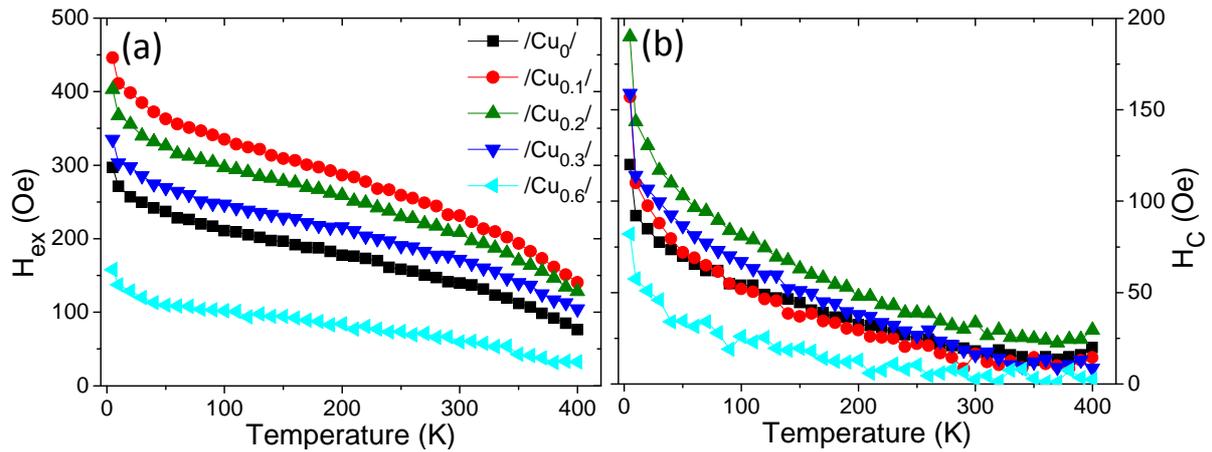


**Fig. 6.7** – Exchange bias (a) and coercivity (b) evolution as a function of temperature for IrMn<sub>12</sub>/Cu<sub>x</sub>/Co<sub>5</sub> bilayers.

In the case of thin (4 nm) IrMn this behaviour in temperature for the dusting regime appears less clearly. By considering a full range of temperatures from 5 to 400 K, it can be observed from Fig.6.8a that in the Cu dusting regime, the  $H_{ex}$  enhancement compared to the simple bilayer case decreases constantly with temperature instead of remaining quite constant like in the thick IrMn case of Fig.6.7a.

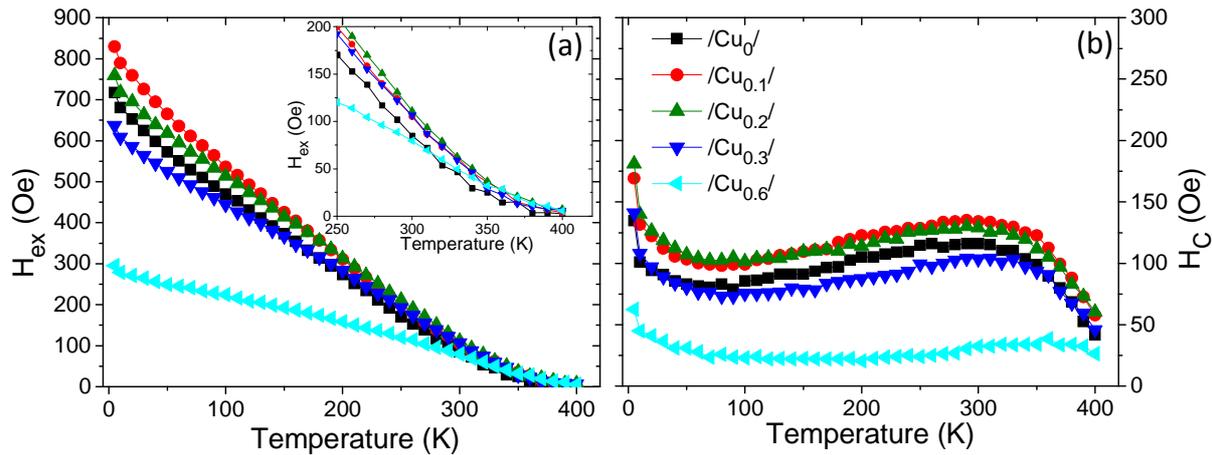


**Fig. 6.8** – Exchange bias (a) and coercivity (b) evolution as a function of temperature for IrMn<sub>4</sub>/Cu<sub>x</sub>/Co<sub>5</sub> bilayers. In (a) the inset shows the  $H_{ex}$  evolution close to  $T_B$ .

The inset of Fig.6.8a shows how the exchange bias for all thicknesses tends to converge to zero at similar temperatures; this behaviour is confirmed by the coercivity curves in temperature of Fig.6.8b.

In order to understand better the differences in blocking temperature in the thick IrMn case, some samples were annealed at 200°C for 150', instead of the usual 30'. The aim of a longer annealing is to favour the interface coupling between IrMn and Co spins, despite the presence of the Cu interlayer. As it can be noticed from Fig.6.9, the longer annealing has no effect for the thinnest Cu interlayer, whereas the blocking temperature is increased for thicker spacers. Fig.6.9b shows the case corresponding to the 0.3 nm thick Cu interlayer, with a  $T_B$

shift of around 30°C. Similar behaviour is observed for thicker Cu interlayers. The longer annealing process has thus stabilized the interface coupling also in presence of a continuous Cu interlayer. Concerning the discrepancy of thermal behaviour between the bilayers with 4 and 12 nm of IrMn layer thickness, it has to be underlined that the blocking temperature for the 12 nm case often overpasses the annealing temperature. In those range of temperatures it becomes difficult to evaluate the contribution to the exchange due to the coupling set during the annealing process. The origin of the increased  $T_B$  with a Cu dusting layer remains thus unclear.

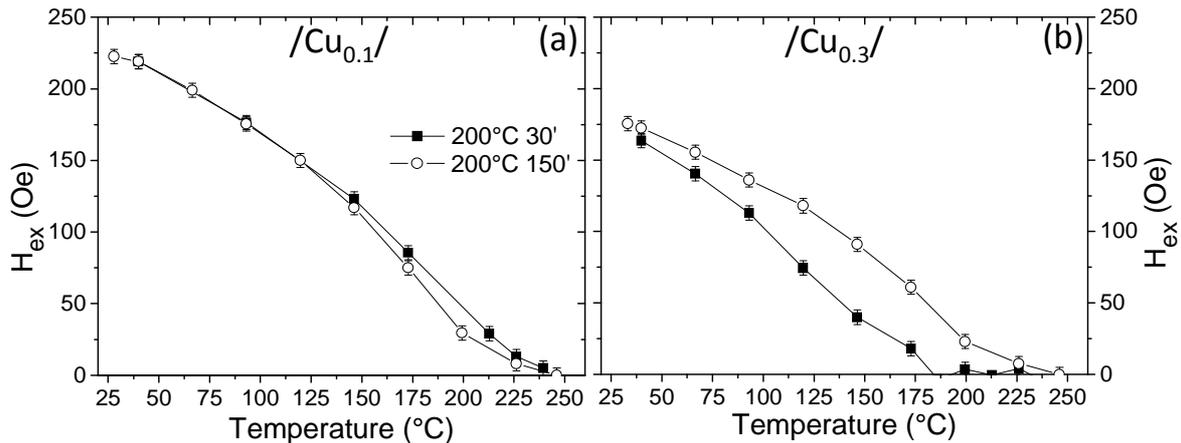


Fig. 6.9 – Exchange bias dependence on temperature for IrMn<sub>12</sub>/Cu<sub>x</sub>/Co<sub>5</sub> bilayers, for 0.1 nm (a) and 0.3 nm (b) Cu thicknesses after 30' (full squares) and 150' (open circles) long annealing at 200°C.

## 6.3 Cu interlayer in (Pt(Pd)/Co)<sub>3</sub>/IrMn/Co trilayers

Due to the positive impact of the Cu dusting layer on  $H_{ex}$  and  $T_B$ , we wanted to verify if the same beneficial effects could be obtained also in the case of the (Pt(Pd)/Co)/IrMn/Co trilayer structure, in order to couple the increase of exchange bias given by the Cu dusting layer with the positive effects given by the additional coupling with the perpendicular multilayer.

### 6.3.1 Effects on exchange bias

Cu dusting was thus inserted into the trilayer structures presented in Chapter 5. The corresponding stacks were (thicknesses in nm):

Ta<sub>3</sub>/(Pt<sub>1.8</sub>/Co<sub>0.6</sub>)<sub>3</sub>/IrMn<sub>4</sub>/Cu<sub>x</sub>/Co<sub>5</sub>/Pt<sub>2</sub> and Ta<sub>3</sub>/(Pd<sub>1.8</sub>/Co<sub>0.6</sub>)<sub>3</sub>/IrMn<sub>4</sub>/Cu<sub>x</sub>/Co<sub>5</sub>/Pt<sub>2</sub>, with x ranging from 0 to 1 nm.

After an in-plane applied field annealing at 200°C for 30' with an in-plane cooling field of 2000 Oe, the VSM measurement of hysteresis loops at room temperature gave the  $H_{ex}(t_{Cu})$  curve shown in Fig.6.10. In the figure, these curves are compared with the corresponding ones obtained for the bilayer stacks.

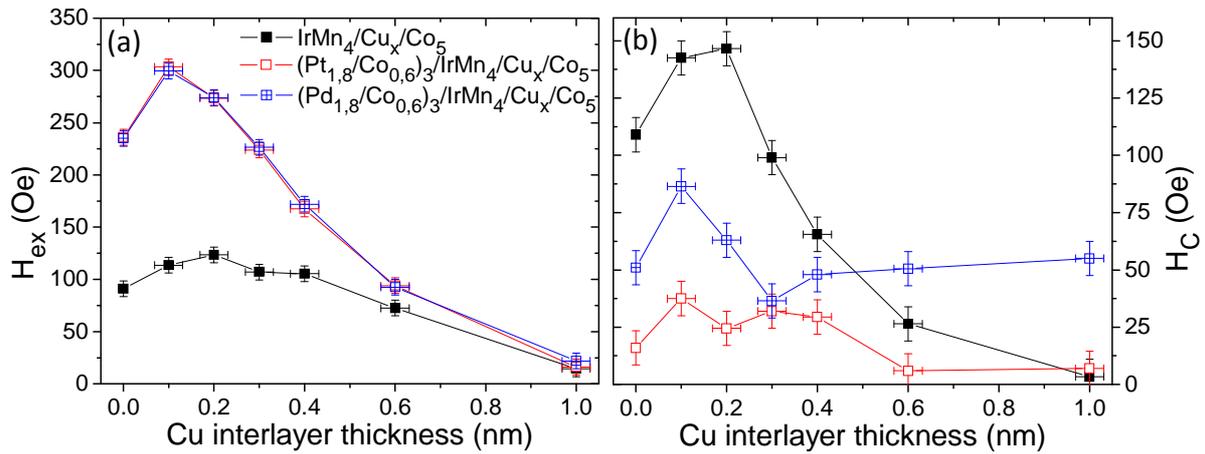


Fig. 6.10 – Exchange bias (a) and coercivity (b) evolution as a function of the Cu interlayer thickness.

If the maximum value of exchange for the trilayer stacks with Cu interlayer (i.e. for a Cu layer thickness of 0.1 nm) is compared to the value of the initial IrMn/Co bilayer stack, the  $H_{ex}$  value has been increased of three times without changing the thickness of either the F or the AF layers. When a thin Cu interlayer (below 0.3 nm thick Cu, i.e. in the dusting regime) is added at the IrMn/Co interface, the exchange bias increases for all the three stacks: the effect is then confirmed also in the trilayer structure. For thicker Cu spacer,  $H_{ex}$  decreases down to vanishing for a 1 nm thick Cu interlayer. Concerning the coercivity, trilayer structures present reduced  $H_C$  compared to the bilayer case in absence of Cu interlayer. In the Cu dusting and continuous regime, no particular trend in  $H_C$  is observed, in contrast to the bilayer case. Fig.6.11 shows the corresponding hysteresis loops at room temperature for the  $Ta_3/(Pt_{1.8}/Co_{0.6})_3/IrMn_4/Cu_x/Co_5/Pt_2$  series.

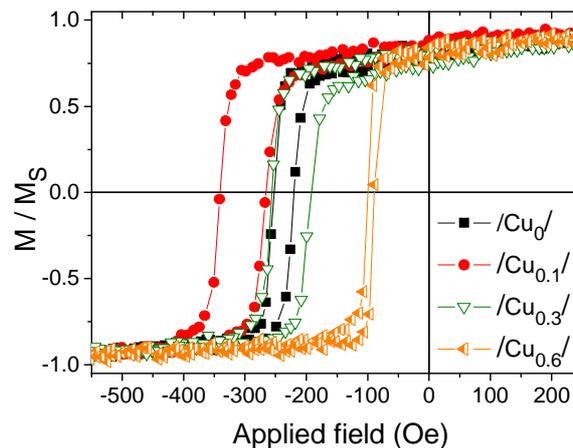


Fig. 6.11 – Hysteresis loops of  $Ta_3/(Pt_{1.8}/Co_{0.6})_3/IrMn_4/Cu_x/Co_5/Pt_2$  series at room temperature for different Cu interlayer thicknesses.

For the trilayer systems, because of the identical IrMn grain population compared to equivalent bilayer systems, it can be assumed that, as for the bilayer case shown in Fig.6.5, the presence of Cu at the IrMn/Co interface does not affect the micromagnetic structure of the

AF layer. So, also for the trilayer series, the variation of  $H_{ex}$  in the dusting regime cannot be due to a variation of the IrMn grain distribution.

### 6.3.2 Effects on blocking temperature

The exchange bias properties of the  $Ta_3/(Pt_{1.8}/Co_{0.6})_3/IrMn_4/Cu_x/Co_5/Pt_2$  series were then analysed as a function of temperature. Fig.6.12 shows the evolution of the corresponding exchange bias and coercivity values as function of temperature. The  $H_{ex}(T)$  behaviour is similar to the one observed for the corresponding bilayer case of Fig.6.8: the exchange enhancement in the dusting regime is important at low temperatures, and tends to disappear when approaching the blocking temperature, as it can be seen in the inset of Fig.6.12a. This is confirmed by the coercivity curve shown in Fig.6.12b: even if the coercivity peaks cannot be observed because of the high  $T_B$ , they start appearing at similar temperatures for all samples.

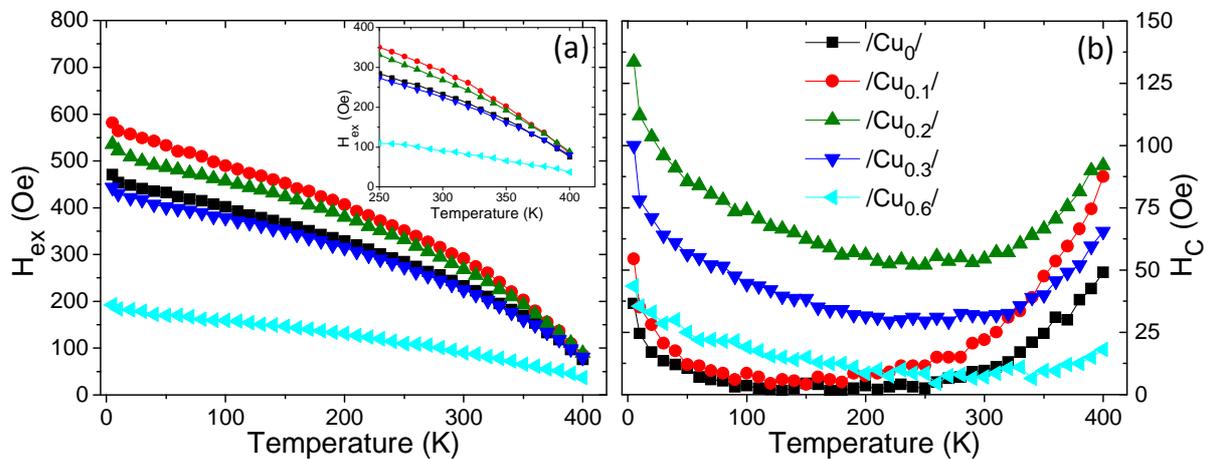


**Fig. 6.12** – Exchange bias (a) and coercivity (b) evolution as a function of temperature for  $Ta_3/(Pt_{1.8}/Co_{0.6})_3/IrMn_4/Cu_x/Co_5/Pt_2$  trilayers. In (a) the inset shows the  $H_{ex}$  evolution close to  $T_B$ .

One final important remark is that, in the dusting regime, the  $H_{ex}(T)$  curve maintains its concave shape, as in the case with no Cu interlayer. As reported in the previous Chapter, this characteristic in temperature is one of the key advantages of the trilayer structures, particularly interesting for technological applications. The fact that the same shape is maintained in presence of the Cu dusting layer make the implemented stack suitable for applications. The effect is much less pronounced in the continuous regime, where the low loop shift makes the concave shape less notable.

When comparing trilayer and bilayer structures, the blocking temperature enhancement is confirmed for all Cu interlayer thicknesses. This means that the stabilizing effect of the out-of-plane layer is not affected by the reduced interface coupling due to the presence of the Cu spacer at the IrMn/Co interface.

## 6.4 Discussion

This paragraph will focus on the Cu interlayer dusting regime, analysing different hypothesis on the origin of the exchange bias increase compared to the IrMn/Co interface case.

Firstly, one of the reasons of the good exchange properties in presence of a Cu interlayer is relatively its good crystallographic properties. As shown in Chapter 4, Cu, IrMn and Co all present a (111) fcc structure. The Cu lattice parameter is in between those of IrMn and Co (Fig.4.23), thus it is a good buffer layer also for Co, whose crystalline growth is not affected by the additional layer. This would not be the case for example for Ta, whose amorphous structure does not allow the following layers to correctly grow (Fig.4.24). Indeed, in case of Ta interlayer the exchange bias drops dramatically to zero [7,11].

Together with its crystallographic properties, Cu acts as a diffusion barrier for Mn between IrMn and Co. Despite the complexity of diffusion barrier phenomena [17], some considerations can still be done. Mn and Co are highly miscible [18]: indeed intermixing takes place already during deposition and worsens after annealing [19]. A reduction of the diffusion has shown to increase the exchange bias properties on perpendicular structures; this was done by adding a thin Pt layer at the (Pt/Co)/IrMn interface [19,20]. It can be assumed that a similar benefit can happen in this case, with Cu acting as barrier diffusion interlayer for IrMn/Co in-plane structures. Concerning Co and Cu, they are almost immiscible [22], thus no additional diffusion of Cu into Co has to be taken into account. On the other hand, Cu and Mn are miscible [23], and the possibility of creating  $\text{IrMn}_{1-x}\text{Cu}_x$  diluted structures has already been studied in the literature [16,24]. However, a reduction of  $H_{ex}$  was observed in case of diluted structures deposited by sputtering [16], contrarily to the case of samples deposited by molecular beam epitaxy [24], where exchange bias increased on diluted structures. It has to be underlined, anyway, that in the epitaxial samples the grain size was way larger than the one present in sputtered systems, and the diluted samples presented smaller grains compared to the reference sample. The difference between the two systems (sputtered [16] and epitaxial [24]) has been modelled in [25,26]. Returning on sputtered systems, the study of ref.[7] addressed systems containing an interlayer within the AF layer at a varying distance  $x$  from the F/AF interface. If the interlayers (Cu, Ta, Pt and Au) were deposited few Angstroms far from the F/AF interface, exchange bias presented a drop compared to the value obtained if they were deposited at the interface. For these reasons, we can assume that the Cu-Mn intermixing and diffusion in the Cu dusting regime takes place close to the interface, giving a

very low  $\text{IrMn}_{1-x}\text{Cu}_x$  dilution rate in the whole IrMn thickness. Finally, it has to be remembered that the formation of Cu and Mn clusters at the interface can create, for Mn percentages over 80%, a different AF phase, having a much lower Néel temperature, below 300 K [27].

Another possible explanation can be taken from the granular model presented in Chapter 1 and applied for the trilayer systems in Chapter 5. The presence of a dusting non-magnetic layer at the F/AF interface locally reduces the interface coupling between IrMn and Co, thus reducing the critical volume  $V_C$  in a manner similar to the canting effect, as schematized in Fig.6.13. In the case of the trilayer structure, the coexistence of spin canting and reduced interface coupling would both contribute to stabilize the AF grains during the magnetization reversal.

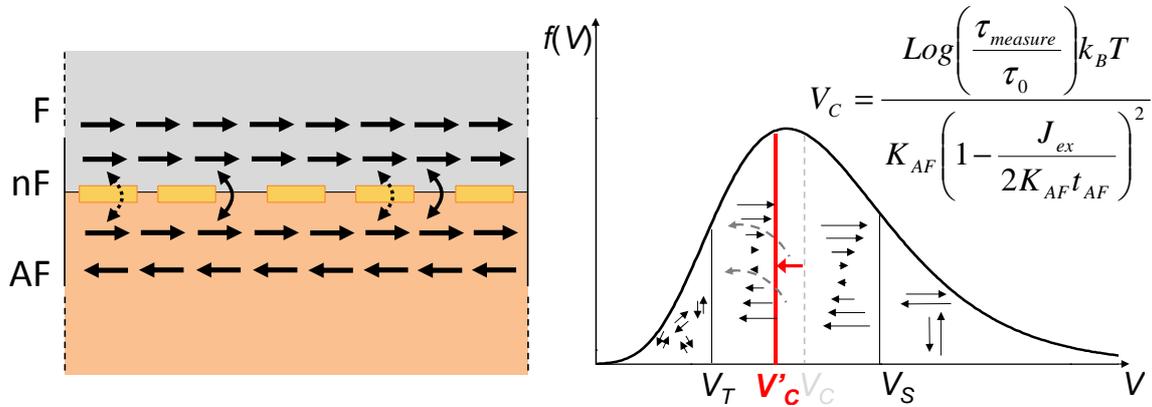


**Fig. 6.13** – On the left, sketch of the interface coupling in presence of a non-magnetic dusting layer at the interface. Dusted curve arrows mark reduced interface coupling. On the right, the granular model with Eq.1.26.

The possibility of increasing the exchange in presence of a non continuous layer at the interface has been observed and simulated for NiO/Au/Co structures [27], where the stability condition  $K_{AF} t_{AF} \gg J_{ex}$  of the Meiklejohn model (see Paragraph 1.2.1) is substituted by  $K_{AF} t_{AF} \gg J_{ex} (1 - S_{cluster})$ , with  $S_{cluster}$  defined as the fraction of the interface covered by Au cluster (which correspond to the orange Cu rectangles at the F/AF interface in Fig.6.13). A similar model can be used in this case. When the Cu layer is further increased so that the Cu layer becomes continuous the interface coupling starts decreasing. In this case, the reduced local interfacial coupling yields a reduction of the loop shift. This is due to the fact that the interfacial coupling gets so small that the AF layer becomes less efficient in pinning the F layer during magnetization reversal.

Finally, another possible effect is a reduction of interfacial frustration of the IrMn spins due to the presence of Cu clusters. As described by Malozemoff [28], the interfacial

roughness between F and AF spins may lead to magnetic frustration, as schematized by Fig.6.14a.

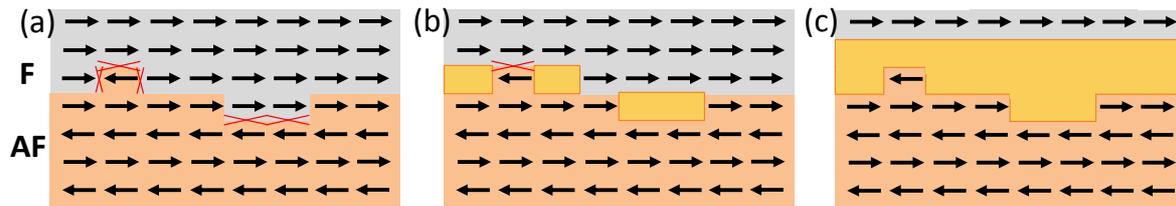


**Fig. 6.14** – (a) Example of a F/AF bilayer with rough interface. The red crosses mark the magnetic frustrations due to bumps, steps and holes. (b) The same rough F/AF interface with non-continuous nF interlayer, which removes partially the frustrations. (c) F/AF interface with continuous nF interlayer. The resulting total coupling is reduced compared to case (a).

This frustration not only affects the value of exchange bias, but also has consequences on coercivity [29] and on the asymmetry of the hysteresis loop [30]. Maximum magnetic frustration is likely to occur at the interface steps. When the Cu particles are deposited on the IrMn layer, they diffuse on the terrace of the rough surface and stick at steps and in the holes, i.e. at zones of maximum magnetic frustration. We can even imagine that the removal of the magnetic frustration can be a driving force in the diffusion of the Cu atoms and that the latter get stabilized wherever the gain in magnetic energy associated with the frustration removal would be the largest. This reduction of interfacial frustration would have positive effects on the effective coupling between F and AF (see Fig.6.14b). Once the Cu layer becomes continuous, the positive effect of reduced frustration is overpassed by the reduced coupling all along the interface, thus causing the drop of exchange bias (see Fig.6.14c).

## 6.5 Conclusions of the chapter

The present chapter has been focused on the exchange bias properties in presence of an ultrathin non-magnetic spacer, nominally a Cu layer whose thickness ranges from 0.1 to 1 nm.

In presence of a non-continuous interfacial layer, exchange biased samples showed an increase of exchange bias compared to the original configuration. This behaviour has been observed independently on the buffer layer thicknesses and IrMn thicknesses for the IrMn/Co bilayer structure and confirmed also on the trilayer structures  $(\text{Pt}_{1.8}/\text{Co}_{0.6})_3/\text{IrMn}_4/\text{Cu}_x/\text{Co}_5$  and  $(\text{Pd}_{1.8}/\text{Co}_{0.6})_3/\text{IrMn}_4/\text{Cu}_x/\text{Co}_5$ . The combination of trilayer system and Cu dusting layer led to an exchange bias value **three times larger** than the one present in the original IrMn/Co bilayer.

In case of thicker Cu layer ( $t_{Cu} > 0.3$  nm), i.e. in presence of a continuous layer, all structures showed a sharp decrease of exchange, going close to zero of 1 nm of Cu spacer, coherently with the results present in the literature.

Concerning the behaviour in temperature, whereas bilayers with 12 nm thick IrMn showed a variation of  $T_B$  in presence of Cu dusting layer, bilayers and trilayers with 4 nm IrMn layer did not show any change in  $T_B$ . This difference may be attributed to the high  $T_B$  of the 12 nm IrMn case, which approaches the annealing temperature thus affecting the evaluation of the  $T_B$  itself.

The increase of  $H_{ex}$  in the Cu dusting regime has been then discussed by comparing the measurements with the different analysis proposed in the literature. Despite the complexity of the interfacial interactions and the range of different parameters playing a role in the quality of the coupling, some hypotheses have been proposed. Cu acts as a good interlayer because of its crystallographic characteristics, compatible with the ones of Co and IrMn. It is also a good barrier against diffusion, separating Mn and Co (highly miscible) without mixing with Co. The creation of CuMn intermixing may create diluted IrMn<sub>1-x</sub>Cu<sub>x</sub> structures, but in the dusting regime the effect is mainly interfacial thus no real diluted system is created. Finally, by using the granular model already described in Chapter 1 and used in Chapter 5, a reduction of the interfacial coupling is proposed. The reduced  $J_{ex}$  at the interface stabilizes AF grains which otherwise would only contribute to the coercivity of the loop; the larger number of stabilized grains thus enhances the value of exchange bias field. Another possible effect responsible of the increased exchange bias on the Cu dusting regime is attributed to a reduction of the interfacial frustration due to Cu particles on bumps and holes at the interface.

This study has been presented at MMM 2013.

## Bibliography

- [1] Gökemeijer N J, Ambrose T and Chien C L 1997 *Phys. Rev. Lett.* **79** 4270
- [2] Thomas L, Kellock A J and Parkin S S P 2000 *J. Appl. Phys.* **87** 5061
- [3] Wang J, Wang W N, Chen X, Zhao H W, Zhao J G and Zhan W Sh 2002 *J. Appl. Phys.* **91** 7236
- [4] Yanson Yu, Petravic O, Westerholt K and Zabel H 2008 *Phys. Rev. B* **78** 205430
- [5] Mewes T, Roos B F P, Demokritov S O and Hillebrands B 2000 *J. Appl. Phys.* **87** 5064
- [6] Cai J W, Lai W Y, Teng J, Shen F, Zhang Z and Mei L M 2004 *Phys. Rev. B* **70** 214428
- [7] Ali M, Marrows C H and Hickey B J 2008 *Phys. Rev. B* **77** 134401
- [8] Liu Y, Jin C, Fu Y Q, Teng J, Li M H, Liu Z Y and Yu G H 2008 *J. Phys. D: Appl. Phys.* **41** 205006
- [9] Geshev J, Nicolodi S, Pereira L G, Nagamine L C C M, Schmidt J E, Deranlot C, Petroff F, Rodríguez-Suárez R L and Azevedo A 2007 *Phys. Rev. B* **75** 214402
- [10] Nicolodi S, Nagamine L C C M, Viegas A D C, Schmidt J E, Pereira L G, Deranlot C, Petroff F and Geshev J 2007 *J. Magn. Magn. Mat.* **316** e975
- [11] Li K, Guo Z, Han G, Qiu J and Wu Y 2003 *J. Appl. Phys.* **93** 6614
- [12] Akmalidinov K, Auffret S, Joumard I, Dieny B and Baltz V 2013 *Appl. Phys. Lett.* **103** 042415
- [13] Tsunoda M, Yoshitaki S, Ashizawa Y, Kim D Y, Mitsumata C and Takahashi M 2007 *Phys. Stat. Sol. (b)* **244** 4470
- [14] Carpenter R, Cramp N C, O'Grady K 2012 *IEEE Trans. Magn.* **48** 4351
- [15] Geshev J, Dias T, Nicolodi S, Cicheler R, Harres A, Acuña J J S, Pereira L G, Schmidt J E, Deranlot C and Petroff F 2011 *J. Phys. D: Appl. Phys.* **44** 095002
- [16] Aley N P, Bonet C, Lafferty B and O'Grady K 2009 *IEEE Trans. Magn.* **45** 3858
- [17] Nicolet M A 1978 *Thin Solid Films* **52** 415
- [18] Tsioplakis K and Gödecke Y 1971 *Metallkunde* **62** 680
- [19] Lechevallier L, Zarefy A, Letellier F, Lardé R, Blavette D, Le Breton J M, Baltz V, Rodmacq B and Dieny B 2012 *J. Appl. Phys.* **112** 043904
- [20] Garcia F, Sort J, Rodmacq B, Auffret S and Dieny B 2003 *Appl. Phys. Lett.* **83** 3537
- [21] Letellier F, Baltz V, Lechevallier L, Lardé R, Jacquot J F, Rodmacq B, Le Breton J M and Dieny B 2012 *J. Phys. D: Appl. Phys.* **45** 275001
- [22] T Nishizawa and K Ishida 1984 *Bukk. Alloy Phase Diagrams* **5** 161
- [23] Wang C P, Liu X J, Ohnuma I, Kainuma R and Ishida K 2007 *J. Alloys and Comp.* **438** 129
- [24] Fecioru-Morariu M, Ali S R, Papusoi C, Sperlich M and Güntherodt G 2007 *Phys. Rev. Lett.* **99** 097206
- [25] Vallejo-Fernandez G and O'Grady K 2011 *IEEE Trans. Magn.* **47** 3304
- [26] Vallejo-Fernandez G, Kaeswurm B and O'Grady K 2011 *J. Appl. Phys.* **109** 07D738

- [27] Ernult F, Dieny B, Billard L, Lançon F and Regnard J R 2003 *J. Appl. Phys.* **94** 6678
- [28] Malozemoff A P 1987 *Phys. Rev. B* **35** 3679
- [29] Leighton C, Nogués J, Jönsson-Åkerman B J and Schuller I K 2000 *Phys. Rev. Lett.* **84** 3466
- [30] Jiménez E, Camarero J, Sort J, Nogués J, Mikuszeit N, García-Martín J M, Hoffmann A, Dieny B and Miranda R 2009 *Phys. Rev. B* **80** 014415

# Conclusions and perspectives

The PhD thesis presented along these pages was done in the framework of a collaboration between Spintec laboratory and Crocus Technology, start-up which develops TA-MRAM. As shown in Chapter 3, this kind of MRAM memory uses exchange bias properties in both reference and storage layer. For this reason, the main objective of the thesis was to *understand the working principles of exchange bias patterned systems and tailor the exchange bias thermal properties, key aspects for optimizing a full TA-MRAM stack.*

Two main aspects were studied: first (A), *the scalability and variability of exchange bias field among identical patterned dots*, and second (B) *the improvement of exchange bias properties in temperature through innovative material improvements (trilayer system for reinforced grain coupling and dusting layer at the interface.* Both of this type of studies had the aim of providing indications for improving reliability, data retention and writability of the exchange biased storage layer in TA-MRAM stacks.

The choice of taking into account simple F/AF bilayers without a full MTJ stack was done with this purpose: isolating the exchange bias phenomenon in order to better observe its behaviour under particular conditions. Exchange bias phenomena were analysed on a granular model, which has shown to correctly describe the  $H_{ex}$  features on sputtered systems.

## (A)

First, we have shown that the variability of  $H_{ex}$  on arrays of IrMn/Co exchange biased square dots was performed in collaboration with different partners in Grenoble: PTA cleanroom for the process steps, L\_Sim laboratory for the atomistic simulations and focused Kerr measurements in Institut Néel of CNRS, and the collaboration with Crocus Technology. Different lateral sizes, ranging from 200 down to 50 nm, were patterned on three different series of samples, each varying one different layer thickness according to the kind of study taken into account.

The first one consisted on IrMn/Co square dots with different Co thicknesses. The variation of the F thickness led, because of the competition between dipolar and exchange energies, to the observation of two different mechanisms of magnetization reversal. In the thin

F regime, dots showed on MFM measurements under in-situ applied field a coherent magnetization reversal; in the thick F regime, dots passed through a multidomain configuration, whose spin configuration was determined by atomistic simulations. ***The presence of two different micromagnetic regimes had important consequences on the exchange bias variability.*** Dots in the multidomain regime showed a larger exchange energy variability compared to those in the single domain regime. This increase in variability becomes even more important if the lateral size is reduced. The origin of this increased variability has been analysed by atomistic simulations. Dots in the thick F regime showed instability of the AF grains at the borders, due to the dipolar interaction with the F spins and to the earlier torque exerted by the F spins at remanence. The results of the study showed how ***the formation of multidomain configurations in the F layer has detrimental effects on the exchange variability, due to an increasing instability of the AF grains in the borders.*** For this reason, the F layer in the storage layer has to be sufficiently thin to avoid multidomain states.

The second study on patterned systems concerned the effects of microstructural properties of the IrMn layer on exchange bias variability, in a coherent reversal regime. IrMn grain size distribution was varied by considering different thicknesses of buffer layer and IrMn layer. We observed an increase of grain average size and distribution width with increasing buffer and IrMn thicknesses. When patterned, samples showed similar trends to the ones of the full sheet samples and no scalability effects concerning the average exchange bias values. Regarding exchange variability, on the other side, two main effects were observed. ***On one side, reducing dot lateral size led to an increase of exchange variability. This was attributed to IrMn grain cutting at the dot edges, which increases the instability of part of the dots present on the dot. Secondly, variability increased with increasing grain dot size and distribution width. This was attributed to the fact that on dots with lateral sizes below 200 nm the number of grains per dot is not sufficiently large to cover the whole grain population.*** Thus, in case of widely distributed grain sizes, the IrMn grain composition may vary a lot from one dot to another one, leading to an increase of exchange bias variability.

The focussed Kerr measurements on patterned dots allowed having a qualitative evaluation of exchange bias variability. The study showed that both micromagnetic and microstructural properties have consequences on exchange variability. ***For applicative purposes, in order to reduce instabilities and increase dots magnetic properties reproducibility and reliability, multidomain configurations have to be avoided and grain size distribution has to be homogenized in order to reduce the variability of grain***

*population from dot to dot.* Another possibility for reducing exchange variability is the use of synthetic antiferromagnets instead of simple F layers. The reduced dipolar field would stabilize the magnetization state at remanence and reduce the detrimental dipolar coupling with the AF layer, which showed to induce an increase of grain instability during magnetization reversal.

## (B)

The second part of the thesis was focused on the study of thermal properties of exchange bias systems, another central aspect of the working principle of TA-MRAM. First, *the introduction of a secondary F layer with out-of-plane magnetization, coupled with the IrMn/Co bilayer, led to a series of improvements of exchange bias properties in a wide range of temperatures.* (Pt/Co) and (Pd/Co) multilayers were selected for the additional F layer. The obtained trilayer structures showed a *reduction of the IrMn critical thickness, together with shift toward thinner thickness values of the exchange bias peak, which resulted larger to the one present in the original IrMn/Co bilayer.* Samples in the range of IrMn thicknesses where (Pt(Pd)/Co)/IrMn/Co trilayer structures showed enhanced exchange bias properties confirmed their improvements also in temperature. *Whereas bilayer structures showed a linear, convex  $H_{ex}(T)$  dependence, trilayers showed a concave curvature and, for IrMn thicknesses below 5 nm, an increase of the blocking temperature.* This combination of results was explained through a granular model of exchange bias. The presence of the additional F layer with out-of-plane magnetization is responsible of two effects. Firstly, an indirect IrMn grain coupling during the whole hysteresis loop, which creates a uniformed effective grain size more stable in temperature and a more homogeneous blocking temperature distribution. Secondly, a canting of the IrMn spins through its thickness because of the propagation of the out-of-plane coupling at the opposite interface of the IrMn/Co one with the (Pt(Pd)/Co)/IrMn one. This canting induces a reduction of the interface coupling, thus stabilizing grains which otherwise would have contributed to the coercivity. The systems of F/AF coupled spins used for atomistic simulations in the scalability and variability study can be further enriched with the introduction of the perpendicular F layer of the trilayer structure. This would allow verifying the canting and indirect coupling effects through a Heisenberg spin model, continuing the study done on bilayer systems.

The combination of these two effects leads to thermal effects which are of great interest for implementation on TA-MRAM systems, specifically on the storage layer, specifically because the benevolent effect of the additional layer is maintained after an annealing process

equivalent to those used on MTJ stacks. *The concave curvature of the  $H_{ex}(T)$  curves guarantee a good reliability on a large  $T$  range and the exchange drop close to  $T_B$  is ideal for a good writing process, being the whole curvature more suitable than the linear one of the initial bilayer stack. These thermal properties are moreover good for application in TMR heads, giving advantages terms of total stack thickness and stability of pinning at very small dimensions.*

Finally, exchange bias properties were further improved with the introduction of a dusting layer of Cu at the IrMn/Co interface. In fact, despite exchange coupling is mainly an interface phenomenon, the coupling is maintained in presence of an ultrathin Cu layer. Exchange bias field showed an increase at room temperature if the Cu interlayer had a thickness value lower than 3 nm, i.e. it was not yet a continuous layer but a “dusting” one. Also in this case it can be foreseen a series of simulations with rough F/AF interface and a non-magnetic dusting layer at the interface, already developed in the past by L\_Sim for similar systems. This  $H_{ex}$  enhancement was confirmed for different buffer layer thicknesses and IrMn thicknesses, which means it is independent on the IrMn microstructural properties, and also for the trilayer structures. *The combination of trilayer stack and Cu dusting layer, for 4 nm IrMn layer, led to 300% enhancement of exchange bias field at room temperature.* Both bilayer and trilayer samples confirmed their behaviour in temperature. This means that *a (Pt(Pd)/Co)/IrMn/Cu/Co stack with optimized IrMn and Cu thicknesses is an exchange biased stack with maximised exchange biased value at room temperature and a concave thermal dependence, two characteristics that mark significant improvements from the initial IrMn/Co bilayer, with characteristics that are ideal for implementation on technological applications.*





# Appendix I

## Macrospin model in Mi\_Magnet simulations

As presented in Paragraph 3.3, atomistic simulations were performed by grouping single spins into macrospins to achieve system sizes comparable to those of experimental patterned dots and for calculation speed purposes. The ferromagnetic (F) macrospins were formed by  $8 \times 8 \times 8$  ( $x \times y \times z$ ) spins, whereas, to preserve the alternating orientations along  $z$  of the AF layers, the antiferromagnetic (AF) macrospins were formed by  $8 \times 8 \times 1$  spins. The use of such cells implies a renormalization of the magnetic interactions from the simple single spin interaction of Eq.3.7 here reproduced:

$$E_{coupling} = J \mathbf{s}_1 \cdot \mathbf{s}_2 = J s_1 s_2 \cos \theta \cong J s_1 s_2 \left(1 - \frac{\theta^2}{2}\right) \quad (1)$$

where  $J$  is the nominal spin coupling. The passage from the single spin representation to the macrospin one is shown in Fig.I.1 in a 2D representation.

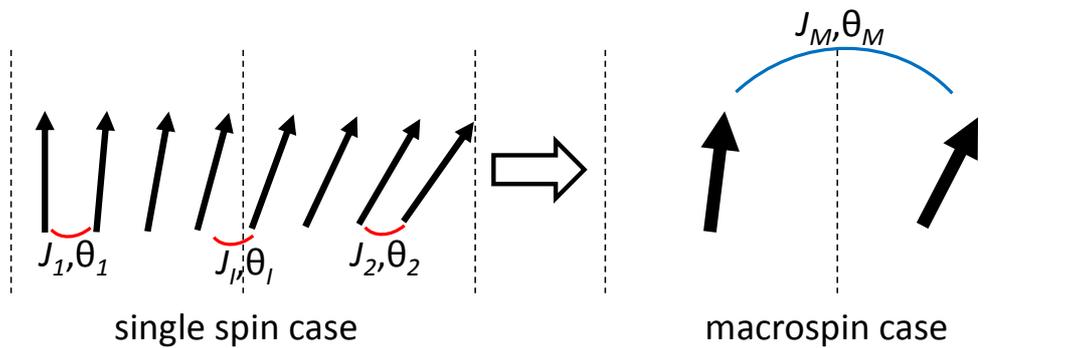


**Fig. I.1** – Series of couplings  $J$  and coupling angles  $\theta$  for the single spin case (left) and resulting interaction after macrospin grouping (right).

The model considers a homogeneous rotation of the spins inside the macrospin, which means that the angle variation  $\theta_i$  inside the macrospins is the same for all the grouped spins. It is a linear approximation, which allowed linearizing the cosine. As a result, once spins are

grouped into macrospins, the resulting coupling  $J_M$  and coupling angle  $\theta_M$  between the two macrospins has to take into account the angle variations  $\theta_1$  and  $\theta_2$  inside the macrospins, and the interfacial angle  $\theta_I$ , with their respective coupling  $J_1$ ,  $J_2$  and  $J_I$ .

The F/AF structures studied during the thesis consider three different macrospin–macrospin interactions, and this for each direction  $x$ ,  $y$ , or  $z$ :

- Coupling between macrospins of the same material (F or AF) in the same grain ( $S_1 = S_2$ ,  $\theta_1 = \theta_2$ ,  $J_1 = J_2 = J_I$ )
- Coupling between AF macrospins at the grain boundaries ( $J_I = J_{AF}$  or  $J_I = 0$ )
- Coupling between F and AF macrospins at the F/AF interface ( $S_1 \neq S_2$ ,  $\theta_1 \neq \theta_2$ ,  $n_{z-F} \neq n_{z-AF}$ )

In the two first cases, where the cell sizes are identical, the macrospin coupling energy formula should be of the form (equivalent to Eq.3.8 in Chapter 3):

$$\begin{aligned} E_{Macrospin} &= J_M \mathbf{S}_1 \cdot \mathbf{S}_2 = J_M S_1 S_2 \cos \theta_M = J_M (n_x n_y n_z)^2 s_1 s_2 \cos \theta_M \cong \\ &\cong J_M (n_x n_y n_z)^2 s_1 s_2 \left(1 - \frac{\theta_M^2}{2}\right) \end{aligned} \quad (2)$$

where the module  $S_i$  of the macrospin  $i$  is  $n_x n_y n_z$ .

Because of the regrouping, this energy interaction between two macrospins will be equalized to the energy between equivalent successive single spin total energy (independently for each axis) in order to get the coupling  $J_M$ :

$$c + E_{Macrospin} = E_{tot}^{singlespin} \quad (3)$$

where the constant  $c$  is an energy term, which is independent of the spin orientation.

## AI.1 Coupling between macrospins of the same material

In this first simple case  $S_1 = S_2 = S$ , with  $\theta_1 = \theta_2 = \theta$  in all three axis. This means that the angle variation inside each macrospin is the same for both macrospins. Considering a linear variation of the angle of rotation inside the macrospin, the relation between the macrospin angle  $\theta_M$  and the single spin angle  $\theta_I$  along the  $x$ -axis is:

$$\theta_1 = \frac{\theta_M}{n_x} \quad (4)$$

where  $n_x$  is the number of spins per macrospin along the  $x$  axis.

If we consider the  $x$ -axis, the equivalent total single spin energy is defined as:

$$E_{SS,x} = J n_x n_y n_z s \cdot s = J n_x n_y n_z s^2 \cos \theta \cong J n_x n_y n_z s^2 \left(1 - \frac{\theta^2}{2}\right) = J n_x n_y n_z s^2 \left(1 - \frac{1}{2} \frac{\theta_M^2}{n_x^2}\right) \quad (5)$$

Equalizing Eq.5 with Eq.2 through Eq.3 we obtain:

$$J_M (n_x n_y n_z)^2 s^2 \frac{\theta_M^2}{2} = J n_x n_y n_z s^2 \frac{1}{2} \frac{\theta_M^2}{n_x^2} \quad (6)$$

so that  $J_{M,x} = \frac{J}{n_x^3 n_y n_z}$ .

The corrective term  $c_x$  can be calculated as:

$$c_x + J_M (n_x n_y n_z)^2 s^2 = J n_x n_y n_z s^2 \quad (7)$$

so that  $c_x = n_x n_y n_z s^2 J \left(1 - \frac{1}{n_x^2}\right)$ .

The same type of calculations is valid for the y and z axes, giving respectively  $J_{M,y} = \frac{J}{n_x n_y^3 n_z}$

and  $J_{M,z} = \frac{J}{n_x n_y n_z^3}$ , with the corresponding corrective terms  $c_y = n_x n_y n_z s^2 J \left(1 - \frac{1}{n_y^2}\right)$  and

$$c_z = n_x n_y n_z s^2 J \left(1 - \frac{1}{n_z^2}\right).$$

This configuration is present for F-F coupling and AF-AF coupling along the three axes. In the case of AF-AF intergrain coupling and if the AF grains are considered uncoupled, then the macrospins at the boundary have  $J_I = 0$  (see Fig.I.1), i.e. they are not interacting.

## AI.2 Coupling at the F/AF interface

A particular case, due to the different number of spins along the z-axis for the AF and F cells, is the coupling at the F/AF interface. In order to maintain the AF spin ordering along z, the system presents  $n_{z-AF} = 1$  whereas  $n_{z-F} = 8$ .

The passage from single spins to macrospins corresponds to the schematic shown in Fig.I.2.

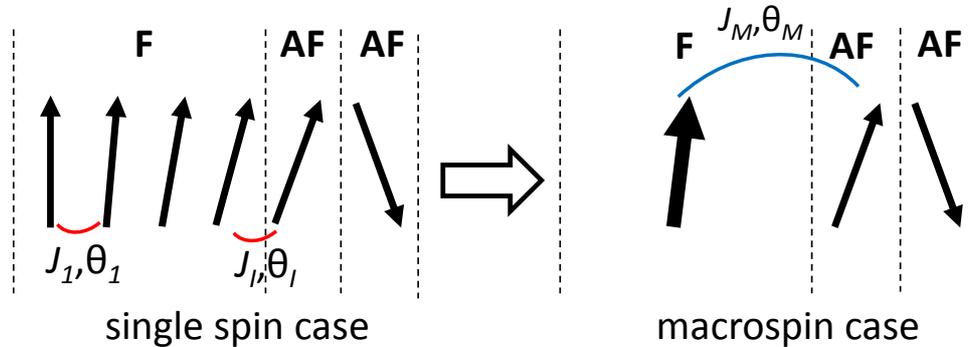


Fig. I.2 – Case of F/AF coupling along the z axis in the single spin case (left) and macrospin case (right).

Because of the different number of atoms along the  $z$ -axis of the two macrospins,  $\theta_M$  is defined as:

$$\theta_M = \frac{(n_{z,F} - 1)}{2} \theta_1 + \theta_i \quad (8)$$

The total single spin energy along the  $z$ -axis results:

$$E_{SS,z} \cong J_1 \frac{(n_{z,F} - 1)}{2} n_y n_{z,F} s_F^2 \left(1 - \frac{\theta_1^2}{2}\right) + J_2 n_y n_{z,F} s_F s_{AF} \left(1 - \frac{\theta_2^2}{2}\right) \quad (9)$$

By solving  $\frac{\partial E_{SS}}{\partial \theta_1} = 0$  we obtain:

$$\theta_1 = \frac{s_{AF} J_2}{s_F J_1 + s_{AF} \frac{n_{z,F} - 1}{2} J_2} \theta_M \quad (10)$$

Substituting Eq.16 into Eq.15, the equivalent total single spin energy is defined as:

$$E_{SS,z} = J_1 \frac{(n_{z,F} - 1)}{2} n_y n_{z,F} s_F^2 \left[ 1 - \left( \frac{s_{AF} J_2}{s_F J_1 + s_{AF} \frac{n_{z,F} - 1}{2} J_2} \right)^2 \frac{\theta_M^2}{2} \right] + J_2 n_y n_{z,F} s_F s_{AF} \left[ 1 - \left( \frac{s_F J_1}{s_F J_1 + s_{AF} \frac{n_{z,F} - 1}{2} J_2} \right)^2 \frac{\theta_M^2}{2} \right] \quad (11)$$

Solving Eq.3 with Eq.17, the following value of  $J_{M,F-AF,z}$  is obtained:

$$J_{M,F-AF,z} = \frac{\frac{n_{z,F} - 1}{2} s_F s_{AF} J_1 J_2^2 + s_F^2 J_1^2 J_2}{n_x n_y n_{z,F} \left[ s_F J_1 + s_{AF} \frac{n_{z,F} - 1}{2} J_2 \right]^2} \quad (12)$$

with a corrective term:

$$c_z = s_F^2 \frac{n_{z,F} - 1}{2} n_y n_z J_1 + n_y n_{z,F} s_F s_{AF} J_2 - n_{z,F} n_x^2 n_y^2 s_F s_{AF} J_{M,x} \quad (13)$$

# Appendix II

## Scalabilité et amélioration des propriétés de couplage d'échange pour TA-MRAM

### AII.1 Introduction

Le magnétisme est un phénomène physique fascinant, décrit pour la première fois par Wang Xu dans le quatrième siècle av. J-C dans la culture Chinoise et par Pline le Vieux en 77 apr. J-C. dans la culture occidentale. Les deux documents décrivent la capacité de la magnétite à attirer le fer. La première application “technologique” date de 3000 ans, en Chine, où la magnétite était utilisée dans les arts divinatoires. L’application dans le domaine navale commence entre le IX et le XI siècle en Chine, et il est reporté pour la première fois en Europe en 1187 par Alexander Neckam. Il s’agit d’une aiguille de magnétite flottant dans un bol d’eau; elle agit comme une boussole qui pointe vers les pôles magnétiques terrestres.

Les premières descriptions des propriétés magnétiques d’attraction et répulsion étaient plus métaphysiques que physiques, autant dans la culture chinoise que dans la culture grecque. Avec la diffusion des boussoles magnétiques dans les bateaux commerciaux et militaires, l’étude des propriétés physiques des aiguilles magnétiques devint fondamental pour améliorer la qualité des voies de navigation. Le premier rapport scientifique sur les propriétés magnétiques fut écrit par Pierre le Pèlerin de Maricourt en 1269 dans l’*Epistola de magnete* et il marqua le point de rupture avec les descriptions métaphysiques et superstitieuses d’avant, en préférant une attitude plus scientifique. Jusqu’au XIXe siècle, toutes les descriptions des phénomènes magnétiques étaient basées sur l’observation du comportement de l’aiguille de magnétite par rapport aux pôles magnétiques terrestres.

Jusqu'aux équations de Maxwell, les principes du magnétisme tels que nous les connaissons aujourd'hui, restèrent inconnus malgré la diffusion d'instruments magnétiques. Avec la description atomistique des phénomènes naturels commence la vision moderne des effets magnétiques. Pendant le dernier siècle, l'étude des propriétés magnétiques a toujours vu une forte liaison entre l'étude théorique et l'application technologique. Des études de Louis Néel sur les propriétés physiques de la matière condensée, en particulier sur les matériaux antiferromagnétique, jusqu'à la découverte des effets magnétorésistifs et leur application dans le stockage et l'enregistrement de données, l'étude des propriétés magnétiques a vu une forte évolution pendant le siècle dernier.

Le laboratoire Spintec et Crocus Technology représentent à Grenoble un excellent exemple de coexistence entre étude fondamentale et application technologique basées sur les matériaux magnétiques. Créé en 2006 comme start-up à partir de Spintec, Crocus Technology développe des mémoires à accès direct magnétiques et non volatiles thermiquement assistées (TA-MRAM, de l'anglais Thermally Assisted – Magnetic Random Access Memory). Il s'agit d'une évolution des MRAM de première génération, entrées sur le marché en 2006 avec Freescale Semiconductor. Le lien entre Crocus Technology et Spintec est toujours étroit à travers un programme de collaboration dans le domaine de recherche et développement. L'un d'entre eux est la thèse Cifre, une thèse de doctorat ciblée sur une étude applicative des phénomènes physiques.

C'est dans cet esprit que l'étude présentée dans ce manuscrit a été menée pendant les trois années de thèse. Le mécanisme de fonctionnement de TA-MRAM est basé sur les propriétés de couplage d'échange dans les couches de référence et de stockage. Le couplage d'échange est un phénomène découvert en 1956 par Meiklejohn et Bean; il décrit le décalage du cycle d'hystérésis due au couplage d'interface entre une couche ferromagnétique et une couche antiferromagnétique. Comme pour l'aiguille de magnétite au Moyen Age il est exploité dans nombreuses applications technologiques sans être complètement compris (mais sans le contour de superstitions, bien sûr).

Le but de la thèse est donc double: d'un côté améliorer les performances des systèmes couplés par échange, de l'autre comprendre les mécanismes fondamentaux à la base de ce phénomène. En particulier, les paramètres clés à optimiser dans les systèmes TA-MRAM sont le control de la dispersion des valeurs de décalage des cycles entre d'un plot à l'autre, l'optimisation des propriétés thermiques dans la gamme de températures d'intérêt, et la maximisation d'échange.

Dans le Chapitre 1, les différents modèles de couplage d'échange sont présentés, en montrant la complexité du phénomène et les efforts accomplis par la communauté scientifique pour essayer de le comprendre. Le chapitre commence par le premier modèle intuitif de Meiklejohn et Bean et termine par les derniers modèles basés sur l'influence de la taille de grain dans la couche antiferromagnétique et ses effets en température. Il présente aussi l'état de l'art des études expérimentales sur systèmes couplés par échange à l'échelle nanométrique.

Le Chapitre 2 décrit les applications les plus importants du couplage d'échange, à partir de la vanne de spin jusqu'à TA-MRAM développée par Crocus Technology.

Dans le Chapitre 3 le lecteur peut trouver la description des étapes suivies au laboratoire Spintec pour fabriquer et caractériser les échantillons, à partir des dépositions par pulvérisation cathodique jusqu'aux étapes de salle blanche pour la création de plots nanométriques, plus les différentes méthodes de caractérisation physique et magnétique. Le chapitre décrit aussi le model de spin utilisé pendant les simulations atomistiques développées en collaboration avec le laboratoire de simulation L\_Sim, utilisées dans le Chapitre 4.

Le Chapitre 4 est dédié à l'étude du couplage d'échange dans système IrMn/Co à taille réduite. Trois paramètres ont été pris en compte : l'épaisseur de la couche de Co, l'épaisseur de la couche d'IrMn et l'influence de la couche tampon. L'étude des systèmes gravés était conduite par mesures d'effet Kerr focalisé. C'est un appareil de mesure qui permet d'analyser le comportement magnétique en focalisant le faisceau sur quelques plots. Cela permet d'obtenir une évaluation directe et qualitative de la variabilité du couplage d'échange entre différents plots, un paramètre très important pour la fiabilité des points mémoire TA-MRAM. Avant de passer à la description des résultats sur les plots, le chapitre présente l'analyse des propriétés physiques sur des échantillons pleine tranche, en particulier les propriétés cristallographiques et la distribution de tailles de grains en fonction des différents paramètres. Le chapitre montre aussi les résultats des simulations atomistiques, en particulier les modes de renversement et les configurations magnétiques en fonction de l'épaisseur de la couche ferromagnétique et la stabilité des grains antiferromagnétiques.

Le Chapitre 5 décrit l'amélioration de la structure classique couplée par échange par l'introduction d'une seconde couche ferromagnétique avec une forte anisotropie perpendiculaire. Ces tricouches présentent une réduction de l'épaisseur critique d'IrMn et une augmentation de la température de blocage par rapport à des systèmes bicouche classique équivalents. Ces deux caractéristiques constituent une amélioration des performances des propriétés de couplage d'échange avec un intérêt applicatif direct dans la couche de stockage

de systèmes TA-MRAM. Ces deux effets sont expliqués par un modèle granulaire du couplage d'échange.

Le Chapitre 6 montre une deuxième possibilité d'augmenter les performances de couplage d'échange, par l'insertion d'une couche ultrafine non-magnétique entre l'IrMn et le Co. Cette augmentation est également mesurée dans les structures tricouches. Le comportement en température des différents systèmes est analysé.

## AII.2 Couplage d'échange: principes physiques et état de l'art

Le couplage d'échange est un phénomène physique observé expérimentalement la première fois en 1956 par Meiklejohn et Bean [1-3]. Dans leur expérience, un matériau composé par une couche de Co (couche ferromagnétique (F)) oxydée en surface (couche antiferromagnétique (AF) de CoO) présentait un décalage du cycle après avoir été refroidie sous champ magnétique au-dessous de la température de Néel de la couche de CoO. Ce phénomène, décrit initialement comme une nouvelle anisotropie unidirectionnelle, prend le nom de couplage d'échange (exchange bias  $H_{ex}$ ) [4,5]. Le modèle intuitif du couplage d'échange est schématisé sur la Figure 1.5. En première lieu, le système est recuit au dessus d'une température  $T$  (nommée température de blocage  $T_B$ ) suffisamment grande pour débloquent les spins de la couche AF, qui deviennent superparamagnétiques. Le système est ensuite refroidit sous un champ magnétique jusqu'à une température de mesure. Au-dessous de  $T_B$  l'AF s'ordonne magnétiquement, et se couple à l'interface avec la couche F selon la direction du champ appliqué. Quand le cycle d'hystérésis est mesuré, le couplage d'interface entre l'AF et le F force les spins dans la couche F à rester dans la direction du champ de recuit, et décale ainsi le cycle d'hystérésis et augmente le champ coercitif  $H_C$  du cycle. Le premier modèle de couplage d'échange proposé par Meiklejohn et Bean était basé sur l'introduction d'un terme additif d'anisotropie unidirectionnelle dans le model de Stoner-Wohlfarth [6] (Equation 1.11). Ce terme donne une valeur de  $H_{ex}$  inversement proportionnelle à l'épaisseur de la couche F. Malheureusement, deux ordres de grandeur séparent les valeurs expérimentales des valeurs obtenues par ce modèle. Le deuxième modèle proposé par Néel [7] et repris par Mauri [8] considère l'introduction des parois de domaine dans l'épaisseur de la couche AF (Figure 1.8). L'énergie dépensé par la formation de la paroi (Equation 1.17) réduit la valeur d'échange (Equation 1.20) et permet de s'approcher des valeurs expérimentales. Pendant que le modèle de Mauri était publié, Malozemoff [9] proposait un

modèle basé sur la théorie des champs aléatoires (“random field theory”) d’Imry [10]. La présence de rugosité à l’interface entre le F et l’AF est la cause de décompensations de la couche AF (Figure 1.9), qui, pour minimiser l’énergie, se divise en domaines avec des parois perpendiculaires à l’interface (Figure 1.10), contrairement aux domaines de Mauri et Néel. Ce deux modèles, encore de référence aujourd’hui, ne considèrent pas la structure granulaire des couches, facteur particulièrement important dans les échantillons déposés par pulvérisation cathodique, comme c’est le cas dans les applications technologiques et pour les échantillons déposés pendant la thèse. Dans ce cas le modèle de Fulcomer et Charap [11] est pris comme référence. Il considère une distribution de grains d’AF indépendants entre eux. Selon leur volume, les grains peuvent être considérés thermiquement instables, couplés par échange ou non couplé. Ce modèle a récemment été développé et confirmé expérimentalement par O’Grady [12]. Le nombre de spins non compensés à l’interface est dépendant de la taille latérale des grains [13]. Les évolutions de  $H_C$  et  $H_{ex}$  et température ont été développés par Stiles and McMichael [14] en combinant le modèle de paroi de Néel avec le modèle de grains de Fulcomer et Charap. Ce modèle permet de déterminer l’origine de l’augmentation de la coercivité dans un modèle de grains.

Pendant les dernières dizaines d’années, l’évolution des techniques de lithographie en salle blanche a permis l’étude des propriétés de couplage d’échange sur des réseaux avec une taille latérale de quelque centaine de nanomètres. Dans ce régime, de nouveaux paramètres comme les effets de taille et de forme doivent être pris en compte [15,16]. Un exemple de la richesse d’effets que présentent à l’échelle nanométrique est résumé dans le Tableau 1.

### **AII.3 Couplage d’échange: applications technologiques**

Dans l’évolution du marché technologique, la réduction de la taille latérale des transistors est une des étapes que les industries doivent suivre. Aujourd’hui la limite physique de cette réduction est proche d’être atteinte. Pour cette raison, beaucoup de recherche est focalisée sur la réalisation de systèmes alternatifs aux transistors pour le stockage de données. C’est dans ce contexte (connue comme “More than Moore”) que la spintronique (l’exploitation des propriétés du spin dans systèmes électroniques) se place, en particulier avec les mémoires à accès aléatoires magnétiques (MRAM). Ces mémoires regroupent plusieurs phénomènes physiques très importants. En première lieu, la magnétorésistance, qui est la propriété des multicouches magnétiques de changer leur résistance selon leur aimantation relative. Ce phénomène, était en première lieu découvert par Fert [17] et Grünberg [18] pour des couches F séparés par une couche non-magnétique, et il est connu

comme Magnétorésistance Géante (GMR), et il est modélisé dans Figure 2.4. L'application technologique de cet effet est la vanne de spin, proposé par Dieny [19]. En couplant une des deux couches F avec un AF, c'est possible avoir une couche fixé (dite de référence) et une libre (Figure 2.5). En changeant l'aimantation de la couche libre on obtienne deux valeurs de résistance qui correspondent à deux valeur numériques "0" et "1". Ces systèmes sont utilisés dans les têtes de mémoire de disques durs.

La différence en résistance devient encore plus importante quand la couche non-magnétique entre les deux couches magnétiques est un isolant. Dans ce cas un effet tunnel de l'électron à travers la barrière prend place (Figure 2.7); cet effet prend le nom de Magnétorésistance Tunnel (TMR) [20] ; son application technologique, sur le même principe de la vanne de spin, est l'MRAM. Les premières générations de MRAM étaient basé sur l'utilisation de deux champs perpendiculaires l'un à l'autre (Figure 2.9). La première amélioration à ce modèle est connue comme toggle-MRAM (Figure 2.10). La couche libre est constitué par un ferromagnétique synthétique, qui permet l'écriture de la couche de stockage par étapes, en augmentant la fiabilité de l'écriture (Figure 2.11). Pendant les dernières dix ans deux autres technologie se battent pour conquérir le marché : les MRAM à transfert de spin (STT-MRAM) et les TA-MRAM. Ce dernier exploite le couplage d'échange aussi dans la couche de stockage, qui est écrite en chauffant le point de mémoire par une courant [21]. Cette méthode augmente la rétention des données et permet l'écriture de plusieurs points de mémoire en parallèle (Figure 2.13) [22].

## **AII.4 Préparation des échantillons, analyse expérimentale et simulations atomistiques**

Tous les échantillons ont été déposés par pulvérisation cathodique (Figure 3.1). Après déposition, ils ont été recuits dans une chambre à vide sous un champ constant, dans le plan, de 2000 Oe. Le recuit typique était de 200°C pour 30 minutes. Les échantillons à taille réduite ont suivi un procès de lithographie en salle blanche (Figure 3.2). Ils ont été couverts par une résine négative dite FOX qui, après recuit, a été processée par lithographie électronique. La résine est après développée dans un bain acide, qui enlève la couche de résine dans les parties de l'échantillon non insolées par le faisceau électronique. L'échantillon est ensuite gravé par gravure ionique (IBE) ; la résine protège les couches magnétiques, qui sont gravées tout autour. La qualité des procédés est vérifiée par un Microscope Electronique à Balayage (MBE, Scanning Electron Microscope SEM en anglais) (Figure 3.4).

Les échantillons ont été caractérisés avec un Microscope à Force Magnétique (MFM), un instrument qui permet, au travers de deux scans (un en mode tapping pour la topographie et un en mode non contact pour les propriétés magnétiques), d'imager le champ dipolaire rayonné par les échantillons (Figure 3.6). Les plots ont été mesurés localement par des mesures d'effet Kerr focalisé. L'effet Kerr définit l'interaction entre un faisceau lumineux (un laser) polarisé et un matériau magnétique. Pendant la thèse, un instrument Kerr focalisé (Figure 3.8) (spot laser de 600 nm sur l'échantillon) a été utilisé pour pouvoir avoir des mesures de cycle d'hystérésis sur quelques plots (Figure 3.9). Sur les couches continues une étude de diffraction des rayons X a également été conduite dans le mode  $\theta$ - $2\theta$  pour obtenir le paramètre de maille et la structure cristalline des différentes couches.

En parallèle des études expérimentales, des séries de simulations atomistiques ont été conduites pour toute la durée de la thèse dans le laboratoire L\_Sim grâce à des codes Python. Le système est modélisé par le modèle de Heisenberg (Equation 3.4) [23], qui considère l'énergie Zeeman, l'énergie dipolaire, l'énergie d'échange et l'énergie d'anisotropie. Les couches F-AF sont modélisées avec les paramètres de l'Equation 3.5. La couche AF est considérée non compensée ; aucune rugosité d'interface n'est prise en compte. Pour des raisons de simulation, les spins F et AF sont groupés dans des "macrospins" de  $8 \times 8 \times 8$  et  $8 \times 8 \times 8$  respectivement (Figure 3.12). L'énergie totale du système est minimisée par le logiciel Mi\_Magnet sous différents champs magnétiques pour simuler un cycle d'hystérésis. La simulation a lieu par la méthode du gradient conjugué (Figure 3.11) [24].

## **AII.5 Variabilité de couplage d'échange dans des réseaux de plots carrés d'IrMn/Co**

Deux études principales ont été menées sur les réseaux de plots. La première était fonction de l'épaisseur de la couche F pour analyser les effets micromagnétiques sur la variabilité de l'échange ; la deuxième était focalisée sur les effets microstructuraux de la couche AF sur la variabilité de l'échange.

***Épaisseur de la couche Co*** Les échantillons avec composition  $Ta_3/Cu_3/IrMn_6/Co_x/Pt_2$ , avec  $x = 2.5, 3.7, 5, 10, 15, 20$  and  $25$  nm ont été considérés. Les images MFM sur les couches continues ont montré un reversement de l'aimantation par nucléation et propagation des parois (Figure 4.1). Pour les réseaux de plots, deux cas se sont présentés. Pour des épaisseurs fines de Co, le reversement s'effectuait par rotation cohérente (Figure 4.4) alors que pour des grandes épaisseurs le reversement passe par un état micromagnétique complexe

(Figure 4.5). Les mesures d'effet Kerr focalisé confirment ces deux comportements, avec un cycle décalé dans le premier cas et un cycle double décalé dans le deuxième cas (Figure 4.7). La valeur de  $H_{ex}$  est inversement proportionnelle à l'épaisseur de la couche Co, avec des valeurs plus faibles pour les couches gravées comparées à la couche continue. Cela est attribué aux différents modes de reversement.

Concernant la variabilité de  $H_{ex}$ , alors que les couches continues montraient une déviation standard autour de 10 Oe, dans les plots ce facteur devient très important (Figure 4.8). En particulier la variabilité d'énergie d'échange  $\Delta E_{ex}$  augmente sensiblement dans le régime de grandes épaisseurs de Co pour les plots de 50 nm de taille (Figure 4.11).

Les deux configurations magnétiques ont été confirmées par les simulations atomistiques. En premier lieu, la validité du model était vérifiée pour des plots F en comparaison avec les résultats expérimentaux de Cowburn [25] (Figure 4.12). Les simulations ont montrées trois configurations magnétiques possibles: le renversement cohérent (Figure 4.13), le renversement par état multidomaine (Figure 4.14) et le vortex (Figure 4.15), aussi confirmées en présence de couplage F/AF. Les deux premières correspondent aux mesures expérimentales pour la forme des cycles d'hystérésis et pour les images MFM simulées. La variabilité d'échange a été étudiée avec un couplage fort entre F et AF pour pouvoir simuler la formation de parois de domaine dans l'AF. Les simulations ont montré une instabilité majeure des grains dans le cas de F épais, dû à un avancement de phase aux bords du plot à la rémanence. Cet effet devient plus important en réduisant la taille latérale des plots. Ces résultats ont été présentés à Intermag 2012 et publiés dans Journal of Physics D: Applied Physics [26].

**Effets microstructurales de la couche IrMn** Dans des systèmes à taille réduite le nombre de grains AF dans chaque plot peut se réduire à quelques dizaines. Pour cette raison il est important de voir quel est l'influence de ce paramètre dans la variabilité de  $H_{ex}$ . Entre les différentes méthodes possibles pour changer la taille de grains, deux ont été choisis : le changement d'épaisseur de la couche AF [27] et de la couche tampon [28]. La distribution de taille de grains était mesurée par Microscope à Force Atomique (AFM) [29]. Les empilements choisis étaient :

- Série couche tampon:  $Ta_3/Cu_x/IrMn_{12}/Co_5/Pt_2$  avec  $x = 1, 2, 6, 9$  and  $12$  nm ;
- Série couche IrMn:  $Ta_3/Cu_2/IrMn_x/Co_5/Pt_2$  avec  $x = 3, 4, 5, 6.5, 10, 12$  and  $15$  nm.

Les mesures ont montré une augmentation de la taille moyenne et de la distribution avec l'augmentation de l'épaisseur de la couche tampon (Figures 4.21 et 4.22) et de la couche IrMn (Figure 4.26). Une fois gravés, les échantillons ont confirmé un reversement cohérent (Figure

4.27) et une importante variabilité (Figure 4.28). En concernant  $H_{ex}$ , les deux séries ont montré des valeurs d'échange moyen qui suivent les valeurs de la couche continue. Aucun effet de taille n'était observé (Figure 4.29).

Pour ce qui concerne  $\Delta E_{ex}$ , deux tendances ont été observées (Figure 4.30). La première est une augmentation de la variabilité en réduisant la taille latérale des plots. Ce résultat est attribué aux effets de coupage de grains aux bords de plots [30], qui réduit la stabilité du couplage. La deuxième tendance est une augmentation de la variabilité avec la taille de grains. Quand la taille des plots est de 50 nm, le nombre de grains dans chaque plot est d'une trentaine environ, donc différents plots peuvent avoir des populations de grains très différentes. Si la distribution de taille est importante, cet effet devient plus évident. Ces résultats ont été présentés à JEMS 2013.

## **AII.6 Amélioration du couplage d'échange: la structure en tricouche (Pt(Pd)/Co)/IrMn/Co**

Les multicouches (Pt/Co) et (Pd/Co) sont des matériaux avec une aimantation hors plan [31,32]. Cette caractéristique est due à plusieurs facteurs tels que les contraintes dans les couches de Co et l'hybridation des orbitales électroniques [33].

Dans le Chapitre 5 les bicouches classiques IrMn/Co sont comparées avec des tricouches (Pt<sub>1,8</sub>/Co<sub>0,6</sub>)/IrMn<sub>x</sub>/Co<sub>5</sub> et (Pd<sub>1,8</sub>/Co<sub>0,6</sub>)/IrMn<sub>x</sub>/Co<sub>5</sub>, avec x entre 2 et 15 nm.

Les mesures pour différentes épaisseurs d'IrMn à température ambiante montrent deux propriétés principales. En première lieu, l'épaisseur critique d'IrMn  $t_C$ , qui est l'épaisseur au-dessus de laquelle le décalage du cycle commence à apparaître, est réduit comparé à la bicouche. Deuxièmement, la valeur d'échange maximale obtenue dans les tricouches dépasse celle de la bicouche (Figure 5.5).

Les échantillons ont été étudiés en température avec des mesures de température de blocage maximale et des distributions de température de blocage [34]. Pour la première méthode de mesure, les bicouches ont montré une décroissance linéaire de  $H_{ex}$  (Figure 5.9), avec une augmentation de  $T_B$  avec l'épaisseur d'IrMn, comme reporté dans la littérature [35]. Dans le cas des tricouches, les échantillons avec une épaisseur d'IrMn inférieure à 5 nm ont montré une augmentation de  $T_B$  comparés à des bicouches équivalentes (Figure 5.12) ; de plus, les courbes  $H_{ex}(T)$  présentent une courbure concave (Figures 5.10 et 5.11). Ce comportement a été confirmé par les mesures de distributions de température de blocage

(Figure 5.15). Ce comportement a également été confirmé après un recuit à 340°C de 90 minutes, recuit typiques des jonctions pour des MRAM (Figure 5.19).

Ces résultats ont été expliqués par un modèle de grain du couplage d'échange (Figure 5.2), comme décrit dans le Paragraphe AII.2. Les mesures AFM ont montré que la distribution de taille de grains ne change pas sensiblement entre bicouches et tricouches pour une épaisseur d'IrMn donnée (Figure 5.20). Les populations de grains peuvent donc être considérés similaires. Les mesures de diffraction de rayons X montrent un décalage du pic d'IrMn dans les tricouches, ce qui représente un paramètre de maille plus serré. Ce changement a des conséquences sur l'anisotropie de la couche AF, et est une des causes de ces phénomènes. Deux autres effets sont tenus pour responsables du changement de comportement de la tricouche par rapport aux bicouches. En première lieu, le *canting* des spins AF à l'interface IrMn/Co due au couplage hors-plan (Pt(Pd)/Co)/IrMn (Figure 5.24). Cet angle à l'interface réduit le couplage  $J_{ex}$  (Equation 5.3) en stabilisant des grains qui auraient contribué à la coercivité autrement. Cette stabilisation réduit l'épaisseur critique  $t_C$  et retarde le renversement des grains en température, en augmentant  $T_B$ . Le deuxième effet est un couplage indirect des grains AF par la couche hors-plan (Figure 5.22), qui reste perpendiculaire pendant les cycles d'hystérésis dans le plan. Ce couplage crée une taille effective de grains plus grande que la taille physique, et augmente ainsi la stabilité des grains pour des épaisseurs fines d'IrMn. Le couplage entre grains homogénéise également le comportement en température, donnant une distribution de  $T_B$  plus serrée (Figure 5.16) et une décroissance en  $T$  plus douce (Figure 5.26). Ces résultats ont été publiés dans deux articles [36,37].

## AII.7 Insertion d'une "poudre" de Cu à l'interface

### IrMn/Co dans des structures bicouche et tricouche

Le couplage d'échange est généralement considéré comme un phénomène d'interface. Néanmoins, il a été montré [38] que le décalage de cycle est maintenu, avec une décroissance exponentielle, en présence d'une couche non magnétique entre le F et l'AF pour une épaisseur qui peut monter jusqu'à quelques nm [39]. Le sujet est encore controversé et peu étudié, en particulier pour des épaisseurs de la couche intermédiaire de quelques Angstroms.

Pendant la thèse, une insertion de Cu a été ajoutée entre l'IrMn et le Co dans les structures bicouche et tricouche. Dans le cas de la bicouche, deux épaisseurs d'IrMn ont été prises en compte, 12 et 4 nm, pour des empilements  $Ta_3/Cu_2/IrMn/Cu_x/Co_5/Pt_2$ , avec  $x$  entre 0

et 1 nm. Dans les deux cas, pour une épaisseur de Cu inférieure à 0.3 nm (i.e. pour une couche non continue de Cu) les échantillons présentent une augmentation de  $H_{ex}$  (Figure 6.2, 6.3), suivie par une décroissance qui approche zéro vers 1 nm de Cu. Cet effet se manifeste également dans les systèmes tricouche pour une épaisseur d'IrMn de 4 nm, ce qui permet de tripler la valeur de l'échange par rapport à la valeur obtenue avec la bicouche de départ (Figure 6.10). Les mesures par images AFM montrent que la couche de Cu n'affecte pas la distribution de taille de grains (Figure 6.5).

Le comportement en température a également été étudié. Dans le cas de 4 nm d'IrMn, les bicouches et les tricouches avec insertion de Cu présentent la même température de blocage indépendamment de l'épaisseur de la couche de Cu (Figure 6.8, 6.12). Par contre, dans le cas de 12 nm d'IrMn en structure bicouche, à l'augmentation d'échange à température ambiante correspond une augmentation de  $T_B$  (Figure 6.6) pour toute la gamme de température (Figure 6.7).

Différentes hypothèses ont été proposées pour décrire l'origine de l'augmentation de l'échange en présence d'une couche non continue de Cu. En premier lieu, la structure cristalline du Cu favorise une bonne croissance du Co, ce qui n'est pas le cas pour le Ta. De plus, le Cu est une bonne barrière de diffusion du Mn dans la couche de Co. Co et Mn sont très miscibles, et une réduction de leur interdiffusion améliore la valeur d'échange. Par ailleurs, le Cu n'est pas miscible avec le Co et la création de CuMn antiferromagnétique à l'interface n'est possible que pour des hauts pourcentages de Mn. Enfin, cet alliage a une température de Néel de 300 K. Dans la littérature les études sur AF dilué du type  $\text{IrMn}_{1-x}\text{Cu}_x$  montrent une réduction de l'échange pour des échantillons déposés par pulvérisation cathodique; la diffusion a donc lieu essentiellement à l'interface.

Une possible explication de l'augmentation d'échange est la réduction du couplage à l'interface due à la présence d'une couche non magnétique et non continue. Dans le modèle présenté dans le chapitre précédent, une réduction du couplage d'échange  $J_{ex}$  permet la stabilisation de grains qui auraient sinon contribué à la coercivité du cycle d'hystérésis. Une autre possibilité est une réduction de la frustration des spins F et AF à l'interface. Dans le cas d'une interface rugueuse, les spins F et AF présentent des couplages défavorables dans les parties irrégulières (bosses ou trous). Dans le régime de couche de Cu non-continu, si les particules de Cu se placent dans les zones à grand frustration, le couplage résultant devient plus grand que dans la configuration sans Cu. Cette augmentation disparaît une fois que la couche de Cu devient continue: dans ce cas, le couplage F-AF est réduit et le décalage du cycle d'hystérésis diminue.

## AII.8 Conclusions et perspectives

La thèse a été réalisée en collaboration entre le laboratoire Spintec et Crocus Technology, start-up impliquée dans le développement des mémoires TA-MRAM. Comme montré dans le Chapitre 3, ce type de mémoires MRAM utilise les propriétés de couplage d'échange dans la couche de référence et également dans la couche de stockage. L'objectif principal de la thèse a été la *compréhension des principes fondamentaux du phénomène de couplage d'échange à l'échelle nanométrique et l'amélioration des propriétés thermiques. Ce sont deux aspects clé pour optimiser un empilement TA-MRAM complet.*

Deux aspects ont été étudiés : (A) *la scalabilité et la variabilité du couplage d'échange entre différents plots nanométriques*, et (B) *l'amélioration des propriétés de couplage d'échange en température avec l'introduction de couches supplémentaires* (systèmes en tricouche avec une couche perpendiculaire pour renforcer le couplage entre les grains et insertion d'une couche non-continue de Cu à l'interface IrMn/Co). Le but de ces deux études était d'indiquer des voies pour améliorer la fiabilité, la rétention des données et la facilité d'écriture de la couche de stockage couplée par échange dans les systèmes TA-MRAM.

Le choix de focaliser l'étude sur la simple bicouche F/AF plutôt que sur un empilement MTJ complet a été pris pour isoler la problématique du couplage d'échange et ainsi mieux comprendre son comportement dans différentes conditions. Le couplage d'échange a été étudié avec un modèle de grain, qui a déjà démontré un bon accord avec l'expérience pour modéliser le phénomène du décalage du cycle pour des échantillons déposés par pulvérisation cathodique.

### (A)

L'étude de la variabilité d'échange sur réseaux de plots carrés IrMn/Co a été conduite en collaboration avec différents partenaires à Grenoble: la salle blanche PTA, le laboratoire L\_Sim pour les simulations atomistiques et l'Institut Néel du CNRS pour les mesures d'effet Kerr focalisé, plus la collaboration avec Crocus Technology. Différentes tailles latérales, entre 200 et 50 nm, ont été fabriquées pour trois différentes séries d'échantillons, chaque série présentant une variation de l'épaisseur d'une couche spécifique dans l'empilement, selon le type d'étude pris en compte.

La première étude concernait des plots carrés IrMn/Co avec différentes épaisseurs de Co. La variation de l'épaisseur de la couche F, à cause de la compétition entre énergie dipolaire et énergie magnétostatique, a conduit à l'observation de deux différents mécanismes de renversement magnétique. Dans le régime d'épaisseur fine de F, les plots ont montré, dans

les images MFM sous champ magnétique, un renversement cohérent de l'aimantation. Dans le régime de grande épaisseur de F, l'aimantation des plots est passée par une configuration multidomaines, reconstruite par simulations atomistiques. ***La présence de deux régimes micromagnétiques a d'importantes conséquences sur la variabilité du couplage d'échange.*** Les plots dans le régime multidomaine présentent une variabilité plus importante comparés aux plots monodomaines. Cette augmentation devient encore plus importante si la taille latérale du plot est réduite. L'origine de cette augmentation de variabilité a été analysée par simulations atomistiques. Les plots avec une couche F épaisse montrent une instabilité des grains AF aux bords du plot, due à l'interaction dipolaire avec la couche F et au couple exercé par les spins F à la rémanence. Ces résultats ont montré que ***la formation d'états multidomaines dans la couche F a des conséquences négatives sur la variabilité du couplage d'échange, à cause d'une plus grande instabilité des grains AF sur les bords.*** Pour cette raison, la partie F de la couche de stockage doit être suffisamment fine pour éviter des états multidomaines.

La deuxième étude sur réseaux de plots a concerné les effets des propriétés microstructurales de la couche IrMn sur la variabilité de couplage d'échange, dans le régime de renversement cohérent. La distribution de taille des grains IrMn a été ajustée en changeant l'épaisseur de la couche tampon et de la couche d'IrMn. Il a été observé une augmentation de la taille moyenne et de la largeur de la distribution avec l'augmentation de l'épaisseur de la couche tampon et de la couche IrMn. Une fois gravés, pour ce qui concerne le décalage moyen, les échantillons ont montré une tendance similaire aux couches continues et aucun effet de taille. Concernant la variabilité d'échange, deux effets ont été observés. D'un côté, ***la réduction de la taille latérale des plots implique une augmentation de la variabilité de l'échange. Cet effet a été attribué au coupage des grains d'IrMn aux bords des plots, qui augmente l'instabilité du couplage.*** La deuxième tendance est une ***augmentation de la variabilité avec la taille des grains. Pour des plots avec une taille latérale inférieure à 200 nm, le nombre de grains par plots n'est pas suffisant pour couvrir toute la distribution de taille des grains.*** Si la distribution est très large, la composition de grains d'IrMn peut être très différente entre différents plots, ce qui donne une plus grande variabilité de couplage d'échange entre plots.

Les mesures au Kerr focalisé sur réseaux de plots carrés ont permis d'avoir une évaluation qualitative de la variabilité du couplage d'échange. Cette étude a montré comment les effets micromagnétiques et microstructuraux ont un impact sur ce paramètre. Dans une vision applicative, ***la réduction des instabilités et l'augmentation de la reproductibilité et fiabilité***

*des propriétés magnétiques sont possibles en évitant les états multidomaines et en homogénéisant la distribution de taille de grains.* Une autre possibilité pour réduire la variabilité est l'utilisation de matériaux antiferromagnétiques synthétiques au lieu des F simples. La réduction du champ dipolaire rayonné pourrait stabiliser l'état magnétique à la rémanence et réduire le couplage dipolaire avec la couche AF, qui induit des instabilités dans les grains.

## (B)

La deuxième partie de la thèse a été focalisée sur l'étude des propriétés thermiques des systèmes couplés par échange, autre thème central dans le fonctionnement des TA-MRAM. *L'introduction d'une deuxième couche F à aimantation perpendiculaire ((Pt/Co) ou (Pd/Co)), couplée à la bicouche IrMn/Co, a apporté une série d'améliorations des propriétés d'échange dans une large gamme de température. Les structures en tricouche ont montré une réduction de l'épaisseur critique d'IrMn et de l'épaisseur d'IrMn pour obtenir un échange maximal, celui-ci étant plus large que l'échange obtenu avec la bicouche.* Dans ce régime d'épaisseurs d'IrMn, les tricouches (Pt(Pd)/Co)/IrMn/Co ont également montré des améliorations en température. *Alors que les courbes  $H_{ex}(T)$  des échantillons bicouches ont une dépendance linéaire en température, les tricouches ont montré une courbure convexe et une augmentation de la température de blocage.* Cette combinaison de comportements a été expliquée par un modèle de grain du couplage d'échange. La couche à aimantation perpendiculaire est responsable de deux effets. Premièrement, un couplage indirect des grains IrMn s'établit, ce qui crée une distribution de taille effective de grains plus stable en température et une distribution de température de blocage plus homogène. Deuxièmement, un *canting* des spins IrMn se propage de la multicouche à aimantation perpendiculaire à travers l'épaisseur de la couche IrMn, jusqu'à l'interface IrMn/Co. Ce tilt des spins réduit l'intensité du couplage d'échange, ce qui stabilise les grains d'IrMn qui auraient contribué à la coercivité autrement. Ces effets pourront être vérifiés par des simulations atomistiques, avec la création de systèmes en tricouche sur la base des simulations développées pendant la thèse. *La combinaison de ces deux effets donne des propriétés thermiques de grand intérêt pour les TA-MRAM, notamment pour la couche de stockage, en particulier parce que ces propriétés sont conservées après un recuit standard des jonctions pour MRAM. La courbure concave des courbes  $H_{ex}(T)$  donne une stabilité de la couche de stockage satisfaisante sur une large gamme de températures, et la décroissance rapide en proximité de  $T_B$  est idéale pour la phase d'écriture. Ces propriétés*

*thermiques sont aussi d'intérêt pour des applications dans des têtes de lecture TMR, en donnant une grande stabilité de couplage pour des tailles réduites.*

Les propriétés d'échange ont été encore améliorées avec l'insertion d'une couche de Cu à l'interface IrMn/Co. Même si le couplage d'échange est principalement un phénomène d'interface, le décalage du cycle d'hystérésis est gardé en présence d'une couche très fine entre le F et l'AF. Le couplage d'échange est augmenté en présence de la couche de Cu pour une épaisseur inférieure à 0.3 nm (i.e. pour une couche non-continue). Dans ce cas, il est également possible envisager une série d'études par simulation atomistique avec l'ajout de paramètres comme la rugosité d'interface et la présence de particules non magnétiques de Cu. Cette augmentation de  $H_{ex}$  a été confirmée soit pour différentes épaisseurs de couche tampon et de couche d'IrMn, ce qui indique qu'elle est indépendante des propriétés micromagnétiques d'IrMn, soit pour les tricouches. ***La combinaison de structure en tricouche et couche non-continue de Cu à l'interface a permis, pour une épaisseur d'IrMn de 4 nm, de tripler la valeur d' $H_{ex}$  par rapport à la bicouche de départ.*** Bicouches et tricouches ont confirmé leur comportement en température. ***L'empilement (Pt(Pd)/Co)/IrMn/Cu/Co, pour des épaisseurs d'IrMn et Cu optimisées, est un système avec un couplage d'échange maximisé à température ambiante et présentant une courbure concave en température, deux caractéristiques qui donnent des améliorations significatives par rapport à la bicouche IrMn/Co de départ, caractéristiques idéales pour l'intégration dans des dispositifs technologiques.***

## Bibliographie

- [1] Meiklejohn W H and Bean C P 1956 *Phys. Rev.* **102** 1413
- [2] Meiklejohn W H and Bean C P 1957 *Phys. Rev.* **105** 904
- [3] Meiklejohn W H 1962 *J. Appl. Phys.* **33** 1328
- [4] Nogués J and Schuller I K 1999 *J. Magn. Magn. Mat.* **192** 203
- [5] Berkowitz A and Takano K 1999 *J. Magn. Magn. Mat.* **200** 552
- [6] Stones E C and Wohlfarth E P 1948 *Phil. Trans. R. Soc. Lond. A* **240** 599
- [7] Néel L 1967 *Ann. Phys. (Paris)* **2** 61.
- [8] Mauri D, Siegmann H C, Bagus P S and Key E 1987 *J. Appl. Phys.* **62** 3047
- [9] Malozemoff A P 1987 *Phys. Rev. B* **35** 3679
- [10] Imry Y and Ma S K 1975 *Phys. Rev. Lett.* **35** 1399
- [11] Fulcomer E and Charap S H 1972 *J. Appl. Phys.* **43** 4190
- [12] O'Grady K, Fernandez-Outon L E and Vallejo-Fernandez G 2010 *J. Magn. Magn. Mat.* **322** 883
- [13] Takano K, Kodama R H, Berkowitz A E, Cao W and Thomas G 1997 *Phys. Rev. Lett.* **79** 1130
- [14] Stiles M D and McMichael R D 1999 *Phys. Rev. B* **59** 3722; *ibid* 1999 **60** 12950; *ibid* 2001 **63** 064405
- [15] Lau J W and Shaw J M 2011 *J. Phys. D.: Appl. Phys.* **44** 303001
- [16] Nogués J, Sort J, Langlais V, Skumryev V, Suriñach S, Muñoz J S and Baró M D 2005 *Phys. Rep.* **422** 65
- [17] Baibich M N, Broto J M, Fert A, Nguyen Van Dau F, Petroff F, Etienne P, Creuzet G, Friederich A and Chazelas J 1988 *Phys. Rev. Lett.* **61** 2472
- [18] Binasch G, Grünberg P, Saurenbach F and Zinn W 1989 *Phys. Rev. B* **39** 4828
- [19] Dieny B, Speriosu V S, Parkin S S P, Gurney B A, Wilhoit D R and Mauri D 1991 *Phys. Rev. B* **43** 1297
- [20] Chappert C, Fert A, Nguyen Van Dau F 2007 *Nature Mat.* **6** 813
- [21] Prejbeanu I L, Kerekes M, Sousa R C, Sibuet H, Redon O, Dieny B and Nozières J P 2007 *J. Phys.: Condens. Matter* **19** 165218
- [22] Prejbeanu I L, Bandiera S, Alvarez-Hérault J, Sousa R C, Dieny B and Nozières J P 2013 *J. Phys. D: Appl. Phys.* **46** 074002
- [23] Ernult F 2002 *Thèse Université Joseph Fourier*
- [24] Press W H, Flannery B P, Teukolsky S A and Vetterling W T 1990 *Numerical recipes (FORTRAN)* Cambridge University Press
- [25] Cowburn R P, Koltsov D K, Adeyeye A O, Welland M E and Tricker D M 1999 *Phys. Rev. Lett.* **83** 1042

- [26] **Vinai G**, Moritz J, Gaudin G, Vogel J, Bonfim M, Lançon F, Prejbeanu I L, Mackay K and Diény B 2013 *J. Phys. D: Appl. Phys.* **46** 345308
- [27] Vallejo-Fernandez G, Fernandez-Outon L E and O'Grady K 2008 *J. Phys. D: Appl. Phys.* **41** 112001
- [28] Nishioka K, Hou C, Fujiwara H and Metzger R D 1996 *J. Appl. Phys.* **80** 4528
- [29] Fecioru-Morariu M, Ali S R, Papusoi C, Sperlich M and Güntherodt G 2007 *Phys. Rev. Lett.* **99** 097206
- [30] Baltz V, Sort J, Rodmacq B and Diény B 2005 *Phys. Rev. B* **72** 104419
- [31] Carcia P F, Meinhardt A D and Suna A 1985 *Appl. Phys. Lett.* **47** 178
- [32] Carcia P F 1988 *J. Appl. Phys.* **63** 5066
- [33] Bandiera S 2011 *Thèse Université de Grenoble*
- [34] Soeya S, Imagawa T, Mitsuoka S and Narishige S 1994 *J. Appl. Phys.* **76** 5356
- [35] Ali M, Marrows C H, Al-Jaward M, Hickey B J, Misra A, Nowak U and Usadel K D 2003 *Phys. Rev. B* **68** 214420
- [36] Moritz J, **Vinai G** and Diény B 2012 *IEEE Magn. Lett.* **3** 4000244
- [37] **Vinai G**, Moritz J, Bandiera S, Prejbeanu I L and Diény B 2013 *J. Phys. D: Appl. Phys.* **46** 322001
- [38] Gökemeijer N J, Ambrose T and Chien C L 1997 *Phys. Rev. Lett.* **79** 4270
- [39] Akmalidinov K, Auffret S, Joumard I, Diény B and Baltz V 2013 *Appl. Phys. Lett.* **103** 042415





## Abstract

The interfacial coupling between a ferromagnetic (F) and an antiferromagnetic (AF) layer, known as exchange bias, is a physical phenomenon largely exploited in technological applications as spin valves and Magnetic Random Access Memories (MRAM). The F-AF coupling is namely employed for pinning the reference layer of the memory. In the innovative Thermally Assisted MRAM developed by Crocus Technology, the exchange bias is exploited to fix the magnetization direction in the storage layer. For the functioning of this type of devices for which reliability and data retention are key parameters, it is crucial to understand and control the finite size effects on exchange bias and its dot to dot variability as well as the thermal variations of magnetic properties.

In this thesis, finite size effects on IrMn/Co exchange biased dots were first studied on patterned arrays of square dots of lateral dimension from 200 to 50 nm. The study was focused on two aspects: the micromagnetic effects due to F thickness on nanometric dots and the microstructural effects due to the AF grain size distribution.

Second, a study on thermal effects was performed on IrMn/Co bilayers and (Pt(Pd)/Co)<sub>3</sub>/IrMn/Co trilayers. The latter structure, thanks to the presence of the out-of-plane layer, shows several improvements of exchange bias properties (IrMn critical thickness, exchange bias maximum value, blocking temperature and  $H_{ex}(T)$  curvature) compared to IrMn/Co bilayer.

**Keywords:** exchange bias, patterned dots, variability, thermal behaviour, structural properties

## Résumé

Le couplage d'échange entre une couche ferromagnétique (F) et une antiferromagnétique (AF) est un phénomène physique largement utilisé dans des applications technologiques comme les vannes de spin et les mémoires magnétiques à accès aléatoire (MRAM). Ce couplage est utilisé notamment pour fixer l'orientation de l'aimantation de la couche de référence de ces dispositifs. Dans une approche innovante de MRAM à écriture assistée thermiquement développée par Crocus Technology, le couplage d'échange est utilisé pour bloquer la direction de l'aimantation de la couche de stockage. Pour le fonctionnement de ce type de dispositifs, pour lesquels fiabilité et rétention des données sont des paramètres clé, il est crucial de comprendre et de contrôler les effets de taille finie sur le couplage d'échange, sa variabilité entre différents plots, ainsi que la dépendance thermique des propriétés magnétiques.

Dans le cadre de cette thèse, les effets de taille finie ont été étudiés sur des réseaux de plots carrés IrMn/Co couplés par échange, avec des tailles latérales allant de 200 à 50 nm. L'étude a été focalisée sur deux aspects: les effets micro-magnétiques dus à l'épaisseur de la couche F et les effets microstructuraux dus à la distribution de taille des grains dans l'AF.

Deuxièmement, les effets thermiques ont été étudiés dans les bicouches IrMn/Co et tricouches (Pt(Pd)/Co)<sub>3</sub>/IrMn/Co. Grâce à la couche à aimantation perpendiculaire supplémentaire dans les tricouches, plusieurs améliorations des propriétés d'échange ont été démontrées (l'épaisseur critique d'IrMn, la valeur maximale d'échange, la température de blocage et la courbure de la dépendance de  $H_{ex}$  avec la température notamment).

**Mots clés :** couplage d'échange, réseaux de plots, variabilité, comportement en température, propriétés structuraux